# Synthesis of spin crossover micro-and nano-particles and study of the effect of their sizes and morphologies on their bistability properties

Haonan Peng

# THÈSE

**En vue de l'obtention du**

## DOCTORAT DE L'UNIVERSITÉ DE TOULOUSE

**Délivré par :**

Université Toulouse 3 Paul Sabatier (UT3 Paul Sabatier)

---

**Présentée et soutenue par :**
**Haonan Peng**
**Le** lundi 20 juillet 2015
**Titre :**

Synthesis of spin crossover micro- and nano-particles and study of the effect of their sizes and morphologies on their bistability properties

---

ED SDM : Chimie moléculaire - CO 046

**Unité de recherche :**

Laboratoire de Chimie de Coordination - CNRS - UPR 8241

**Directeur(s) de Thèse :**

Lionel SALMON et Azzedine BOUSSEKSOU

**Rapporteurs :**

M. Yannick GUARI, Directeur de Recherche CNRS, Montpellier
M. Jose Antonio REAL, Professeur à l'Université de Valence, Espagne

**Autre(s) membre(s) du jury :**

Mr Eric BENOIST, Professeur à l'Université Paul Sabatier, Toulouse
M. Bruno DOMENICHINI, Professeur à l'Université de Bourgogne, Dijon
M. Lionel SALMON, Chargé de Recherche CNRS, Toulouse
M. Azzedine BOUSSEKSOU, Directeur de Recherche CNRS, Toulouse

# Acknowledgements

# Table of Content

# General Introduction

Nowadays, the idea that molecules can be used as active elements in an electronic device stimulates scientific activity of chemistry and physics laboratories worldwide. The information storage capacity from technological demands is growing exponentially and relies much on the development of nanosciences. The objective is to store data as quickly as possible in a device as small as possible. One of the most promising strategies is based on the concept of molecular bistability, the switching between two electronic states of a molecule in the same way as a binary switch. It is thus possible to pass in a reversible and detectable manner from one state (OFF = 0) to another state (ON = 1) under the influence of a controlled external stimulus.

The spin crossover (SCO) phenomenon also called spin transition (ST) phenomenon that switches the system between high spin (HS) and low spin (LS) states is a typical example of molecular bistability. The two states can be distinguished with different magnetic, optical and structural properties and can be induced by an external perturbation like temperature, light, pressure, magnetic field or the inclusion of a guest molecule. When the structural changes associated with the spin transition are transmitted in a cooperative manner across the molecular network, the transition will occur with steepness and possibly accompanied by a hysteresis loop (the first order transition).

Thus, spin transition molecular materials should offer many opportunities in terms of applications in the field of electronics, information storage, digital display, photonics and photo-magnetism. Among the different families of compounds, coordination polymers arouse much interest due to their bistability near room temperature. The judicious choice of ligands and counter-anions make possible to modulate the final properties of these compounds and even in some cases to synergistically combine different physical properties. The work developed in this thesis attempt to address the different issues related to the challenge of coordination polymers based nanoscale materials with spin transition. The synthesis of inorganic bistable materials, their development in micro- and nanoparticles, thin layers, their organization and their physical properties are addressed and presented.

The materials in the microscopic scale have mostly the same physical properties as those measured at the macroscopic scale. However, at the nanoscale, materials can exhibit physical properties that are far from those of bulk compounds. It is therefore imperative to understand more about the phenomena related to material size decrease to develop nanotechnology. The fundamental study of these nanomaterials is necessary and represents a major challenge today,

which is of prime importance for the development of future generation of applications. The development of nanoscale materials through the control of certain systematic models permits to improve our understanding of specific effects at the nanoscale. For example, in the case of spin crossover complex, the most important question is: how downsizing effect influences the transition temperature, the cooperativity and the width of hysteresis loop?

In this context, this thesis is devoted to the design and the synthesis of various size spin crossover nano and micro-materials with different morphologies. To accomplish this, we developed the reverse-micelle technique and adopted innovative matrix-free synthetic approaches.

The first section (1) of this thesis is divided into three subsections. The first sub-section (1.1) presents a general introduction to the spin transition by introducing the conceptual aspects and the most important historical facts on this phenomenon. In the second subchapter (1.2) we present the most important work in the field of spin crossover nanomaterials. This section included the development of thin films and patternings (introduction of various preparation methods), and nanoparticles (preparation, size and matrix effects and potential application). The third sub-section (1.3) addresses the general objective of this thesis.

The second part (2) is devoted to the synthesis of $[Fe(pz)\{Ni(CN)_4\}]$ nanoparticles and to the detailed size effect study on their SCO property. The first subchapter (2.1) is dedicated to the research progress already reported on the size and matrix effects on spin crossover $[Fe(pz)\{M(CN)_4\}]$ (M = Ni and Pt) nanoparticles. The second subchapter (2.2) will introduce the reverse nanoemulsion technique and details of the synthesis of a series of $[Fe(pz)\{Ni(CN)_4\}]$ nanoparticles. The subchapters (2.3-2.5) deal with the study of the composition and size of the $[Fe(pz)\{Ni(CN)_4\}]$ nanoparticles by elemental analysis, thermal analysis, X-ray powder diffraction, Raman spectroscopy, TEM (Transmission Electron Microscopy) and HRTEM (High Resolution Transmission Electron Microscopy) associated with EDX (Energy Dispersive X-ray Spectroscopy). In the sixth subchapter (2.6), the study of the spin crossover properties of the $[Fe(pz)\{Ni(CN)_4\}]$ nanoparticles by optical microscopy, Raman and Mössbauer spectroscopies and magnetic measurements is reported. In addition, the stiffness of the different nanoparticles was studied by measuring their Debye temperature exploring the Mössbauer data. In the seventh subchapter (2.7), in order to understand the behaviour of the spin crossover nanoparticles as a function of their size, a theoretical study based on a core-shell nanothermodynamic model is presented. In the last subchapter (2.8), by means of NIS spectroscopy (Inelastic Mössbauer spectroscopy), the size dependent vibrational DOS (Density of State) and its spin-state dependence have been probed and

permitted us to determine the speed of sound which also depends on the elastic properties of the different samples.

In the third chapter (3), spin crossover nanometric and micrometric rod-shaped particles of compounds from the Fe-triazole family were synthesized and fully characterized. Following a brief introduction on this family of compounds (3.1), the second subchapter (3.2) will introduce an original homogeneous acid medium method used to control the size of nano- and micro-rods of the $[Fe(Htrz)_2(trz)](BF_4)$ and $[Fe(Htrz)_3](BF_4)_2$ derivatives. Syntheses and spin crossover properties of the corresponding Zn diluted complexes are also reported and allow us to study the electrical charge transport properties in these materials. In the third subchapter (3.3), using similar homogeneous acid medium method, the synthesis of the new triflate $[Fe(Htrz)_2(trz)](CF_3SO_3)$ and $[Fe(Htrz)_3](CF_3SO_3)_2$ micro-rods derivatives is also reported. The full physico-chemical characterization reveals a very interesting and appealing room temperature bistability.

# Chapter 1

# Introduction of the Spin Crossover (SCO) Phenomenon

## 1.1 The Spin Crossover Phenomenon

### 1.1.1 Introduction

The first report of spin crossover (SCO) phenomenon can be retraced to 1930s, when Cambi and co-workers were studying on iron(III) dithiocarbamate complex.[1] A significant magnetic moment change of these complexes could be observed as a function of temperature, which means the electronic configuration within iron(III) ion changed. However this phenomenon attracted the extensive interest of scientists until 1964, when Baker and Bobonich synthesized the first spin crossover complex [Fe(1,10-Phenanthroline)$_2$-(NCS)$_2$].[2] Then in 1967 Konig and Madeja performed extensive magnetic and Mössbauer spectroscopic studies on these complexes and developed the nature of thermal induced spin transition from the low spin (LS) to the high spin (HS) state in some of the first iron(II) SCO complexes.[3] In 1984, scientists found that a green light could switch the spin state from LS to HS at low temperature, which is referred as the Light Induced Excited Spin State Trapping phenomenon (LIESST).[4] Now it is well known that not only temperature and light but also pressure, magnetic field[5] can be used to switch the spin crossover materials. In the basis of this knowledge and the discovery of hysteretic spin crossover at room temperature,[6] studies for future applications in photonic, electronic and spintronic devices have intensified. The orientation of the field towards such applications required the development and organization of nano-sized objects based upon spin crossover complexes. Nanomaterials possess unique nano-scale, size-dependent physical and chemical properties that can be controlled in a way that is not feasible in bulk materials. The first results concerning the synthesis of SCO nanoparticles were reported in 2004.[7,8] These authors described the synthesis of [Fe(NH$_2$trz)$_3$]Br$_2$ (NH$_2$trz = 4-amino-1,2,4-triazole) nanoparticles of ca. 70 nm size with a thermal hysteresis loop using a water-in-oil microemulsion technique. Since that, numerous reports about the design and synthesis of spin crossover nanoparticles and thin films have been reported.[9-12] As we all know, the macroscopic behavior of bulk SCO materials is

strongly influenced by electron–lattice coupling effects. In particular the modification of the volume and the shape of the molecules accompanying the spin-state change leads to considerable elastic interactions between them. These interactions give rise to various cooperative phenomena, such as first-order phase transitions or self-accelerating relaxations and thus, an important still open question in our field is: what is the effect of the size reduction of materials on their spin crossover properties?

Recent reviews on the diverse aspects of the field concerning different family of spin crossover material[13-15], the different stimuli used[16-19], the structural-properties relationship[20,21], the spin transition at room temperature[22], the synthesis of nano-material[9-12], and thin films[11,12,23] and the applications[10,24] have been recently reported.

## 1.1.2 Crystal Field Theory

Crystal Field Theory was proposed by the physicist Hans Bethe in 1929.[25] Subsequent modifications were proposed by J. H. Van Vleck in 1935 to allow for some covalency in the interactions.[26] Crystal Field Theory describes the interaction between a central metal ion that is surrounded by anions, which was developed to describe important properties of complexes (magnetism, absorption spectra, oxidation states, coordination,). A quantum mechanical description of the metal ion is employed, with attention focused on the valence shell d, s, and p orbitals. The surrounding anions are typically treated as point charges.

To understand Crystal Field Theory, one must understand the description of the five degenerate d- orbitals (see figure 1.1.1):

•$d_{xy}$: lobes lie in-between the x and the y axes.

•$d_{xz}$: lobes lie in-between the x and the z axes.

•$d_{yz}$: lobes lie in-between the y and the z axes.

•$d_{x^2-y^2}$: lobes lie on the x and y axes.

•$d_{z^2}$: there are two lobes on the z axes and there is a donut shape ring that lies on the xy plane around the other two lobes.
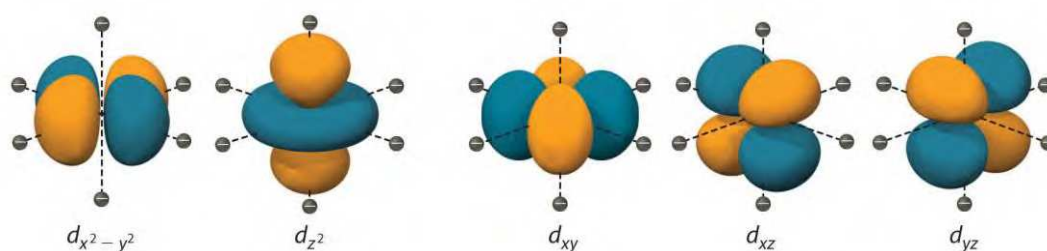


Figure 1.1.1: Representation of the 3$d$ orbitals.

Following Hund's rule, orbitals are filled in order to have the highest number of unpaired electrons. For example, for a $d^3$ complex, there would be three unpaired electrons. If one add an electron, however, it has the ability to fill a higher energy orbital ($d_{z^2}$ or $d_{x^2-y^2}$) or pair with an electron residing in the $d_{xy}$, $d_{xz}$, or $d_{yz}$ orbitals. This splitting of the electrons requires energy $\Delta$ (the crystal-field splitting energy). For octahedral complexes, crystal field splitting is denoted by $\Delta_o$ (or $\Delta_{oct}$). where the $d_{xy}$, $d_{xz}$ and $d_{yz}$ orbitals will be lower in energy than the $d_{z^2}$ and $d_{x^2-y^2}$, which will have higher energy, because the former group is farther from the ligands than the latter and therefore experience less repulsion. The three lower-energy orbitals are collectively referred to as $t_{2g}$, and the two higher-energy orbitals as $e_g$.

The $\Delta_{oct}$ of the d-orbitals plays an important role in the electron spin state of a coordination complex. There are three factors that affect the $\Delta_{oct}$: the period (row in periodic table) of the metal ion, the charge of the metal ion, and the ligand field strength of the complex as described by the spectrochemical series. The strength of $\Delta_{oct}$ determines the electronic structure of the $3d^4$ - $3d^7$ transition metal ions. In complexes of metals with these d-electron configurations, the non-bonding and anti-bonding molecular orbitals can be filled in two ways: one in which as many electrons as possible are put in the non-bonding orbitals before filling the anti-bonding orbitals, and one in which as many unpaired electrons as possible are put in.
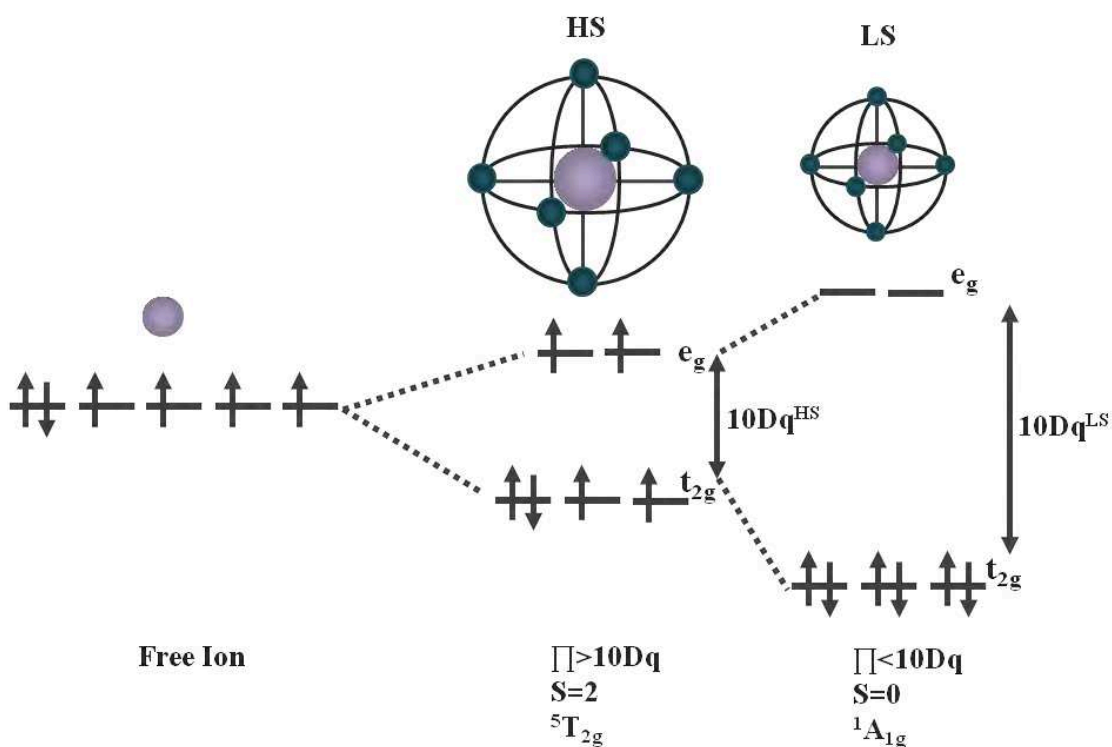


Figure 1.1.2: Separation of the d orbitals in an octahedral environment induced by the ligand field strength 10Dq.

The former case is called low-spin **(LS)**, while the latter is called high-spin **(HS)**. A small $\Delta_{oct}$ can be overcome by the energetic gain from not pairing the electrons, leading to high-spin. When $\Delta_{oct}$ is large, however, the spin-pairing energy becomes negligible by comparison and a low-spin state arises (see figure 1.1.2).

The origin of these two spin states can be predicted by Tanabe Sugano diagrams[27,28] (see figure 1.1.3). In this method the energy of the electronic states are given on the vertical axis and the ligand field strength increases on the horizontal axis from left to right. The Tanabe-Sugano diagram shows electronic states and the energies of excited states in units of the Racah parameter of electron-electron repulsion B relative to the respective ground state, versus the ligand field strength in 10$Dq$, also in units of B. Among the 3d transition metal ions which do show typical spin crossover behaviour, the largest number of examples is found for the configuration d$^6$ (Fe$^{II}$): from a point of view, the low-spin configuration d$^6$ has maximum ligand field stabilisation energy; from another point of view, the relatively large Fe(II) ion induces a weaker ligand field with most ligands. Hence here we take the Fe(II) complexes as an example, with weak-field ligands, the high-spin $^5T_{2g}(t_{2g}^4 e_g^2)$ state results as the ground state, which arises from the $^5D$-ground state of the free ion. Thus, with strong-field ligands, the low-spin $^1A_{1g}(t_{2g}^6)$ state becomes the ground state.
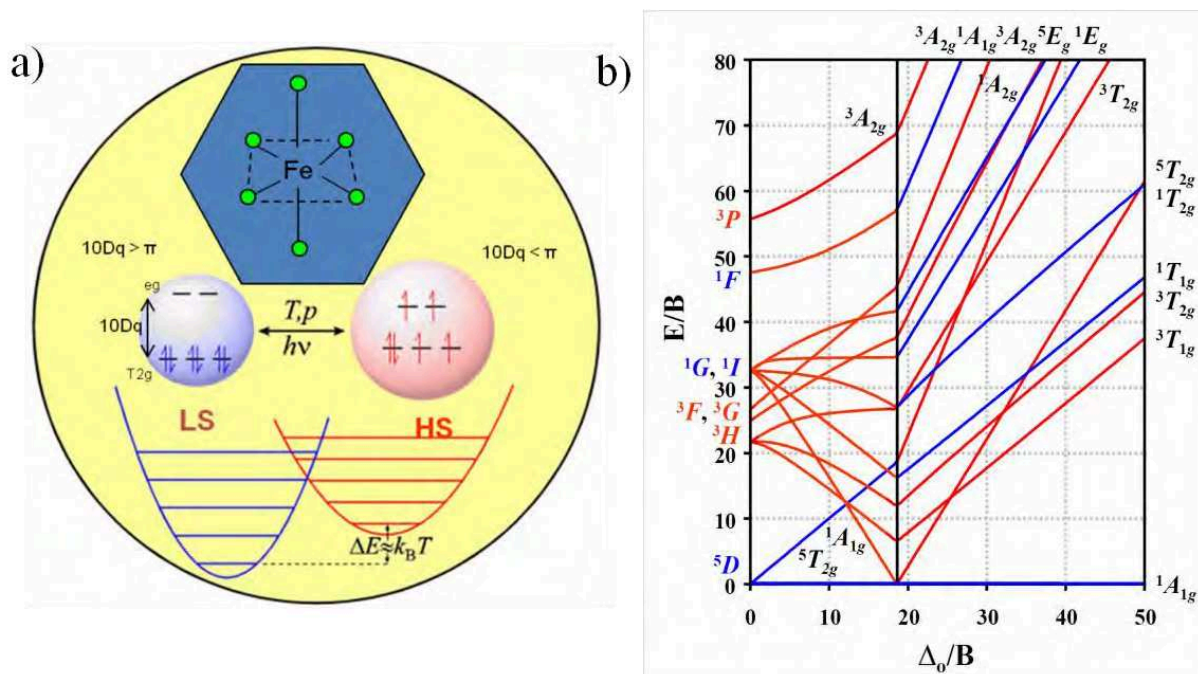


Figure 1.1.3: High spin (weak ligand field) and low spin (strong ligand field) electronic configurations of 3d$^6$ Fe(II) in an octahedral complex (left); Tanabe-Sugano diagram for a transition metal ion with six d electrons.

Crystal field theory is based primarily on symmetry of ligands around a central metal/ion and how this anisotropic (properties depending on direction) ligand field affects the metal's atomic orbitals; the energies of which may increase, decrease or not be affected at all. Once ligands' electrons interact with electrons of the d-orbitals, the electrostatic interactions cause the energy levels of the d-orbital to fluctuate depending on the orientation and the nature of the ligands. The spectrochemical series is an empirically-derived list of ligands ordered by the strength of the splitting Δ that they produce. It can be seen that the low-field ligands are all π-donors (such as I$^-$), the high field ligands are π-acceptors (such as CN$^-$ and CO), and ligands such as $H_2O$ and $NH_3$, which are neither, are in the middle.

$I^- < Br^- < S^{2-} < SCN^- < Cl^- < NO^{3-} < N^{3-} < F^- < OH^- < C_2O_4^{2-} < H_2O < NCS^- < CH_3CN <$ py (pyridine) $< NH_3 <$ en (ethylenediamine) $<$ bipy (2,2'-bipyridine) $<$ phen (1,10-phenanthroline) $< NO^{2-} < PPh_3 < CN^- < CO$.
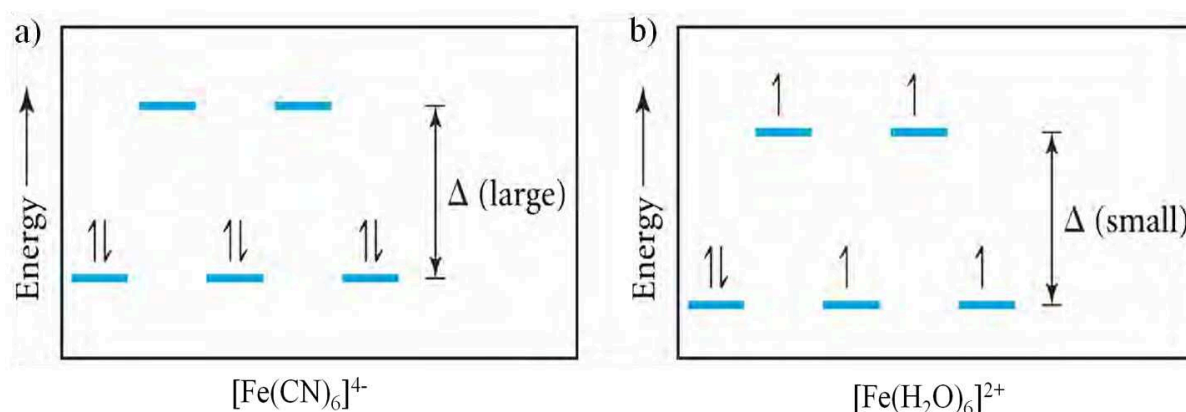


Figure 1.1.4: **a)** Low Spin $[Fe(CN)_6]^{4-}$ crystal field diagram; **b)** High Spin $[Fe(H_2O)_6]^{2+}$ crystal field diagram.

The ligand field splitting depends not only on the properties of the ligands but also on the metal-to-ligand distance r, so the electronic energies of the particular spin states have to be considered as a function of r (see figure 1.1.5). Independently of the ligand properties, the $^5T_2$-potential well is shifted to a higher metal-to-ligand distance compared to the $^1A_1$-potential well, as two electrons occupy the σ-anti-bonding $e_g$-orbitals in the HS state ($t_{2g}^4 e_g^2$ configuration), whereas the six d-electrons are situated in the σ-non-bonding $t_{2g}$-orbitals in the LS state ($t_{2g}^6$ configuration), which affects the bond lengths in a minor degree.[29,30] Spin crossover is expected, when the zero-point energy difference of both states ($\Delta E^0_{HL} = \Delta E^0_{HS} - \Delta E^0_{LS}$) is in the order of magnitude of the thermal energy ($k_B T \approx \Delta E^0_{HL} \approx 200$ cm$^{-1}$ at $T = 295$ K). In this case, at low temperatures, the $^1A_1$-state of lowest enthalpy is the

thermodynamically stable ground state. On the other side, at temperatures higher than a equilibrium temperature $T_{1/2}$, the $^5T_2$-state becomes the thermodynamically stable state, as the entropy associated with the HS state is much larger than the entropy associated with the LS state and therefore the entropy gain overcomes the enthalpy loss.[31] In detail, approximately 25% of the total entropy gain accompanying the LS to HS change arises from the change in spin multiplicity. The major contribution originates from changes in the intramolecular vibrations.[32,33] Against this background, ranges for $10Dq^{HS}$ and $10Dq^{LS}$ can be specified, at which HS, LS or SCO complexes are expectable.

Except temperature, other external stimuli such as magnetic fields, pressure or electromagnetic radiation, besides the LIESST-effect,[34] or chemical parameters such as counter-ions, substituent and solvent effects can also influence the spin transition.
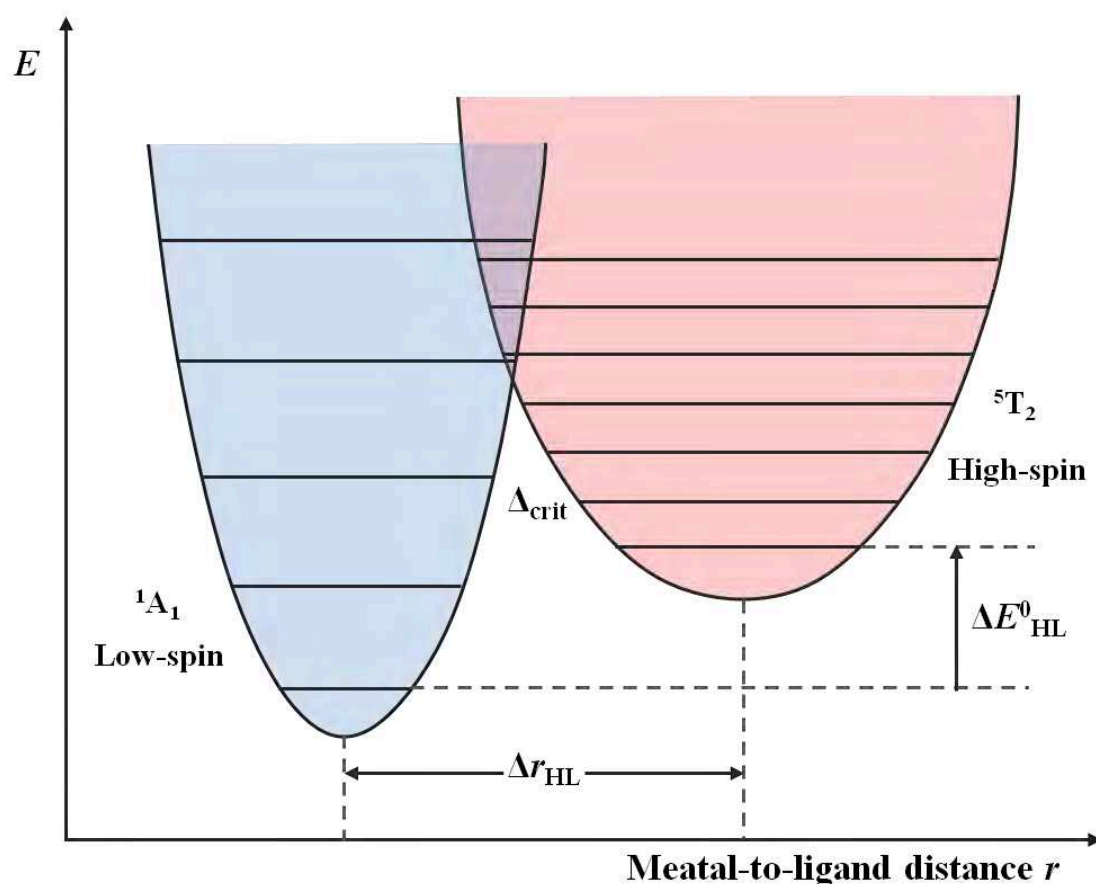


Figure 1.1.5: Potential energy of the high spin ($^5T_{2g}$) and low spin ($^1A_{1g}$) states along the totally symmetric metal – ligand stretching coordinate in the harmonic approximation.

## 1.1.3 Entropic Origin of the Thermal Spin Crossover

The spin transition can also be characterized as phase transition in a system constituted by an assembly of isolated spin crossover molecules without interaction with each other. Under common experimental conditions (isothermal and isobaric), the thermodynamical function for this particular system is the Gibbs free energy variation $\Delta G = \Delta G_{HS} - \Delta G_{LS}$ between the HS and LS phases[33,35]:

$$\Delta G = \Delta H - T\Delta S \qquad (1.1)$$

where $\Delta H$ and $\Delta S$ correspond to the enthalpy and entropy variations during the transition LS $\rightarrow$ HS, respectively. Equation **1.1** shows that at low temperatures, the system is dominated by the term of the enthalpy; conversely, at high temperatures it is the term of the entropy that becomes the dominant factor privileging the statistical disorder. $\Delta H$ can be divided into two contributions, an electronic part $\Delta H_{el}$ estimated in 0 - 1000 cm$^{-1}$ (0 - 12000 J·mol$^{-1}$) and a vibrational part $\Delta H_{vibr}$ estimated in 100 cm$^{-1}$ (1200 J·mol$^{-1}$). Hence, we can assume that the main contribution to $\Delta H$ is in most cases electronic ($\Delta H \approx \Delta H_{el}$) and its sign is most of the time positive during a LS $\rightarrow$ HS transition.

The entropy variation $\Delta S$ has also two different main parts. First, there is an electronic contribution $\Delta S_{el}$ that is attributed to the change of the total spin momentum S ($\Delta S_{el}^{spin}$) and the change of the angular orbital momentum L ($\Delta S_{el}^{orb}$) when a LS $\rightarrow$ HS transition takes place. These two quantities can be written as a function of the ratio of the spin and orbital multiplicities in the two molecular states:

$$\Delta S_{el}^{spin} = N_a k_b ln \left(\frac{2S_{HS}+1}{2S_{LS}+1}\right), \qquad (1.2)$$

$$\Delta S_{el}^{orb} = N_a k_b ln \left(\frac{2L_{HS}+1}{2L_{LS}+1}\right), \qquad (1.3)$$

where $N_a$ and $k_b$ are the Avogadro's number and the Boltzmann constant, respectively. However, the orbital degeneracy is taken only in the case of a perfect octahedral symmetry which is unusual for the complexes of molecular systems. In consequence, most of the times

the approximation $\Delta S \approx \Delta S_{el}^{spin}$ is considered and in the case of a spin transition between $^{1}A_{1}$ and $^{5}T_{2}$, $\Delta S_{el}^{spin} = 13.38$ J·K$^{-1}$·mol$^{-1}$.

Heat capacity measurements in Fe(II) based SCO complexes have demonstrated that the $\Delta S_{Total}$ during the spin crossover has typical values between 40 J·K$^{-1}$·mol$^{-1}$ and 80 J·K$^{-1}$·mol$^{-1}$.[35] Since these values are considerably higher to that of a simple change of spin multiplicity during the transition, an additional contribution of vibrational origin $\Delta S_{vib}$ has to be considered. This contribution comes mainly from the stretching mode of the elongating distance Fe-N and also from the distortional modes of the octahedron FeN$_{6}$ (15 vibrational modes). Additionally, it is worth noting that the degeneracy of vibrational origin is higher in the HS state than that of the LS state, then during a LS $\rightarrow$ HS SCO there will be a large increase of the statistical disorder.

As a result, it is possible to conclude that at low temperature $\Delta H_{el}$ is the dominant term and the LS state is stable; on the contrary, as the temperature increases the entropic term T$\Delta S_{Total}$ becomes more important and the state with higher degeneracy becomes stable, i.e. the HS state. Furthermore, there is a temperature of equilibrium ($T_{eq}$) at which G$_{HS}$ = G$_{LS}$. It is obtained when the quantity of molecules in the HS and LS state are the same; from equation **1.1** we can infer that Teq = $\Delta H_{el}$ / S. Hence, the thermal SCO is governed by entropic phenomena of mainly vibrational origin ($\approx$ 70%).[36]

## 1.1.4 Spin Transition Curves

A spin transition curve is conventionally obtained from a plot of high spin fraction ($\gamma_{HS}$) as a function of temperature (see figure 1.1.6). a) The gradual transition is perhaps the most common and is observed when cooperative interactions (the cooperativity signifies the strength of the intermolecular interactions) are relatively weak. As an example, transitions in solution may be interpreted as a thermal Boltzmann distribution. b) The abrupt transition results from the presence of strong cooperativity. c) When the cooperativity is particularly high, hysteresis may results. There are two principal origins of hysteresis in a spin transition curve: the transition may be associated with a structural phase change in the lattice and this change is the source of the hysteresis; or the intramolecular structural changes that occur along with a transition may be communicated to neighbouring molecules via a highly effective cooperative interaction between the molecules. The mode of this interaction is not always clear but three principal strategies have been adopted in an attempt to generate it: (i) linkage of the SCO centres via covalent bonds in a polymeric system; (ii) incorporation of

hydrogen bonding centres into the coordination environment allowing interaction either directly with other SCO centres or via anions or solvate molecules; (iii) incorporation of aromatic moieties into the ligand structure which promote π-π interactions through stacking throughout the lattice. Partial success has been achieved for all three approaches but a full understanding of the factors involved remains one of the major challenges of the area. d) The multistep transition was first reported in 1981 for an iron(III) complex of 2-bromo-salicylaldehyde-thiosemicarbazone, are relatively rare and have their origins in several sources.[37] The most obvious is the presence of two lattice sites for the complex molecules. In addition, binuclear systems can give rise to this effect, even when the environment of each metal atom is the same.[38] e) The transition accompanied by residual high (or low) spin fraction may also arise from various reasons. A fraction of the complex molecules may be in a different lattice site in which the field strength is sufficiently reduced to prevent the formation of low spin species. In addition, it is possible in a number of instances to freeze-in a large high spin fraction by quenching of the sample. This effect is often observed around liquid nitrogen temperature but would obviously be more common at still lower temperatures.[39]
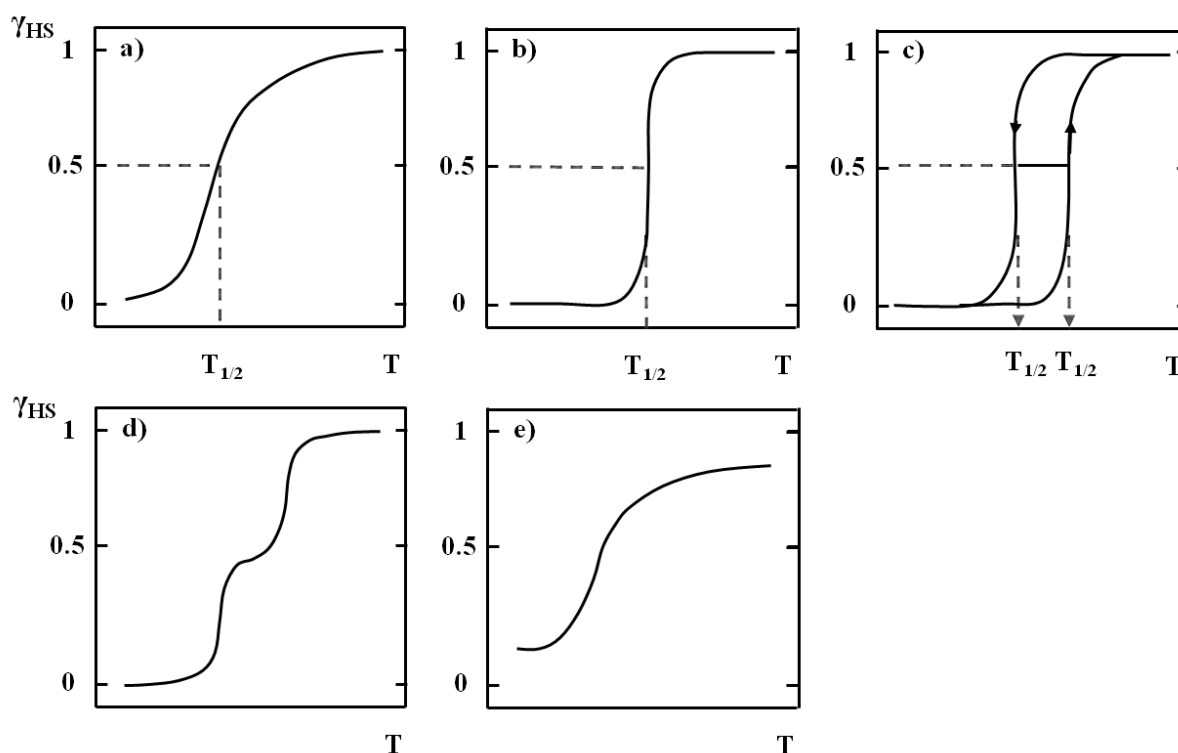


Figure 1.1.6: Principle types of the thermal SCO responses plotting the high spin fraction ($\gamma_{HS}$) as a function of temperature. **a)** gradual, **b)** abrupt, **c)** with hysteresis, **d)** two steps and **e)** incomplete.

## 1.1.5 Examples of Spin Crossover Materials

Although there are many different families SCO complexes, we will focus mainly on two: Hofmann clathrates and Fe-triazoles. Since 2005, our group has devoted many efforts into the synthesis and physical-chemical characterization for various members of these two families. One of the main motivations for working with these types of compounds is their characteristic transition around room temperature and with hysteresis. It is precisely this feature that has potential to create promising research axes towards the development of spin crossover based photonic and electronic devices for gas and temperature sensing applications employing diverse techniques such as Surface Plasmon Resonance (SPR)[40,41], diffraction gratings[42], luminescence[43,44] and Atomic Force Microscopy (AFM)[45].

## 1.1.5.1 Hofmann Clathrates

The quest for improving the "communication" between the SCO centres has led to the search of new compounds that allow not only more rigid frameworks, but also more versatile systems from a chemical and structural point of view. For these reasons, heteronuclear systems with the architecture of Hofmann clathrate type $((M1(L)_x[M2(CN)_y])\cdot G$, where L is an organic ligand, M1 is the SCO center, M2 is a metal such as Ni(II), Pd(II), Pt(II), Ag(I), etc and G is a guest molecule, are of particular interest.
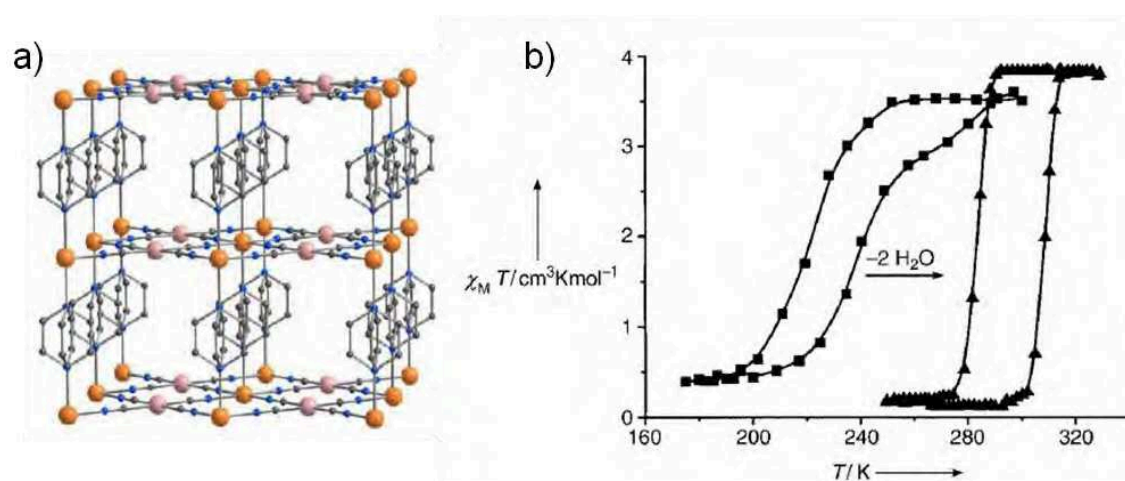


Figure 1.1.7: **a**) Perspective of a fragment of [Fe(pyrazine){Pt(CN)$_4$}] 3D coordination polymer (Color code: Fe, pink; Pt, orange; N, blue; C, gray). **b**) Graph of $\chi_M T$ versus $T$ for [Fe(pyrazine){Pt(CN)$_4$}] in the cooling and heating modes before and after thermal treatment at 430 K.

This family of compounds can be two or three dimensional depending on the type of ligands[46]. The first SCO compound of this family was the 2D complex [Fe(pyridine){Ni(CN)$_4$}] and it was synthesized by the group of Kitazawa.[47] A few years later, Real et al. changed the ligand of the same compound to pyrazine and obtained a SCO compound with a 3D framework [Fe(pyrazine){M(CN)$_4$}]·2H$_2$O (with M = Ni, Pd, Pt).[48] These 3D compounds are characterized by a strong cooperativity. It was found that the 3D compounds (pyrazine based) presented a SCO response more cooperative than their 2D analogs (pyridine based) with wide hysteresis (from 20 K to 40 K width) and at higher temperatures (see figure 1.7). This fact was attributed to the internal pressure induced by the more rigid 3D structure that tends to stabilize the LS state in the case of the pyrazine complex.

Generically formulated [Fe(L){M(CN)$_4$}] have been reported (L=bpac (4,4′-bis(pyridyl)acetylene)[49,50], azpy (4,4-azopyridine)[51], dpe (trans isomer)[52], dpa (1,2-di(4-pyridyl)ethane)[53], dpsme (4,4′-di(pyridylthio)methane)[54] and bpeben (1,4-bis(4-pyridylethynyl)benzene)[55] and M = Pd, Pt or Ni, see figure 1.1.8). The ligand is bis-bidentate bridging between two atoms of Fe (II). The study of the physical properties[56,57] (magnetism, XRD, Raman ...) shows various spin transition temperatures for the different compounds (see table 1.1). For example, for compound [Fe(bpac){Pt(CN)$_4$}], the magnetic measurements show a spin transition with a loop hysteresis 63 K centered at room temperature ($T_{1/2}(\downarrow)$ = 262 K and $T_{1/2}(\uparrow)$ = 325 K) for the product in its dehydrated form while in the case of the [Fe(azpy){Pt(CN)$_4$}] compound (dehydrated monocrystals), the transition is shifted to lower temperatures by showing a cycle hysteresis 18 K centered at 181 K ($T_{1/2}(\downarrow)$= 172 K  and $T_{1/2}(\uparrow)$= 190 K).
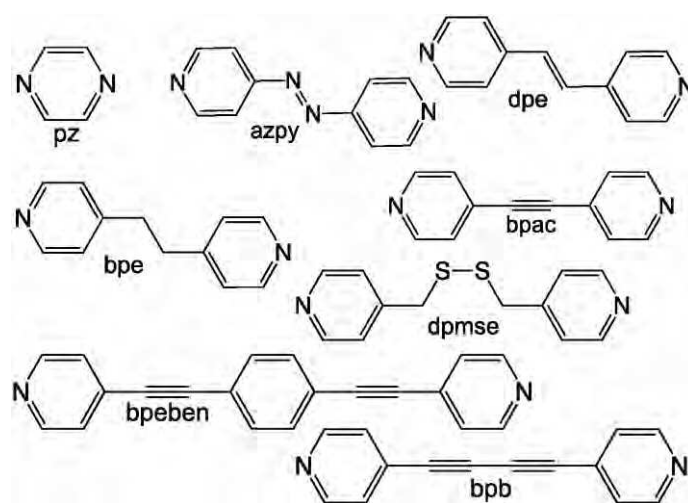


Figure 1.1.8: Structure of different ligands incorporated in 3D Hofmann clathrate complexes.

| Ligand | Metal | T/SCO (K) hydrated form | T/SCO (K) dehydrated form |
|--------|-------|------------------------|---------------------------|
| pz | Pt | 220/240 | 285/310 |
| | Pd | 233/266 | Not reported |
| | Ni | 280/305 | 290/300 |
| bpac | Pt | 310/310 | 262/325 |
| | Pd | 308/328 | 260/317 |
| | Ni | 238/251 | 225/225 |
| azpy | Pt | 275/285 | 175/190 |
| | Pd | 287/296 | 181/202 |
| | Ni | 245/245 | 245/245 |
| dpe | Pt | *243/243, 275/275 | 135/150 |
| bpa | Pt | **240/240, 212/216, 197/200 | **210/210, 178/181, 162/164 |
| dpsme | Pt | **134/154, 130/153, 117/148 | Not reported |

Table 1.1: Common [Fe(L){Pt(CN)$_4$}] systems reported in the literature and their thermal SCO temperatures for hydrated and dehydrated form. Two steps (∗) and three steps (∗∗) SCO transition.

The SCO 3D coordination polymers are currently an active research field due to their characteristic cavities at the nanometric scale; these have the potential for hosting guest molecules inside the molecular frameworks that could eventually modulate the SCO response of the system.[58-61] In the Hofmann clathrates frameworks, there are two host-guest interaction sites: one is on the organic bridges and another one is in the M tetracoordinated metal center, which are active to many kinds of guests[54,55,62-65]. As a result, applications of storage, filtration and sensors can be imagined. The most studied Hofmann clathrate is [Fe(pz){M(CN)$_4$}] (M = Pt, Ni and Pd). For example, for the adsorption of dihalogen guest[66] although a trend was observed (the larger the halogen is, the higher of the induced transition temperature shift is), the effect on [Fe(pz){Pt(CN)$_4$}] can be either HS stabilization (Cl$_2$) or LS stabilization (Br$_2$ and I$_2$). After that, a remarkable control over the transition temperature

was realized by the system [Fe(pz){Pt(CN)$_4$}(I)], in which controlling the iodine content in the porous complex permitted to obtain consecutive $T_{1/2}$ from 300 to 400 K while keeping the hysteresis loop[67] (see figure 1.1.9). For aromatic molecules,[68,69] due to the interaction with the pyrazine ligands via π-π stacking, the aromatic rings can stabilized the HS state. In contrast, the CS$_2$ has been reported to stabilize the LS state, which was explained by a strong interaction of CS$_2$ with both the ligand and metal sites with electronic structure methods.[70-72] In addition, water and hydroxyl solvents stabilized the HS state of [Fe(pz){M(CN)$_4$}] complexes too.[72]
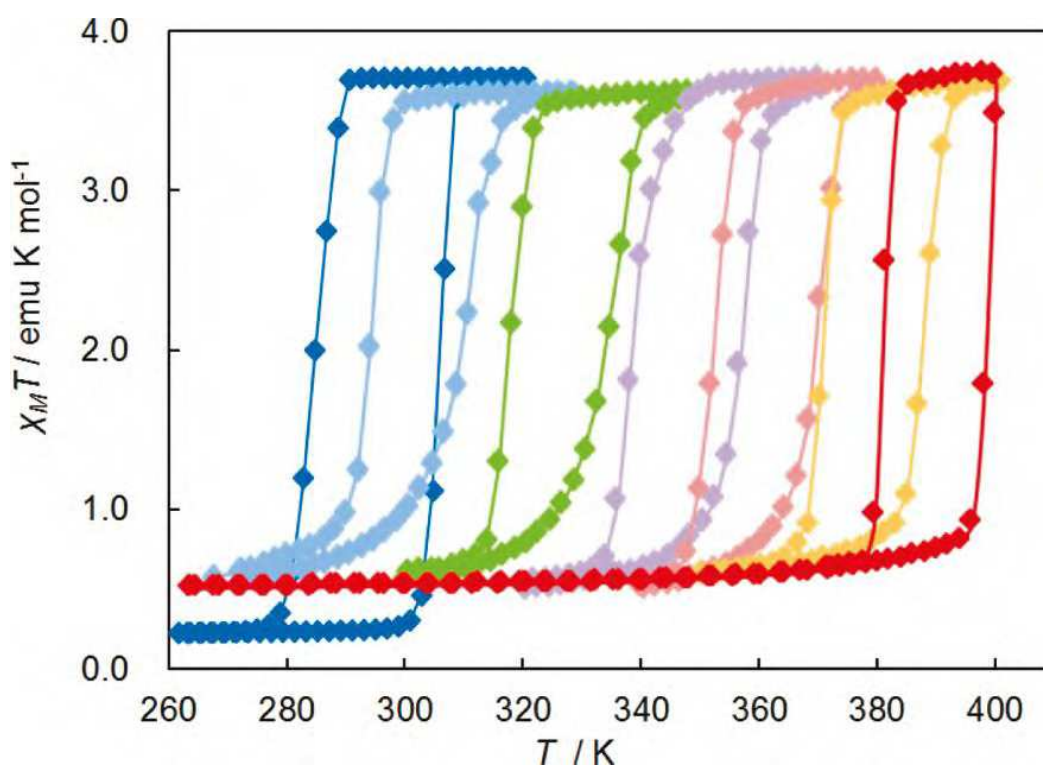


Figure 1.1.9: Magnetic behavior of [Fe(pz){Pt(CN)$_4$(I)$_n$}] (1-I$_n$); n = 0.0 (blue); 0.1 (sky blue); 0.3 (green); 0.5 (violet); 0.7 (pink); 0.9 (orange); (blue); 0.1 (sky blue); 0.3 (green); 0.5 (violet); 0.7 (pink); 0.9 (orange); 1.0 (red).

The guest effect on Hofmann clathrate [Fe(bpac){M(CN)$_4$}] (M = Ni, Pd and Pt) which has a larger pore volume was studied by our group. The adsorption of 2, 4, 6-trichlorophenol show a significant π-π stacking interaction between guest molecule with the bridging bpac ligand and similar contacts are expected for pyridine,[73,74] and mono-halogen substituted benzenes (chlorobenzene, bromobenzene, iodobenzene) as guests.[75-77] These volatile guests

allowed to prepare guest-free [Fe(bpac){Pt(CN)$_4$}] MOF, which show potential in sensing application (see figure 1.1.10).
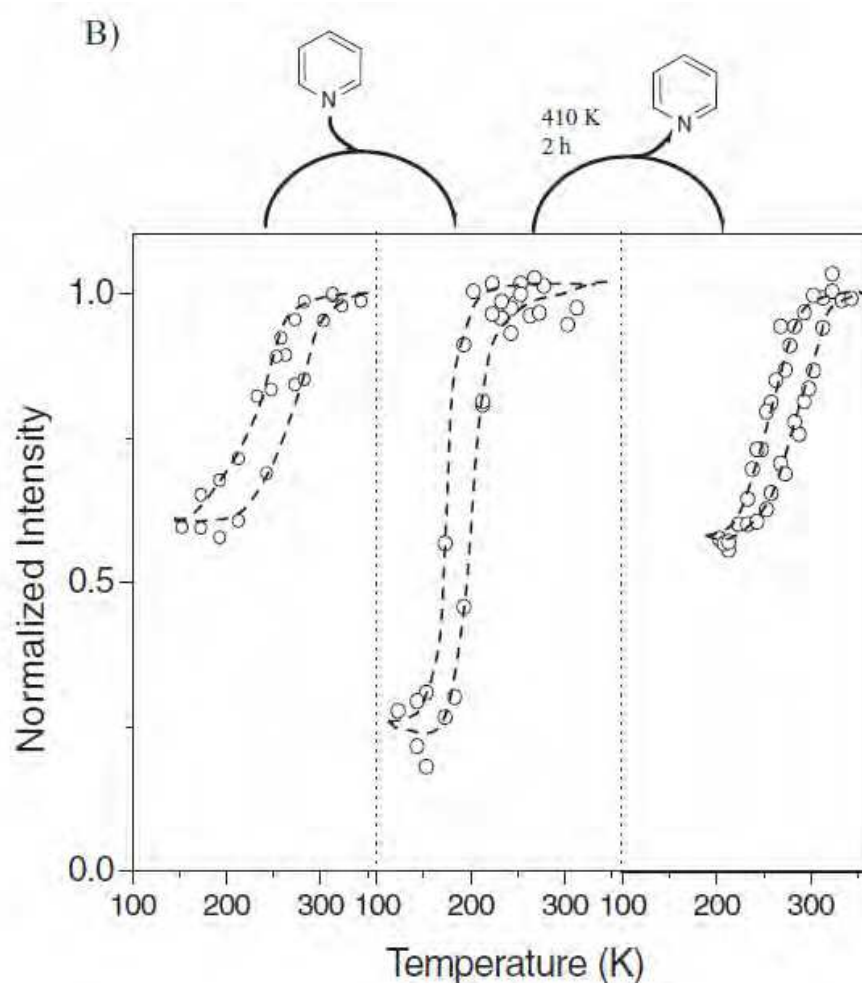


Figure 1.1.10: Effect of pyridine uptake and thermal desorption on the spin crossover properties of [Fe(bpac){Pt(CN)$_4$}].

Taking advantage of the versatility of these materials, active ligand[62] and guest active molecule[78] were also used to regulate or switch the spin crossover properties. The adsorption of maleic anhydride guest in [Fe(pz){Pt(CN)$_4$}] MOF was studied.[78] The active guest turns the cooperative spin transition of [Fe(pz){Pt(CN)$_4$}] into two-step transition. But due to the chemical conversion from maleic anhydride to maleic acid upon exposure to moisture at room temperature, the transition became incomplete. Moreover, this conversion can be recovered by heating the material (see figure 1.1.11).
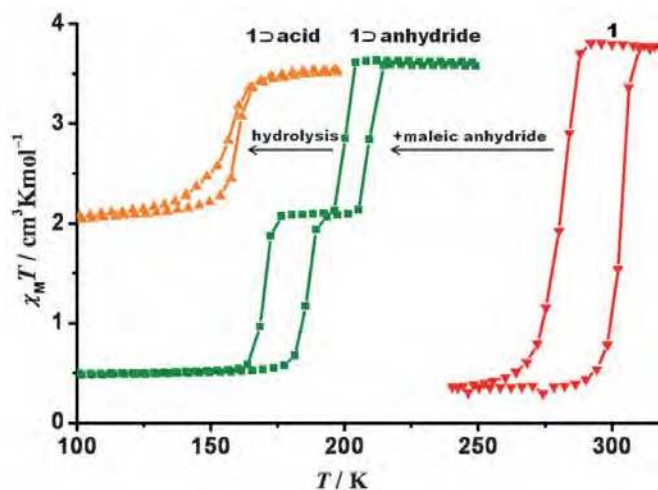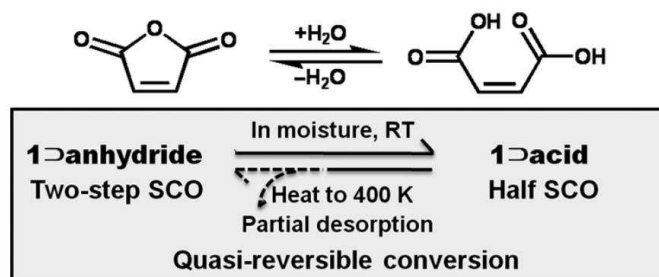
Figure 1.1.11: Interconversion between maleic anhydride and maleic acid (above); variable-temperature magnetic susceptibility studies of [Fe(pz){Pt(CN)$_4$}], [Fe(pz){Pt(CN)$_4$}]⊃anhydride, and [Fe(pz){Pt(CN)$_4$}]⊃acid (below)

## 1.1.5.2 Fe-Triazoles SCO Polymers

There is a large number of SCO complexes with the form of polymer chains including the ligand 1,2,4-triazole (trz) and its derivatives.[79] This type of [Fe(Rtrz)$_3$]A$_2$·nH$_2$O (with R = different substrant, A = counter ion) are composed of 1D "polymeric" chains of triazole-bridged metal ions (see figure 1.1.12).[80,81] Nevertheless, the first single crystal-based description of compound of this family concerns the compound [Fe(NH$_2$trz)$_3$](NO$_3$)$_2$·2H$_2$O.[82] This study definitively proves the 1-D polymeric nature of the crystal structure and allows a description of the [Fe(Rtrz)$_3$] chains, as well as of the anions and water implementation within the crystal lattice. The high cooperativity generally obtained in these compounds can be due to the short Fe-Fe distances and also the rigidity of the triazole ligands and its covalent connectivity.
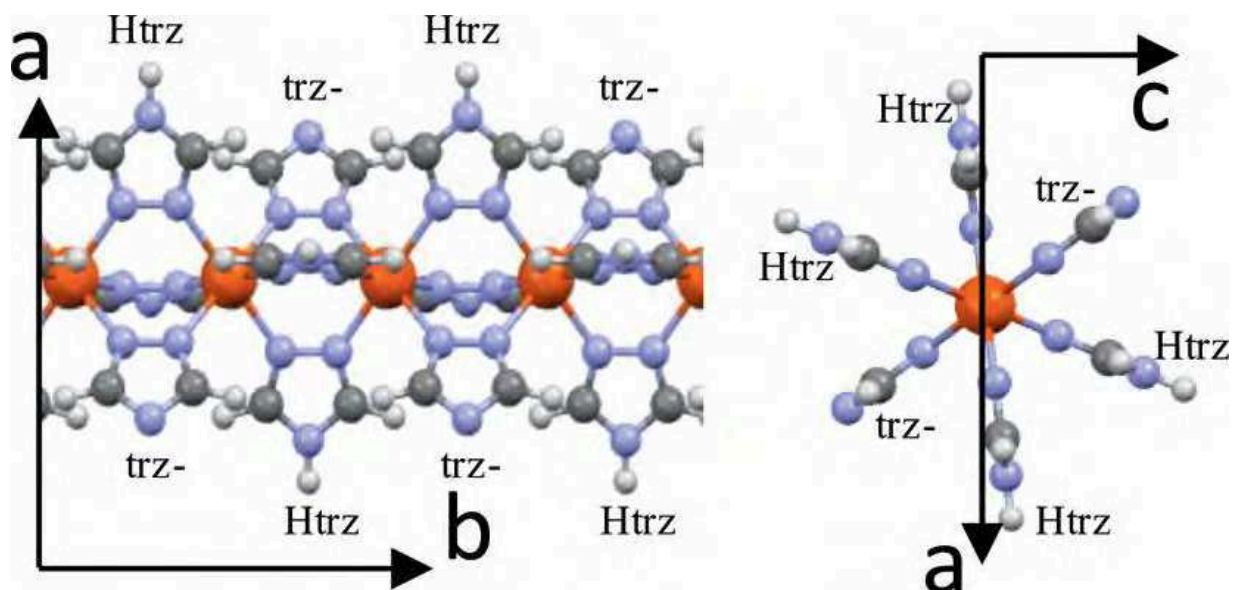
Figure 1.1.12: View of a segment of the [Fe(Htrz)$_2$(trz)]$_n$ chain (left) along c and (right) along b. Both views underline the specific positions of Htrz and trz$^-$. Blue: nitrogen; orange: iron; dark-grey: carbon; light-grey: hydrogen.
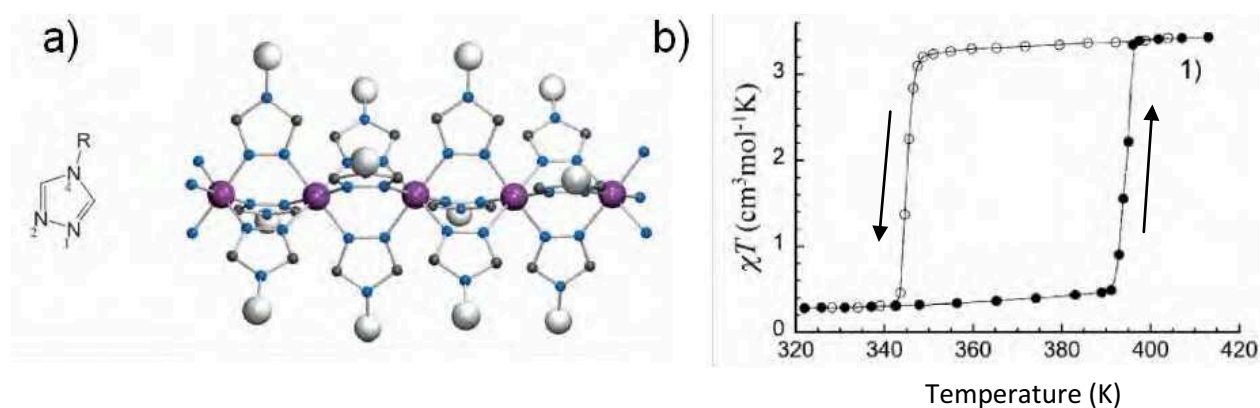


Figure 1.1.13: **a)** Fragment of a 1D [Fe(R-trz)$_3$]$_n^{2+}$.[83] **b)** Magnetic susceptibility measurement of the compound [Fe(Htrz)$_2$(trz)](BF$_4$).[84]

Because of the possibility to modify the nature of the 4-substituent on the triazole ligand and/or the choice of the counter-anion ([Fe(Rtrz)$_3$][A]$_2$), the SCO temperature and cooperative character can be tuned. In the table 1.2, we show a selection of Fe-triazole complexes.

| Triazole | Anion | $T$/SCO (K) | Triazole | Anion | $T$/SCO (K) |
|---|---|---|---|---|---|
| (Htrz)$_2$trz (A) | BF$_4^-$ | 345/385 | | Cl$^-$/Br$^-$/I$^-$ | 270/316 |
| (Htrz)$_2$trz (B) | BF$_4^-$ | 323/343 | | NO$_3^-$ | 310/347 |
| (Htrz)$_2$trz | CF$_3$SO$_3^-$ | 162/166 | NH$_2$trz | TaF$_7^{2-}$ | 217/217 |
| Htrz | BF$_4^-$ | 323/345 | | SiF$_6^-$ | 241/255 |
| | ClO$_4^-$ | 341/358 | | TiF$_6^{2-}$ | 179/230 |
| | PF$_6^-$ | 269/279 | | ZrF$_6^{2-}$ | 179/230 |
| | B$_{10}$H$_{10}^-$ | 233/246 | | SnF$_6^{2-}$ | 179/230 |
| | SiF$_6^-$ | N/A | | BF$_4^-$ | 180/255 |
| | CF$_3$SO$_3^-$ | 278/327 | | ClO$_4^-$ | 165/240 |
| NH$_2$trz | BF$_4^-$ | 250/260 | C$_n$trz | Cl$^-$ | 290/361 |
| | ClO$_4^-$ | 247/249 | | NO$_3^-$ | 270 |
| | PF$_6^-$ | 180 | n=18 | | |
| | B$_{10}$H$_{10}$ | HS | | CF$_3$SO$_3^-$ | 195/240 |
| | CH$_3$SO$_3^-$ | 273/288 | | ptol$^-$ | 285/335 |

Table 1.2: Common [Fe(Rtrz)$_3$][A]$_x$ systems reported in the literature and SCO temperatures (hydrated and dehydrated). See reviews for an exhaustive list of [Fe(Rtrz)$_3$][A]$_x$ complexes.[85-87]

## 1.1.5.3 Diluted Fe complex

In the solid state, the existence of intermolecular interactions leads to a large variety of transitions, going from very gradual to discontinuous ones. In order to know more about these interactions, scientists try to move the spin-crossover molecules away from each other by diluting them. From 1993, the diluted Fe$_x$M$_{1-x}$- L complex was studied by different groups[88-91]. Lavrenova et al. synthesized and studied three series of heterometallic solid phases based on iron(II) nitrate complexes with 4-amino-1,2,4-triazole as ligands, such as [Fe$_x$Zn$_{1-x}$(NH$_2$trz)$_3$](NO$_3$)$_2$ (0.01 < x < 0.8),[14] [Fe$_x$Ni$_{1-x}$(NH$_2$trz)$_3$](NO$_3$)$_2$ (0.1 < x < 0.9),[91] and [Fe$_x$Ni$_{1-x}$-(Htrz)$_3$](NO$_3$)$_2$ (0.1 < x < 0.9).[92] It was found that as x decreases, that means, Zn$^{2+}$ or Ni$^{2+}$ substitute Fe$^{2+}$ ions, a modification of T$_{1/2}$ and a gradual SCO is observed. Similar results were obtained for the [Fe$_x$Ni$_{1-x}$(pz){Pt(CN)$_4$}] derivatives (see figure 1.15).
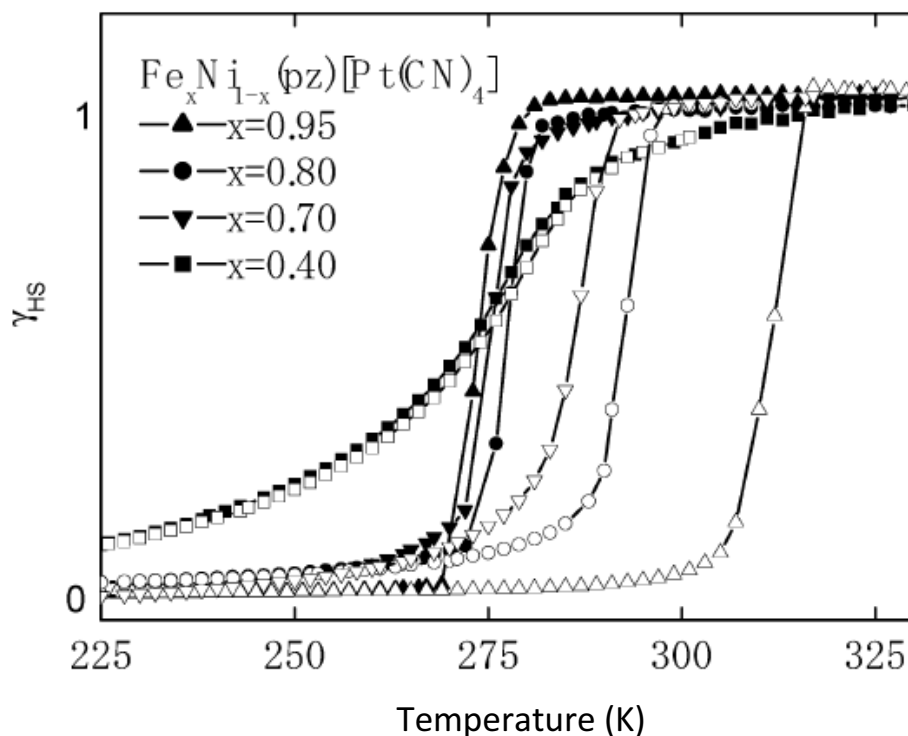
Figure 1.1.14: $\gamma_{HS}$ vs $T$ curves for some selected x values in the cooling (●,▲,■,▼) and heating (○, △,□,▽) modes for the $[Fe_xNi_{1-x}(pz)\{Pt(CN)_4\}]$ derivatives.

Zarembowitch et al. studied the metal dilution effects of $[Fe_xCo_{1-x}(btr)_2(NCS)_2]\cdot H_2O$(btr = 4,4'-bis-1,2,4-triazole by magnetic and calorimetric measurements, and $^{57}$Fe Mössbauer spectrometry, and also found that the hysteresis loop became narrower and the spin transition became less abrupt as the percentage of Co metal increases.[93]

Another approach to design diluted spin crossover complex is mixing two types of ligands. For complex $[Fe(Htrz)_3](ClO_4)_2\cdot nH_2O$, the spin transition hysteresis loop is just above room temperature, which can be modified by replacing Htrz by a mixture of Htrz and 4-$NH_2$trz. The formula of the diluted compound is $[Fe(Htrz)_{3-x}(4-NH_2trz)_{3x}(ClO_4)_2\cdot nH_2O$, when x = 0.05, the transition occurs on either side of room temperature[94] (see figure 1.1.15).

Another kind of diluted method involves mixed counter anions instead of mixed ligands. The spin-transition temperatures for a given type of cationic chains $[Fe(Rtrz)_3]$ have been found to depend on the nature of the counter anion A, hence the spin-transition regime can be also fine tuned through the composition of alloys of the formula $[Fe(Rtrz)_3]A_xA'_{1-x}\cdot nH_2O$.[95]
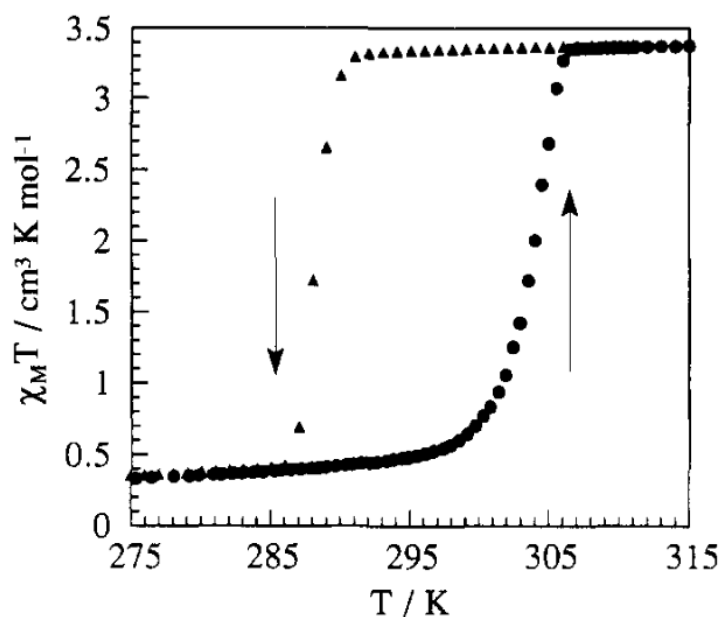
Figure 1.1.15: $\chi_M T$ versus $T$ plot for $[Fe(Htrz)_{3-x}(4-NH_2trz)_{3x}(ClO_4)_2 \cdot nH_2O$ with x = 0.05 in both the warming and the cooling modes.

## 1.1.6 Detection of the Spin Crossover Phenomenon

As a function of the stimulus employed for triggering the spin crossover phenomenon (temperature change, pressure, magnetic field, or light …), diverse experimental techniques can be used to monitor the electronic state of the spin crossover centre. An overview of the experimental techniques that are used in this thesis is provided by table 1.3.

| Experimental Techniques | Characteristic Value |
|---|---|
| Magnetic measurements | Magnetic susceptibility |
| Mössbauer spectroscopy | Isomer shift and electric quadrupole splitting |
| Nuclear Inelastic Scattering | Vibrational Density of State, speed of sound |
| Vibrational Spectroscopy | Metal-ligand vibrational frequencies |
| Optical Spectroscopy | Metal-to-ligand charge transfer |
| Calorimetric Measurements | Heat capacity |

Table 1.3: Experimental techniques used in this thesis to follow a spin transition

## 1.1.6.1 Magnetic Measurements

As the spin transition corresponds to a change in the number of unpaired electrons, for example, in the case of iron (II) the high spin state is paramagnetic with four unpaired electrons and the low spin state is diamagnetic, so measurement of magnetic susceptibility as a function of temperature, $\chi(T)$, has always been the principal technique for characterisation of SCO compounds. The Evans NMR method is generally used for liquid state measurements. For the solid state measurements Faraday balance or SQUID (Superconducting Quantum Interference Device) are usually used. A comprehensive survey of the techniques and computational methods used in magnetochemistry is given by Palacio et al.[96]. As the susceptibility of the sample is proportional to the percentage of material in the high spin state this can be used to construct a spin transition curve. However, it should be noticed that magnetism is a property of the bulk material while the spin transition is a feature of individual molecules and that a change in magnetism alone is not sufficient to prove the existence of the spin transition. According to $\chi(T) = \gamma_{HS} \cdot \chi_{HS} + (1 - \gamma_{HS}) \cdot \chi_{LS}$, the mole fraction of the high spin state (or low spin state) $\gamma_{HS}$ in function of the temperature is derived and plotted to produce the spin transition curve.

## 1.1.6.2 Mössbauer Spectroscopy

Mössbauer spectroscopy, also known as nuclear gamma resonance fluorescence spectroscopy, is a technique that probes transitions between the ground and low-lying excited states of the nucleus[97] (see Annex 2). The most favourite nucleus to Mössbauer spectroscopy is $^{57}$Fe and hence iron containing compounds are widely investigated. The most important Mössbauer spectral parameters are the isomer shift, electric quadrupole splitting and magnetic dipole splitting. They arise from the hyperfine interactions between the nucleus and its surrounding electric and/or magnetic field. The isomer shift is proportional to the s-electron density at the nucleus, and hence is directly influenced by the s-electron population and indirectly (via shielding effects) by the d-electron population in the valence shell. It is only weakly temperature dependent and gives valuable information about the oxidation state, spin state, and bonding properties. For example, the isomer shift of $Fe^{(II)}$ compounds is usually more positive than that of Fe(III), as the extra electron in the d-shell present in $Fe^{(II)}$ decreases the s-electron density at its nucleus. Electric quadrupole splitting $\Delta E_Q$ is observed when an inhomogeneous electric field at the Mössbauer nucleus is present. In general, two factors can contribute to the electric field gradient, a non-cubic electron distribution in the valence shell

and/or a nearby, non-cubic lattice environment. Thus $\Delta E_Q$ data yield informations on local molecular symmetry, in a complementary manner to the isomer shift, oxidation and spin state.

## 1.1.6.3 Nuclear Inelastic Scattering (NIS)

In Mössbauer spectroscopy, the process of recoil-free absorption or scattering of resonant photons by an ensemble of nuclei is essentially an elastic scattering process. The corresponding probability is given by the Lamb-Mössbauer factor $f_{LM}$. However, nuclear resonant scattering is also possible for the incident photons due to the influence of lattice dynamics on the absorption of γ-quanta by nuclei. In this case, the interaction involves the recoil of the scattering nucleus with energy transfer from or to the crystal lattice in order to fulfill the resonance condition. This process of absorption with recoil (recoil fraction, 1−f) is called nuclear inelastic scattering (NIS), which appears as sidebands over an energy range of about ±100 meV.

Soon after the discovery of the Mössbauer effect, it was proposed by theoretician that lattice vibrations should occur as sidebands of the absorption line, permitting the measurement of a phonon spectrum. However, in a conventional Mössbauer experiment it is very difficult to observe such vibrational sidebands that appear roughly ±100 meV in the vicinity of the resonance transition energy. NIS generally performed at synchrotron radiation sources does not deal with phonon dispersion relations but gives direct access to the vibrational density of phonon states (VDOS).

## 1.1.6.4 Vibrational Spectroscopy

Accompanying a transition from high spin to low spin, the strengthening of the metal-donor atom bonds occurs. In a series of far-infrared or Raman spectra measured as a function of temperature, the vibrational bands belonging to the HS and the LS species can be readily recognized because of the corresponding position shift and intensity change. Typical examples are the N-coordinated ligands $NCS^{-1}$. As in the system $[Fe(phen)_2(NCS)_2]$, in the high spin state the C-N stretching bands are found as a strong doublet near 2060–2070 $cm^{-1}$, while in the low spin state the intensity of this doublet decreases in favor of a new doublet appearing at 2100–2110 $cm^{-1}$.[98]

### 1.1.6.5 Optical Spectroscopy

The drastic color change accompanying the spin transition due to the change of the electronic configuration of the spin crossover centers gives a possibility to monitor the spin crossover phenomenon by means of optical reflectance and absorption spectroscopy. Since the absorbance is closely proportional to the concentration of the color centre, when normalized appropriately, these absorption spectra directly yield the temperature dependence of the molar fraction of the metal ions in the LS or HS states.

### 1.1.6.6 Calorimetric Measurements

Thermodynamic parameters such as enthalpy and entropy changes accompanying the spin transition can be estimated by calorimetric measurements (Differential Scanning Calorimetry). The spin transition can be considered as a phase transition associated with a change of the Gibbs free energy $\Delta G = \Delta H - T\Delta S$, as discussed in chapter 1. 1. 2. The enthalpy change $\Delta H = H_{HS} - H_{LS}$ is typically 10 to 20 KJ·mol$^{-1}$, and the entropy change $\Delta S = S_{HS} - S_{LS}$ is of the order of 50 to 80 J·mol$^{-1}$·K$^{-1}$.[99]

### 1.1.6.7 Other Techniques

The temperature dependence of X-ray powder and crystal diffraction data can be diagnostic of the nature of the spin transition (gradual or abrupt), and of changes in the lattice parameters. Positron annihilation spectroscopy (PAS), the muon spin rotation (MuSR) technique, Atomic Force Microscope (AFM)[45], diffraction[100] and fluorescence technique[101] were also used to detect spin transition.

# 1.2 Spin Crossover Nano-Materials

The spin-transition complexes exhibit some fundamental features such as magnetic and optical transitions, and bistability that make them relevant for further investigation as storage media. The increasing importance of storage media reveals a need, and in the meantime a challenge, for small size (for example nano scale) and high-density storage media. In the last few years research with the aim of synthesizing nano scale spin crossover (SCO) materials (thin films and nanoparticles), manipulating them at reduced length scales, investigating their size dependent properties and exploring their possible applications in future nanophotonic, nanoelectronic and spintronic devices has intensified.[12]

## 1.2.1 SCO Thin Film and Patterning

Over the past few decades, the assembly of thin films and patterns with spin crossover complex has attracted enormous research interest for its potential utility in emerging nanotechnologies such as molecular memories, sensors, displays[9,10,12,102-107] and more recently in hybrid electronics[108] and optoelectronics media[109]. However, there are several major challenges for the application of spin crossover complexes in many of the aforementioned technologies. For example the fragility of the SCO phenomenon depends on the fact that SCO properties critically depend on the molecular environment (e.g. packing, crystallinity, solvent molecules, anions, etc.). Recently a great effort has been made towards the growth of thin films and the fabrication of nanostructures. The synthesis of new more stable and processable compounds and the development of new specifically dedicated procedures for processing have permitted important progress, opening new technological perspectives for SCO compounds, and renewing the interest in the field.

### 1.2.1.1 Langmuir–Blodgett

A Langmuir-Blodgett (LB) film was first found by Irving Langmuir and Katharine B. Blodgett in 1930th,[110] which can be defined as one or more monolayers of material deposited from a liquid surface onto a solid substrate by dipping the substrate through a floating monolayer at a constant molecular density (see figure 1.2.1). Then in 1998, Soyer and co-workers fabricated the first SCO thin film by the LB technique.[111] By modifying the sub-phase, the amphiphilic iron(II) complex [$Fe^{II}L_2(NCS)_2$], where L is a substituted bipyridine]

was deposited on $CaF_2$ substrate with stable chemical properties. Infrared spectroscopy at variable temperature showed that the spin transition still occurs in this lamellar material. Then in 1999, the same group synthesized a semi-fluorinated derivative of a spin crossover complex that shows astonishing stability in the Langmuir film, allowing the formation of perfectly defined LB films of such a molecule. Furthermore, for the first time the spin crossover process in multilayers can be followed by SQUID susceptometer.[112] Another appealing result on LB films was reported by J. A. Kitchen et al. in 2010, in which the long alkyl chain substituent Fe(II)-triazole complex facilitates the formation of a stable Langmuir–Blodgett film at an air–water interface and displays spin transition property at room temperature.[113] It is in the ideal range for functional devices, i.e. systems that operate at or near room temperature.
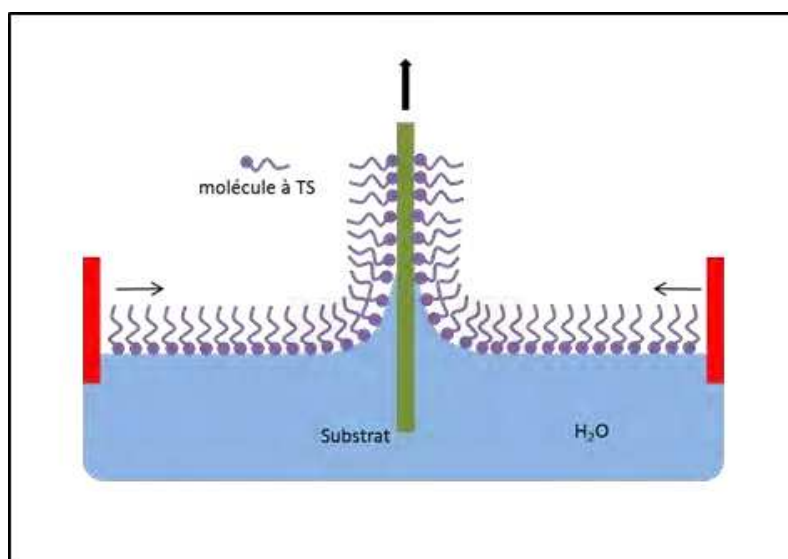


Figure 1.2.1: Schematic diagram of the Langmuir-Blodgett film preparation.

The LB technique can provide very good homogeneity and thickness control of the order of one monolayer, but as a disadvantage requires the presence of specific amphiphilic functional groups in the SCO, and is therefore materials-dependent.

## 1.2.1.2 Drop Casting

Drop casting is a very simple way for the fabrication of thin film. In this way a drop of solvent is left on top of a surface until all solvent evaporates, then the thin film with drying spots or non-uniform coverage is obtained (see figure 1.2.2). These difficulties may arise in particular from micro-flows within the drop. Because of the differences in evaporation rate

between the center and the edge of the drop, there is creation of concentration gradients and temperatures that will hinder the formation of a uniform film thickness. This is a very rustic method, however it's very easy to implement in the laboratory and is often used for preliminary tests or to filmmaking when homogeneity is not critical.
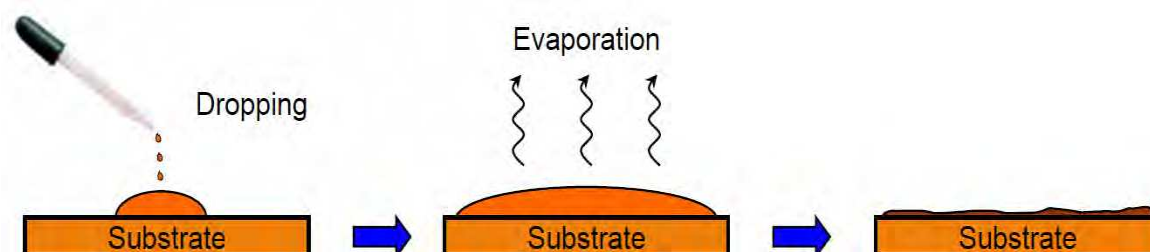


Figure1. 2.2: Process flow diagram of drop casting technique

In 2011, Massimiliano and co-workers reported a drop casting thin film of a room-temperature-switchable 1-D spin-crossover compound.[114] By controlling the experimental conditions (the partial pressure of the solvent), the film thickness deposited ranges from 5 to 50 μm, however, they did not contribute to SCO application. Keita and co-workers also developed a casting film with Fe(II)-1,2,4-triazole complexes, which exhibited sluggish spin-crossover behavior compared with the bulk sample and no thermal hysteresis.[115] The absence of the abrupt spin transition in the casting film can be attributed to the decrease in interchain interactions (and cooperativity) among 1D Fe(II)(triazole)$_3$ coordination chains, which results from the introduction of long alkyl substituents.[116] The drop casting method is both simple and applicable to all soluble complexes, but it yields inhomogeneous and micron-thick films.[114,116]

## 1.2.1.3 Spin Coating

This technique, illustrated in figure 1.2.3, is most commonly used for making homogeneous films of functional materials. In particular, this is the classic technique for depositing lithographic resins in microelectronics. It consists of depositing on a substrate a solution of molecules quickly spreads, and then comes a solvent evaporation step. Thus we can obtain thin layers of material.
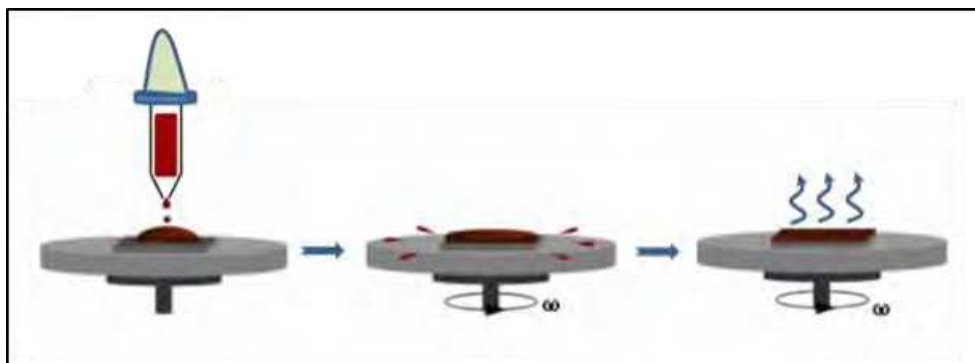
Figure 1.2.3: Process flow diagram of spin coating technique

Spin-coating is a simple, widely-used method in organic/polymer electronics, but there are very few reports on films obtained by spin-coating because the solubility of most SCO complexes in standard solvents is low. This was used for the first time in 2004, by Bousseksou and colleagues,[117] then in 2007, Masaki and co-workers prepared a spin coated thin film of spin crossover complex $[Fe(dpp)_2](BF_4)_2$ (dpp = 2,6-di(pyrazollyl)pyridine), which exhibited spin transition at around 260 K.[118] Furthermore, they found that the temperature dependence of the electrical resistance of the film changes with the spin transition. So in the subsequent work, they fabricated a novel electroluminescent (EL) device consisting of $[Fe(dpp)_2](BF_4)_2$ and chlorophyll, which showed reproducible on–off switching of light emission accompanied by the spin transition.[109] In 2011, our group developed a thin film with the thickness about 30 nm by spin coating. The spin crossover phenomenon of the spin-coated films of $[Fe(hptrz)_3](OTs)_2$ can be characterized by the temperature dependence of the plasmon resonance angle. The observed plasmon resonance angle shift occurs primarily due to the volume change (density) accompanying the SCO.[119] Then, also in our group the spin crossover complex $[Fe(hptrz)_3](OTs)_2$ doped with the acridine orange was deposited on the quartz substrate by spin coating. Owing to a radiationless energy transfer process between the low spin Fe(II) ions of the complex and the luminophore, we have been able to follow the spin state changes through luminescence measurements even in thin films at thicknesses below 100 nm (see figure 1.2.4).[43] In 2014, Ogawa et al. synthesized spin crossover nanoparticles, which can disperse well in various organic solvents. By spin coating technique, the nanoparticles form homogeneous thin films on substrates and can keep the abrupt spin transition property.[120]
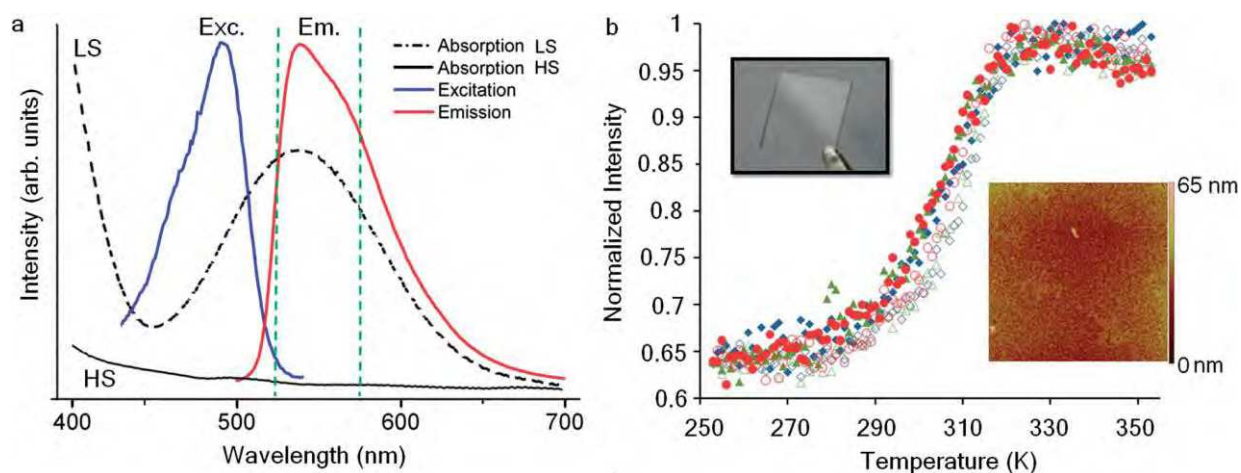
Figure 1.2.4: **a**) Normalized excitation and emission spectra of [Fe(hptrz)$_3$](OTs)$_2$ doped with acridine orange in the solid state at room temperature (RT). Blue: excitation spectrum for 560 nm emission; red: emission spectrum for 450 nm excitation; black: absorption spectra of an undoped chloroform solution of [Fe(hptrz)$_3$](OTs)$_2$ at RT (dashed line, LS state) and 320 K (solid line, HS state). Vertical dashed lines depict the spectral pass band used in fluorescence microscopy experiments. **b**) Normalized thermal variation of the luminescence intensity at 550 nm with an excitation at 450 nm in a spin coated thin film (85 nm) of [Fe(hptrz)$_3$](OTs)$_2$ doped with acridine orange during three consecutive thermal cycles (*dT*/dt ¼ 2 K min$^{-1}$; open and closed symbols for heating and cooling modes, respectively). Insets: photograph of a spin coated SCO thin film on a 1 cm$^2$ quartz substrate and AFM image (34 × 34 μm$^2$) of its surface.

## 1.2.1.4 Chemical Deposition

This approach consists to construct layer by layer thin films by successive chemical bonding, and can directly synthesis spin crossover complex on the surface of different substrates. In 2003,[121,122] Akio and co-workers developed the first chemical deposition thin film with the [Fe$^{II}$(H-trz)$_3$]n complex through ion-exchange resin (Nafion) as counter anion (see figure 1.2.5). The thin film presented spin crossover phenomenon at around 260 K. During this process, because the electrical negative charge mobile anions (SO$_4^{2-}$) was identical to that of the ion-exchange group (SO$_3^{2-}$) in the Nafion matrix, it is difficult to guarantee the homogeneity of the thin films. Furthermore, it is interesting to study the optimization of the surface, as the size distribution can influence the spin crossover.
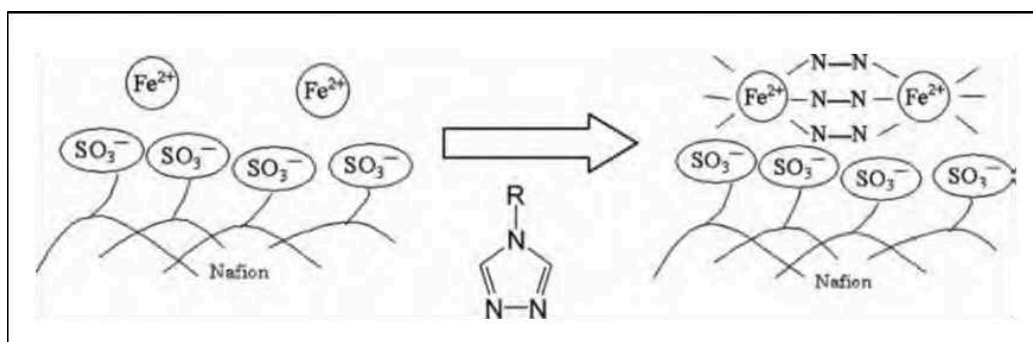
Figure 1.2.5: Film preparation process of Fe$^{II}$(R-trz) - Nafion (N-N means the R-trz ligand).

By layer-by-layer assembly method, a number of examples for successful multilayer assembly through coordination bonding have been reported.[123-125] Inspired by these studies, our group reported the successful deposition of the three dimensional (3D) spin-crossover coordination polymers, [Fe(pyrazine){M(CN)$_4$}] (M=Ni, Pd, or Pt) on Au substrate (see figure 1.2.6).[126] By the temperature dependence of the normalized Raman intensity ratio of modes corresponding to the pyrazine ligand, we successfully showed that the spin crossover still occurs with hysteresis and around room temperature.
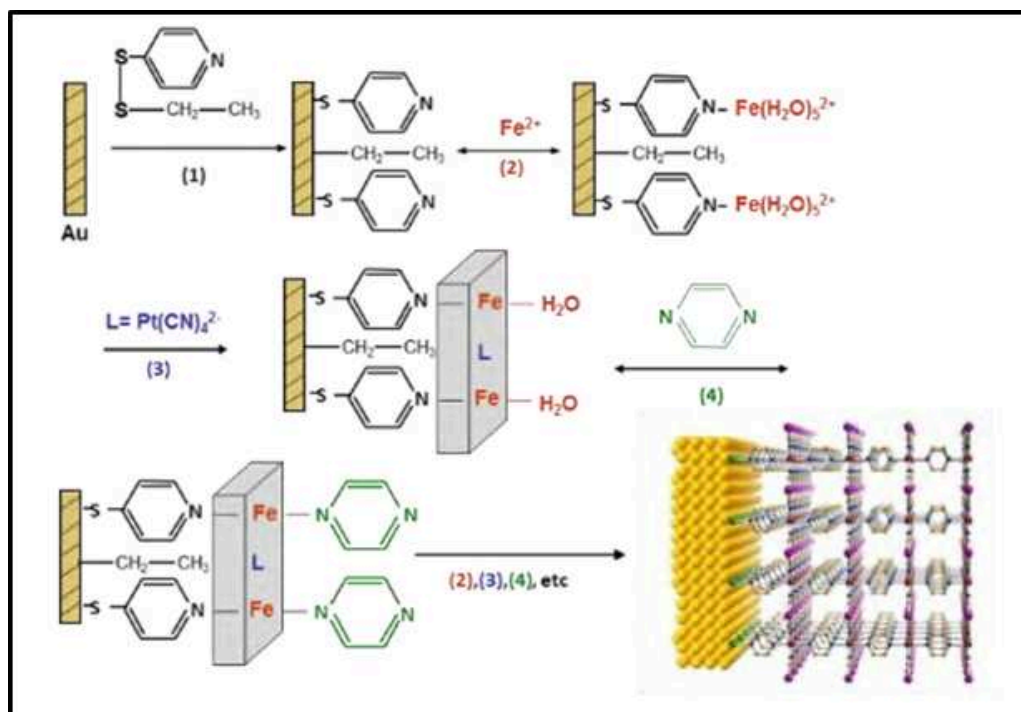


Figure 1.2.6: Film preparation process (layer by layer) of the compound [Fe(pyrazine){Pt(CN)$_4$}]

## 1.2.1.5 Vacuum Deposition

High vacuum deposition is a method used in organic/polymer electronics. It produces high-quality films with a precise control of the thickness and morphology, and can be fully integrated within routine thin-film elaboration methods used in electronics (see figure 1.2.7). Very limited number of spin crossover compounds can be applied by this technique. The appropriate compounds must be neutral, thermally stable, have a low molecular weight and do not include solvent molecules.
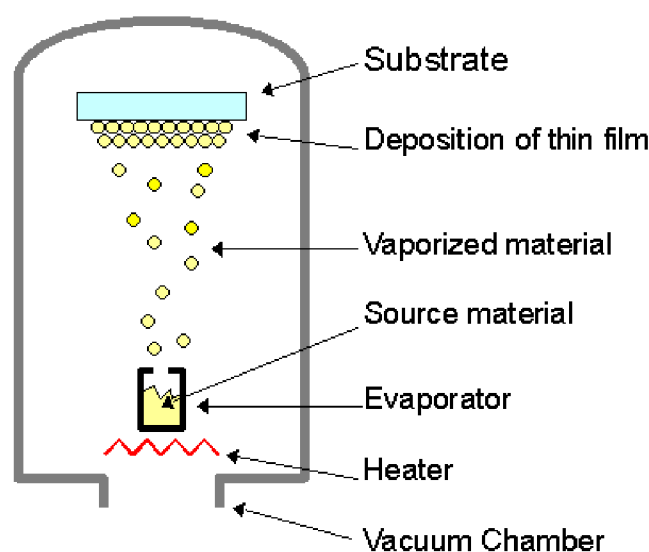


Figure 1.2.7: Schematic diagram of vacuum deposition process.

For example, the compound [Fe(HB(pz)$_3$)$_2$] (where pz = pyrazolyl) which presents a gradual spin transition above room temperature was purified by sublimation 463 K.[127] The solid sample was introduced into an evaporator and was heated by a current (joule effect) in vacuum to obtain 200 nm thick film deposited on gold interdigitated microelectrodes preserving the spin crossover properties. In 2009, Shi and co-workers reported the high-quality thin films of Fe(phen)$_2$(NCS)$_2$ (phen = 1,10-phenanthroline), that were constructed by high vacuum deposition method (see figure 1.2.8).[128] The SQUID measurement showed that the spin transition of the thin film of 280 nm thickness is more gradual than that of the powder sample, probably because of structural defects.
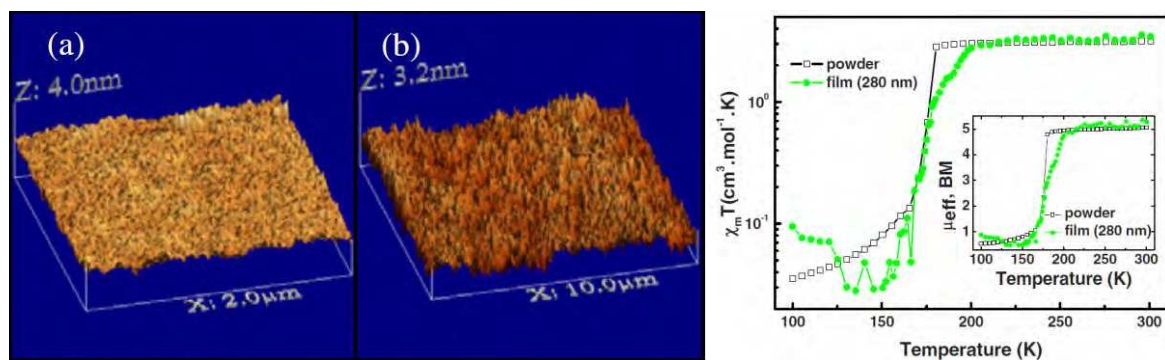
Figure 1.2.8: AFM images of Fe(phen)$_2$(NCS)$_2$ thin films deposited by high vacuum evaporation (left); Temperature dependence of $\chi_m T$ for the powder and the 280-nm-thick film on silicon substrate. Inset: the temperature dependence of the magnetic moment per molecule (right).

Then in 2011, Holger and coworkers using vacuum deposition prepared thin films of [Fe(H$_2$Bpz)$_2$(phen)] and [Fe(H$_2$Bpz)$_2$(bipy)], which presented more gradual spin transition compared with the bulk sample (see figure 1.2.9). Interestingly, for this type of film, Light-Induced Excited Spin State Trapping (LIESST) was observed for the first time.[129]
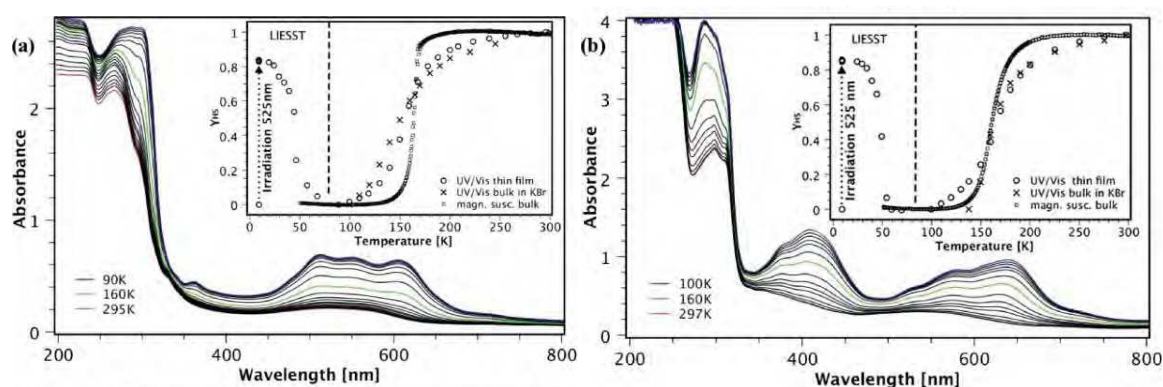


Figure 1.2.9: UV/Vis spectra of thin films of [Fe(H$_2$Bpz)$_2$(phen)] (**a**) and [Fe(H$_2$Bpz)$_2$(bipy)] (**b**) between 300 and 90 K. Insets: High-spin fraction $\gamma_{HS}$ of [Fe(H$_2$Bpz)$_2$(phen)] (**a**) and [Fe(H$_2$Bpz)$_2$(bipy)] (**b**) determined from UV/Vis spectroscopy and magnetic susceptibility of the bulk materials. Insets, left: High-spin fraction after irradiation at 10 K.

Dougherty and co-workers prepared bilayer to multilayer films of [H$_2$B(pz)$_2$]Fe(II)(bpy) on Au(111) substrate in an ultrahigh vacuum (see figure1.2.10).[130] These films were observed to be air-stable in terms of color-changes associated with spin crossover for at least six months. They found that for the bilayer film geometry the spin composition is independent

33

of temperature between 130 K and 300 K due to film packing effects that alter the cooperative effects on spin crossover compared to the bulk material.[131] Submono-, mono- and multilayers of the Fe(II) spin-crossover (SCO) complex [Fe(bpz)$_2$(phen)] (bpz = dihydrobis(pyrazolyl)borate, phen = 1,10-phenanthroline) were also prepared by vacuum deposition on Au(111) substrates. Spin transition properties of the film were investigated by near edge X-ray absorption fine structure (NEXAFS) spectroscopy, and they found that molecules of the second layer exhibited a thermal spin-crossover transition, but with more gradual characteristics compared to the bulk material.[132]
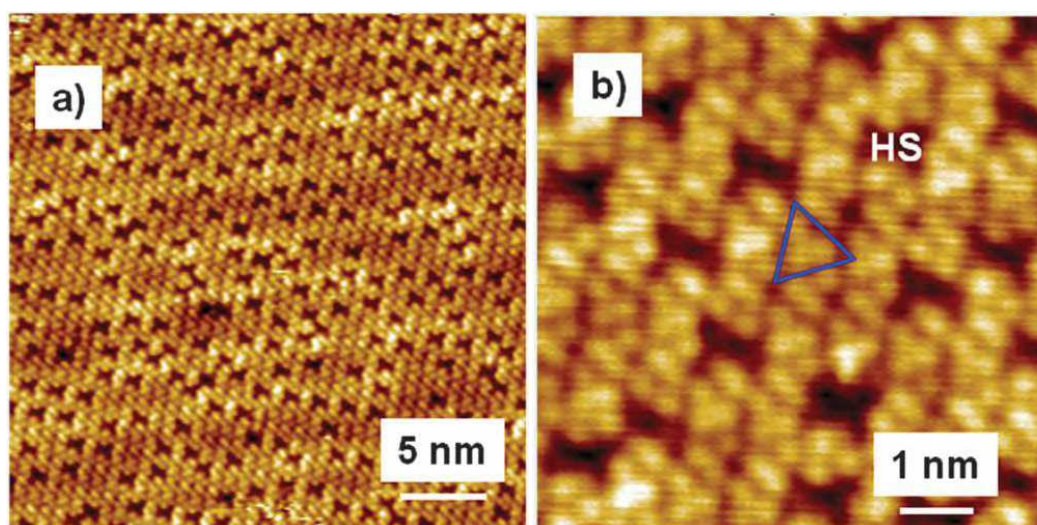


Figure 1.2.10: a) STM image of a bilayer film on Au(111); b) small-scale STM image of bilayer film on Au(111) that shows an example of the low-spin molecule highlighted with a triangle and an example of an apparent depression corresponding to a high-spin molecule pair labeled as ''HS''.

## 1.2.1.6 Micro and Nanopatterning

To make nanoscale objects through nanopattering technique, scientists use two major techniques: top-down and bottom-up fabrication. In top-down fabrication, scientists start with a (relatively) large object and cut it into smaller pieces until it is nanosized. While bottom-up fabrication, consists to build an object atom-by-atom until it is nanosized. At present, various lithographic and nonlithographic methods-such as deposition on chemically patterned surfaces, inkjet printing, lift-off processes, etching, direct photopatterning, and microcontact printing—have been explored to generate distinct patterns of the multilayer films.[133]

In 2007, for the first time our group reported a process for nano and microscale assembly of the 3D spin-crossover coordination polymer [Fe(pyrazine){Pt(CN)$_4$}] by using a

combination of top-down (lift-off) and bottom-up (multilayer sequential assembly) methods (see figure 1.2.10). At first, a gold-coated silicon surface was covered by a conventional polymethylmethacrylate (PMMA) EBL resist, in which square-shaped patterns of different size and density have been written by a focused electron beam. Then the spin crossover complexes were deposited both in the openings of the resist as well as on top of the PMMA. Finally, the patterns were transferred by lifting off the PMMA.[134] Noticeably [Fe(pyrazine){Pt(CN)$_4$}] forms Hofmann clathrate-like coordination compounds on the surfaces, which display temperature- and light-induced SCO properties. Furthermore, the films with thicknesses in the 40–90 nm range exhibit a clear cooperative thermal spin transition with large hysteresis loops very similar to the bulk samples.
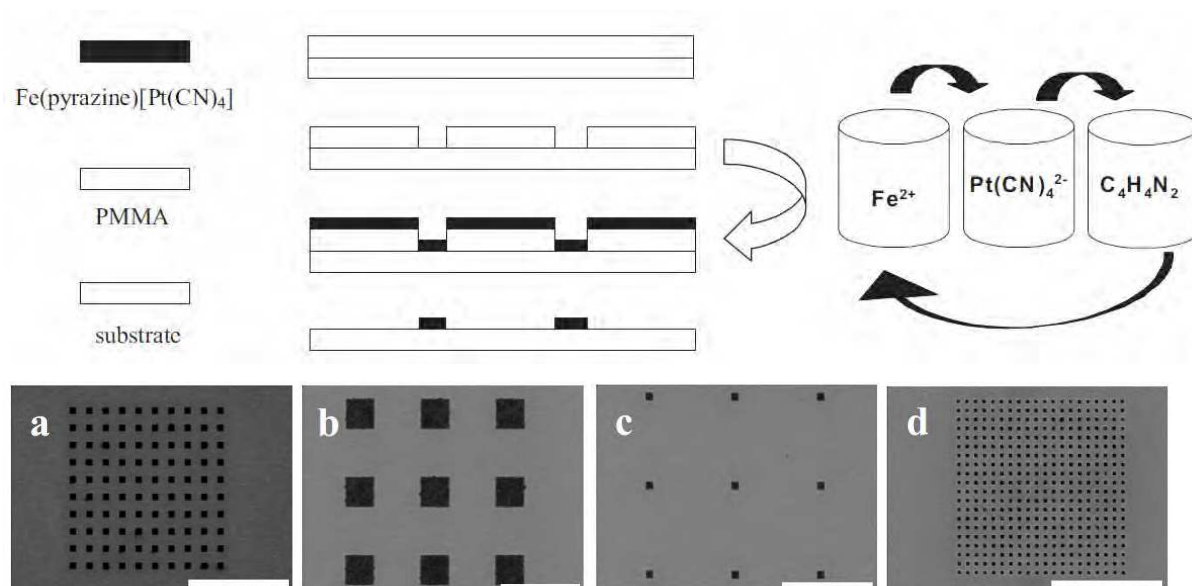


Figure 1.2.10: Schematic procedure for the patterning of [Fe(pyrazine){Pt(CN)$_4$}] (up) and Low-energy SEM image of patterns of [Fe(pyrazine){Pt(CN)$_4$}] (down).

In principle, any MOF physical property (e.g. electrical, magnetic,…) changing with the absorption of guest molecules could be used as a transducing signal for a plausible sensing device. This is the case, for example, of MOFs displaying spin-crossover (SCO) behavior.[50,100,135-138] Hence, in the follow-on work, by nanopatterning technique our group studied the host-guest interaction on a family of porous coordination polymers of the Hofmann-type which displayed thermal and light-induced spin crossover phenomena around room temperature and with a large hysteresis loop.[51,139] Recently, our group has reported the SCO properties coupled to the host–guest chemistry behavior of the Hofmann clathrate

[Fe(bpac){Pt(CN)$_4$}] (bpac = bis(4-pyridyl)acetylene), which revealed a shift of the spin transition temperature when absorbing aromatic VOCs (volatile organic compounds) such as iodobenzene (IBz), bromobenzene (BrBz) or chlorobenzene (ClBz) (see figure 1.2.11) .[140] The effect was revealed following diffraction efficiency ($\eta$) of specific gratings.
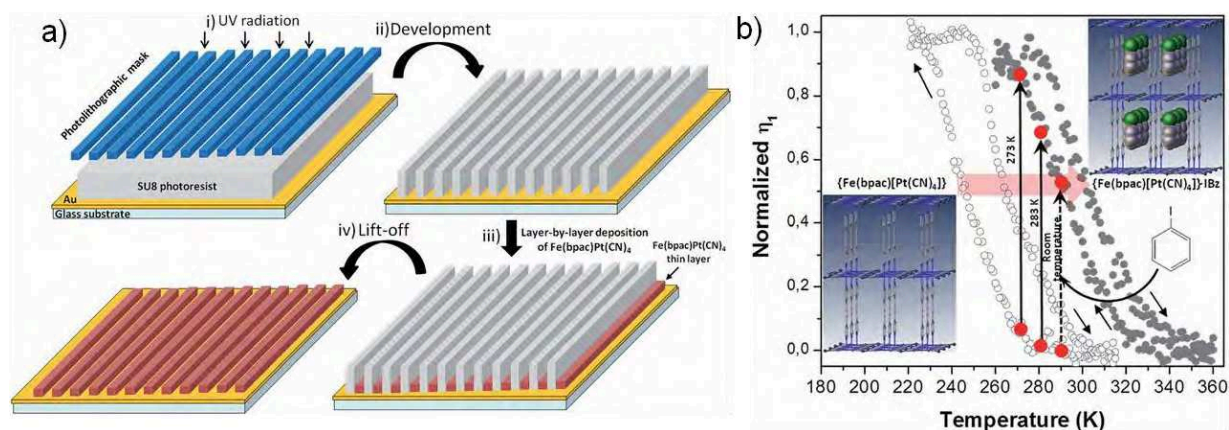


Figure 1.2.11: a) Schematic representation of the fabrication of the SCO diffraction gratings: (i) UV irradiation of the photoresist, (ii) development, (iii) deposition of the SCO thin film through a layer-by-layer method, and (iv) lift-off the photoresist. b) Temperature dependence of the first-order diffraction efficiency (normalized) in the heating and cooling modes (see arrows) for a diffraction grating of [Fe(bpac){Pt(CN)$_4$}] before and after the absorption of IBz molecules. The differences in the value of $\eta$1 between the empty and the loaded grating at 273, 283 K and room temperature are highlighted by the arrows joining the red points.

Such combination of sequential assembly and electron beam lithography techniques was a real breakthrough but this powerful type of nanopatterning method is very expensive and slow. For this reason, a soft lithography method for the fabrication of SCO units in ordered nanopatterns would be very desirable. Because it is known that the SCO properties depend critically on the local molecular environment (e.g., packing, solvent molecules, anions, etc.), the development of methods giving access to nanostructures that preserve the integrity of the material is technologically of the utmost importance for applications of SCO compounds. Soft lithographic refers to a family of techniques for fabricating or replicating structures using "elastomeric stamps, molds, and conformable photomasks".[141] Several techniques like controlled wetting lithography, capillary assembly and micro-transfer molding have been developed. For example, controlled wetting lithography can be applied to any soluble material or suspension and allows the formation of micro and nano organized structures. This

technique just requires non-specific interaction between the compound molecules and the surface. Cavallini et al. have successfully demonstrated that microinjected molding in capillaries (MIMIC) and lithographically controlled wetting (LCW) can be used to fabricate micronic and nanometric stripes of SCO materials. They fabricated reliably nanopatterns of SCO compounds of $Fe(phen)_2(NCS)_2$ by lithographically controlled wetting technique (see figure 1.2.12).[114] For the first time SCO compounds could be directly processed into highly oriented crystalline micro- and nanostripes as well as into logic patterns on technologically relevant surfaces, preserving the transition temperature of the bulk material. In principle, this method is suitable for a large number of soluble materials and can be pushed down to the limit where spin transition molecules are patterned into ordered arrays, this process being ultimately limited only by coarsening of the individual molecules. However, these techniques suffer from several drawbacks, such as thickness inhomogeneity between the stripes and, of course, the fact that only stripes can be achieved. They are also very dependent on the nature of the solvent, and only protic solvents (water, ethanol, etc.) can be used.
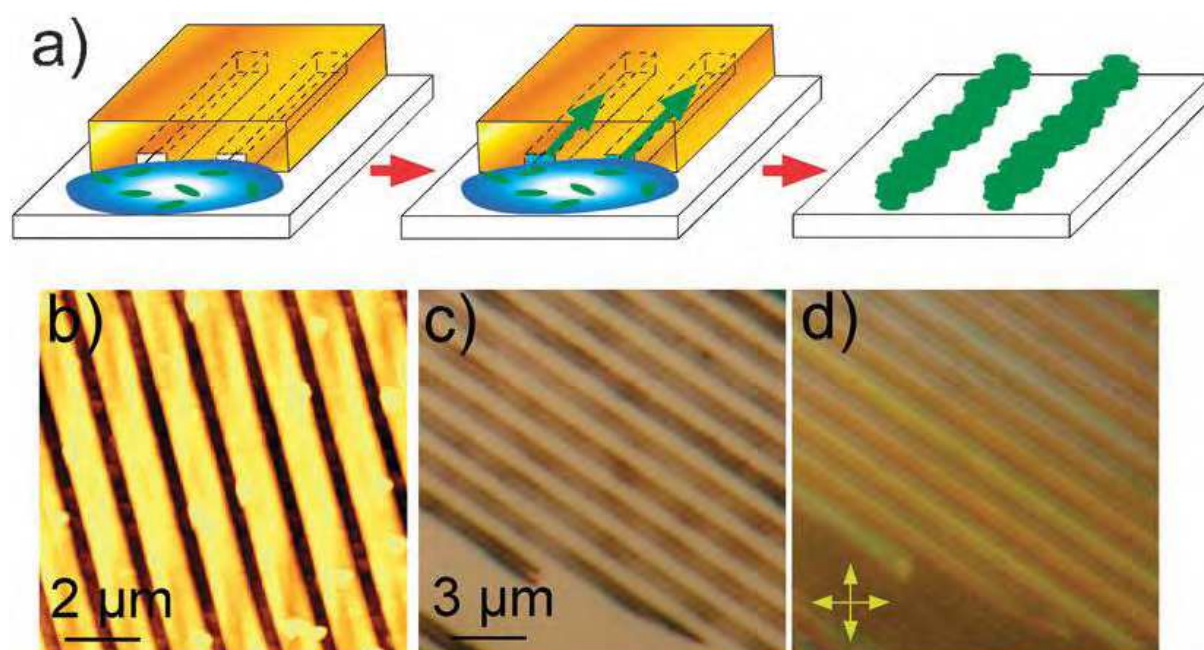


Figure 1.2.12: **a**) Scheme of micro molding in capillaries. **b**) AFM topography (z scale is 50 nm) of m-stripes of $Fe(phen)_2(NCS)_2$ fabricated by MIMIC on silicon surface. **c**) Optical micrographs taken in bright field and **d**) with crossed polars oriented along the axes of the image.

In 2010 our group reported the successful patterning of $[Fe(NH_2trz)](tos)_2$ (tos = tosylate, $NH_2trz$ = 4-amino-1,2,4-triazole) SCO nanoparticles at the frontier of micrometric (i.e.,

optically accessible) and nanometric scales with different types of features using more versatile soft lithographic techniques.[142] We used microtransfer molding (µTM) to fabricate micrometric and nanometric structures. The obtained patterns were characterized by atomic force microscopy (AFM), dark-field optical microscopy, and Raman microscopy.

In 2014, Chandrasekar *et al*. reported synthesis of a highly soluble and solution processable SCO Fe(II) coordination polymer $[Fe^{II}(L)]_n \cdot 2nClO_4$ (L = 4-octyl-2,6-bispyrazolylpyridine), which can form a several micron long nano-tape network. Then by lithographically controlled wetting technique, they produced 1D arrays of SCO nano-tape bundles (see figure 1.2.13).[143]
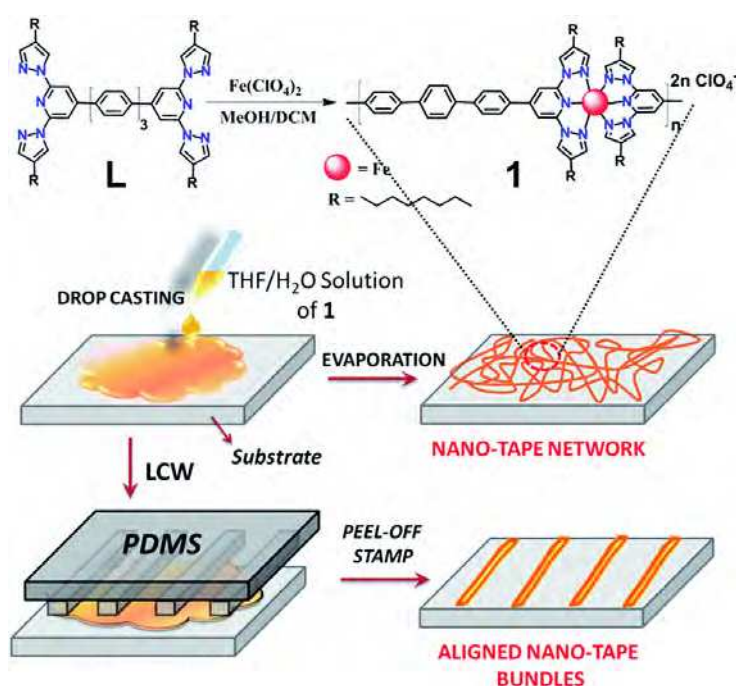


Figure 1.2.13: Formation of coordination polymer $[Fe^{II}(L)]_n \cdot 2nClO_4$ and its bottom-up and top-down self assembly into nano-tape network and aligned nano-tape bundles, respectively.

## 1.2.2 SCO Nanoparticles

Spin crossover nanoparticles are of particular interest due to the obvious data storage applications into high density media because of the hysteresis phenomenon, as was suggested by Kahn and Martinez.[95] In addition, functionalized spin crossover nanoparticles can offer a wide variety of additional applications, specially for medical usage, protein detection, drug delivery, or tumor treatment are some other applications where spin crossover nanoparticles can make a difference.

## 1.2.2.1 Synthesis of Spin Crossover Nanoparticles

Up to now, numerous studies have been reported for the preparation of SCO particles of various sizes in homogeneous and heterogeneous media, such as reverse micelle technique, polymer and biopolymer stabilization method, sol–gel technique and so on.

Reverse micelles consist on liquid polar droplets stabilized by a surfactant, S, in an oil phase (see figure 1.2.14). Water is readily solubilized in the polar core, forming a so-called "water pool", characterized by $\omega$, the water-surfactant molar ratio ($\omega$ = [H$_2$O]/[S]). The aggregates containing a small amount of water (below $\omega$ =15) are usually called reverse micelles whereas microemulsions correspond to droplets containing a large amount of water molecules (above $\omega$ =15).[144] The droplet size of reverse micelles can be readily modulated in the nanometer ranges by various parameters, in particular, the water-surfactant molar ratio, stirring speed and temperature.
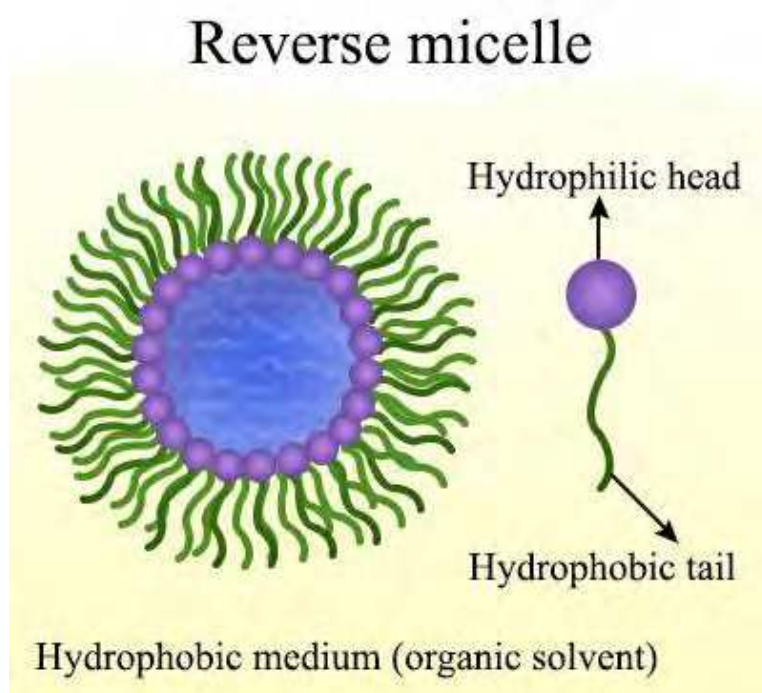


Figure 1.2.14: Structure of reverse micelle

The first results concerning the synthesis of 70 nm [Fe(NH$_2$trz)$_3$](Br)$_2$ SCO nanoparticles were prepared using a binary water/lauropal system, the lauropal playing both the role of oil

phase and surfactant.[7,8,145] In this study, the nanoparticles were obtained following a precipitation stage with diethyl ether (see figure 1.2.15).
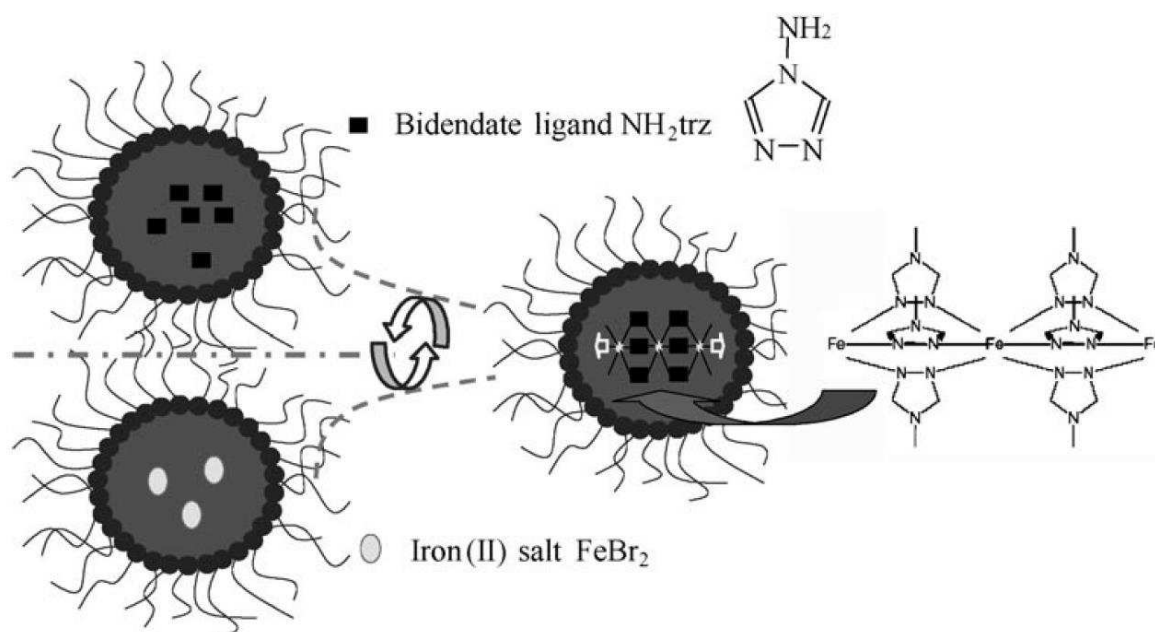


Figure 1.2.14: Structure of reverse micelle

In 2010 by our group, nanoparticles of the $[Fe(NH_2trz)_3](tos)_2$ (tos = p-toluene sulfonate anion) spin crossover complex of 3-4 nm size were synthesized.[146] In this work, Tergitol was used as a non-ionic surfactant, because it is free of the counter-ion exchange and also its polyether hydrophilic moiety has a potential to self-assembly by means of hydrogen bonding. The non-covalent interactions between the amphiphile species and the surface of the particles may have a positive effect on the colloidal stability. The selected Tergitol has also a wide liquid range, a relatively low viscosity and very low vapor pressure, which are useful assets for sample characterization. The polar phase of the microemulsion was evaporated under reduced pressure and ultrafine (ca. 3-4 nm) well dispersed colloids were obtained in surfactant. We have also found that solvent precipitation or thermal treatment of the colloidal systems leads to the formation of different nano-objects (large particles, nanofibers . . .).

Figure 1.2.15: Schematic representation showing the preparation procedure of SCO [Fe(NH$_2$trz)$_3$](tos)$_2$ nanoparticles. A stable colloidal suspension or a nanocrystalline solid was obtained after vacuum treatment or solvent precipitation, respectively. A transparent SCO gel was obtained by thermal treatment.

Another method to control the growth of complex nanoparticles in solution involves the use of a stabilizing polymer. In this homogeneous medium approach, a solution of the ligand was added to an iron salt solution both containing a polymer. In 2012, our group synthesized [Fe(hptrz)$_3$](OTs)$_2$ (hptrz = 4-heptyl-1,2,4-triazole, Ts = para-toluenesulfonyl) nanoparticles in the presence of different kinds of polymer (Triton X-100 (with a hydrophilic polyethylene-oxide group and a hydrocarbon lipophilic group), TOPO (trioctylphosphine oxide), PVA (polyvinyl alcohol), and PEGs (polyethylene glycols)) as well as different solvents (water and EtOH).[147] By varying the polymer concentration, we observed the changes in the length and shape of the nanorods. The spin transition of these different samples is comparable to that of the bulk sample, indicating that the morphology has no impact on the SCO properties for these larger particles. Furthermore, in this work, we also reported two other kinds of synthesis methods: a polymer-free synthetic pathway in CHCl$_3$ and a hybrid approach. In the first synthetic route, the reaction between [Fe(H$_2$O)$_6$](OTs)$_2$ and hptrz in chlorinated organic solvents, such as CHCl$_3$ or trichloroethylene, in the presence of alcohols (up to 5% v/v) yielded relatively stable solutions of a low-level "polymerization" SCO complex. The addition of alcohols effectively prevented the precipitation of the complex. Thus, we suppose that the alcohol can play the role of a terminal ligand, slowing down the growth of the oligomers into larger structures. In the second route, we proposed to obtain precipitation of nanoparticles from the previous solution (in CHCl$_3$) by adding other chemicals that are able to

destroy the stability of the oligomers and cause their growth into nanometer-sized objects. All of these results mentioned above are extremely important for future applications giving the possibility to obtain SCO nano-objects of different sizes and morphologies with a controlled matrix.

Using the biopolymer chitosan as matrix,[148] our group collaborated with Guari's group to obtain ultra-small monodisperse nanoparticles of the 3D spin crossover coordination polymer [Fe(pz){Ni(CN)$_4$}] (see figure 1.2.16) following a layer by layer approach. The advantages of this strategy consist of 1) the possibility to covalently anchor the cyano-bridged metallic network at the reactive functional amino groups of the chitosan; 2) the possibility to afford ultra-small nanoparticles (less than 10 nm corresponding to the natural size of pores into the chitosan polymer); 3) the water solubility of the chitosan matrix that permits removal of the nanoparticles from the matrix. Similar syntheses were realized using the alginate polymer as polysaccharide matrix.[149]
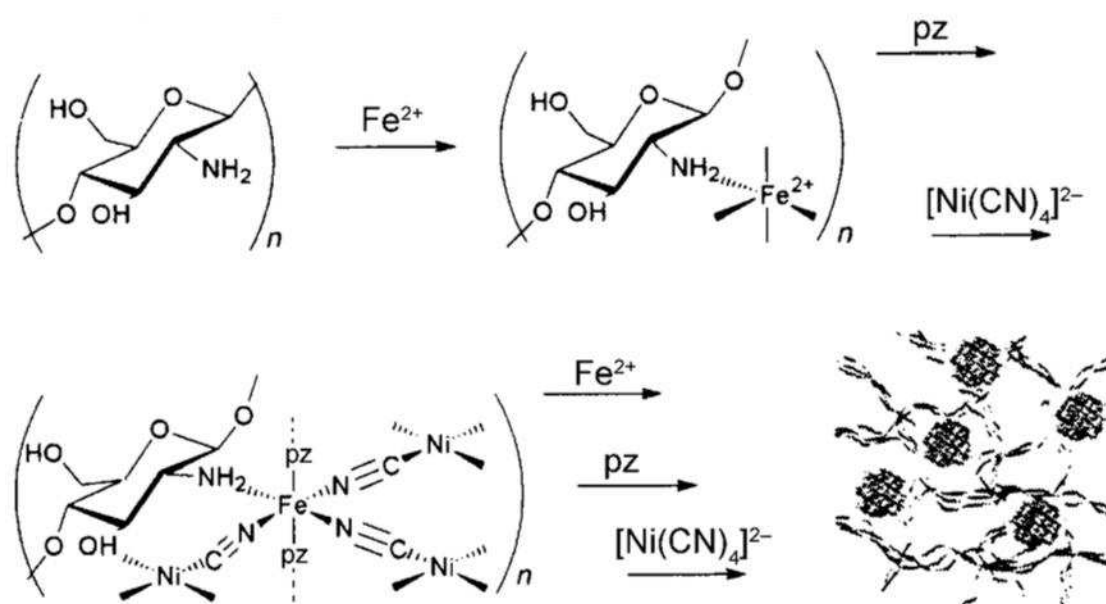


Figure 1.2.16: Schematic representation of the synthesis of [Fe(pz){Ni(CN)$_4$}]/chitosan nanocomposite beads.

The sol-gel process is a method for producing solid materials from small molecules. The method is used for the fabrication of metal oxides, especially the oxides of silicon and titanium. The process involves conversion of monomers into a colloidal solution (sol) that acts as the precursor for an integrated network (or gel) of either discrete particles or network

polymers. As sol–gel silica shows good optical and mechanical properties, and the mesoporosity of a xerogel, which can also be used as a confining medium to elaborate spin crossover nanoparticles.[150] In 2013, Pillet *et al*. reported the preparation and characterization of a SCO NP-silica nanocomposite using a two-step nanocasting synthetic method by confined growth of NPs of the SCO coordination polymer [Fe(Htrz)$_2$(trz)](BF$_4$) in a pre-formed silica xerogel matrix with well controlled porosity.[151] The temperature dependence of the magnetization of the FeHtrz-silica nanocomposite indicated an uncompleted reversible spin transition with a hysteresis loop of 65 K width (see figure 1.2.17).
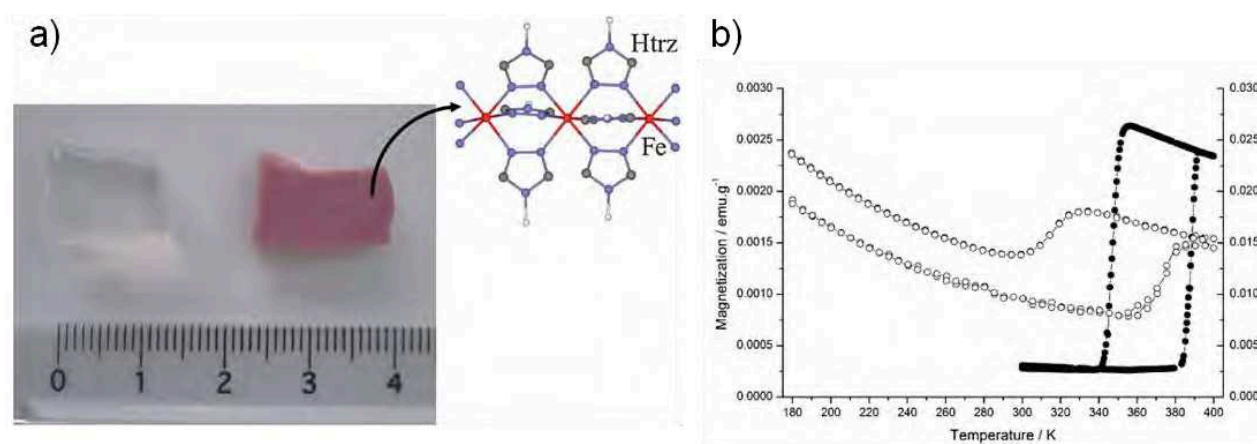


Figure 1.2.17: **a**) Photographs of the transparent empty silica monolith (left) and FeHtrz–silica nanocomposite (right); **b**) Magnetization versus temperature for the FeHtrz–silica nanocomposite (opened circles, left scale) and [Fe(Htrz)$_2$(trz)](BF$_4$) microcrystalline powder reference material (filled circles, right scale), $H$ = 1000 Oe.

## 1.2.2.2 Size Effect Study on SCO Properties

In 2008, the group of Real (see figure 1.2.18) and Mallah (see figure 1.2.19) reported the synthesis of a series of different-size nanoparticles of the 3D coordination polymer [Fe(pz){Pt(CN)$_4$}] using the reverse micelle method. Upon a reduction of the size, the particles have a magnetic behavior different from that of the bulk, the spin transition is incomplete with residual high and low spin fraction, the transition temperature shifted downwards and reached a value of 240 K for the 8 nm particles, and the hysteresis loop is narrower and almost vanishes for the smaller particles.[152,153]
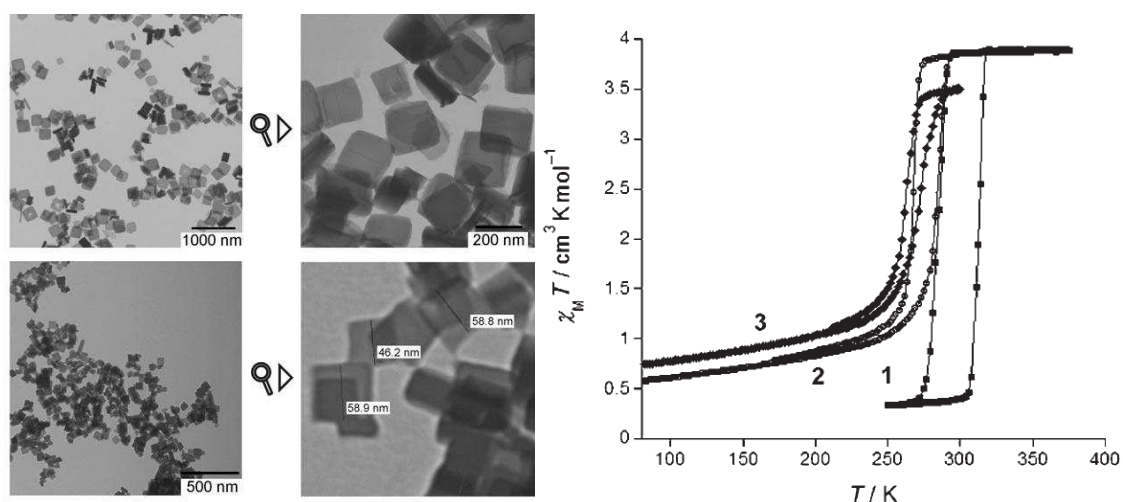
Figure 1.2.18: TEM images of [Fe(pz){Pt(CN)$_4$}] nanoparticles (sample **2**, up and sample **3**, bottom) and the corresponding temperature dependence of the magnetization (sample **1** corresponding to the bulk sample)
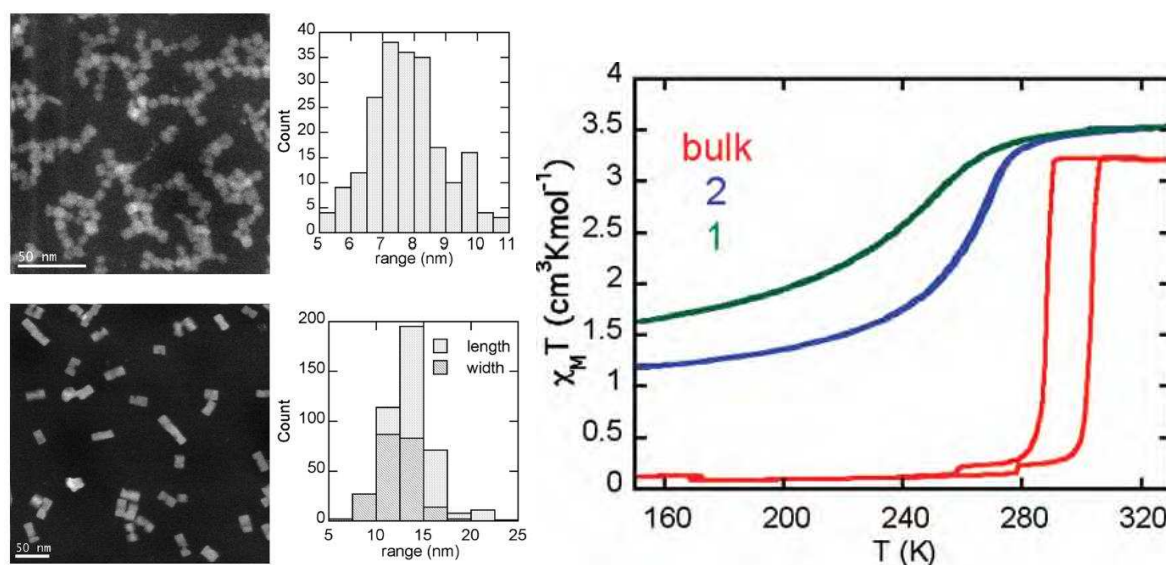


Figure 1.2.19: TEM images of [Fe(pz){Pt(CN)$_4$}] nanoparticles (sample **1**, up and sample **2**, bottom) and the corresponding temperature dependence of the magnetization

Then in 2007, Coronado and co-workers using a similar approach succeeded in synthesizing nanoparticles of the [Fe(Htrz)$_2$(trz)](BF$_4$) complex with a medium statistical size of ca. 15 nm, which exhibited a remarkable 43 K wide hysteresis loop.[154] Later, the same authors succeeded to tune the mean size of the nanoparticles down to 6 nm in diameter with a narrow size distribution. A 29-K-wide hysteresis was found in this case (centred around 357

K), with a higher HS residual fraction (33%). These nanoparticles were also investigated using nanoelectrodes and a thermal hysteresis of the conductance was reported.
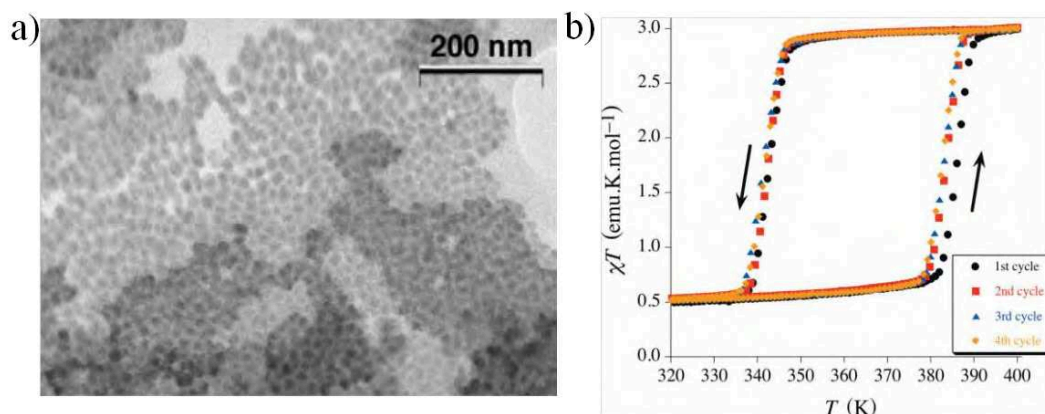


Figure 1.2.20: **a**) TEM image and thermal hysteresis of the magnetic susceptibility of [Fe(Htrz)$_2$(trz)](BF$_4$) nanoparticles.

A study of the effect of particle size of [Fe(NH$_2$trz)$_3$]Br$_2$ on its spin crossover properties was reported by the group of Létard.[155] For particle sizes of 50 nm and 30 nm a relatively gradual thermal spin crossover occurs without clear existence of thermal hysteresis although the equilibrium temperature of the transition is almost unaffected by the decrease of the size.
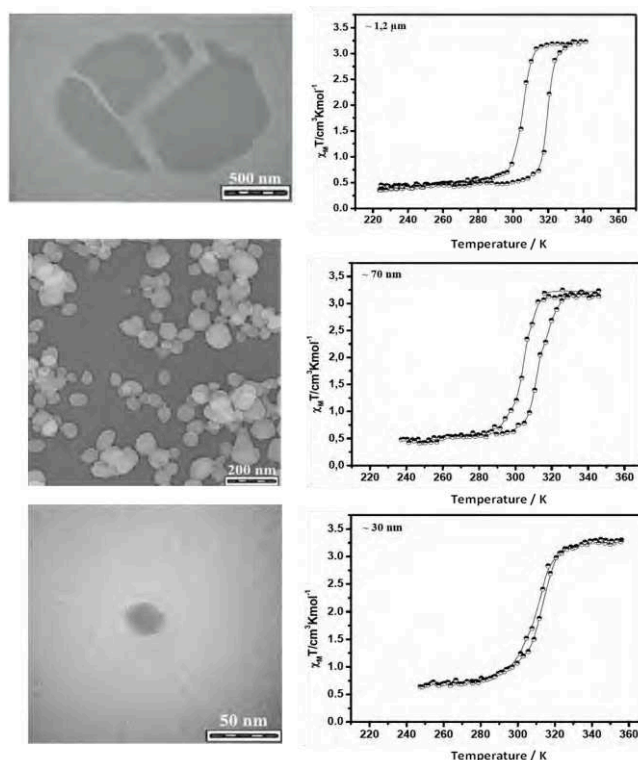


Figure 1.2.21: TEM images and magnetic measurements on various sizes [Fe(NH$_2$trz)$_3$]Br$_2$ nanoparticles

The authors suggested by means of powder X-ray diffraction analyses that the bistability regime implies that at approximately 30 nm individual particles consist of one coherent domain. Using the corresponding bulk material, the same group has reported for the first time the study of a single isolated particle. A differential interference microscope (DIC) set-up operating in transmission mode was used to follow the thermal hysteresis loop of individual objects, the size of which was undetermined, but certainly sub-micrometre. The same group has also studied the effect of the particle size reduction on the light induced spin state switching at 10 K. According to the authors, one of the most important results of this study is the retention of the same light-induced SCO effect whatever the size of the particles, highlighting that the light-induced SCO properties are governed by the molecular scale, whereas the thermal SCO regime is governed by solid-state cooperative interactions.

In 2010,[146] our group reported the synthesis $[Fe(NH_2trz)_3](tos)_2$ (tos = p-toluene sulfonate anion) and $[Fe(NH_2Trz)_3](NO_3)_2$ nanoparticles with SCO properties. We have carried out UV-visible absorption measurements on stable limpid purple suspension of 10 nm nanoparticles of $[Fe(NH_2trz)_3](tos)_2$, which revealed an abrupt spin transition with a hysteresis loop, while only a sharp transition with no detectable hysteresis was observed for 3–4 nm particles of $[Fe(NH_2trz)_3](tos)_2$ and $[Fe(NH_2Trz)_3](NO_3)_2$. Using directly the colloidal suspension, we provided an irrefutable proof that even extremely small (3–4 nm) particles exhibit cooperative (first order) spin transitions. Because the properties of these latter are difficult to compare with other samples, a comparison based exclusively on the size difference is certainly erroneous and other parameters such as chemical composition, defects, crystallinity as well as elastic properties of the dispersing medium should be considered.
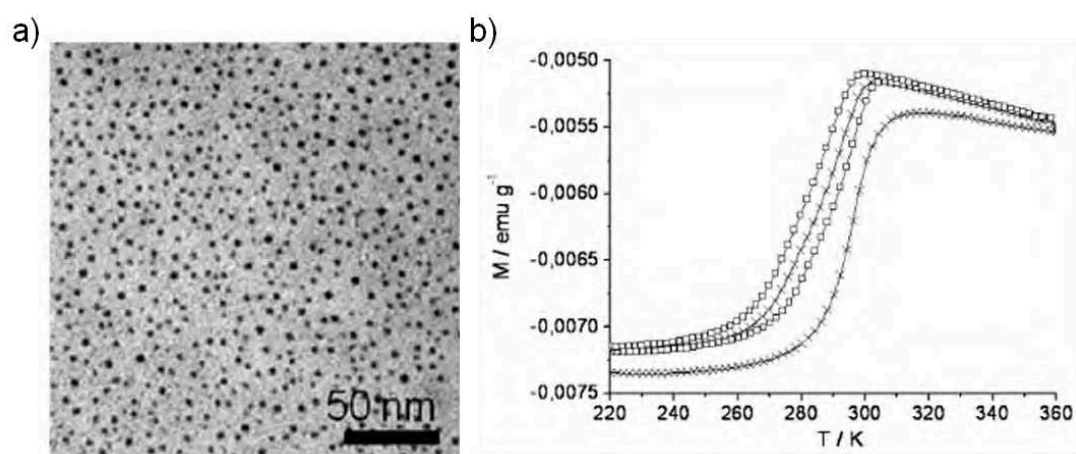


Figure 1.2.22: **a)** TEM image of the 3–4 nm $[Fe(NH_2trz)_3](tos)_2$ nanoparticles in a surfactant matrix; **b)** Temperature dependence of the magnetisation obtained when $[Fe(NH_2trz)_3](tos)_2$ nanoparticles suspension goes through the first (×) and second (□) thermal cycles.

The ensemble of results concerning compounds of the triazole family seems to indicate that the evolution of the spin crossover properties is not only dependent on the size, but depends critically on the chemical nature of the compounds and certainly more precisely on the structural arrangement of the chains, which is influenced by the nature of ligands, counter anions and in certain cases solvent molecules.

In 2014, the group of Boillot synthesized $Fe(Me_2\text{-bpy})_2(NCSe)_2$ particles size varying between ca. 4500 and 56 nm. The particles were prepared in the component solvent (ethanol and toluene) and in presence of PMMA (poly(methyl methacrylate). The different-size particles were separated by a PTFE membrane. Whatever the particle size, the magnetic behavior is preserved and the spin-crossover process is quantitative.[156]
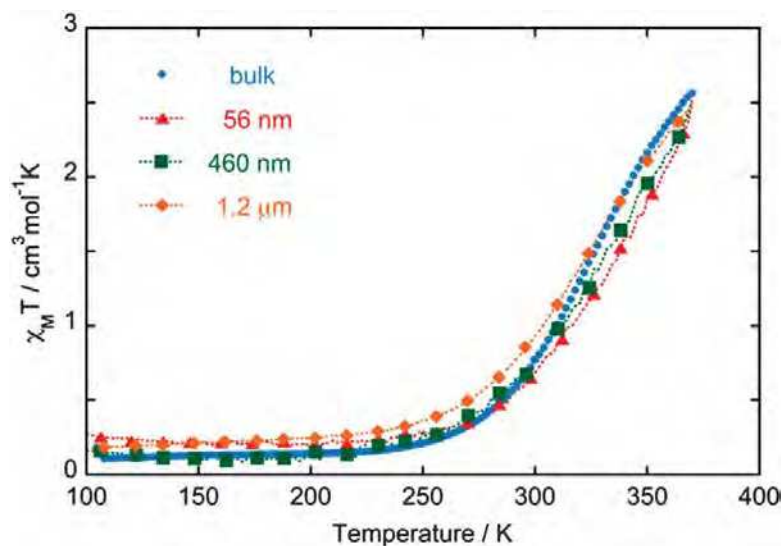


Figure 1.2.23: Temperature dependence of $\chi_M T$ for $Fe^{II}(Me_2\text{-bpy})_2(NCSe)_2$ in the form of a polycrystalline powder (●), microparticles (▲) and in-PMMA nanoparticles (◆) (■, 460(190) × 80(30) $nm^2$) or (▲, 56(15) nm).

Anti-solvent was used to synthesize spin crossover molecular nanoparticles by the group of Boillot.[157] In their work, nanoparticles of $[Fe^{III}(_3\text{-MeO-SalEen})_2]PF_6$ (H-3-MeO-SalEen being the condensation product of 3-methoxy-substituted salicylaldehyde and N-ethylethylenediamine) ranging from 7500 nm to 18 nm were obtained by a sudden precipitation approach using butan-1-ol as an anti-solvent (see figure 1.2.24). After the series of micro- and nanocrystals studied, they concluded a reduction of cooperative interactions with the particle size.
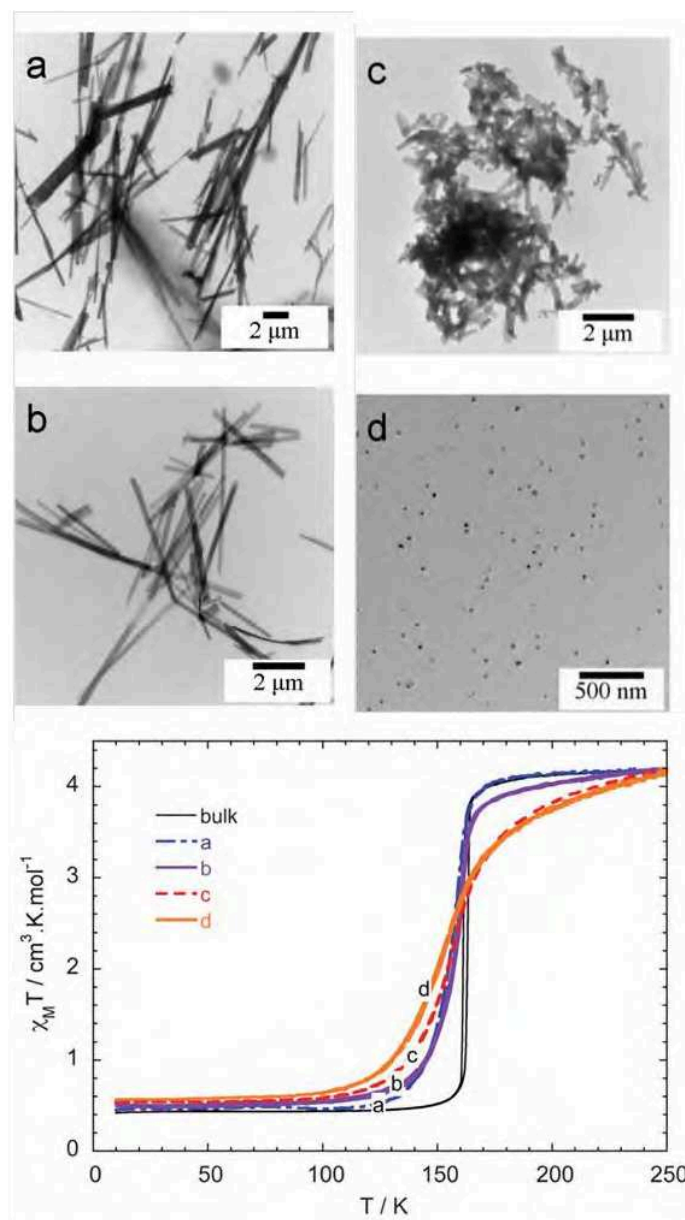
Figure 1.2.24: TEM images of different-size [Fe$^{III}$(3-MeO-SalEen)$_2$]PF$_6$ particles (up); Temperature dependence of $\chi_M T$ for in-PEG dispersion of nano- and microparticles (bottom).

## 1.2.2.3 Matrix Effect in Spin Crossover Nanoparticles

The variation of the long range elastic interactions, as we know, is mainly attributed to the electron–phonon couplings within the crystal network. Hence, the adjusting of mechanical/elastic properties of the matrix surrounding the SCO nanoparticles is a possible way to induce a cooperative thermal spin transition. In 2008,[148] our group collaborating with Guari's group reported the synthesis and study of ultra-small monodisperse nanoparticles of the 3D spin crossover coordination polymer [Fe(pz){Ni(CN)$_4$}], obtained using the biopolymer chitosan as matrix. The study of the physical properties of nanoparticles around 4

nm revealed that approximately 1/3 of the iron(II) ions in the nanoparticles undergo a cooperative thermal spin transition with a hysteresis loop. Besides, we thought the hysteresis should mainly associate with the surrounding chitosan matrix.
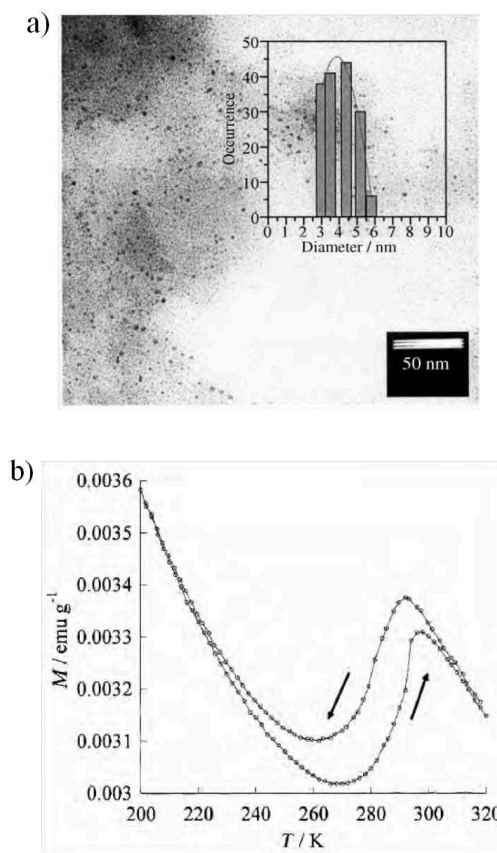


Figure 1.2.25: **a**) TEM images of [Fe(pz){Ni(CN)$_4$}] nanoparticles; **b**) Temperature dependence of the magnetization measured for the nanocomposite beads under an applied field of 10000 Oe at heating and cooling rates of 0.5 K·min$^{-1}$.

In 2011, Mallah and co-workers demonstrate that the environment of the nanoparticles may play a crucial role in the crossover process and that the cooperativity may be tuned by the matrix surrounding the nanoparticles within the nanocomposites.[158] They found that the more rigid matrix such as silica restores the hysteresis loop due to a stronger cooperativity. This phenomenon may be understood through the mechanical/elastic properties of the matrix surrounding the SCO nanoparticles, as we all known, which are mainly attributed to the electron–phonon couplings within the crystal network.
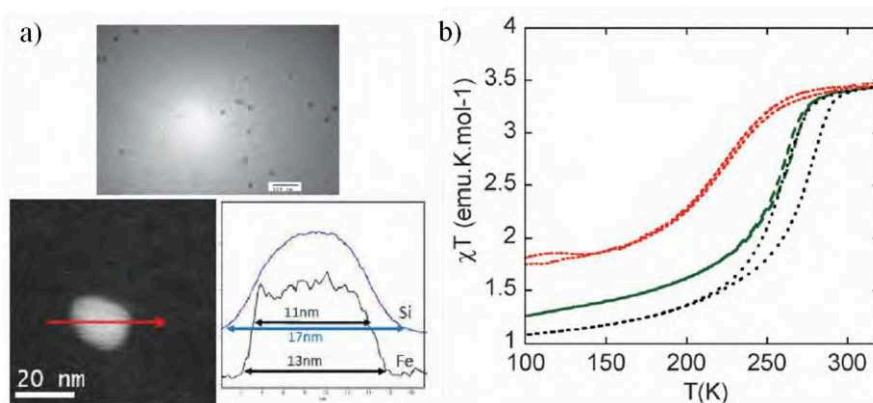
Figure 1.2.26: **a)** STEM image of nanoparticles after dispersion in methanol (top) and EELS map of one particle showing the presence of Si and Fe in the particle's core (left and right); **b)** $\chi$T = $f$(T) for calix-covered particles (green), particles with thin $SiO_2$ shell (black) and the particles with thick $SiO_2$ shell (red).

Boillot *et al*. synthesized spin transition microparticles (($1600 \pm 600$) × ($1600 \pm 600$) × ($300 \pm 200$) $nm^3$) of $Fe(phen)_2(NCS)_2$,[159] which were dispersed in matrixes of glycerol, eicosane, and nujol. In all these matrices, a progressive HS to LS transition curve shifted toward smaller temperatures is observed. Interestingly, the LS to HS transition curve, obtained after full LS conversion closely follows the one from the powder, thus defining impressively large hysteresis loops. By measuring a series of first-order reversal curves and then simulated in the framework of a simple mean-field model, they proved the hypothesis considering additional interactions between the spin-transition microparticles and the embedding matrix, which compares to a negative pressure on the particles (see figure 1.2.27).
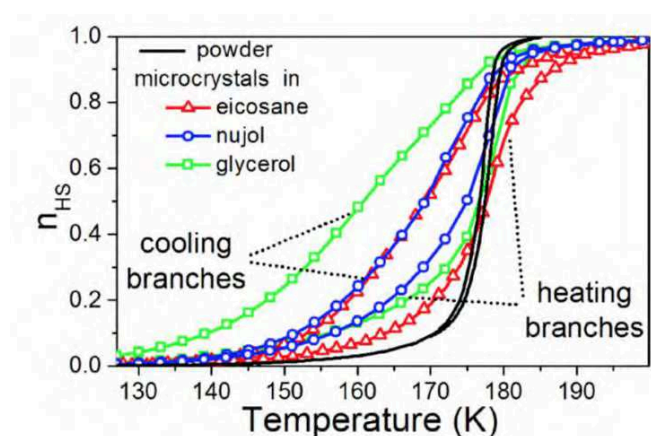


Figure 1.2.27: The major hysteresis loop for bulk and for dispersions of microparticles in different matrixes of nujol, eico- sane, and glycerol.

## 1.2.2.4 Functional Spin Crossover Nanoparticles

### 1.2.2.4.1 Optical Properties

As one would expect, the change in spin state is accompanied by a change in the optical properties of the material. The spin-state and associated changes in light absorption can be most conveniently brought about by a variation of the temperature of the SCO material. For this aim, one can simply follow the absorbance changes as a function of the temperature, but from a practical point of view it appears more interesting to use fluorescent detection, which usually allows for a better contrast with the environment around the probe. In 2010, in order to develop a more versatile approach to applications in thermometry and thermal imaging, our group[160] designed a two-component system comprised of ultra-small $[Fe(NH_2Trz)_3](NO_3)_2$ SCO nanoparticles and an appropriate luminophore rhodamine-110 (Rh110) displaying negligible thermal quenching on its own. Experimental results show that the luminescence can conveniently probe the spin state of the system. The main advantage of using very small nanoparticles arises from the fact that light scattering by such particles is weak, which is an important consideration for optical measurements. Furthermore, in contrast to the bulk materials, nanoparticles can be easily processed in liquid phase or deposited to surfaces.
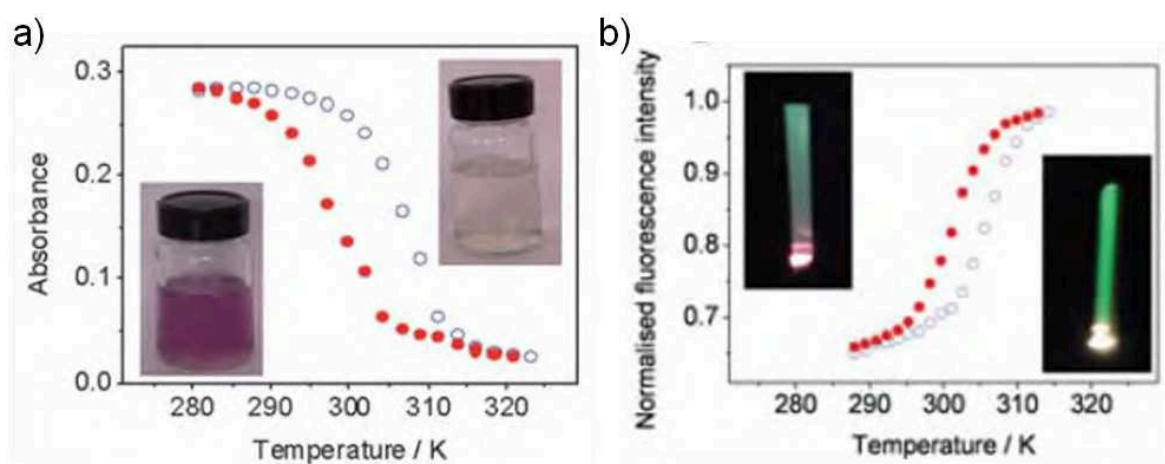


Figure 1.2.28: **a**) Thermal variation of the absorbance of the suspension at 540 nm in the heating (open symbols) and cooling (closed symbols) modes. The insets show the photographs of the sample at 295 K (violet) and 320 K (transparent). **b**) Thermal variation of the emission intensity at 540 nm in the heating (open symbols) and cooling (closed symbols) modes. The insets show the photographs of the sample (0.001%) under white light excitation at 295 K and 320 K.

## 1.2.2.4.2 Electrical Properties

In the last few years, several research groups have focused their attention on the charge transport properties of the SCO compounds, due to their great interest for applications in nanoelectronics and spintronics.[108,127,161-169] The spin crossover phenomenon accompanied by intramolecular structural change involves a deformation of the electronic molecular orbitals of the complex. For $Fe^{II}$ complexes in a pseudo-octahedral ligand field symmetry, the anti-bonding orbitals (eg) become occupied in the HS state leading to the increase of metal-ligand bond lengths. Therefore, the local electrical dipoles in the material must be different in the HS and LS states, leading to a change in dielectric properties of the material upon spin crossover.[104] In 2003, our group obtained the thermal variations of the dielectric constant at 10 kHz frequency in the heating and cooling modes for the spin crossover complex $[Fe(NH_2trz)_3](NO_3)_2$ as shown in figure 1.2.29-a. For comparison, spin crossover curves obtained by magnetic susceptibility measurements are also shown in figure 1.2.29-b. The complex $[Fe(NH_2trz)_3](NO_3)_2$ exhibits a wide (50 K) dielectric hysteresis loop around room temperature in agreement with the magnetic susceptibility measurements.
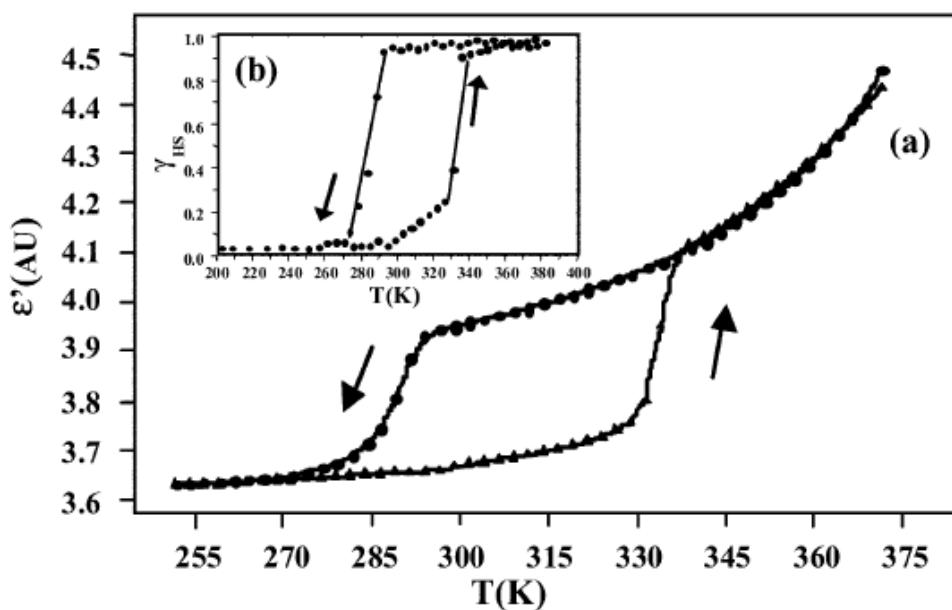


Figure 1.2.29: **a**) Thermal hysteresis of the dielectric constant associated with the spin-transition of $[Fe(NH_2trz)_3](NO_3)_2$. **b**) The corresponding thermal variation of the proportion of high-spin molecules ($\gamma_{HS}$) obtained through magnetic susceptibility measurements. (Data points are connected to guide the eye.)

Recently, our group reported, for the first time, an unambiguous spin-state dependence of the electrical conductivity in powder (both bulk and nanoparticle) samples of the compound [Fe(Htrz)$_2$(trz)](BF$_4$) (Htrz = 1H-1,2,4-triazole) by using macroscopic dc conductivity measurements.[170] Temperature dependence of the dc electrical conductivity (see figure 1.2.30) suggested that the conductivity hysteresis is essentially the molecular spin state switching phenomenon of the particles and not dominated by grain boundary contribution. We have found that the conductivity of this compound is much higher in the LS phase-due to the lower activation barrier in this spin state. Perhaps even more important, we have also shown that the modification of the synthesis conditions can drastically modify the charge transport behavior of the complex and can even inverse the sign of the conductivity change, albeit the spin crossover properties remain nearly unaltered.
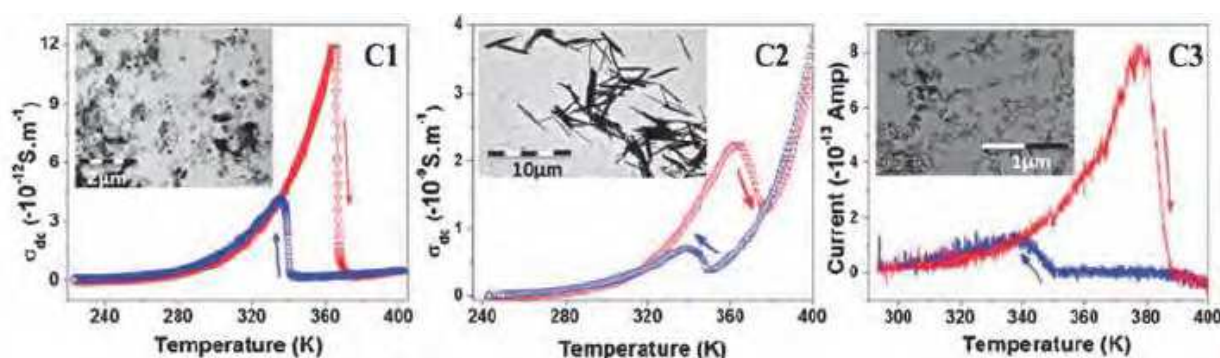


Figure 1.2.30: Temperature dependence of the dc electrical conductivity of compounds (C1) and (C2) in the heating (red) and cooling (blue) modes. For (C3) we show the I = f(T) curve because the conductivity could not be determined accurately. The insets show typical TEM images of the samples.

Because of the flexibility, light-weight, easy processing and low-cost of organic conducting polymer (polypyrrole), Galán-Mascarós *et al*. prepared the composite film with spin crossover polymer [Fe(Htrz)$_2$(trz)](BF$_4$).[171] Due to flexibility of polypyrrole, it's conductivity showed a high pressure dependence. Hence the SCO volume change during the LS → HS expansion can change the internal pressure and, therefore, the conducting regime with differences between 50% and 300% (see figure 1.2.31).
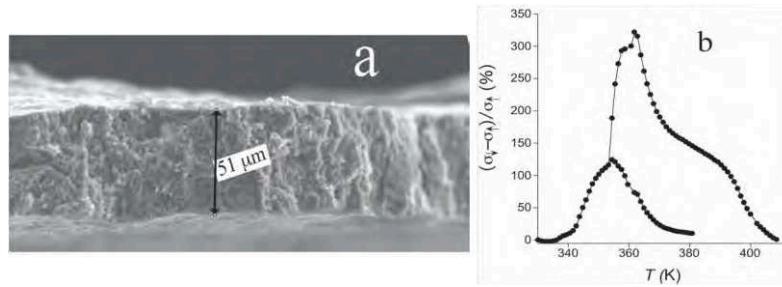
Figure 1.2.31: TEM images of composite film and difference in conductivity during a cooling and heating cycle.

In 2015, Dugay *et al*. studied the difference of transport properties between different-size [Fe(Htrz)$_2$(trz)](BF$_4$) rod shape particles.[172] These SCO NPs were self-assembly on the ultrathin conductivity sheets, and presented a thermal hysteresis loop in the electrical conductance near room temperature. Moreover, they found that the 25/10 nm sized SCO NPs show an unprecedentedly large change in the electrical conductance of the two spin states (see figure 1.2.32).
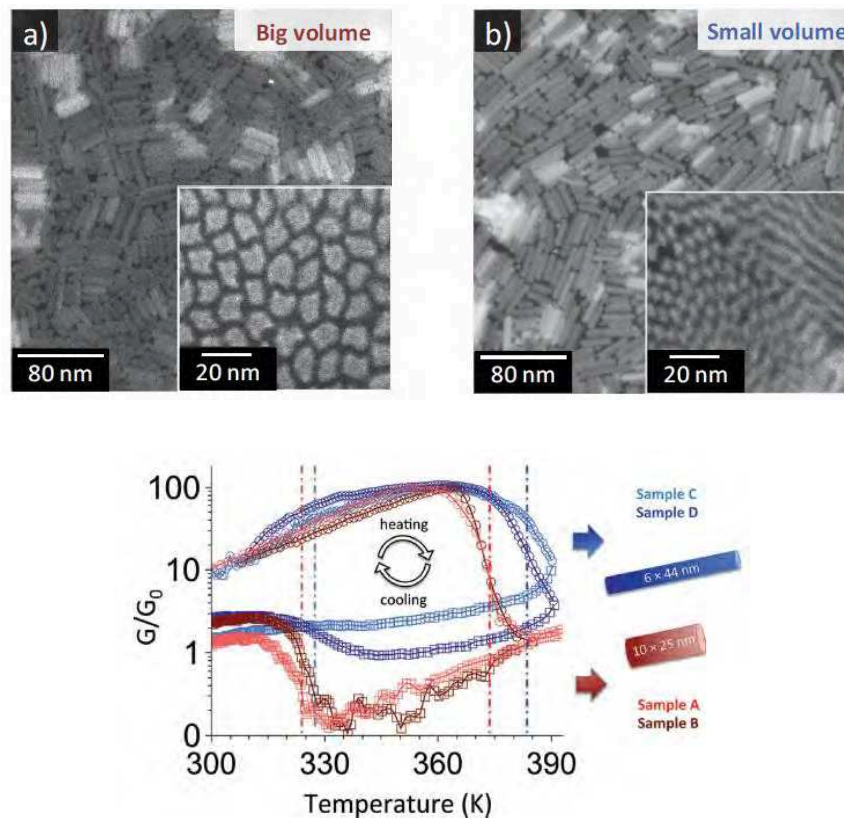


Figure 1.2.32: TEM images of SCO NPs prepared by μ-contact printing and electrical characterization of the SCO NP 2D sheets (up). Corresponding thermal variation of the electrical current plotted for different applied voltages in the heating and cooling modes (bottom).

### 1.2.2.4.3 Mechanical Properties

The change in material volume that accompanies the molecular switching between HS and LS states during spin crossover is usually around 5%, although values up to 13% have been observed for the $[Fe(L)\{M(CN)_4\}]$ framework materials.[173] It is also interesting to note that the spin-state switching is often associated with hysteresis phenomena, implying a potential for shape-memory functions. SCO molecules would thus seem to be a perfect candidate for the development of micro- and macroscopic molecular machines, with mechanical properties that are highly tunable to the desired application. As an example, figure 1.2.33 shows the thermal expansion properties of needle-like tetragonal crystals of the three-dimensional SCO coordination polymer $\{Fe(3\text{-}CNpy)[Au(CN)_2]_2\}\cdot\frac{2}{3}H_2O$ (py = pyridine) investigated using variable temperature X-ray diffraction.[174] A uniaxial negative thermal expansion (NTE) property of the crystals in the HS state was observed, where the long axis of the crystal (the crystallographic c-axis) slightly increases on cooling from 290 to 130 K. Subsequently the first-order HS $\rightarrow$ LS spin transition causes a substantial spontaneous strain ($\Delta c/c$ = 0.01), $ca.$ $10^4$ times larger than the strain associated with thermal expansion in an equivalent range of temperature.
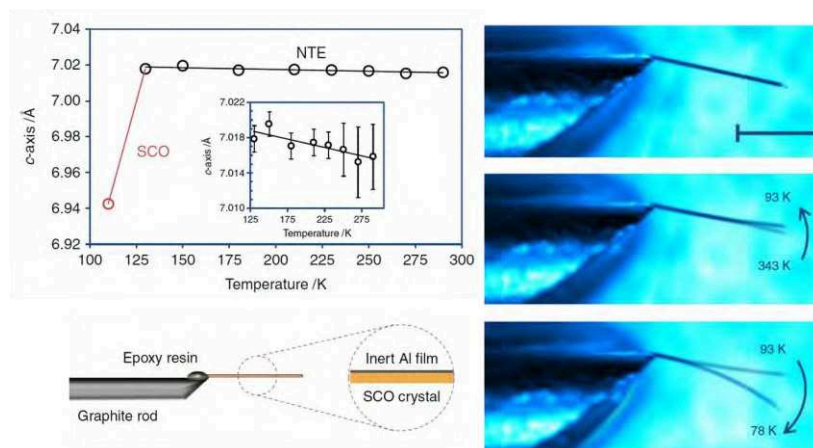


Figure 1.2.33: NTE and SCO effects on a $\{Fe(3\text{-}CNpy)[Au(CN)_2]_2\}\cdot\frac{2}{3}H_2O$ crystal and illustration of the composite structure of the cantilever (left); optical microscope image of the cantilever at 343 K and comparison of the cantilever highlightling the deflection caused by NTE and spin transition (right).

These highly anisotropic crystals were anchored to graphite rods with epoxy resin, and were subsequently coated with a thin film of Al metal to produce freestanding composite cantilevers as shown in figure 1.2.34. Both thermal variation and light irradiation were used to induce SCO and thus motion in these bilayers. The effect of changing temperature on the

cantilever shape was recorded between 343 and 78 K, as shown in the figure (right part). We can clearly see the opposite effects of the NTE and the spin crossover. This study was extended using composite bilayer leading to highly versatile approach which allows to use virtually any compound from the vast library of SCO complexes as the active layer. By dispersing $[Fe(Htrz)_2(trz)](BF_4)$ nanoparticles in a poly(methylmethacrylate) (PMMA) matrix, the freestanding bilayer (SCO/PMMA)/PMMA film was obtained.[101] Based on spin transition phenomenon of this prototype device, electrical energy was converted to mechanical motion through Joule heating. The efficient electromechanical actuating device with a volumetric work density of ca. 150 mJ cm$^{-3}$ exhibited repeatable and tunable actuation via temperature, frequency and current variation and provided both large force (several mN) and large displacement (several mm).
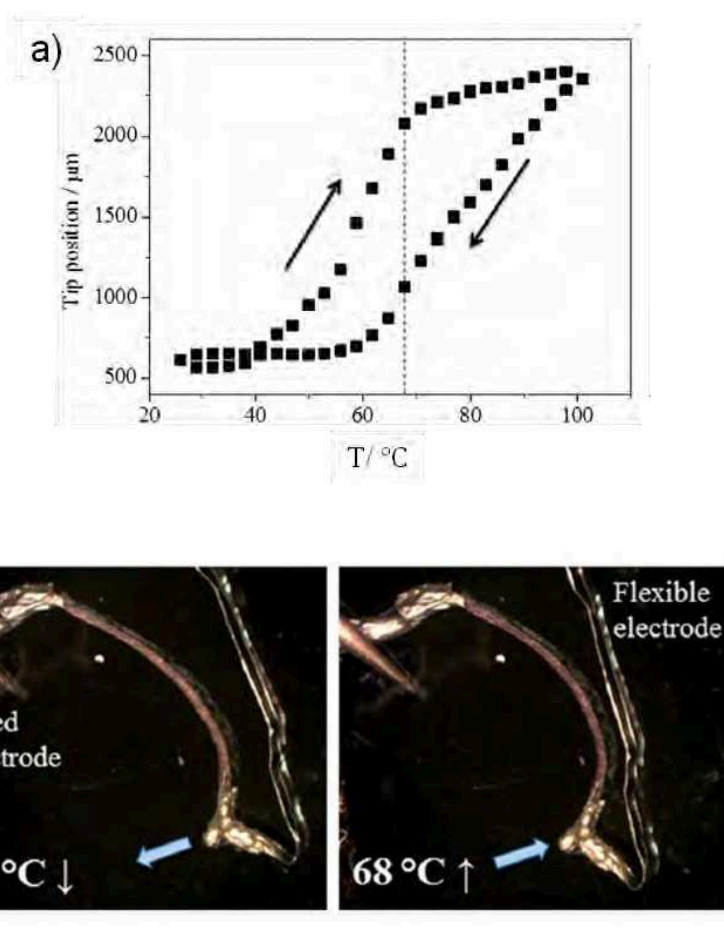


Figure 1.2.34: Thermal actuation of a bimorph (SCO/PMMA)/PMMA cantilever. **a)** Tip position of the cantilever as a function of temperature. Heating and cooling modes are indicated by arrows. **b)** Photographs (8.6 mm- 7.6 mm) of the cantilever at 68 °C in the cooling and heating modes demonstrate a shape memory effect, which occurs due to the thermal hysteresis of the spin transition. The color change associated with the spin transition is also observed.

Then, in Tong's group[175] by drop-casting [Fe(Htrz)$_2$(trz)](BF$_4$) / polycarbonate composite on the surface of a prefabricated 120 Ω polyimide/constantan alloy/polyimide sensitive plate, a conductive spin crossover cantilever with an immobilized wiring terminal and a free end was fabricated. The hysteretic electrical resistivity was further converted by a Wheatstone bridge into highly sensitive bistable voltages.
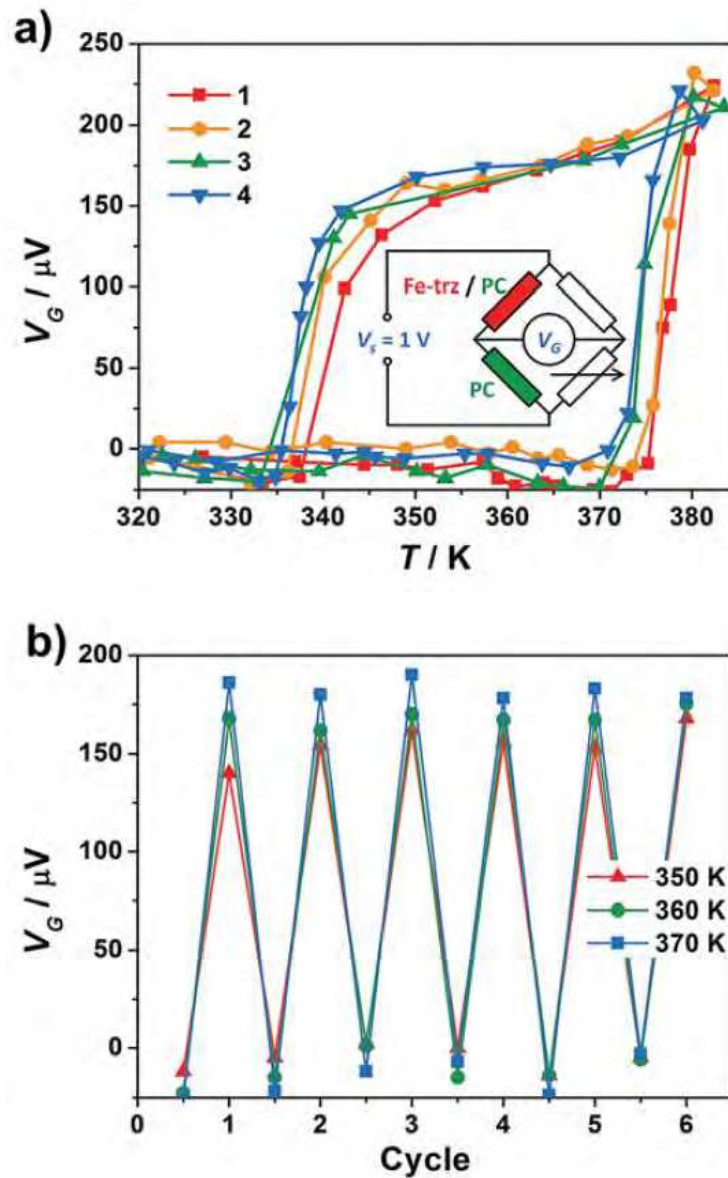


Figure 1.2.35: **a**) Bistable voltages of the Wheatstone bridge; **b**) Wheatstone bridge voltages at various temperatures during consecutive thermal cycles.

# 1.3 Objective of the Thesis

Due to the specific behaviors of spin crossover materials at nanocale, many efforts have to be devoted to the investigation of their size and morphology dependent properties and the exploration of their possible applications in future nanophotonic, nanoelectronic and spintronic devices. Furthermore, a big challenge in this area of research is how to obtain stable spin crossover nanomaterials with specific transition temperatures (often room temperature) and a large hysteresis loop (memory effect) and thus, the development of new synthetic chemistry method will play a key role in this field.

The main objective of this thesis is to synthesize spin crossover nanomaterials with various sizes and various shapes, on one hand in order to probe what is the effect of the size reduction on the spin crossover properties and in the other hand to obtain room temperature spin transition materials\objects for potential future applications. Thus the work focused on the synthesis of various sizes 3D Hofmann like Clathrate [Fe(pz){Ni(CN)$_4$}] nanoparticles and rod-shaped spin crossover particles based on compound from the well-known Fe-triazole family. To accomplish this, we have developed the nano-emulsion technique and adopted innovative matrix-free synthetic technique. Indeed, in the last few years, syntheses in microemulsion have clearly demonstrated the possibility to obtain nano-sized spin crossover materials. We decided thus to pursue the development of this technique since it seems to be the more efficient way to obtain a series of different-size nanoparticles with the same environment. However, in many cases, the coating around spin crossover materials could be undesirable for practical applications, thus it is also really important to explore other methods like surfactant free synthetic approaches to reach this aim. Then different spin crossover particles were also synthesized in homogeneous acid media. All the particle samples were fully characterized notably by a fine electronic microscopy study coupled with Energy Dispersive X-ray Diffraction analyses. Their optical, magnetic and electrical properties are also presented.

# Chapter 2

# Synthesis of [Fe(pz){Ni(CN)$_4$}] Nanoparticles: Size Effect Study on their SCO Properties

## 2.1 Introduction and Objectives

Recently, we have assisted a strong renewed interest in the field of molecular spin crossover complexes as demonstrated by the emergence of nanosized spin crossover materials through synthesis of nanopatterned thin films[9,11,176] and coordination nanoparticles[9,145-147,149-151,157,168,170,176-195]. Indeed, the synthesis of nanometer sized spin crossover materials, their manipulation at reduced length scales and the investigation of their size dependent properties contribute to explore their possible practical applications in future nanophotonic, nanoelectronic and spintronic devices. An important challenge in this context is to preserve the bistability through the conservation of the cooperative spin transition properties during the downsizing of the compound at the nanoscale. As it is well known, the macroscopic behaviour of bulk SCO materials is strongly influenced by electron-lattice coupling effects. In particular the modification of the volume and the shape of the molecules accompanying the spin-state change leads to considerable elastic interactions. These interactions give rise to various cooperative phenomena, such as first-order phase transitions or self-accelerating relaxations. In a first approximation, size reduction effects in spin crossover materials are expected to occur primarily due to the reduction in the number of interacting metallic centres leading to the decrease of the cooperativity. Nevertheless, this picture is far too simplistic and many other parameters and material properties have to be considered in order to interpret the experimental observations obtained with SCO nanomaterials.

The groups of J. A. Real and T. Mallah reported the size dependent properties of nanoparticles of the three-dimensional SCO coordination polymer [Fe(pz){Pt(CN)$_4$}] (pz = pyrazine) obtained in microemulsion.[178,194] They found that reducing the particle size, leads to more gradual spin transitions with a shift to lower transition temperatures and a shrinking

until a total disappearance of the hysteretic behavior for particle sizes smaller than 15 nm. The modification of the spin crossover behavior is also accompanied by an increase of the residual high spin fraction at low temperature. On the other hand, Mallah's group demonstrated that the spin crossover properties not only depend on the size, but also on the particle's environment (matrix effect).[188] In this case, the cooperativity could be dramatically affected by the surrounding matrix. Such effect has been discussed for [Fe(pz){Pt(CN)$_4$}] nanoparticles coated with various stabilizers such as silica, AOT (Bis(2-ethylhexyl) sulfosuccinate sodium salt) surfactant and calixarene. They suggested that this effect is associated with interparticle interactions mediated by the matrix. In this scope, in collobration with Guari's group, we previously reported the syntheses of nanocomposites in which [Fe(pz){Ni(CN)$_4$}] spherical nanoparticles of 3-4 nm were embedded into porous polysaccharide matrixes.[149,184] A special emphasis in this work has been devoted to the investigation of magnetic properties of these nanocomposites and the understanding of the role of the different matrixes. The nanocomposite [Fe(pz){Ni(CN)$_4$}]/chitosan beads present spin transition centred at 280 K exhibiting a hysteresis loop with the width of 10 K. The transition temperatures as well as the shape of the hysteresis in this nanocomposite are close to those observed for the bulk analogues, while the hysteresis width decreases from 26 K to 10 K. The preservation of the cooperativity and the hysteresis loop could be explained by the specific matrix effect generated by the chitosan polymer. Thanks to Mössbauer measurements, an important inactive fraction corresponding to approximately 65% of the total area was measured and was attributed to the iron atoms (both in the HS and LS state) localized at the surface of the nanoparticles. Indeed, the approximate theoretical percentage of these iron atoms fraction for a 4 nm diameter nanoparticle is approximately 60-70% (taking into account the *ca.* 400 Å$^3$ unit cell volume measured by X-ray diffraction on single crystal).

These works highlight the crucial feature of the mechanical/elastic properties of the nanocomposite as a whole and open up interesting questions regarding the role of the elastic properties of the particles, that of their matrix as well as the possible role of the inter-particle interactions when the particles are in close proximity. In addition, other hypotheses also exist such as the chemical or mechanical influence of the surface on the properties of the particle. In many cases, a SCO inactive (either high spin or low spin) residual fraction was reported for small particles and this residue is usually associated with the iron centres located on the surface. Indeed it seems likely that molecules on surfaces have different SCO properties with respect to the inner molecules and this may drastically influences the properties of the whole particle in this very low size range.

In a very recent study in collaboration with the group of Y. Guari,[196] our group performed a $^{57}$Fe Mössbauer spectroscopic study to follow the evolution of the elastic properties of coordination nanoparticles (particles without phase transition) embedded in the same matrix (polyethylene glycol) as a function of their size. A sharp increase in the stiffness at very small particle sizes was shown. This theoretical and experimental study clearly shows that elastic properties of nanoparticles can change with the particle size. This implies many consequences in the case of spin crossover materials. One hypothesis is that the surfaces are more rigid than the core of the particle. In a first time, a size decrease would lead to a decrease of cooperativity until a certain size (about 50 nm). Then the influence of surfaces would become greater and there would be an increase of cooperativity. In the spin crossover context, it would possibly mean a loss of hysteresis in a first time and its reappearance, in a second time. In any case, it appears necessary to carry out size studies using the same spin crossover compound in the same matrix. From an experimental point of view, this represents a big challenge for chemists as different synthesis methods are often necessary to produce nanoparticles with different-size. In order to better understand this phenomenon, the elastic properties of SCO particles with sizes between *ca*. 3 and 30 nanometres have to be explored systematically and confronted with the theoretical models based on non-extensive nano-thermodynamic or statistical physics recently developed.[196-201]

The objective here is to study the evolution of the spin crossover properties of a complete series of [Fe(pz){Ni(CN)$_4$}] nanoparticles with different size, but with the same environment in order to demonstrate experimentally the influence of the surface and the particle stiffness on the cooperativity and spin crossover properties for nanoparticles with ultra-small sizes (10 nm) in particular using the conventional Mössbauer spectroscopy. Besides, compared to the conventional and powerful Mössbauer spectroscopy, the NIS (Nuclear Inelastic Spectroscopy) method can provide the complete 57-Fe phonon absorption spectrum in solids, liquids or gases. Besides, as in Raman spectroscopy, the Stokes and anti-Stokes peaks are very weak compared to the Rayleigh peak and the intensity of conventional γ-ray sources is not strong enough to observe them. Currently, the only source that enables to overcome this problem is the synchrotron radiation. So different-size [$^{57}$Fe(pz){Ni(CN)$_4$}] nanoparticles were also synthesized starting with metallic 57-Fe powder, and then NIS technique was used to study the acoustic modes which can give access to the vibrational density of states (DOS) at low energies and thereby, provide some important thermo-dynamical and lattice dynamical parameters as well as their spin-state dependence.

# 2.2 Synthesis of Different-Size [Fe(pz){Ni(CN)$_4$}] Nanoparticles

The reverse nanoemulsion technique has been used previously for the synthesis of [Fe(pz){Pt(CN)$_4$}] nanoparticles and the preparation conditions are listed in table 2.1. Modifying the corresponding experimental conditions: the reactant concentration and ω (the polar phase/ surfactant molar ratio), different-size nanoparticles ranging from *ca.* 8 nm to several hundred nm were synthesized.

| Group | [Fe]/mol·L$^{-1}$ | ω | V$_{oil}$ (mL) | Temperature/K | Size (nm) |
|-------|-------------------|-----|----------------|---------------|-----------|
| Real | 0.05 | 5 | 44 | 293 | 230 |
|  | 0.01 | 5 | 44 | 293 | 61 |
| Tallal | 0.08 | 10 | 33 | 293 | 14 |
|  | 0.14 | 10 | 33 | 293 | 8 |
|  | 0.02 | 10 | 33 | 293 | 40 |

Table 2.1**:** [Fe(pz){Pt(CN)$_4$}] nanoparticles with different sizes prepared by different research groups

In contrast with the previously reported synthesis methods and in order to reach ultra small nanoparticles (< 10 nm) both the preparation of the starting nanoemulsions and the micellar exchange reaction were performed at different low temperatures, playing also with the reactant concentration, the ω ratio being maintained constant.
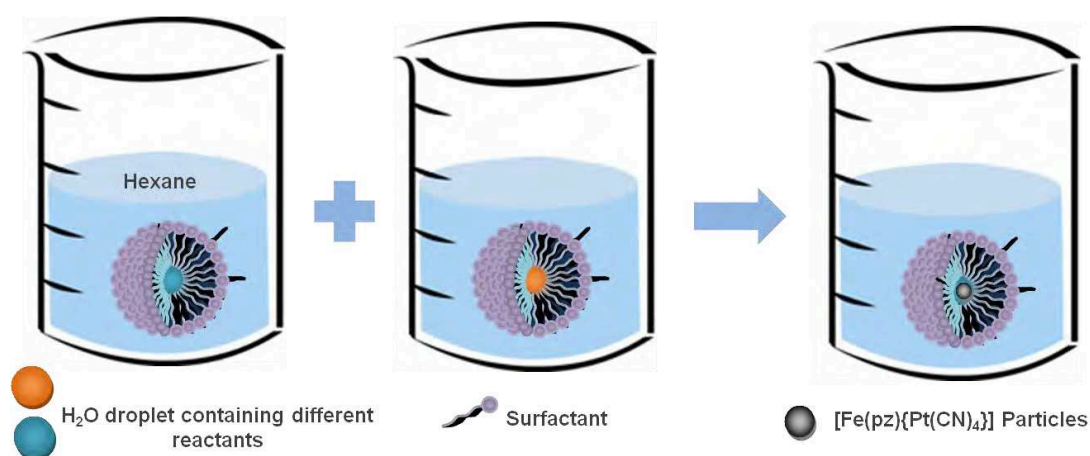


Figure 2.1: Scheme of the preparation of nanoparticles using the reverse emulsion technique.

In our case, the surfactant is NaAOT (sodium bis(2-ethylexyl sulfosuccinate)), the oil phase is hexane, the polar phase is water and the target sample is the [Fe(pz){Ni(CN)$_4$}] complex. We selected this compound because of several reasons: I) the tetracyanonickelate salt is cheaper compare to the platinum derivative; II) for this complex there is a small effect of guest solvent on the spin crossover properties and III) the spin crossover occurs at room temperature. The preparation process of micro-emulsion is shown in the figure 2.1.

Two reverse emulsions were prepared separately, one containing Fe(BF$_4$)$_2$·6H$_2$O and pyrazine and the other containing K$_2$Ni(CN)$_4$. To the solution of NaAOT in hexane, K$_2$Ni(CN)$_4$ aqueous solution was added and the biphasic system was stirred until a clear emulsion was obtained. The same procedure was applied to aqueous solution containing both Fe(BF$_4$)$_2$·6H$_2$O salt and pyrazine ligand (in Annex 1). The two emulsions were cooled overnight in a fridge (278 K) to be stabilized and then mixed (dropwise) with a slow addition rate at room temperature. The color of the mixture changes from yellow to orange. After 10 minutes of stirring, EtOH was added to the reaction mixture. The resulting flocculate was centrifuged, washed with ethanol and then dried under vacuum. This led to sample **1**.

Sample **2** was obtained by the same procedure as sample **1**, but with a fast addition rate (direct addition) of the two reverse nanoemulsions.

Sample **3** was obtained by the same procedure as sample **1**, but with a higher concentration of metal ions.

Sample **4** was obtained by the same procedure as sample **3**, but mixing the two reverse emulsions at low temperature (243 K).

Sample **5** was obtained with a higher concentration of metal ions and mixing the two reverse emulsions at low temperature (258 K).

| Sample | [Fe]/mol.L$^{-1}$ | $\omega$ | V$_{H2O}$(mL) | V$_{Hexane}$(mL) | Temperature/K |
|--------|-------------------|----------|---------------|------------------|---------------|
| 1      | 0.1               | 10       | 6             | 66               | 293           |
| 2*     | 0.1               | 10       | 6             | 66               | 293           |
| 3      | 0.15              | 10       | 6             | 66               | 293           |
| 4      | 0.15              | 10       | 6             | 66               | 243           |
| 5      | 0.2               | 10       | 6             | 66               | 258           |

Table 2.2: Preparation conditions of different samples, * fast mixture of the two nanoemulsion, and $\omega$ = [H$_2$O]/[AOT]

Based on the synthetic condition of sample **4**, we also tried to decrease more the reaction temperature, but obtained fast precipitation during the starting nanoemulsion stabilization process. Furthermore, the maximum concentration of metal solution which can be stabilized in nanoemulsion is *ca.* 0.2 mol·L$^{-1}$. Nevertheless, for such concentration, the lowest temperature avoiding the precipitation is 258 K.

Figure 2.2 shows the characteristic color change of the samples from orange to yellow when passing from low spin to high spin state (for sample **1**). See subchapter 2.6 for the color change of the other samples and discussion concerning the color/size relationship.



Figure 2.2: the characteristic color change of [Fe(pz){Ni(CN)$_4$}] nanoparticles at high (left) and low (right) temperature

# 2.3 Composition of [Fe(pz){Ni(CN)$_4$}] Nanoparticles

## 2.3.1 Thermal analysis

Thermogravimetric analysis (TGA) was acquired using a Perkin–Elmer Diamond thermal analyzer.
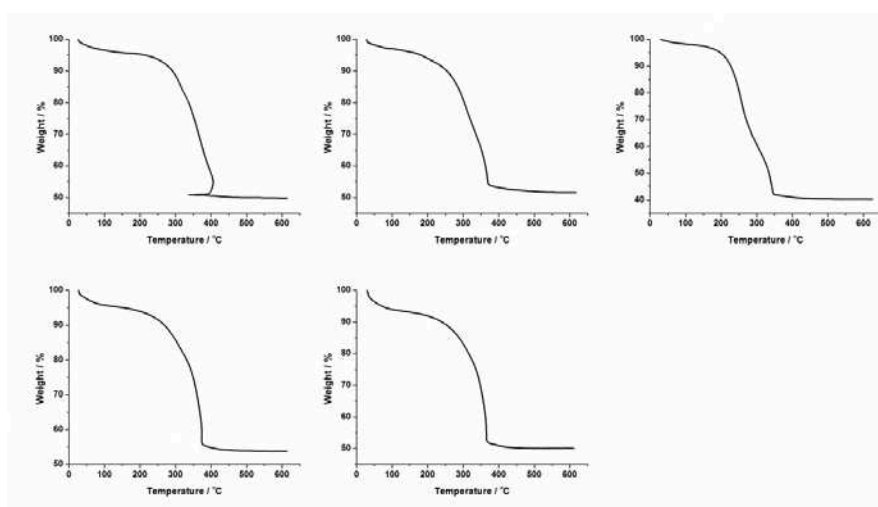


Figure 2.3: TGA measurements on samples **1-5**

The weight loss of $H_2O$ for the step 1 and decomposition of the compound for the step 2 of each sample are listed in the table 2.3.

| Weight loss step | Sample **1** | Sample **2** | Sample **3** | Sample **4** | Sample **5** |
|---|---|---|---|---|---|
| 1 (%) | 4.0 (0.7·$H_2O$) | 3.3 (0.8·$H_2O$) | 2.1 (0.6·$H_2O$) | 4.1 (1·$H_2O$) | 6.2 (1·$H_2O$) |
| 2 (%) | 46 | 45 | 56 | 40 | 42 |

Table 2.3**:** The weight loss of samples **1-5** during the thermogravimetric process

The quantities of water molecules were taken into account for the determination of the chemical composition in combination with the elemental analyses.

## 2.3.2 Elemental analysis

Analysis for C, H, and N were performed after combustion at 850°C using IR detection and gravimetry by means of a Perkin–Elmer 2400 series II device.

| Compound | | C / % | H / % | N / % | Calculated Formula |
|---|---|---|---|---|---|
| **1** | exptl | 30.87 | 1.74 | 26.25 | [Fe(Pyrazine)Ni(CN)$_4$]•0.7$H_2O$ |
| | calcd | 30.14 | 1.66 | 25.77 | |
| **2** | exptl | 32.26 | 2.03 | 25.95 | [Fe(Pyrazine)Ni(CN)$_4$]•0.8$H_2O$•0.02S |
| | calcd | 31.74 | 1.58 | 25.95 | |
| **3** | exptl | 34.65 | 2.18 | 20.07 | [Fe(Pyrazine)$_{0.6}$Ni(CN)$_4$]•0.6$H_2O$•0.2S |
| | calcd | 35.25 | 2.56 | 19.18 | |
| **4** | exptl | 27.70 | 1.63 | 22.18 | [Fe(Pyrazine)$_{0.3}$Ni(CN)$_4$]•1$H_2O$•0.08S |
| | calcd | 27.45 | 1.84 | 22.18 | |
| **5** | exptl | 26.60 | 2.24 | 20.44 | [Fe(Pyrazine)$_{0.2}$Ni(CN)$_4$]•1$H_2O$•0.13S |
| | calcd | 26.07 | 1.85 | 20.44 | |

Table 2.4**:** Elemental analyses of samples **1-5** and the corresponding formula

Each sample was washed several times by EtOH to remove the surfactant on the surface of the nanoparticles. From the elemental analysis results, it seems that for sample **1** the surfactant was removed completely. In contrast, as the nanoparticle size decreases it becomes difficult to remove all the surfactant maybe due to the large surface to volume ratio. Moreover, a significant decrease of the pyrazine amount as the measured nanoparticle sizes decrease. Supported by all the physico-chemical measurements, we have good reason to think that the iron atoms localized at the surface of the particles (whatever their size) have different crystal field environments (different geometry and/or different ligands) compared to the core iron atoms and in particular these surface atoms exhibit a missing pyrazine molecule which can be replaced by a solvent molecule. Moreover, this modification induces different effect on the global composition of the nanoparticle as a function of their size: for the larger particle, the percentage of iron atoms localized at the surface is negligible and a stoechiometric formula is obtained. A *contrario*, this percentage becomes more and more preponderant for smaller size particles and as a consequence the percentage of missing pyrazine molecule increases as well and becomes significant.

# 2.4 Morphological Characterization of [Fe(pz){Ni(CN)$_4$}] Nanoparticles

Transmission electron microscopy (TEM) and high resolution transmission electron microscopy (HRTEM) were used to determine the size of the nanoparticles. A TEM JEOL JEM 1400 (120 kV) and a high-resolution TEM JEOL JEM 2100F (200 kV) equipped with a PGT X-ray analyzer were used for size and composition analysis of the nano-objects.

## 2.4.1 Transmission Electron Microscopy Analysis

TEM samples were prepared by deposition of the nanoparticle suspension in ethanol on a carbon-coated copper grid. For each sample, the mean size of the nanoparticles was carefully checked by performing several TEM measurements with different grid preparations and considering more than hundred nanoparticles (each synthesis and associated sample characterization was repeated at least twice).

Figure 2.4 shows selected TEM pictures of the corresponding bulk sample. Compared to the following nanoparticle samples, although large size square-shaped particles can be observed, the image shows rather aggregated and polydisperse object size.
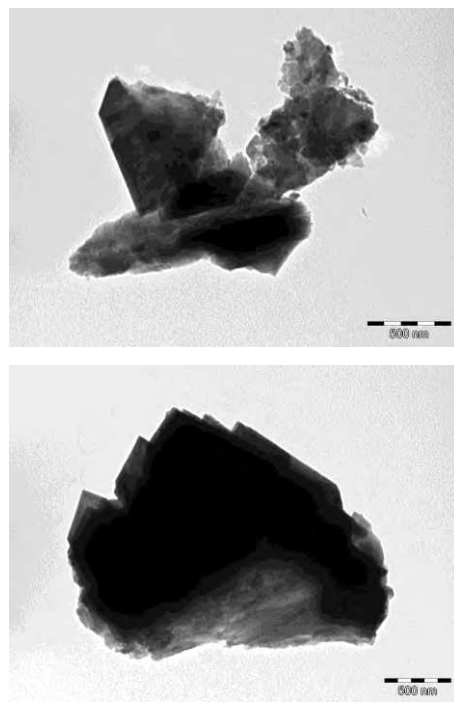
Figure 2.4: TEM images of the [Fe(pz){Ni(CN)$_4$}] bulk sample

Figure 2.5-2.9 present a selected TEM image for each nanoparticles sample and associated size distribution histogram (see also Annex 2 for complementary TEM images). As already reported for numerous nanoparticle syntheses and validated for the elaboration of [Fe(pz){Pt(CN)$_4$}] derivative nanoparticles, increasing reactants concentration, while maintaining constant the polar phase / surfactant molar ratio (ω), leads to the decrease of the mean size of the nanoparticles. Indeed, while increasing the concentration from 0.1 to 0.15 M, a clear decrease of mean size of the particles was observed from 71 nm (sample **2**) to 12 nm (sample **3**). In fact it is well known that for high concentrations of the reactants, the nucleation is favorized compared to the growth of the nanoparticles. Nevertheless, while playing with the concentration, it was not possible to decrease the nanoparticle size below *ca.* 12 nm because of the insolubility of the starting materials. Comparison of the TEM for samples **1** (107 nm) and **2** (71 nm) also shows that the addition speed of the emulsions plays also a key role on the nanoparticles size. Eventually, reducing the reaction temperature to 243 K permitted us to reach nanoparticle sizes smaller than 10 nm (3 nm for sample **4**). We tried to reduce even further the reaction temperature, but these experiments resulted repetitively to the immediate destabilization of the nanoemulsions. By modifying both the temperature and reactant concentration even smaller 2 nm sized particles were obtained (sample **5**).
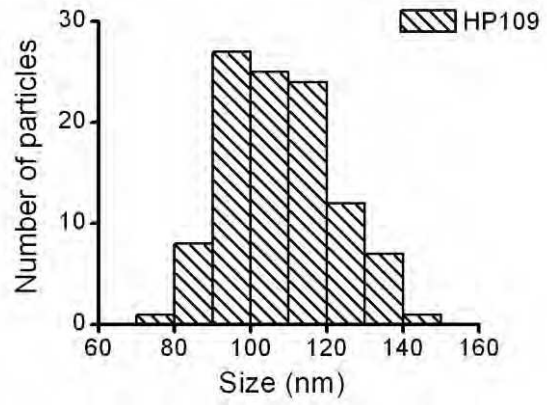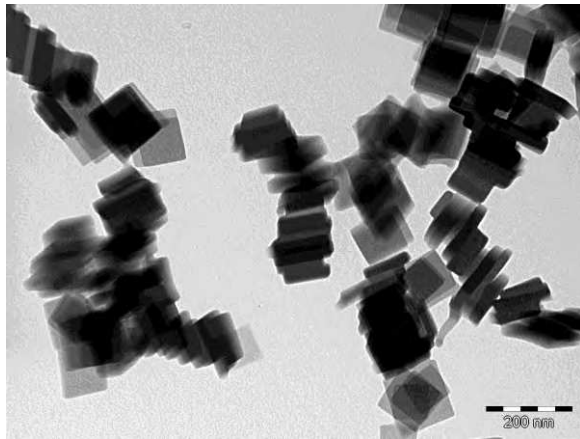
Figure 2.5: TEM image and associated size distribution histogram of sample **1**
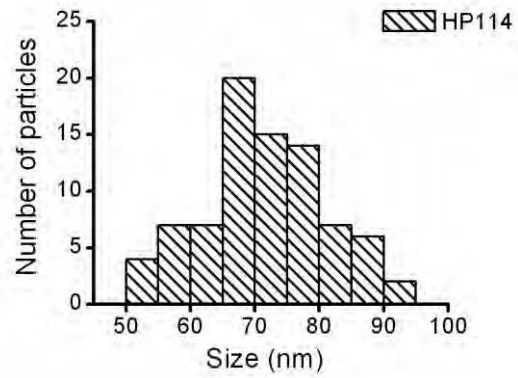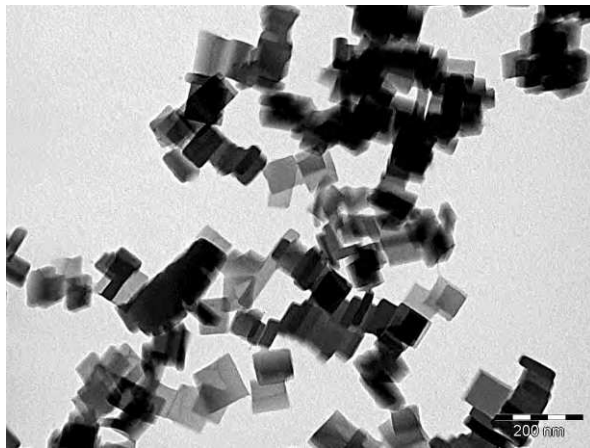


Figure 2.6: TEM image and associated size distribution histogram of sample **2**
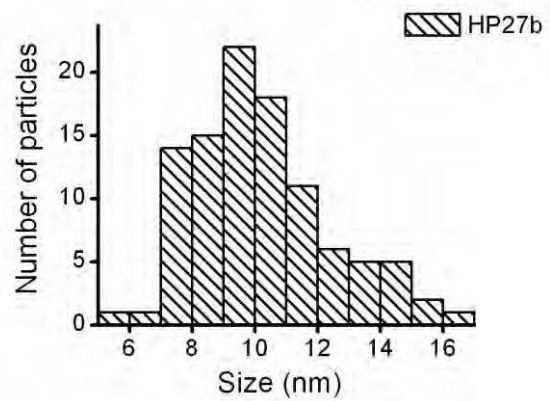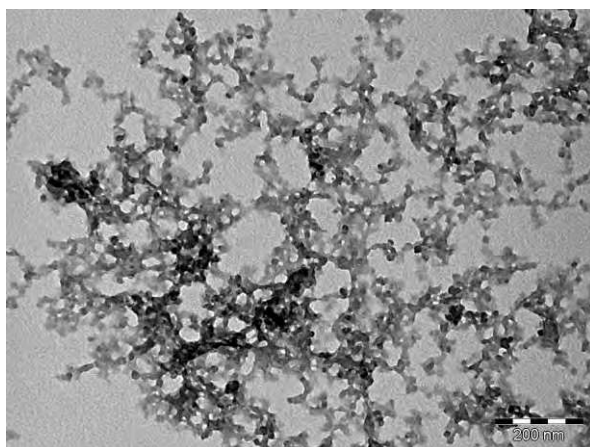


Figure 2.7: TEM image and associated size distribution histogram of sample
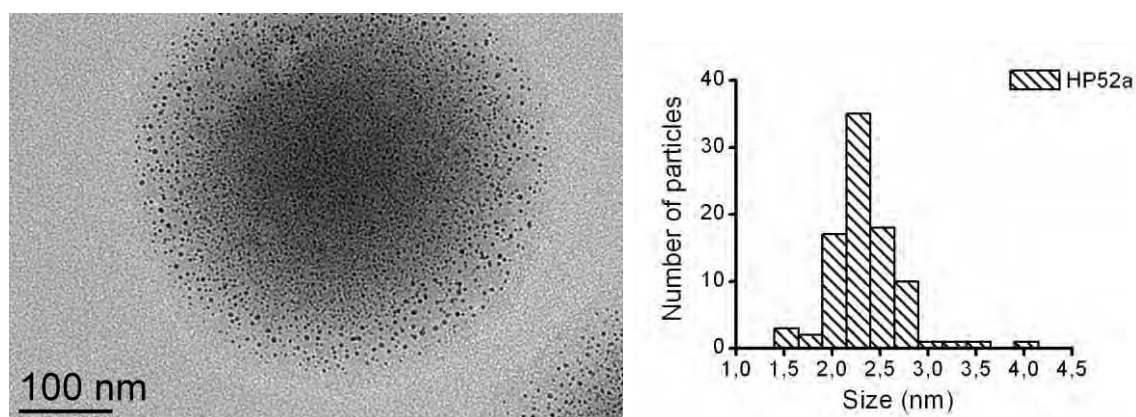
Figure 2.8: TEM image and associated size distribution histogram of sample **4**
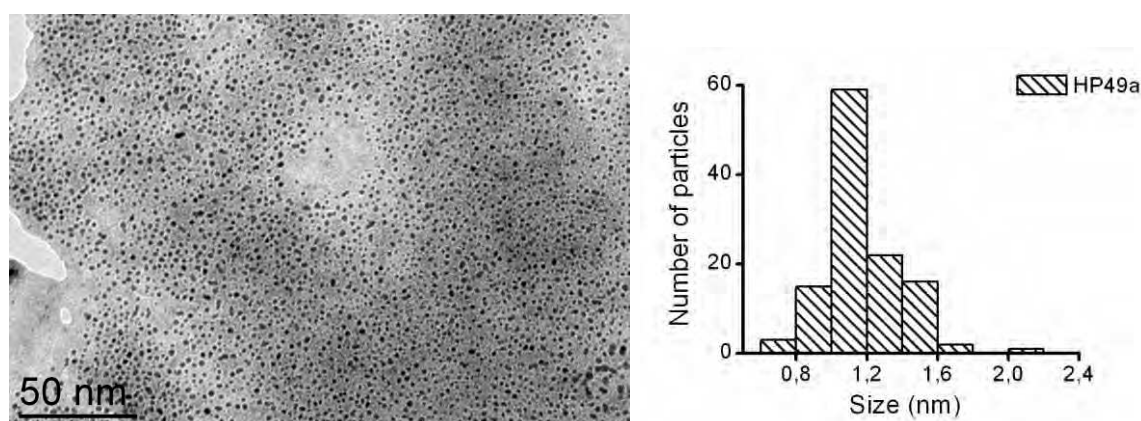


Figure 2.9: TEM image and associated size distribution histogram of sample **5**

| Sample | [Fe]/mol.L$^{-1}$ | Temperature/K | Nps Size/nm |
|--------|-------------------|---------------|-------------|
| 1 | 0.1 | 293 | 107±14 |
| 2 | 0.1 | 293 | 71±10 |
| 3 | 0.15 | 293 | 12±3 |
| 4 | 0.15 | 243 | 3.1±0.4 |
| 5 | 0.2 | 258 | 2.0±0.3 |

Table 2.5**:** Mean size of the nanoparticle samples

It is interesting to notice that for the ultra-small size nanoparticles (sample **4** and **5**), the morphology of the nanoparticles seems to evaluate from the cubic to the spherical shape. Such structural modification could contribute to explain the modification of the elastic interaction in the particles and the concomitant evolution of their spin crossover properties. So, control of

the experimental conditions permits us to obtain a sample series with nanoparticle sizes ranging from 2.0 to 107 nm (this size corresponding to the in-plane width). All these results are gathered in table 2.5. **For the first time such ultra small (< 5 nm) Hofmann like clathrate's polymer nanoparticles were synthesized.**

## 2.4.2 High Resolution Transmission Electron Microscopy Analysis

High Resolution Transmission Electron Microscopy (HRTEM) associated with EDX spectrometry was used to better characterize the morphology and the composition of the nanoparticles. EDX is an analytical technique used for the elemental analysis or chemical characterization of a sample. It relies on an interaction of some source of X-ray excitation and a sample. Its characterization capabilities are due in large part to the fundamental principle that each element has a unique atomic structure allowing unique set of peaks on its X-ray emission spectrum. Figure 2.10-2.11 also show HRTEM images of samples **4** and **5** where one can distinguish the ultra-small particles (mean size about 3 nm for sample **4** and 2 nm for sample **5**). It is important to note that while passing from 100 kV TEM to 210 kV HRTEM, the increase of the resolution is associated with a diminution of the contrast of the nanoparticles. In order to be sure that the SCO properties are not biased by the presence of a small amount of larger particles, we have scanned several TEM grids and analyzed carefully the larger aggregates. All the EDX analyses on such large particles and/or aggregates showed the absence of the Fe(pyrazine)[Ni(CN)$_4$] complex and the presence of the organic surfactant phase.

Moreover, Energy Dispersive X-ray (EDX) spectrometry was also employed in order to determine the composition of the particles (see figure 2.12 (sample **3**) and 2.13 (sample **5**)). Whatever the considered area, from 500 nm$^2$ (several dozens of particles localized in the square area - figure 2.12) to 1 nm$^2$ (two measurements on single particle localized by the cross - figure 2.13), and whatever the nanoparticle size, the quantitative EDX analyses showed equivalent percentage of iron and nickel atoms, confirming the presence of the [Fe(pyrazine){Ni(CN)$_4$}] complex. For sample **3**, a small amount of sulfur was also determined by EDX analysis in agreement with the presence of remaining AOT surfactant. Figure 2.12 shows also the compositional maps for Fe and Ni atoms in the selected square and indicates a homogeneous distribution of the Fe and Ni atoms in the nanoparticles confirming again the good composition of the sample.
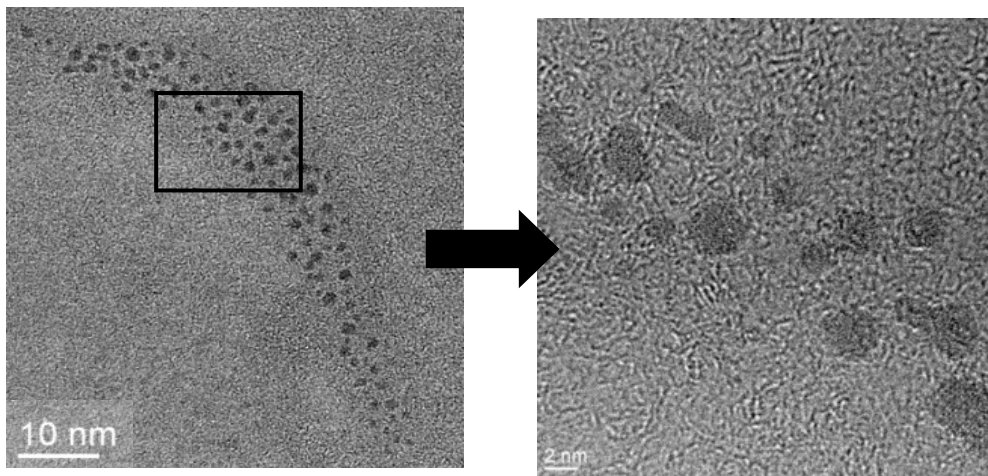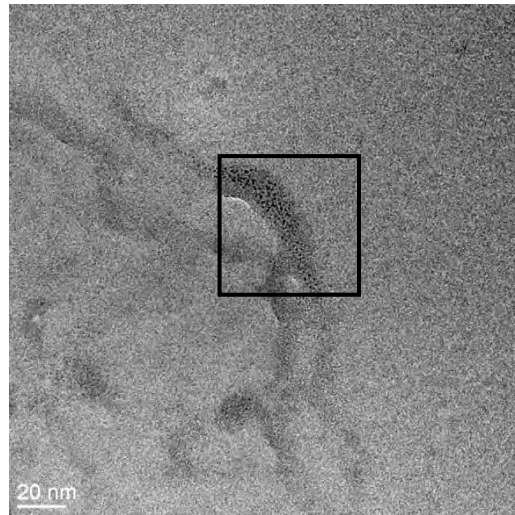
Figure 2.10: HRTEM image of sample **4**
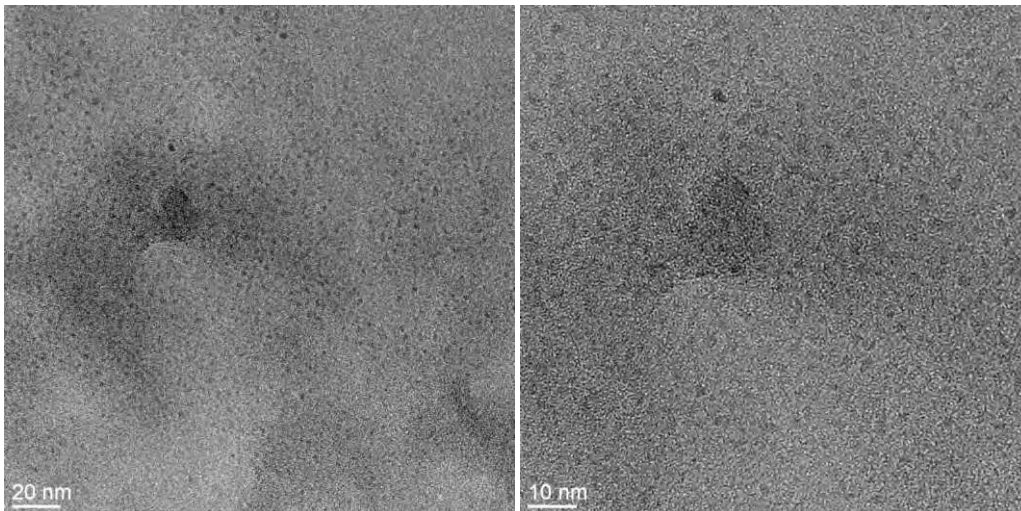


Figure 2.11: HRTEM images of sample **5**
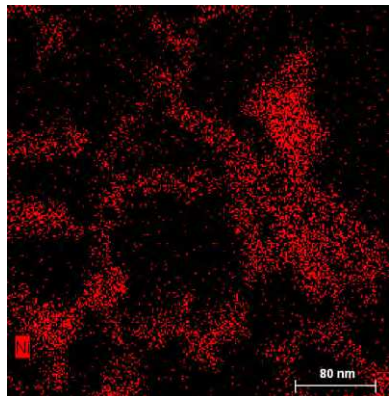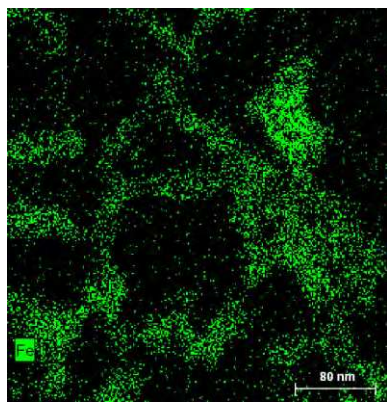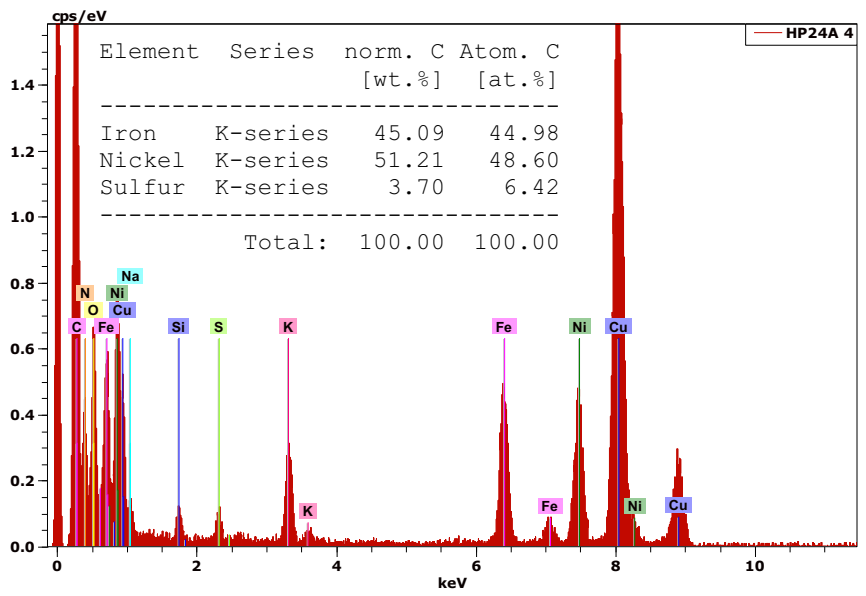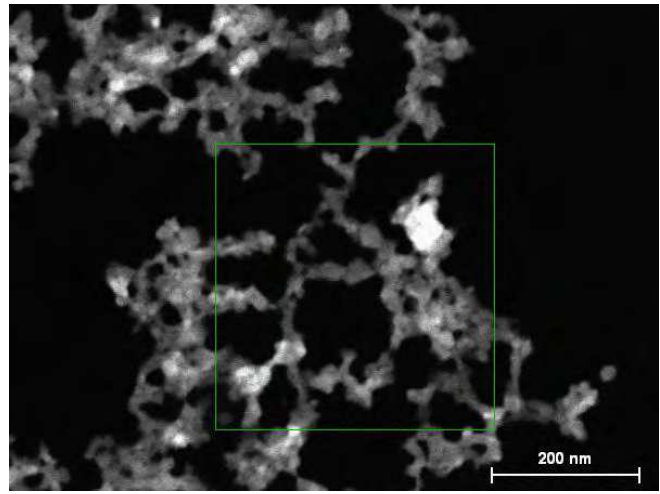
Figure 2.12: HRSTEM dark-field image and EDX analyses of sample **3**, EDX measurements were collected from the square area indicated in the STEM image. STEM EDX compositional maps for Fe and Ni atoms.
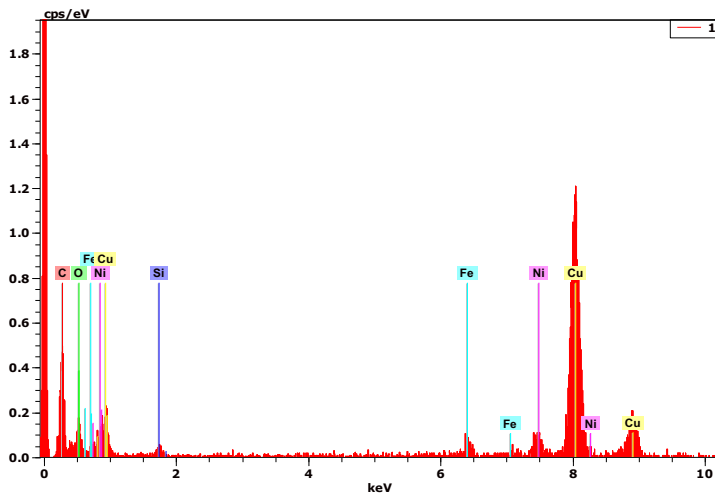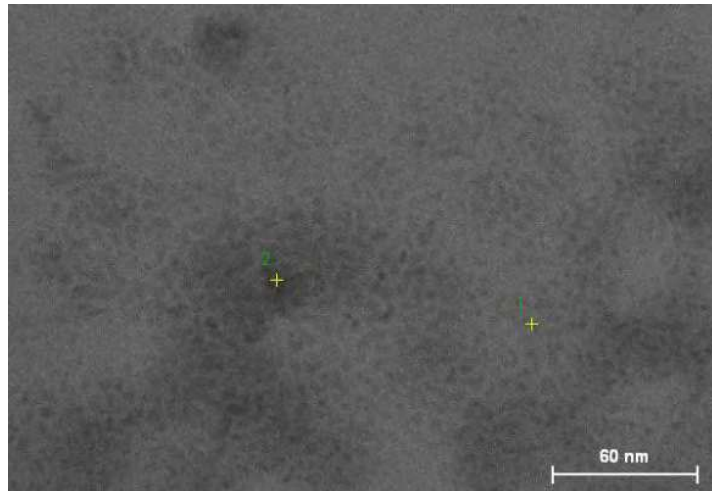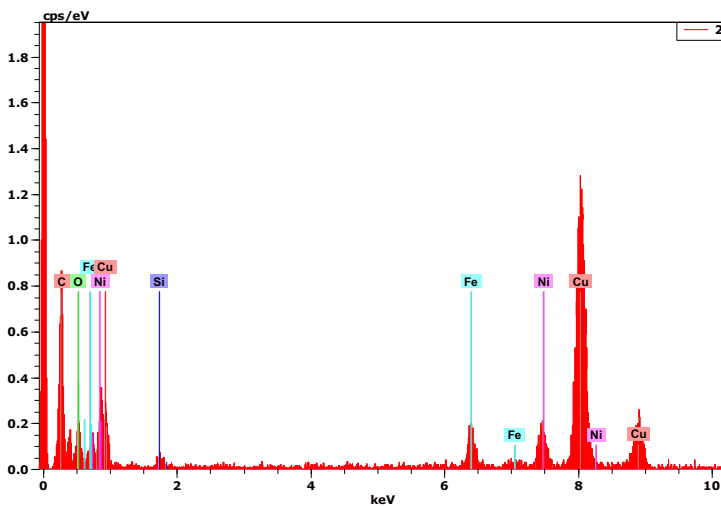
Figure 2.13: HRSTEM image and EDX analyses of sample **5**, EDX measurements were performed at two different positions.

# 2.5 Structural Characterization of the [Fe(pz){Ni(CN)₄}] Nanoparticles

## 2.5.1 X-Ray Diffraction on Single Crystal

The structure was reported by C. J. Kepert and coworkers[70]: it adopts the general topology reported previously,[173] consisting of 2-D FeNi(CN)$_4$ layers bridged through the six-coordinate Fe(II) centers by bis-unidentate pyrazine bridges (see figure 2.14).
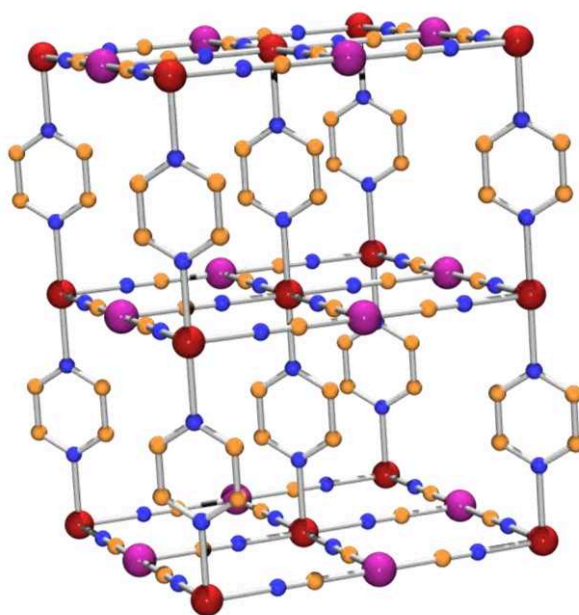


Figure 2.14: Crystal structure of [Fe(pz){Ni(CN)₄}], yellow: C, blue: N, red: Fe and pink: Ni.

From a non-twinned crystal the material was determined to crystallize in the orthorhombic space group *Pmmm* (see table 2.6), rather than in the tetragonal space group *P*4/*m* as determined previously for the platinum derivative.[173] The majority of crystals measured were found to be merohedrally twinned, yielding a and b parameters that represent averaged values within an apparent tetragonal lattice; datasets collected on these crystals yielded excellent structural refinements in P4/mmm with 50:50 occupation of orthogonal pz orientations but were refined instead in Pmmm with a twin relation. The Fe-N bond lengths for two structures obtained at 150 K (non-twinned and twinned) and one at 300 K of Fe-Ncyanide = 1.944(3) Å Fe-Npyrazine = 1.986(3) Å (150 K non-twinned), Fe-Ncyanide =

1.946(5) Å, Fe-Npyrazine = 1.971(5) Å (150 K twinned), and Fe-Ncyanide = 2.128(4) Å, Fe-Npyrazine = 2.226(6) Å (300 K) are indicative of low-spin (LS) and high-spin (HS) $Fe^{II}$ centers, respectively.

| [Fe(pz){Ni(CN)$_4$}]·2H$_2$O | | |
|---|---|---|
| Spin state | HS | LS |
| FW/ g mol$^{-1}$ | 334.76 | 298.73 |
| Space group | *Pmmm* | *Pmmm* |
| a/Å | 7.2666(3) | 7.016(1) |
| b/Å | 7.2696(3) | 7.019(1) |
| c/Å | 7.2421(3) | 6.785(1) |
| V/Å$^3$ | 382.57(3) | 334.16(9) |
| $\rho_{calc}$/Mg m$^{-3}$ | 1.453 | 1.664 |
| μ/mm$^{-1}$ | 2.180 | 2.496 |
| data/restraints/parameters | 688/1/37 | 561/1/36 |
| R$_1$($F^2$) [$I > 2\sigma(I)$, all] | 00393, 0.0541 | 0.0362, 0.0688 |
| ωR$_2$($F^2$) [$I > 2\sigma(I)$, all] | 0.1083, 0.1200 | 0.0779, 0.0943 |
| GoF | 1.227 | 1.153 |

Table 2.6: Crystal Data and Refinement Details for [Fe(pz){Ni(CN)$_4$}]·2H$_2$O at different spin states.[70]

### 2.5.2 X-ray Powder Diffraction

Powder X-ray diffraction patterns were recorded using a PANalytical X'Pert equipped with a Cu X-ray tube, a Ge(111) incident beam monochromator (λ = 1.5406 Å) and an X'Celerator detector. The extraction of peak positions and the determination of the crystallite size by means of the Scherrer equation were performed with the PC software package Highscore + supplied by PANalytical.

Figure 2.15 shows the powder X-ray diffraction patterns of the different-size nanoparticle samples. The pattern observed for the bulk sample[184] corresponds to those measured for each nanoparticle sample, but a significant increase of the peak widths is observed when the size of the nanoparticles is decreasing. X-ray diffraction allows also for the estimation of the crystallite size using the Scherrer equation. The crystallite size (D) can be calculated using the equation D = kλ/β cosθ, where k is the shape factor, λ the wavelength of the incident irradiation, β is the full-width at half maximum (FWHM) of the peak and θ is the Bragg angle.

In the Scherrer equation, the β parameter needs to be corrected to eliminate instrumental effects; in our case this correction was achieved measuring a $LaB_6$ reference sample. The average crystallite size for each sample are gathered in table 2.7 and compared with the nanoparticle sizes obtained by transmission electronic microscopy. For the smaller particles, the sizes of the crystallites found using the Scherrer equation are similar or slightly larger than those found with the TEM; this effect could be explained by the uncertainty of the PXRD method for these nanoparticle sizes. For sample **3**, the size of the crystallites is in agreement with the mean nanoparticle size indicating that the nanoparticles are composed by only one domain. Eventually, larger nanoparticles and also the bulk sample are formed by several domains of about 30 nm.
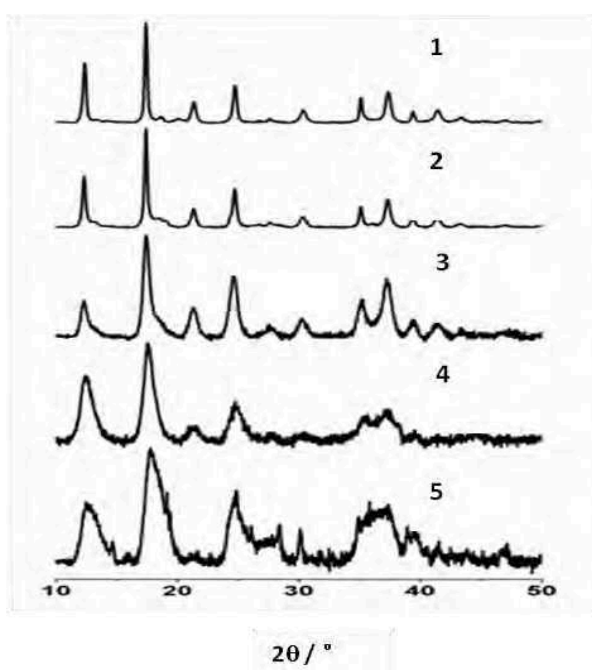


Figure 2.15: Powder X-ray diffraction patterns of samples **1-5** at room temperature

| Sample | Crystallite Size/nm | Nps Size/nm |
|--------|--------------------|-------------|
| 1 | 29 | 107±14 |
| 2 | 30 | 71±10 |
| 3 | 13 | 12±3 |
| 4 | 5.8 | 3.1±0.4 |
| 5 | 4.3 | 2.0±0.3 |

Table 2.7: Crystallite size for samples **1-5** obtained with the Scherrer equation compared with the nanoparticle size

## 2.5.3 Raman Spectroscopy

Raman spectra were collected between 350 and 150 K using a LabRAM-HR (Jobin–Yvon) Raman micro-spectrometer and a Linkam THMS-600 cryostage. The 632.8 nm line of a He–Ne laser was used as the excitation source and a spectral resolution of approximately 3 cm$^{-1}$ was obtained.

Raman spectra of sample **1-5** were recorded to characterize the composition and the structure of the complexes (see figure 2.16). The observed spectral features of the coordination nanoparticles can be clearly attributed to the [Fe(pyrazine){Ni(CN)$_4$}] complex by comparison with their bulk spectra:[202]

I.    The CN stretch, as expected, appears around 2200 cm$^{-1}$ as a well-resolved doublet (symmetric and asymmetric stretches) in the Raman spectra (see table 2.8). Compared to the corresponding K$_2$Ni(CN)$_4$ compounds, $v$(CN) modes are shifted to higher frequencies (40-50 cm$^{-1}$), which is a general trend when going from the terminal (Ni-CN) to the bridging (Ni-CN-M') cyanide ligands.

II.   Assignment of the internal mode of pyrazine is fairly straightforward. It appears in the mid-IR region mainly between 600 and 1600 cm$^{-1}$ (see table 2.8). Compared to the free ligands, a small upward shift of the wave numbers (0-30 cm$^{-1}$) occurs upon complexation due primarily to kinematic coupling. Larger shifts (*ca.* 40-70 cm$^{-1}$) are observed only for certain low-frequency modes.

III.  Spectral features below 600 cm$^{-1}$ are attributed mainly to metal-ligand vibrations, but their assignment is difficult because of the low signal intensity and the strong coupling between the different modes. However, a major simplifying feature is the apparent absence of internal pz bands in this spectral region. It is also known that the "metal-centered" deformation modes-$\delta$(CMC), $\delta$(NFeN)-appear at very low frequencies, usually well below 200 cm$^{-1}$. The large, unresolved spectral features below 100 cm$^{-1}$ should be associated mostly with external modes. Any mode between 200 and 600 cm$^{-1}$ can be attributed without too much uncertainty to coupled vibrations in which the major involvement comes from the $v$(Fe-N), $v$(M-C), and $\delta$(MCN) modes. Involvement of the latter two mode types should be readily discernible since they would be expected to be very sensitive to the metal (M) substitution. Considering now the remaining "FeN$_6$ modes", the stretching modes are expected to have the highest frequency. Those that are largely insensitive to the ligand substitution can be identified

as $v$(Fe-N$_{NC}$) vibrations. The ligand-sensitive bands appearing between 300 and 320 cm$^{-1}$ can finally be assigned as $v$(Fe-Npz) modes. Table 2.8 summarizes all the data.
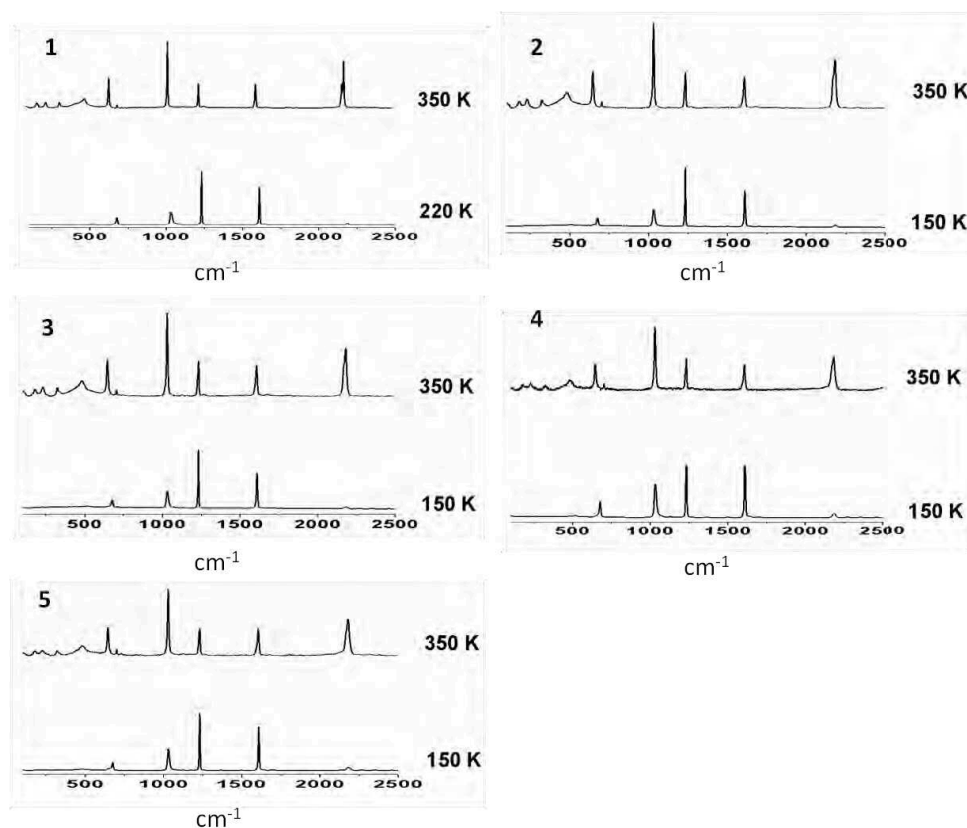


Figure 2.16: Raman spectra at selected temperatures for samples **1-5**

| Raman mode | | LS State | HS state | Free Pyrazine ligand |
|---|---|---|---|---|
| $v_{ring}$ | A$_g$ | 1607s, 1031s | 1603m, 1029s | 1580s, 1016s |
| $v$(CN) | A$_{1g}$ | 2192m | 2182m | |
| | B$_{1g}$ | 2183m | 2172m | |
| $v$(CM) | A$_{1g}$ | 528w | 486m | |
| | B$_{1g}$ | 518w | | |
| $v$(FeN$_{NC}$) | A$_{1g}$ | 394w | 176m | |
| | B$_{1g}$ | 388w | 231m | |
| $v$(FeN$_{cycle}$) | A$_{1g}$ | 320w | 176m | |

Table 2.8: Main Raman vibrational wavenumbers (in cm$^{-1}$) associated with the polymeric sheet structure in the [Fe(pz){Ni(CN)$_4$}] complex and its tentative assignments. Abbreviations: s, strong; m, medium; w, weak.

The variable temperature Raman spectra of the sample clearly reveal the shift of the in-plane bending mode of the pyrazine ring from 645 cm$^{-1}$ (high temperature) to 675 cm$^{-1}$ (low temperature) and the variation of the intensity ratio of two vibrational modes associated to pyrazine at about 1030 and 1230 cm$^{-1}$. These observations are discussed in details in the following subchapter 2.6.2.

# 2.6 Spin Crossover Properties of [Fe(pz){Ni(CN)$_4$}] Nanoparticles

## 2.6.1 Optical Microscopy Observation

It is interesting to note that a significant color change of the powder samples could be observed as a function of the particle size (see figure 2.17). The darkening of the sample can be explained by the increasing residual LS fraction at room temperature when the size of the nanoparticles decreases (see details hereafter). Moreover when the size of the nanoparticles is smaller than 10 nm, even with macroscopic size of the sample, the color change is not obvious anymore in agreement with low amount of active iron centres (see Mössbauer measurement).
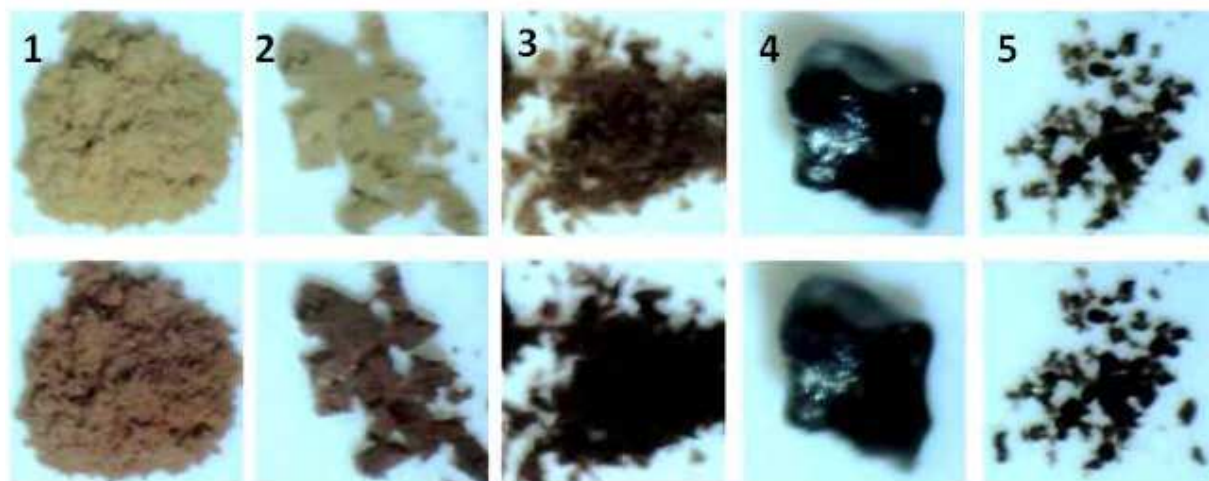


Figure 2.17: Color change of the samples as a function of the nanoparticle size and temperature. Sample **1-5** from the left to the right (room temperature for the upper panel and liquid nitrogen temperature for the bottom panel)

## 2.6.2 Raman Spectroscopy

Raman spectra of sample **1-5** were recorded at selected temperatures to better characterize the spin transition properties of the complexes. The variable temperature Raman spectra of the sample reveal the shift of the in-plane bending mode of the pyrazine ring from 645 (HS) to 675 (LS) $cm^{-1}$ and the variation of the intensity ratio of two vibrational modes associated to pyrazine at about 1030 and 1230 $cm^{-1}$. These spectral changes are well-known signs of the spin crossover in these compounds.[202] Figure 2.18 reports a zoom in the 900-1400 $cm^{-1}$ region of the Raman spectra for samples **1-5** at selected temperatures. It is interesting to notice that the thermal variation of the Raman intensity ratio $I_{1030}/I_{1230}$ indicates a quasi-complete spin transition in sample **1** and **2** in agreement with the bulk sample. Conversely, measurements at 350 and 150 K indicated, the presence of a small residual LS fraction in **4** and **5** and a residual HS fraction in **3-5**, respectively. Nevertheless, these observations are in contradiction with the Mössbauer measurements (see hereafter), which point out the occurrence of very incomplete spin transitions for samples **3-5**. We believe that this (apparent) discrepancy occurs because the smaller nanoparticles contain an increasing amount of inactive iron(II) species, which are localized at the surface of the particles. The majority of these inactive species do not contribute significantly to the Raman scattering of the samples, but they contribute obviously to their Mössbauer signal. Similar effects were also encountered for the corresponding [Fe(pyrazine){Ni(CN)$_4$}] nanoparticles embedded in chitosan.
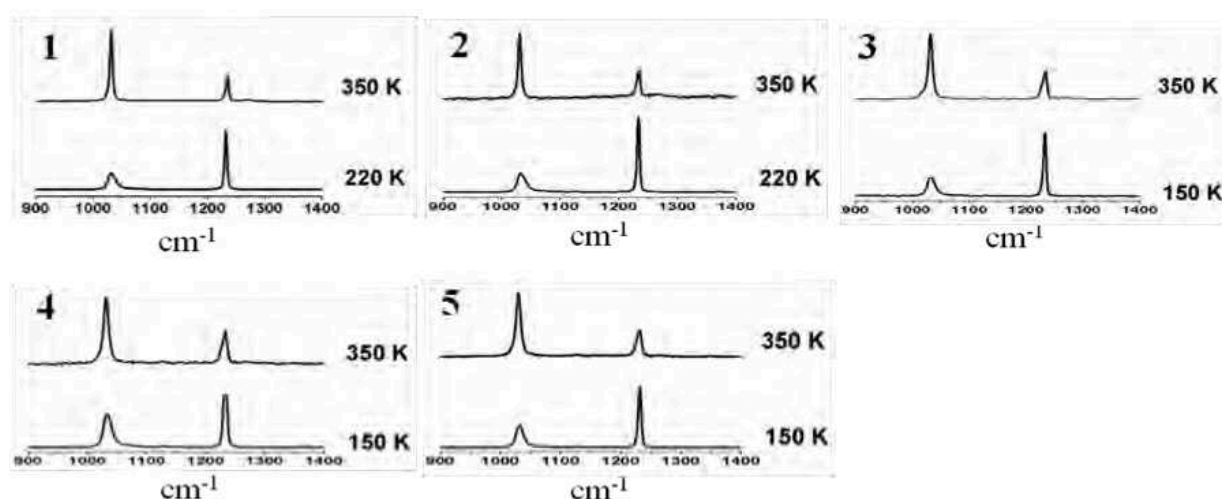


Figure 2.18: Selected Raman spectra of samples **1-5**

## 2.6.3 Mössbauer Spectrometry

[57]Fe Mössbauer spectra have been recorded using a conventional constant-acceleration-type spectrometer equipped with a [57]Co(Rh) source (*ca.* 20 mCi) and a liquid-nitrogen cryostat. Spectra of the powder samples (*ca.* 50 mg) were recorded between 80 and 310 K. Least-squares fittings of the Mössbauer spectra have been carried out with the assumption of Lorentzian line shapes using the "Recoil" software. $\delta$, $\Delta_{EQ}$ and $\Gamma$ stand for the isomer shift, the quadrupole splitting and the half-height line width, respectively (see Annex 3).

Compared with Raman spectroscopy, [57]Fe Mössbauer measurement is a more quantitative method, which was carried out, on one hand, to determine the residual LS and HS fractions at high and low temperatures, respectively, and on the other hand, to probe the low temperature region (where the HS and LS fractions were constants) to determine the Debye temperature ($\theta_D$) which reflects the stiffness of the environment of the iron ions (chapter 2.6.5). With the aim to determine more precisely the fraction of iron centres involved in the spin transition, and suitably calibrate the magnetic measurements presented hereafter, we have recorded the [57]Fe Mössbauer spectra for the different samples at different temperatures. Figures 2.19 shows the selected Mössbauer spectra for samples **1-5**. Whatever the sample, at 310 K the Mössbauer spectrum consists of two doublets, both with an isomeric shift $\delta$ close to 1 mms$^{-1}$ and large quadrupole splittings ($\Delta E_Q$ = 1.2 and 2 mms$^{-1}$) typical of a HS iron(II) (S = 2). In addition, a third LS doublet with isomeric shift $\delta$ close to 0.4 mms$^{-1}$ appears for smaller nanoparticles. All these data are gathered in table 2.10.



Sample 1                    Sample 2
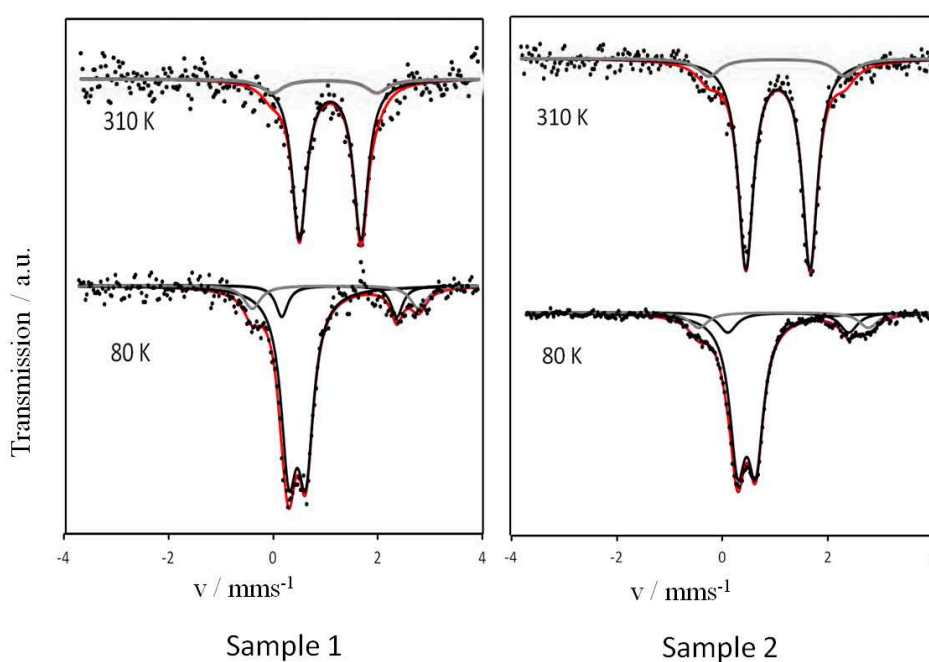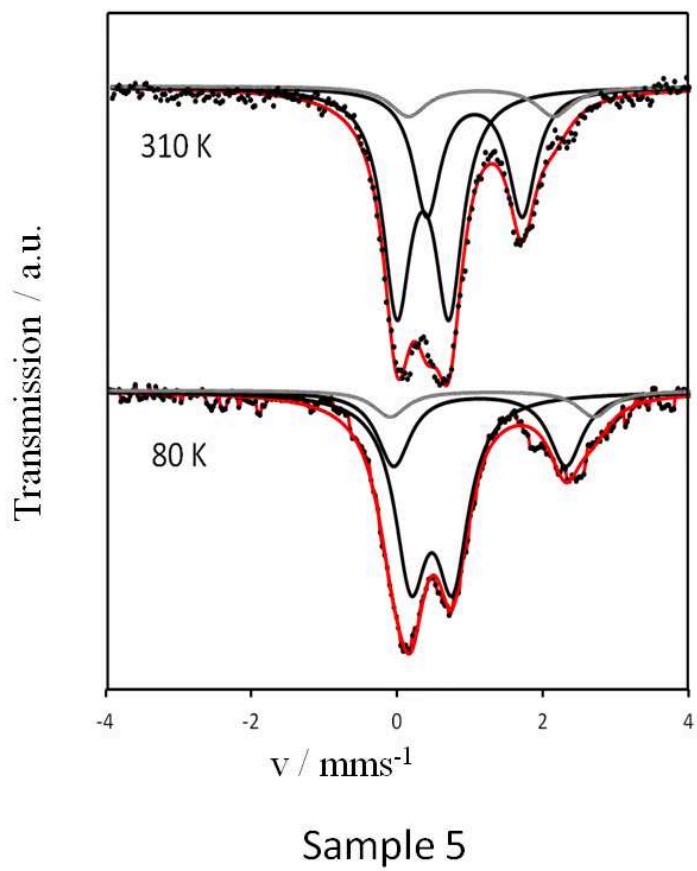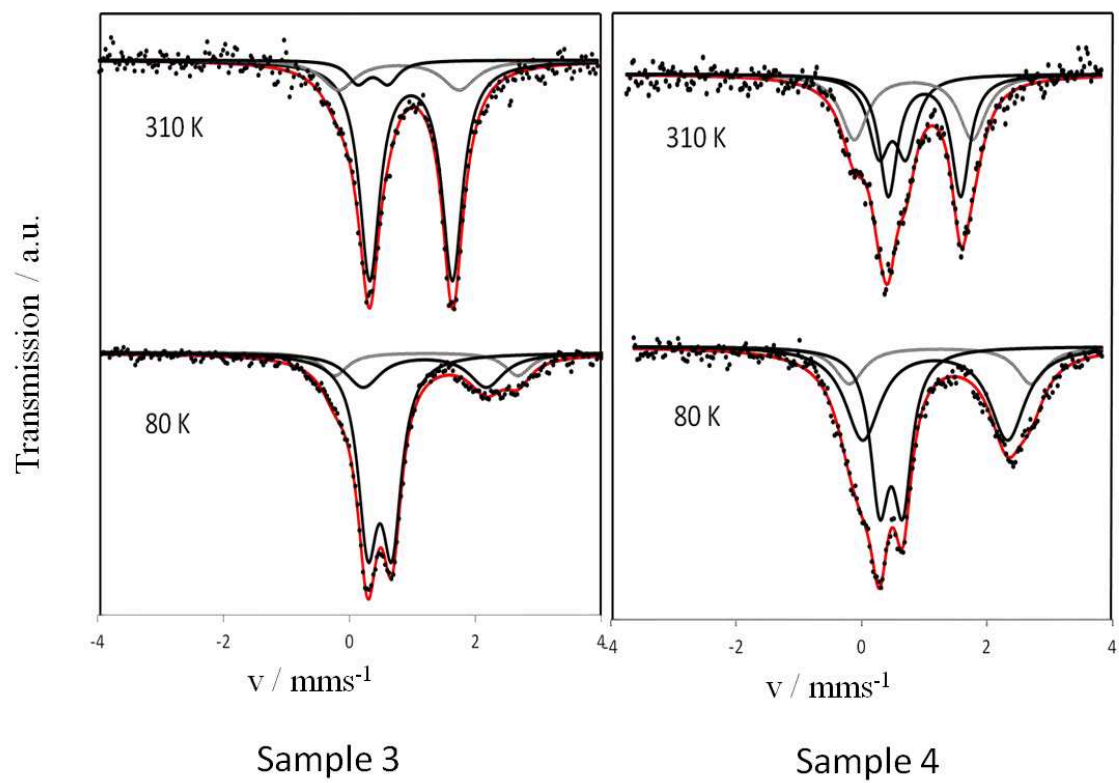
Figure 2.19: Selected $^{57}$Fe Mössbauer spectra (dots) and fit (line) for samples **1-5**

The *ca.* 10% fraction associated with the larger quadrupole splitting HS species in each sample can be explained by the presence of defects in the coordination network. Such result is in agreement with previous magnetic measurement reported for crystals[70] and bulk sample (see chapter 2.6.4). Indeed, in each case the magnetic susceptibility at low temperature is higher than that expected for fully low spin state. The large $\Delta E_Q$ value indicates a local symmetry lower than cubic, but with a rather well-isolated ground orbital singlet (in a well-isolated singlet case, $\Delta E_Q$ is in the 3-4 mm$^{-1}$ range), which corresponds to an axial compression of the octahedral structure. The increasing residual LS fraction while the size of the nanoparticles decreases, 8% for 12 nm particles, 16% for 3 nm particles and 56% for 2 nm particles might be related to the increase of the quantity of iron atoms localized at the surface of the nanoparticles. When the samples are cooled down, the area of the HS doublet with the smaller quadrupole-splitting decreases and, conversely, the area of the LS doublet increases; whereas the area of the HS doublet with the larger quadrupole-splitting remains constant. The important $\Delta E_Q$ variation of both HS doublets (1.18(2)-2.20(1) mms$^{-1}$ and 2.00(4)–3.20(9) mms$^{-1}$ for sample **1**) between 310 and 80 K is characteristic of a strongly distorted equatorial environment associated with a small energy gap between the $d_{xy}$ orbital and the thermally accessible $d_{xz}$ or $d_{yz}$ orbitals. The variable temperature Mössbauer spectrum for samples **1-5** reveals that while decreasing the size of the nanoparticles, the fraction of the SCO active species decreases from 77% for sample **1** to 7% for sample **5** (77% for sample **2**, 58% for sample **3** and 23% for sample **4**) (see table 2.9).

| sample | LS residual fraction (%) | HS residual fraction (%) | Active species (%) |
|:---:|:---:|:---:|:---:|
| **1** | 0 | 23 | 77 |
| **2** | 0 | 23 | 77 |
| **3** | 8 | 34 | 58 |
| **4** | 16 | 61 | 23 |
| **5** | 56 | 37 | 7 |

Table 2.9: Percentage of the LS, HS residual fractions and active species from the Mössbauer fit for samples **1**-**5**.

| Sample | T (K) | HS doublet | | | HS doublet | | | LS doublet | | | Area |
|---|---|---|---|---|---|---|---|---|---|---|---|
| | | $\delta$ | $\Delta E_Q$ | $\Gamma/2$ | $\delta$ | $\Delta E_Q$ | $\Gamma/2$ | $\delta$ | $\Delta E_Q$ | $\Gamma/2$ | |
| **1** | 310 | 1.07(1) | 1.18(2) | 0.17(1) | 0.96(1) | 2.00(4) | <u>0.25</u> | | | | 89/11/0 |
| | 80 | 1.26(5) | 2.20(1) | <u>0.20</u> | 1.19(5) | 3.20(9) | <u>0.20</u> | 0.461(9) | 0.33(1) | 0.18(1) | 12/11/77 |
| **2** | 310 | 1.047(5) | 1.19(1) | 0.169(9) | 1.02(8) | 2.21(2) | 0.25(2) | | | | 89/11/0 |
| | 80 | 1.25(3) | 2.29(5) | 0.20(5) | 1.16(3) | 3.21(7) | 0.21(6) | 0.459(4) | 0.343(6) | 0.181(5) | 13/10/77 |
| **3** | 310 | 1.06 (1) | 1.28(1) | 0.2(1) | 0.89(1) | 2.1 | 0.3 | 0.44 | 0.36 | 0.2 | 80/11/8 |
| | 80 | 1.15 | 1.96(1) | 0.33(1) | 1.22(1) | 2.91(1) | 0.25 | 0.487(5) | 0.383(8) | 0.187(7) | 22/12/66 |
| **4** | 310 | 1.06(1) | 1.22(3) | 0.20(1) | 0.92(1) | 2.01(1) | 0.28(2) | 0.51(1) | 0.49(1) | 0.20(1) | 63/21/16 |
| | 80 | 1.17(1) | 2.31(1) | 0.34(1) | 1.25(5) | 2.9 | 0.28(1) | 0.472(9) | 0.37(1) | 0.18(1) | 46/15/39 |
| **5** | 310 | 1.054(8) | 1.31(1) | 0.23(1) | 1.14(2) | 2.0 | 0.3 | 0.348(7) | 0.68 | 0.224(8) | 33/10/56 |
| | 85 | 1.13(1) | 2.36(1) | 0.27(1) | 1.3 | 2.8 | 0.28(1) | 0.47(1) | 0.57(1) | 0.27(1) | 28/10/63 |

Table 2.10: Selective least-squares fitted Mössbauer data for samples **1-5** at selected temperature. δ, $\Delta_{EQ}$ and Γ stand for the isomer shift vs metallic α-Fe at room temperature, the quadrupole splitting and the half-height line width, respectively.

## 2.6.4 Magnetic Properties

The thermal variation of the high spin fraction ($n_{HS}$) for the different nanoparticle samples (figure 2.20) was deduced from the magnetic susceptibility data and thanks to the determination of the residual HS and LS fractions in the low and high temperature regions by Mössbauer spectroscopy (assuming the approximation that $f_{HS} \approx f_{LS}$ and thus that $A_{HS} / A_{tot} \approx n_{HS}$) and the sample composition by TGA and elemental analysis. Although a small shift of the transition curves to higher temperatures is observed after the isothermal holding of samples,[184] all comparisons have been realized on dehydrated samples. As expected, the large particles present physical properties close to the bulk sample (see figure 2.21) with a spin transition close to room temperature ($T_{1/2}\uparrow$ = 285 K and $T_{1/2}\downarrow$ = 297 K) so with a hysteresis loop of 12 K.[203] The decrease of the size to 12 nm leads, as already reported for the platinum derivative,[194] to a more gradual transition without hysteresis and with a shift to lower temperature. The modification of the spin crossover behavior is also accompanied by an increase of the residual HS fraction at low temperature.
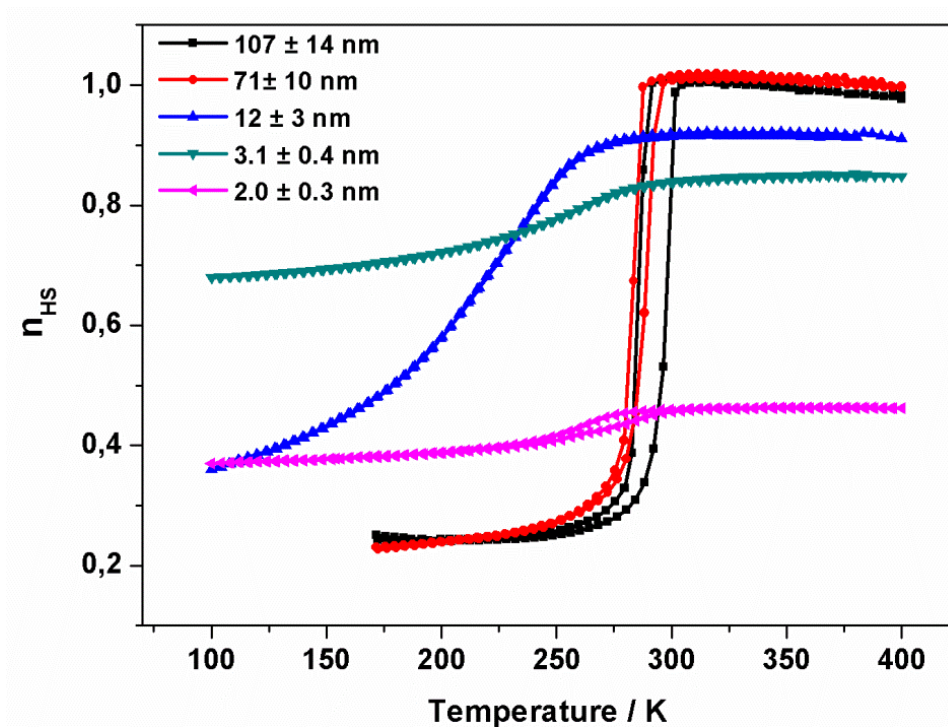
Figure 2.20: Calibrated $n_{HS}$ = f($T$) curves for samples **1-5** obtained from magnetic and Mössbauer measurements.
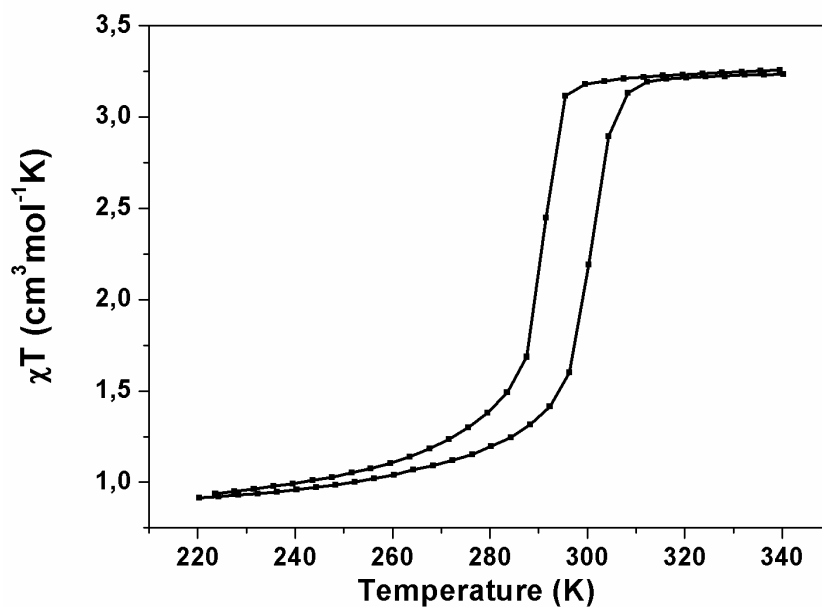


Figure 2.21: Magnetic susceptibility as a function of the temperature in the heating and cooling modes for [Fe(pyrazine){Ni(CN)$_4$}] dehydrated bulk sample

| Sample | Transition temperature (K) |
|---|---|
| *crystal | 287/307 |
| Bulk | 286/297 |
| **1** | 285/297 |
| **2** | 283/289 |
| **3** | 217/217 |
| **4** | 245/245 |
| **5** | 260/268 |

Table 2.11: Transition temperatures for each dehydrated sample, * from ref 70.

Nanoparticles with sizes of about 3 nm revealed an even higher residual HS fraction and also significant residual LS fraction together with an apparent re-increase of the transition temperature (see table 2.11 for detailed transition temperature for each sample). These effects were more clearly demonstrated in the case of the smallest 2 nm particles exhibiting important "inactive" HS and LS fractions, a higher transition temperature and even the re-opening of the hysteresis loop. This latter phenomenon was predicted in our recent theoretical investigation but was never reported experimentally.[196] **To the best of our knowledge, this 2 nm particle sample constitutes the smaller size spin crossover nanoparticles reported in the literature.** In fact there are only two other examples of bistability reported for ultra small (< 10 nm) nanoparticles. This concerns 4 nm [Fe(pz){Ni(CN)$_4$}] nanoparticles synthesized in chitosan matrix and 6 nm Fe[(Htrz)$_2$(trz)](BF$_4$) nanoparticles obtained using the reverse micelle method. **Nevertheless in the present study and for the first time we have demonstrated that following the disappearance of the hysteresis for intermediate sizes it is possible to observe the re-appearance of the bistability for ultra small nanoparticles.** In order to explain this novel phenomenon, Mössbauer spectrometry was used to probe the stiffness of the nanoparticles thanks to the determination of the Debye temperature.

## 2.6.5 Debye Temperature

In Debye theory, the Debye temperature is the temperature of a material's highest normal mode of vibration, i.e., the highest temperature that can be achieved due to a single normal vibration. The Debye temperature is given by the following equation, where *h* is Planck's

constant, $k$ is Boltzmann's constant, and $v_m$ is the Debye frequency. The table hereafter indicates the common Debye temperature values reported for different kind of materials.

$$\theta_D = \frac{hv_m}{k} \tag{2.1}$$

| Material | Debye temperature ($\theta_D$) |
|---|---|
| Carbon (diamond) | 3000 |
| Metal, metal alloy | 100-500 K[204] |
| Organic ligand | 50-90 K[205] |
| Coordination complex | 50-250 K[206] |

Table 2.12: Debye temperature values reported for different kind of materials (non-exhaustive list)

Using the Debye model we can determine the so-called "Mössbauer Debye temperature", $\theta_D$ from the temperature dependence of the full area ($A$) of the Mössabuer spectrum by means of the relationship:[207,208]

$$\log(A) \approx \log(Cf) = \log(C) - \frac{3E_R}{2k_B\Theta_D}\left[1 + 4\left(\frac{T}{\Theta_D}\right)^2 \int_0^{\Theta_D/T} \frac{\alpha}{\exp(\alpha)-1}\,d\alpha\right] \tag{2.2}$$

with $C$ a constant, $f$ the Lamb-Mössbauer factor, $E_R$ the recoil energy of iron, $\theta_D$ the Debye temperature, T the temperature and α a dimensionless variable for the integral ($\alpha = \frac{hv}{kT}$). A higher value of $\theta_D$ signifies that the crystal lattice is stiffer. Measurements were realized in a temperature range for which the spin state was constant. A least-squares fit of ln(A) vs. T allowed us to determine the values of $\theta_D$. Figure 2.22 represents the variation of $\theta_D$ as a function of the nanoparticle size. For the larger nanoparticles (107 and 71 nm) the same $\theta_D$ value of about 170 ± 4 K was measured. The decrease of the particle size to 12 nm leads to a significant increase of $\theta_D$ to 197 ± 9 K. Finally, samples with the smallest nanoparticle sizes revealed a very important increase of $\theta_D$ with 222 ± 4 K for sample **4** and 261 ± 6 K for sample **5**.
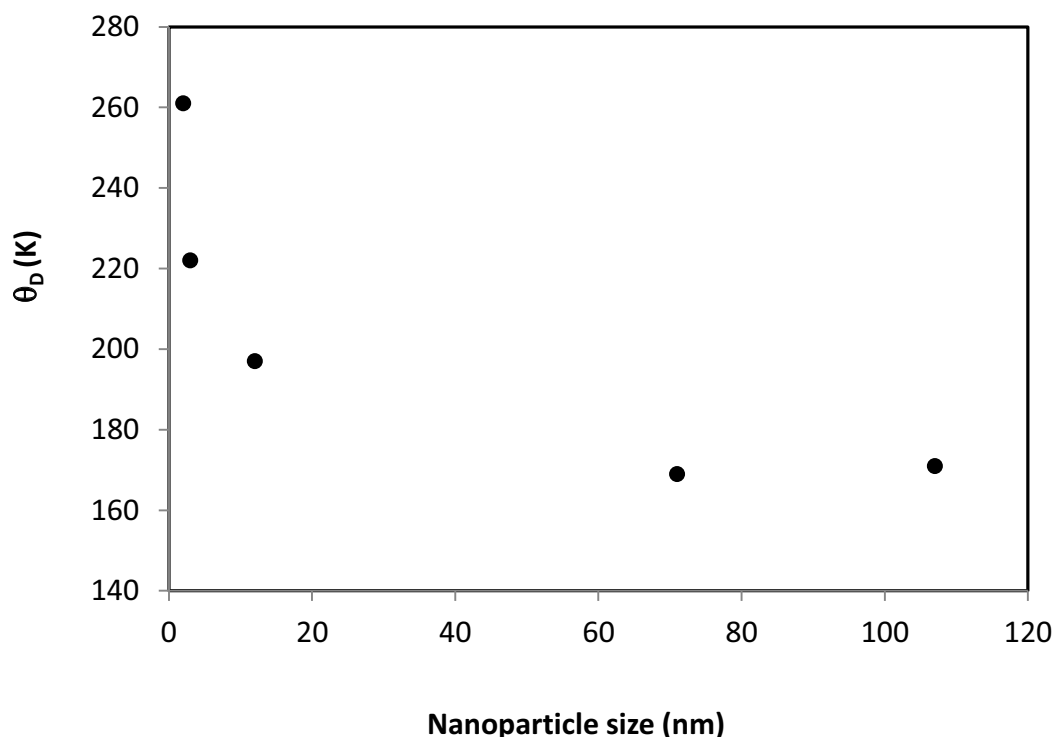
Figure 2.22: Variation of the Debye temperature as a function of the size of the particles. (The statistical error is comparable or smaller than the size of the symbols.

It is worth noting that the $\theta_D$ value measured for the small nanoparticles is underestimated taking into account the important HS residual fraction in the considered low temperature range. Indeed, as it is well known when going from the HS to the LS state the spin crossover phenomenon is accompanied by a lattice contraction which tends to increase the $\theta_D$ value. These measurements undeniably put in evidence an increase of the $\theta_D$ value when decreasing the nanoparticle size below *ca.* 15-20 nm. This increase of the $\theta_D$ value reveals thus an increase of the stiffness of the nanoparticles. It is important to underline that the environment of the particles (the matrix) was maintained similar in the different samples. In view of these experimental results, we suggest that the re-increase of the cooperativity observed for the smallest nanoparticles is closely related to the increase of the stiffness of the particles. In order to explain these behaviors we can suggest that two independent mechanisms have to be considered when the nanoparticle size is decreasing. On one hand, the increasing surface-to-volume ratio leads to the downshift of the spin transition temperature and the loss of hysteresis. On the other hand the increase of the stiffness of the particles in ultra-small particles leads to an opposite effect. Additionally, despite the fact that the X-ray powder pattern is similar for all the samples, the presence of a single domain (only one crystallite per

particle) and/or a possible modification of the shape of the particles[201] could also play an important role on the SCO properties. Indeed, for samples **4** and **5**, TEM and HRTEM measurements seem to show nanoparticles with rather a spherical shape in contrast to the cubic shape encountered for larger nanoparticles. It is worth noting that these conclusions are specifically related to the behavior of the present Hofmann like clathrate material and cannot be easily generalized for all spin crossover compounds. Finally, even if the matrix is different, the unexpectedly strong cooperativity observed for the 4 nm [Fe(pyrazine){Ni(CN)$_4$}] nanoparticles embedded in chitosan supports also the present results. [184]

# 2.7 Theoretical Model

To understand the behaviour of the spin crossover nanoparticles as a function of their size, a theoretical study based on a core-shell nanothermodynamic model has been realized (works thesis of Felix Gautier in the group). The simulations are performed on a cubic nanoparticle, with a lattice parameter (*a*) of 0.6 nm. The spin state of face, edge and volume iron atoms are considered statistically independent. The number of metal sites in each location is calculated as follows:

$$n = \frac{l}{a} + 1, N = n^3, N_c = (n-2)^3, N_f = 6 \times (n-2)^2, N_e = N - N_c - N_f, N_s \tag{2.3}$$

with *l* the length of the nanoparticle, *n* the number of site in one edge, *N* the total number of sites, and $N_c$, $N_f$, $N_e$ and $N_s$ which are the number of sites in the core, on the faces, on the edges and on the surface, respectively.

Figure 2.23 shows thermal SCO curves of cubic nanoparticles, where *l* is either 100 nm, 70 nm, 10 nm, 3 nm or 2 nm. The particles of 70 nm and 100 nm are similar and can be considered as bulk material. A residual fraction of $n_{HS} = 0.2$, for the core centres, is added in the calculation to obtain comparable curves as the experiment. This residual fraction is roughly associated with defects in the crystal structure, leading to 20 % of inactive iron centres. When decreasing the size, a new kind of defect appears: the surface. In the simulation, the iron centres at the surface are inactive, and this can be physically explained by local deformations of the octahedral structure around the metallic ion. However, the octahedral deformation may be different from the edge to the face, which can lead to different stable states for the edge and face centres. With this consideration, the sites of the face and the edge

are fixed in the simulations in the HS and LS states, respectively. It is important to note that the smaller the particle is, the higher the numbers of centre are located at the surface. The diminution of the number of core centres leads to a reduction of the number of structural defects in the core. For this reason, the residual fraction of $n_{HS} = 0.2$ is not added in the simulation of 2 nm particle. All these approximations lead to a residual HS fraction at low temperature in big particles, then an increase of the residual HS fraction at low temperature between 100 nm and 3 nm, and to finish an increase of a residual LS fraction at high temperature between 10 nm and 2 nm.
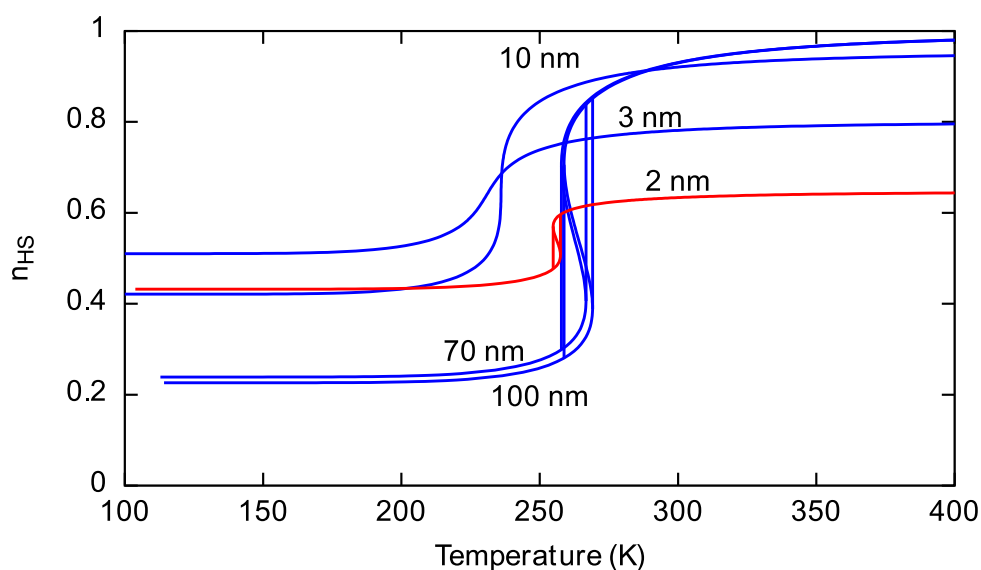


Figure 2.23: Thermal evolution of the total HS fraction for different sizes of cubic nanoparticles, calculated using a nanothermodynamic core–shell model [1]. The model parameters for the simulations are $\Delta H = 18000$ J.mol$^{-1}$ and $\Delta S = 60$ J.mol$^{-1}$, and the values of $\Gamma$ are listed in the table 2.12.

| Size (nm) | $\Gamma_{LS}$ (J.mol$^{-1}$) | $\Gamma_{HS}$ (J.mol$^{-1}$) |
|---|---|---|
| 100 | 9140 | 6290 |
| 70 | 9140 | 6290 |
| 10 | 10510 | 7230 |
| 3 | 12800 | 10060 |
| 2 | 23770 | 20210 |

Table 2.12: Values of the intermolecular interaction terms ($\Gamma$) for the LS and the HS states, as a function of nanoparticle sizes.

It was shown that the residual fractions lead to a shrinking of the hysteresis loop.[196,199] It was also shown that residual HS and LS fractions lead to a decrease and an increase of the transition temperature, respectively, due to the change of the phase stability of the surfaces.[196] The reopening of the hysteresis in the 2 nm particles is the consequence of the hardening of the particles (increasing of $\Gamma$, $\Gamma$ being proportional to $\theta_D^2$) with the diminution of size. Indeed, in the simulations, the stiffness of the particle is progressively increased until an augmentation of 160 %.

# 2.8 Synchrotron Mössbauer Measurement

Conventional Mössbauer spectroscopy is an important technique to characterize Fe-based SCO compounds,[209,210] and it was also used in few occasions to investigate their lattice dynamics through the measurement of $f_{LM}$.[211,212] On the other hand, the NIS method can provide the complete 57-Fe absorption spectrum in solids, liquids, or gases. However, as in Raman spectroscopy, the Stokes and anti-Stokes peaks are very weak compared to the Rayleigh peak and the intensity of conventional $\gamma$–ray sources is not strong enough to observe them. Currently, the only source that enables to overcome this problem is the synchrotron radiation. However, this technique is time consuming and it is more convenient to synthesize fully 57-Fe complexes.

## 2.8.1 Synthesis of Different-Size [$^{57}$Fe(pz){Ni(CN)$_4$}] Nanoparticles

$^{57}$Fe(BF$_4$)$_2\cdot$6H$_2$O salt was obtained starting with metallic 57-Fe (metal plate) in presence of HBF$_4$. The reaction was performed at 70 °C under a N$_2$ atmosphere. White powder was collected after an evaporation stage. [$^{57}$Fe(pz){Ni(CN)$_4$}] nanoparticles were synthesized under the same condition as reported in chapter 2.2. Sample **6** was synthesized as sample **2**, sample **7** as sample **5**. See Annex 1 for details of the syntheses.

| Sample | [Fe]/mol.L$^{-1}$ | $\omega$ | $V_{H2O}$(mL) | $V_{Hexane}$(mL) | Temperature/K |
|--------|----------|-----|-----|-----|-----|
| 6 | 0.1 | 10 | 6 | 33 | 293 |
| 7 | 0.2 | 10 | 6 | 33 | 258 |

Table 2.13: Preparation conditions of different samples

## 2.8.2 Charaterization and SCO Properties of [$^{57}$Fe(pz){Ni(CN)$_4$}] Nanoparticles

### 2.8.2.1 Electronic Microscopy Analysis

Transmission electron microscopy (TEM) was used to determine the size of the nanoparticles. For each sample, the mean size of the nanoparticles was carefully checked by performing several TEM measurements with different grid preparations and considering more than one hundred nanoparticles. Figures 2.24-2.25 present the selected TEM images for sample **6** and **7**. The mean size for each nanoparticle sample is reported in table 2.14.
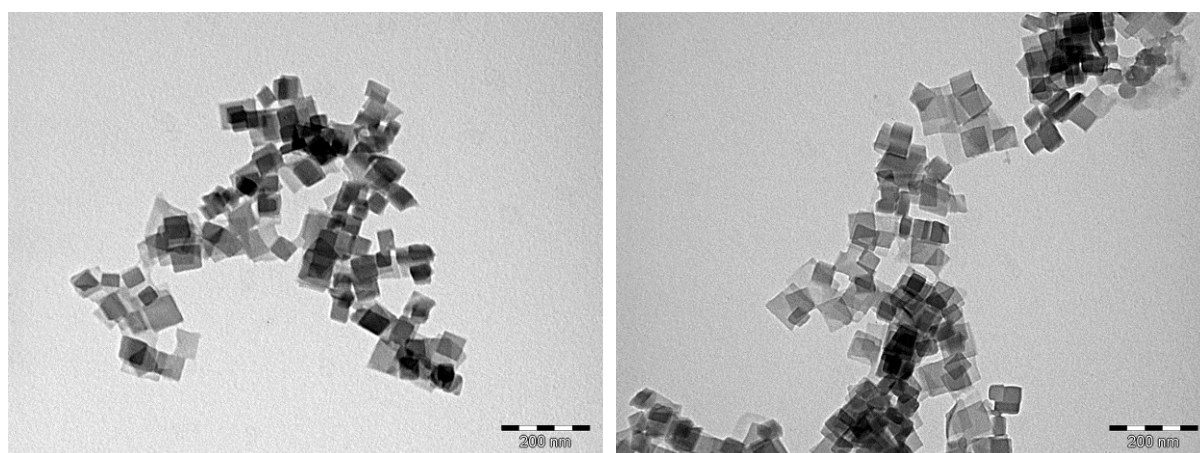


Figure 2.24: Selected TEM images of sample **6**.
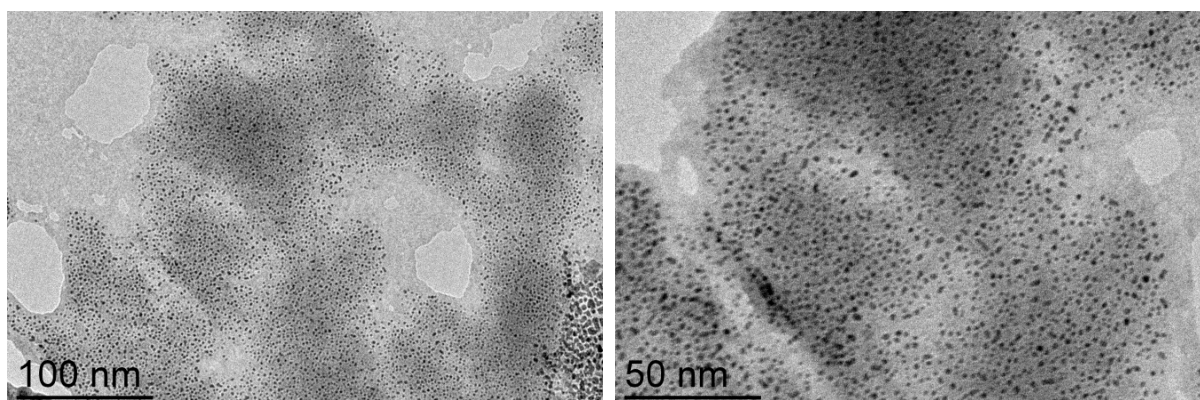


Figure 2.25: Selected TEM images of sample **7**.

| Sample | [Fe]/mol.L$^{-1}$ | Temperature/K | Nps Size/nm |
|--------|-------------------|---------------|-------------|
| 6 | 0.1 | 293 | 50±4 |
| 7 | 0.2 | 258 | 2±0.3 |

Table 2.14: Mean size of each sample.

The size measured for these two preparations confirms the effect of reaction temperature on the nanoparticle size; low temperature leading to small size nanoparticles. It is interesting to notice that although sample **6** was synthesized as sample **2**, slightly small nanoparticle size was obtained and could be explained by the difficulty to control the fast addition rate or by remaining traces of $HBF_4$ coming from the starting synthesis of the 57-Fe metal salt.

### 2.8.2.2 X-ray Powder Diffraction

Powder X-ray diffraction patterns were recorded using a PANalytical X'Pert equipped with a Cu X-ray tube, a Ge(111) incident beam monochromator ($\lambda$ = 1.5406 Å) and an X'Celerator detector.
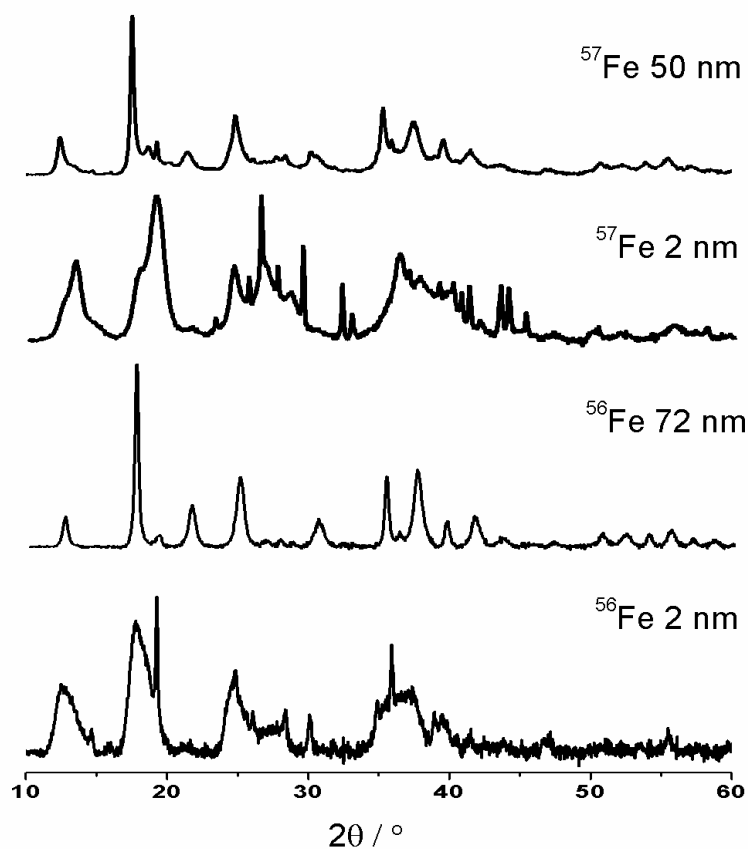


Figure 2.26: Comparison of the powder X-ray diffraction patterns of different 56- and 57-Fe samples at room temperature.

Figure 2.26 shows the powder X-ray diffraction (PXRD) patterns of the different-size nanoparticle samples. Whatever the size, the PXRD analysis of $[^{57}Fe(pz)\{Ni(CN)_4\}]$ nanoparticle shows similar patterns as the $[^{56}Fe(pz)\{Ni(CN)_4\}]$ sample. Indeed, compared to the 56-Fe based nanoparticles, a similar peak broadening effect is also observed for 57-Fe based nanoparticles when the size of the nanoparticles is decreasing.

## 2.8.2.3 Magnetic Measurement
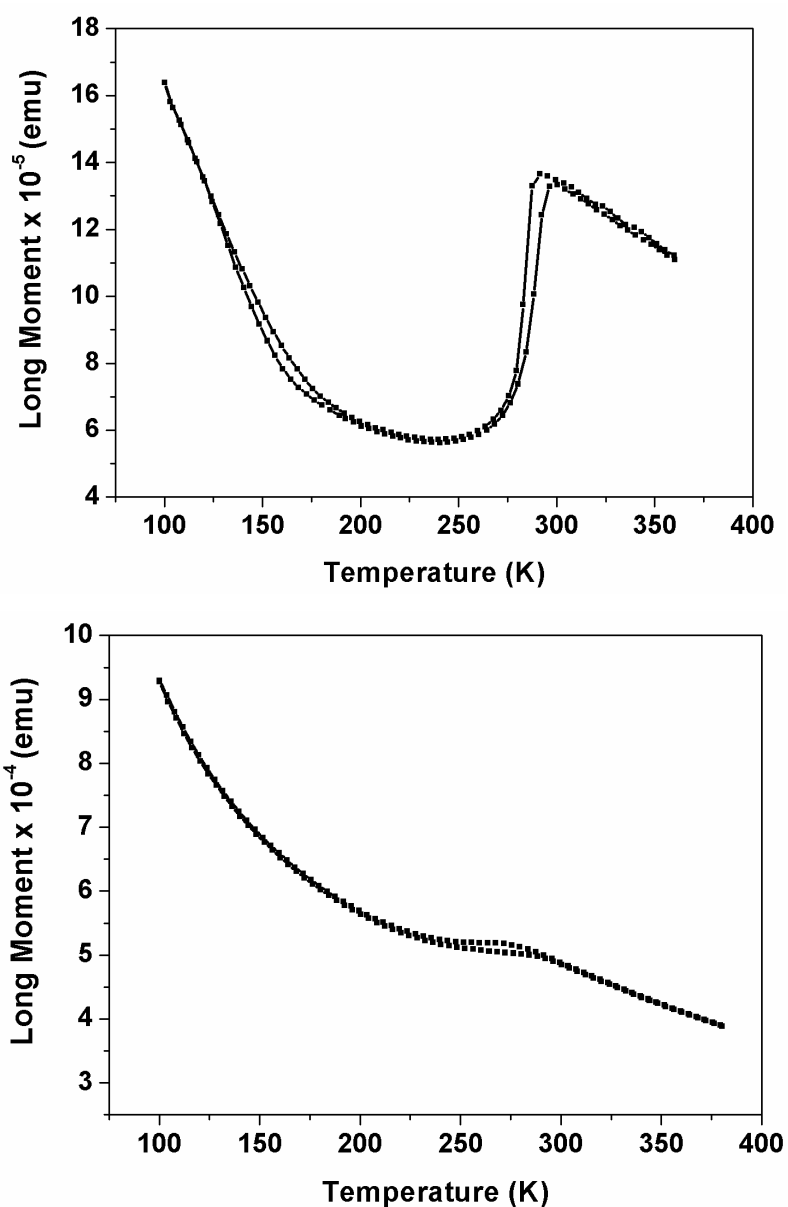


Figure 2.27: Magnetization as a function of the temperature in the heating and cooling modes for dehydrated 50 nm (up) and 2 nm (bottom) $[^{57}Fe(pyrazine)\{Ni(CN)_4\}]$ particles.

| Sample | Transition temperature (K) |
|--------|---------------------------|
| **2** | 283/289 |
| **5** | 260/268 |
| **6** | 282/288 |
| **7** | 255/264 |

Table 2.15: Transition temperatures for dehydrated samples

The thermal variation of the magnetization of the samples is shown in the figure 2.27. Although a small shift of the transition curves to higher temperatures is observed after the isothermal holding of samples, all experiments have been realized on dehydrated sampled. As expected, Sample **6** and **7** present spin transition temperatures similar to those measured for sample **2** and **5**.

## 2.8.3 Nuclear Inelastic Scattering

In the SCO field, NIS has already been used to characterize the optical modes,[213-216] but this technique has not yet been used to study the acoustic modes, which can give access to the vibrational Density of States (DOS) at low energies[217] and thereby, provides some important thermodynamical and lattice dynamical parameters and their spin-state dependence. These elastic constants are largely ignored in the spin crossover field and their knowledge is of outmost importance in order to rationalize the origin of the first-order phase transition (cooperativity and associated memory effect) and the ultrafast dynamics in these compounds as well as to develop applications based on the spontaneous strain accompanying this transition. A particular interest of the NIS technique is that it can be used to probe the DOS (and thus the elastic constants) of spin crossover nanoparticles and other nano-objects as well. In the present study, NIS technique was used to investigate the lattice dynamics (Debye temperature) in SCO nanoparticles and especially the acoustic phonon modes. The sound velocity in the two spin states is extracted from the low-energy part of the DOS. The experiment is performed at the Nuclear Resonance beamline ID18 in 7/8 + 1 bunch mode at the European Synchrotron Radiation Facility (ESRF) using different-size $[Fe(pyrazine)\{Ni(CN)_4\}]$ nanoparticle sample (2 and 50 nm) fully enriched with 57-Fe (see figure 2.28). Powder nanoparticle samples were introduced in thin aluminum foil (see figure 2.31).
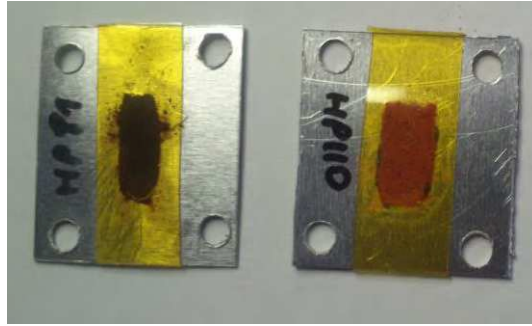
Figure 2.28: Sample container for NIS measurement

## 2.8.3.1 Nuclear Inelastic Scattering of 50 nm Nanoparticles

Variable temperature NIS spectra were collected for the sample containing 50 nm [$^{57}$Fe(pyrazine){Ni(CN)$_4$}] and processed[217] to obtain the iron DOS (Density of State). Figures 2.29a and 2.29b show, respectively, the NIS spectra and the vibrational DOS in the two spin states (50 K: LS, 310 K: HS).
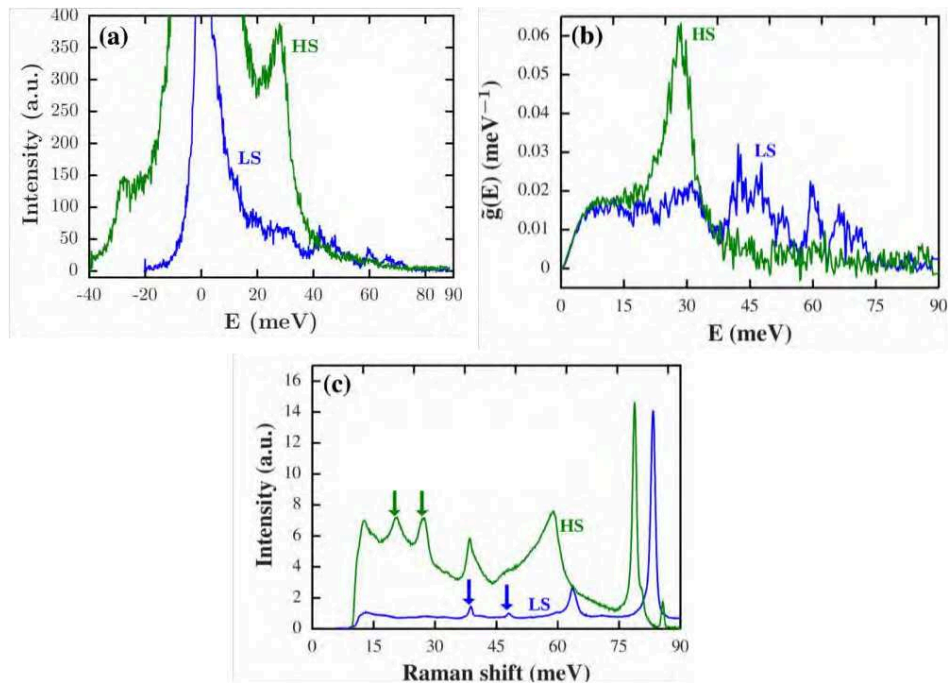


Figure 2.29: (Color online) NIS spectra (a), iron-DOS (b), and Raman spectra (c) of 50-nm [Fe(pyrazine){Ni(CN)$_4$}] nanoparticles in the two spin states. The central peak of (a) is the elastic absorption, while the peaks on the right and on the left are the Stokes (phonon creation) and the anti-Stokes (phonon annihilation) peaks respectively. Their ratio depends on the temperature. Thereby, in the LS state, the anti-Stokes peaks have a very low intensity when compared to the Stokes peak. In (c), the arrows show, from the left to the right, the $\nu$(FeN$_{cycle}$) and the $\nu$(FeN$_{NC}$) modes in the two spin states.

In the LS state, several Fe-ligand vibrational modes are observed between 20 and 70 meV. In the HS state, one large peak is observed around 30 meV. This latter is clearly composed of several modes, which could not be resolved. As expected, the vibrational frequencies in the LS state are higher than in the HS state. This is linked to the volume expansion (approximately 25%) of the coordination octahedron when going from the LS to the HS state. The Raman spectra (633-nm excitation) of the sample were also collected in the two spin states (see figure 2.29 c). In the HS (LS) state, Raman modes are observed at 165 (306) and 218 (381) $cm^{-1}$, which can be assigned[202] to the $\nu(FeN_{cycle})$ and $\nu(FeN_{NC})$ metal-ligand stretchings, respectively. There is a reasonably good concordance between the peak positions of the NIS and the Raman spectra. In particular, the NIS data, which imply only the vibrational modes for which the mean-squared displacement of iron ions ($<u_{Fe}^2>$) is significant, provide a direct proof for the very important increase of the metal-ligand frequencies ($\nu_{LS}/\nu_{HS} = 1.33$) and the associated mean force constants ($C_{LS}/C_{HS} = 1.7$) when going to the LS state. These values are consistent with DFT calculations performed on different SCO compounds.[218]

Once the phonon DOS is known, various thermodynamical and lattice dynamical parameters can be deduced. Although these parameters may depend on the temperature, we suppose the main contribution is due to the spin transition, especially for the [Fe(pyrazine){Ni(CN)$_4$}] compound, which does not exhibit significant thermal expansion. Table 2.16 summarizes the extracted values. Of particular interest in the SCO field are the specific heat and the entropy. Indeed, the specific heat properties of spin-crossover systems are tightly related to their vibrational properties and the vibrational entropy change is the main driving force of the thermal spin transition. The specific heat, latent heat, and entropy change associated with the SCO is usually determined by calorimetric measurements and the vibrational contribution to the entropy change is calculated.[219] In the compound [Fe(pyrazine){Ni(CN)$_4$}], the vibrational entropy change extracted from calorimetry measurements is 55 J $K^{-1}$ $mol^{-1}$, but this value was probably underestimated. From Raman spectroscopy, the contribution of the octahedral modes to this entropy change was estimated of about $47 \pm 15$ J $K^{-1}$ $mol^{-1}$,[202] while from our NIS measurements, we obtain 27 J $K^{-1}$ $mol^{-1}$ (neglecting the temperature dependence of the entropy). This lower value has two reasons. First, the technique probes only the iron vibrational modes. Nevertheless, because the spin transition occurs in the iron, the most important part of the vibrational entropy change is provided by the iron mode.[202] On the other hand, some modes do not appear due to the fact

that NIS technique only probes modes for which $<u_{Fe}^2> = 0$. Thereby, the deduced entropy change takes into account only a part of the FeN$_6$ octahedron modes.

| Thermodynamical parameters | LS (50 K) | HS (310 K) |
|---|---|---|
| Norm. mean force constant C (*N/m*) | 367 | 218 |
| Specific heat | 0.51 $k_B$ | 2.70 $k_B$ |
| Entropy | 0.34 $k_B$ | 3.62 $k_B$ |
| $f_{LM}$ | 0.838 | 0.377 |
| $\theta_D$ (K) | 245 | 209 |

Table 2.16: Main lattice dynamical parameters extracted from the NIS spectra

From the NIS, the extracted Debye temperatures $\theta_D(f_{LM})$ are 245 and 209 K for the LS and HS states, respectively. On the other hand, for 70-nm nonenriched particles, the Debye temperature has been extracted $\theta_{LS}$ D = 170 ± 4 K from the conventional Mössbauer spectra (in this case, $\theta_D$ can be deduced only in the LS state due to the experimental constraints).[220] This difference is not surprising because NIS overestimates $\theta_D$ for the same reasons as discussed above for $f_{LM}$. It is worth to note that the Debye model is intended to describe acoustical modes. Therefore, using the Debye model to characterize the complete phonon spectrum (acoustic and optical modes) of a specific compound leads to the determination of the "effective Debye temperature". In any case, our main interest is the variation of the Debye temperature with the spin state of the system. From the NIS data, we obtain $\theta_{LS}$ D /$\theta_{HS}$ D = 1.17, which indicates a variation of the bulk modulus $B_{LS}/B_{HS}$ = 1.37.

An important part of the phonon DOS concerns the acoustic modes, from which the sound velocity can be also extracted. This latter parameter is directly related to the lattice stiffness. In the Debye model and because our sample is a powder, the DOS can be related to the sound velocity,[221] where $\hbar$ is the reduced Planck constant, $\tilde{m}$ is the atomic mass of 57-Fe, $\rho$ is the volumetric mass density of [Fe(pyrazine){Ni(CN)$_4$}][70] and $\upsilon_s$ is the Debye sound velocity.

$$\frac{\tilde{g}(E)}{E^2} = \frac{\tilde{m}}{2\pi^2 \rho \hbar^3 \upsilon_s^3} \tag{2.4}$$

Figure 2.30 plots $\tilde{g}(E)/E^2$ as a function of the energy E. The low-energy part of the curves is linear, which corresponds to the Debye model prediction and is therefore proportional to $1/v_s^3$. The sound velocity values extracted from the experimental data are ($v_{LS}$ = 2073 ± 31 m s$^{-1}$) and ($v_{HS}$ = 1942 ± 23 m s$^{-1}$) for the LS and HS states, respectively.
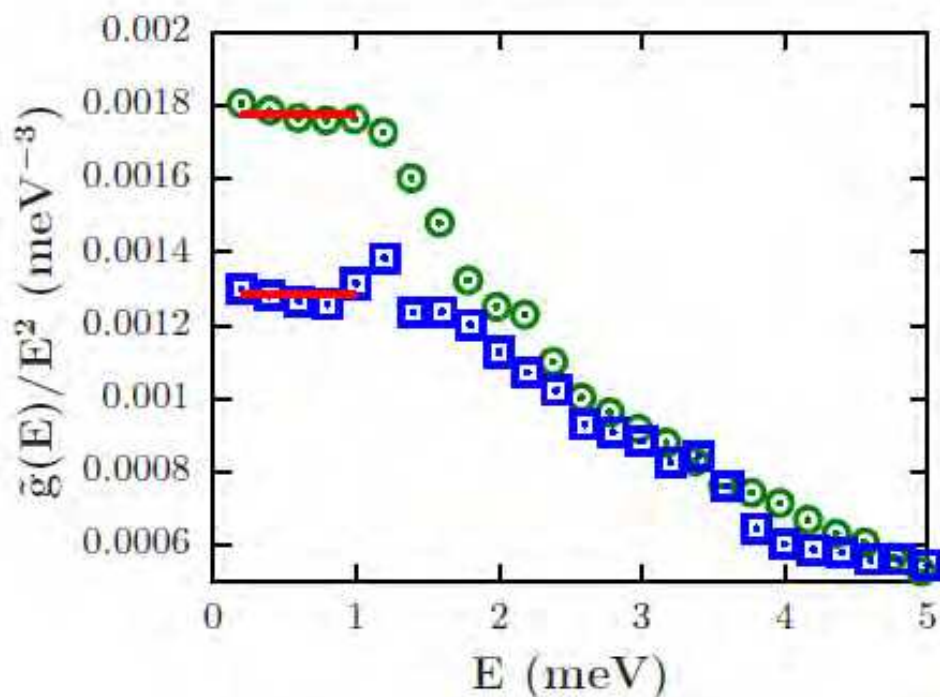


Figure 2.30: (Color online) Linear fit (solid line) of f (E) = $\tilde{g}(E)/E^2$ for the HS (circle) and the LS (square) states.

## 2.8.3.2 Comparison of Nuclear Inelastic Scattering for Different Nanoparticle Sizes

Figure 2.31 shows the vibrational DOS for different-size nanoparticles (50 nm and 2 nm) at 100 K. Compared to the 50 nm nanoparticle sample, similar Fe-ligand vibrational modes are observed between 20 and 70 meV for the 2 nm nanoparticles sample but the intensity of the large peak observed around 30 meV and attributed to the HS state is higher in the latter case in accordance with more incomplete spin transition. From the acoustic part of the phonon DOS, the sound velocity was also extracted for the small size particle sample and compared with the larger size particle sample (table 2.17).
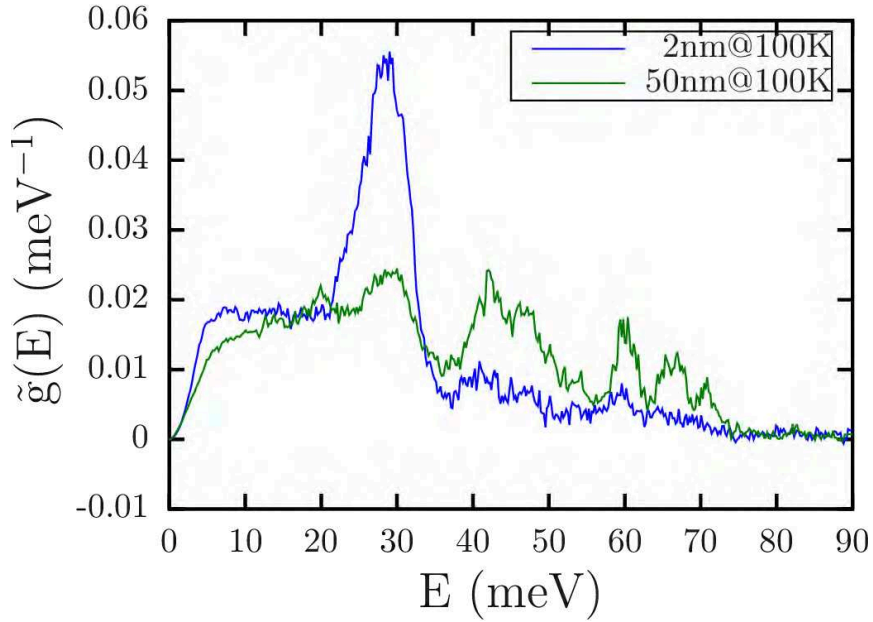
Figure 2.31: DOS spectrum of 50 nm and 2 nm [$^{57}$Fe(pyrazine)(Ni(CN)$_4$)] nanoparticles at low temperature.

| sample | Size (nm) | $v_{LS}$ (m s$^{-1}$) | $v_{HS}$ (m s$^{-1}$) |
|--------|-----------|-----------------------|-----------------------|
| **6**  | 50        | 2073 ± 31             | 1942 ± 23             |
| **7**  | 2         | 2240 ± 36             | 2125 ± 33             |

Table 2.17: Sound velocity values extracted from the experimental data for the LS and HS states of sample **6** and **7**

As expected and in agreement with the compression of the structure associated with the spin transition when going from the HS to LS state, the sound velocity value at low temperature is higher than that of the high temperature for both nanoparticle samples. Comparing the sound velocity between 50 nm and 2 nm nanoparticles, we observe a clear increase of this value for the small size nanoparticles. Moreover, the speed of sound of 2240 m s$^{-1}$ measured for the small nanoparticle size at low temperature is underestimated because of the presence of a larger residual high spin fraction in comparison with the larger nanoparticle size. This result tends to conclude that the stiffness increases for the ultra small size nanoparticles and confirms the evolution of the Debye temperature as a function of the size obtained by conventional Mössbauer measurements.

# 2.9 Conclusion

In conclusion, nanoreactors built using reverse nanoemulsion were used for the synthesis of a series of [Fe(pz){Ni(CN)$_4$}] nanoparticles with sizes ranging from 2 to 107 nm and with the same NaAOT matrix. For the first time it was possible to obtain a series of ultra-small nanoparticles smaller than 15 nm. Composition and size of the particles were probed with TEM and HRTEM investigations associated with EDX analyses. The size diminution was also evidenced by X-ray powder diffraction analyses through the determination of the crystallite size with the Scherrer equation. Raman and Mössbauer spectroscopy and magnetic measurements were combined to determine the spin crossover behavior with accuracy for the different samples. The results obtained for the larger [Fe(pz){Ni(CN)$_4$}] nanoparticles (107, 71 and 12 nm) namely the loss of the cooperativity, the shift of the transition to lower transition temperatures and the increase of the residual HS fraction at low temperature for decreasing size, corroborate previous reports obtained for the analogous [Fe(pz){Pt(CN)$_4$}] nanoparticles. On the other hand, the properties of the ultra-small nanoparticles (2 and 3 nm) revealed the re-increase of the cooperativity as well as the transition temperature with even the re-opening of a hysteresis loop for the smallest nanoparticles. This finding is in agreement with our previous results revealing the possibility of a memory effect (i.e. hysteresis) in ultra-small SCO particles. In order to find an origin to this unexpected behavior for such small SCO nanoparticles, we carried out a detailed Mössbauer study to determine the stiffness of the different nanoparticles by measuring their Debye temperature and we revealed a significant increase of $\theta_D$ for the smallest nanoparticles. Thus, the unusual SCO properties observed at low size can be explained thanks to the consideration of the size dependent elastic properties of the particles. Besides, by means of NIS spectroscopy the size dependent vibrational DOS and its spin-state dependence have been probed. These spectra revealed the well-known high-frequency shift of the DOS when going from the HS to the LS state. The analysis of the vibrational entropy change accompanying the spin transition has put in evidence the main contribution coming from the metal-ligand vibrational modes. The stiffness change of the material with the spin state change has been analyzed through the Debye sound velocity calculated from the acoustic part of the DOS. The study tends to conclude that the stiffness increases for the ultra small size (2 nm) nanoparticles and confirms the increase of the Debye temperature as a function of the size obtained by the more conventional Mössbauer investigation.

# Chapter 3

# Nanometric and Micrometric Rod-Shaped Spin Crossover Particles Synthesized in Homogeneous Acid Media

## 3.1 Introduction and Objectives

One of the relevant great challenges in the field of spin crossover materials is to produce size and morphology controlled objects that exhibit properties at room temperature and with large hysteresis loop.[222] An important family of compounds presenting such properties is the Fe[II]-triazole complexes[86,87] forming one-dimensional (1D) chains.[223] In 1977, Hasnoot and coworkers reported the first example of such compound, the [Fe(Htrz)$_2$(trz)](BF$_4$) complex[224] (Htrz = 1,2,4-triazole and trz = 1,2,4-triazolato) and its study was completed in 1994 by the group of Kahn.[225] In this latter paper several compounds have been obtained as a function of the experimental conditions. Using a water/ethanol mixture or methanol as a solvent, two polymorphs of the [Fe(Htrz)$_2$(trz)](BF$_4$) derivative were obtained while using high diluted methanol solution led to the precipitation of the [Fe(Htrz)$_3$](BF$_4$)$_2$·H$_2$O derivative which exhibits a phase transformation (phase α to phase β) upon heating around 440 K. Only the β phase showed an abrupt ST around room temperature with a narrow hysteresis of about 6 K, due to it is metastability, after several weeks, it changed back to the α phase with a rather abrupt transition around 335 K. On the other hand, the more stable [Fe(Htrz)$_2$(trz)](BF$_4$) polymorph presents a large hysteresis loop of 50 K centered at 370 K. All these appealing properties can be exploited into applications only if reduced sized and organized objects are fabricated. Indeed, if we look at the morphology of the elements forming the bulk samples, rather polydisperse and micrometric sized particles are observed. It is also interesting to note that in comparison with the rather spherical shape particles encountered for the majority of the bulk samples of this family,[183] a rod-like shape particles with length ranging from 300 to 800 nm was observed for the bulk sample of the [Fe(NH$_2$trz)$_3$](NO$_3$)$_2$ derivative.[226] In the frame of the study of the size reduction effects on the spin crossover properties, different methods

have been used to obtain controlled size and monodisperse nanoparticles based on these materials. Following the pioneering works of Létard and coworkers several groups used the reverse micelle technique or other matrixes (heterogeneous media) to obtain such nanoparticles with size ranging from 6 to 1000 nm.[41,145,150,151,182,192,227] The morphology of the particles was observed rather as nanoplaquette. In our group we have also used homogeneous media to obtain such type of nanoparticles.[147] Using different stabilizing agents, it was possible to obtain different sizes but also different shapes micro- and nano-particles. For example, using triton X, a non-ionic polymeric amphiphilic compound as stabilizers, rod-shaped particles of [Fe(NH$_2$trz)$_3$](tosylate)$_2$ with length ranging from 200 to 1000 nm were obtained, the width being comprised between 20 and 40 nm. As demonstrated by recent published papers, such anisotropic shape of the particles can be important for their organization onto surface or in between electrodes, notably for the measurements of their electrical and transport properties.[163,168,228] In the present chapter, we report an original homogeneous acid medium method to synthesize controlled sized nano- and micro-rods based on the BF$_4$ (tetrafluoroborate) and CF$_3$SO$_3$ (triflate) derivatives of the Fe-triazole family of compounds. Their optical, magnetic and electrical properties are also presented.

# 3.2 BF$_4$ Derivatives of the Fe-Triazole Family of Compounds

### 3.2.1 Synthesis of Different-Size Particles

The synthesis of the particles was carried out in a homogeneous medium without any stabilizing agent just mixing the precursors Fe(BF$_4$)$_2$·6H$_2$O salt and Htrz ligand in presence of different concentrations of tetrafluoroboric acid (HBF$_4$) in water. The first tries led inexorably to the formation of unexpected samples containing Si atoms which can be explained by the presence of SiF$_6$ anions formed when the wall of the glass (SiO$_2$) containers dissolve in HBF$_4$, replacing the BF$_4$ counter-anions in the complex. The presence of such Si Atoms was revealed by high resolution scanning transmission electron microscopy coupled quantified energy dispersive X-ray spectroscopy (HRSTEM EDX) analyses (see Annex 2). This undesirable complex does not present any spin crossover properties and remains in the HS state whatever the temperature. In order to avoid such problem, all the syntheses were performed using plastic containers. So, while increasing the concentration of tetrafluoroboric acid from 0.1 to 5

wt% and modifying the evaporation speed of the solvent and the synthetic method (see Annex 1 for the detailed synthesis), crystalline purple powders were obtained after an increasing period ranging from few minutes to *ca.* one month.
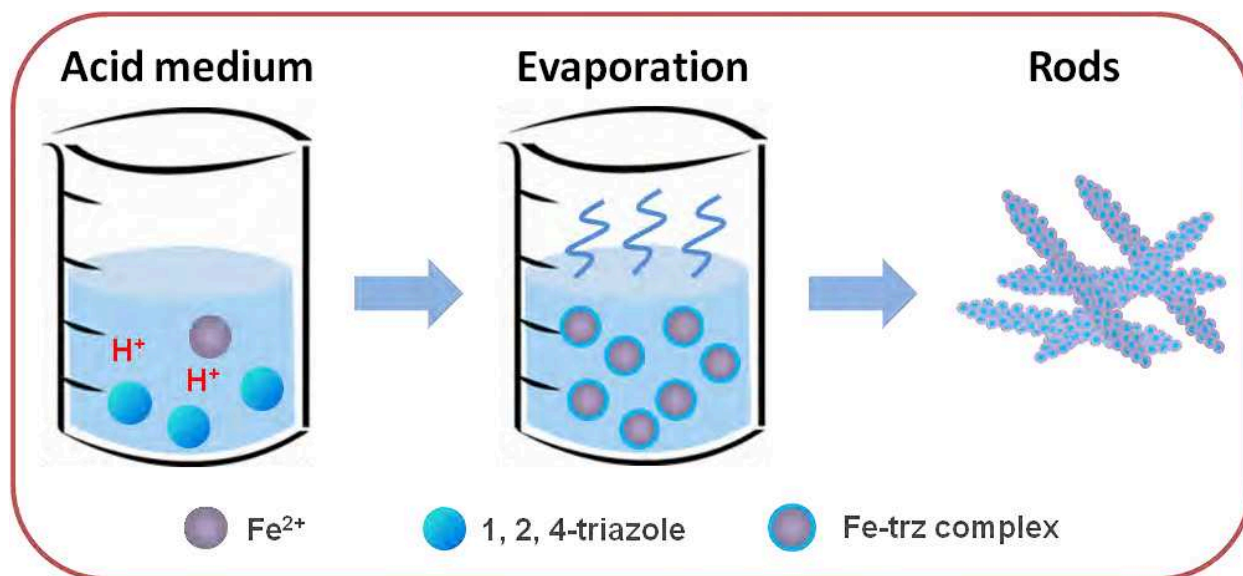


Figure 3.1 Scheme of the synthetic process used for the elaboration of microrods in homogeneous acid condition

Samples **1**-**5** were prepared by rapidly mixing two aqueous solutions of $HBF_4$ containing $Fe(BF_4)_2 \cdot 6H_2O$ and the 1,2,4-triazole ligand (see table 3.1). The resulting limpid solutions were let for slow evaporation at room temperature; the flask being half covered (see Annex 1). Following a specific period, the flocculates were centrifuged, and washed by distilled water and absolute ethanol and finally dried under vacuum. Sample **3'** was prepared as sample **3** (2 wt% $HBF_4$) but the evaporation speed was decrease opening less the cover of the flask (see scheme in Annex 1). Sample **6** and **6'** were prepared with 5 wt% of $HBF_4$ but the evaporation speed was increased (using such acid concentration and slow evaporation as that used for the elaboration of sample **1**-**5**, no precipitation was obtained after several months). Sample **7** was prepared using the same reactant concentrations as sample **3** (2 wt% $HBF_4$) but a liquid-liquid (water-water) diffusion synthetic method was carried out instead of the direct mixture of the two reagents. A named bulk sample obtained using the same concentrations in an aqueous solution and in absence of acid was synthesized as a reference sample.

| Sample | 1 | 2 | 3 | 4 | 3' | 5 | 6 | 6' | 7 |
|---|---|---|---|---|---|---|---|---|---|
| HBF$_4$ (wt%) | 0.1 | 0.5 | 2 | 3 | 2 | 4 | 5 | 5 | 2 |
| Synthetic Method | Direct mixture | Direct mixture | Direct mixture | Direct mixture | Direct Mixture | Direct mixture | Direct mixture | Direct mixture | Liquid-liquid diffusion |
| Evaporation speed | slow | slow | slow | slow | very slow | slow | very fast | fast | slow |
| Time | 15 min | 1 hour | 1 day | 3 days | 5 days | 1 month | 1 week | 2 weeks | 1 month |
| Yield (%) | 72 | 62 | 35 | 38 | 28 | 61 | 50 | 33 | 24 |

Table 3.1 Synthetic condition of sample **1**-**7** (see also Annex 1)

**In comparison with the previous reported bulk synthesis of this complex,[225] the presence of acid lengthen the crystallization process and we have good reason to think that the acid solution slows down the deprotonation of the Htrz ligand precluding the rapid precipitation of the [Fe(Htrz)$_2$(trz)](BF$_4$) complex.**

## 3.2.2 Composition and Morphology of the Particles

The composition of the samples was studied by Raman and infrared spectroscopy, elemental analyses, NMR, TGA and X-ray powder diffraction while the morphology of the powder was probed by TEM (Transmission Electronic Microscopy) and HRTEM (High Resolution TEM) coupled EDX (Energy Dispersive X-ray spectrometry) analyses.

### 3.2.2.1 Composition of the Particles

The fine composition of the samples was obtained thanks to combined thermogravimetric analysis (TGA), C, H, N elemental analyses and various nucleus ($^1$H, $^{13}$C and $^{19}$F) solid state NMR. TGA (figure 3.2) revealed the absence of water molecules for sample **1**-**4** and **3'**, while *ca.* 3 molecules of water per iron atom were identified for sample **5** and **7** (see table 3.2). Additional C, H, N elemental analyses and NMR data (see next chapter concerning NMR) revealed the [Fe(Htrz)$_2$(trz)](BF$_4$) (form A) composition for samples **1**-**4** and **3'**, while the [Fe(Htrz)$_3$(BF$_4$)$_2$]·3H$_2$O (form B) composition for samples **5** and **7** (see table 3.3). Regarding samples **6** and **6'**, *ca.* 1.5 molecules of water per iron atom were identified in agreement with mixture samples incorporating about 40% of form A and 60% of form B. **In fact, both the higher concentrations of acid which preclude the deprotonation of the Htrz ligand and**

**the slow evaporation speed of the complex solution lead to the slow stabilization of the fully protonated ligand [Fe(Htrz)₃](BF₄)₂·3H₂O derivative.**
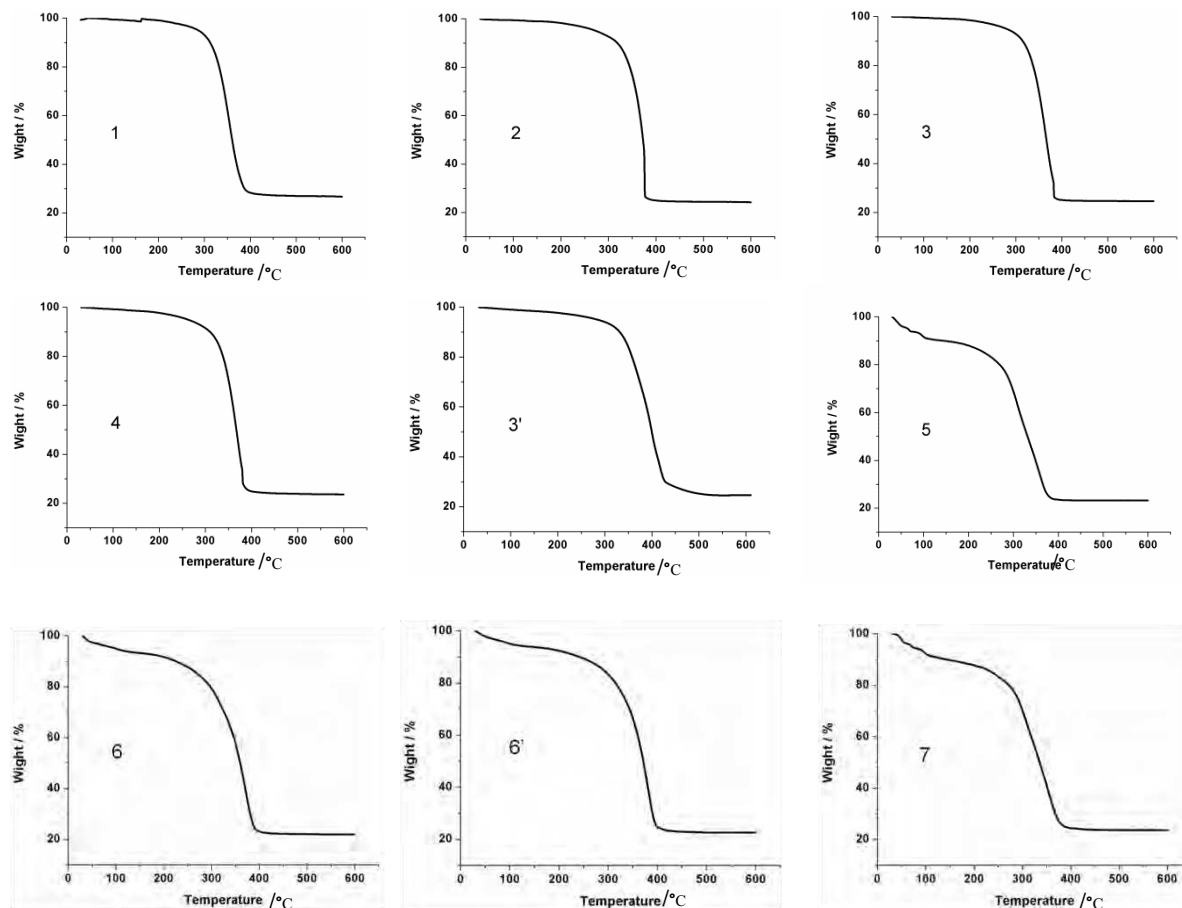


Figure 3.2: TGA analyses of sample **1-7, 3'** and **6'**.

| Weight loss step | Sample **1** | Sample **2** | Sample **3** | Sample **4** | Sample **3'** | Sample **5** | Sample **6** | Sample **6'** | Sample **7** |
|---|---|---|---|---|---|---|---|---|---|
| 1 (%) | 77 | 78 | 76 | 77 | 79 | 10 $3·H_2O$ | 6 $1.8·H_2O$ | 7 $1.8·H_2O$ | 11 $3·H_2O$ |
| 2 (%) | | | | | | 68 | 73 | 72 | 66 |

Table 3.2: Weight loss of samples **1-7** during the thermogravimetric process

| Compound | | C / % | H / % | N / % | Calculated Formula |
|---|---|---|---|---|---|
| 1 | exptl | 19.59 | 2.01 | 34.35 | $[Fe(Htrz)_2(trz)](BF_4)$ |
| | calcd | 20.66 | 2.31 | 36.14 | |
| 2 | exptl | 19.15 | 1.88 | 35.21 | $[Fe(Htrz)_2(trz)](BF_4)$ |
| | calcd | 20.66 | 2.31 | 36.14 | |
| 3 | exptl | 19.74 | 1.74 | 34.79 | $[Fe(Htrz)_2(trz)](BF_4)$ |
| | calcd | 20.66 | 2.31 | 36.14 | |
| 4 | exptl | 19.80 | 2.21 | 35.71 | $[Fe(Htrz)_2(trz)](BF_4)$ |
| | calcd | 20.66 | 2.31 | 36.14 | |
| 3' | exptl | 19.82 | 1.93 | 34.24 | $[Fe(Htrz)_2(trz)](BF_4)$ |
| | calcd | 20.66 | 2.31 | 36.14 | |
| 5 | exptl | 15.62 | 2.33 | 26.72 | $[Fe(Htrz)_3](BF_4)_2 \cdot 3H_2O$ |
| | calcd | 15.85 | 2.44 | 27.73 | |
| 6 | exptl | 16.83 | 2.47 | 28.97 | $[[Fe(Htrz)_3](BF_4)_2 \cdot 3H_2O]_{0.6}[[Fe(Htrz)_2(trz)](BF_4)]_{0.4}$ |
| | calcd | 16.79 | 2.79 | 29.39 | |
| 6' | exptl | 16.33 | 2.72 | 28.91 | $[[Fe(Htrz)_3](BF_4)_2 \cdot 3H_2O]_{0.6}[[Fe(Htrz)_2(trz)](BF_4)]_{0.4}$ |
| | calcd | 16.79 | 2.79 | 29.39 | |
| 7 | exptl | 15.38 | 2.65 | 26.29 | $[Fe(Htrz)_3](BF_4)_2 \cdot 3H_2O$ |
| | calcd | 15.85 | 2.44 | 27.73 | |

Table 3.3: Elemental analysis of samples **1-7** and the corresponding formula

## 3.2.2.2 Spectroscopic Investigation

### 3.2.2.2.1 Infrared Spectroscopy

Infrared spectra of all samples are also measured to characterize the composition as shown in figure 3.3. Clearly, sample **1-4** exhibit similar spectrum than that corresponding to

the $[Fe(Htrz)_2(trz)](BF_4)$ bulk sample with in particular vibrational modes at 1536 and 1497 $cm^{-1}$ which can be attributed to the stretching deformation of the protonated and unprotonated ligands, respectively (see the selected zoom area of the IR spectra in figure 3.4).
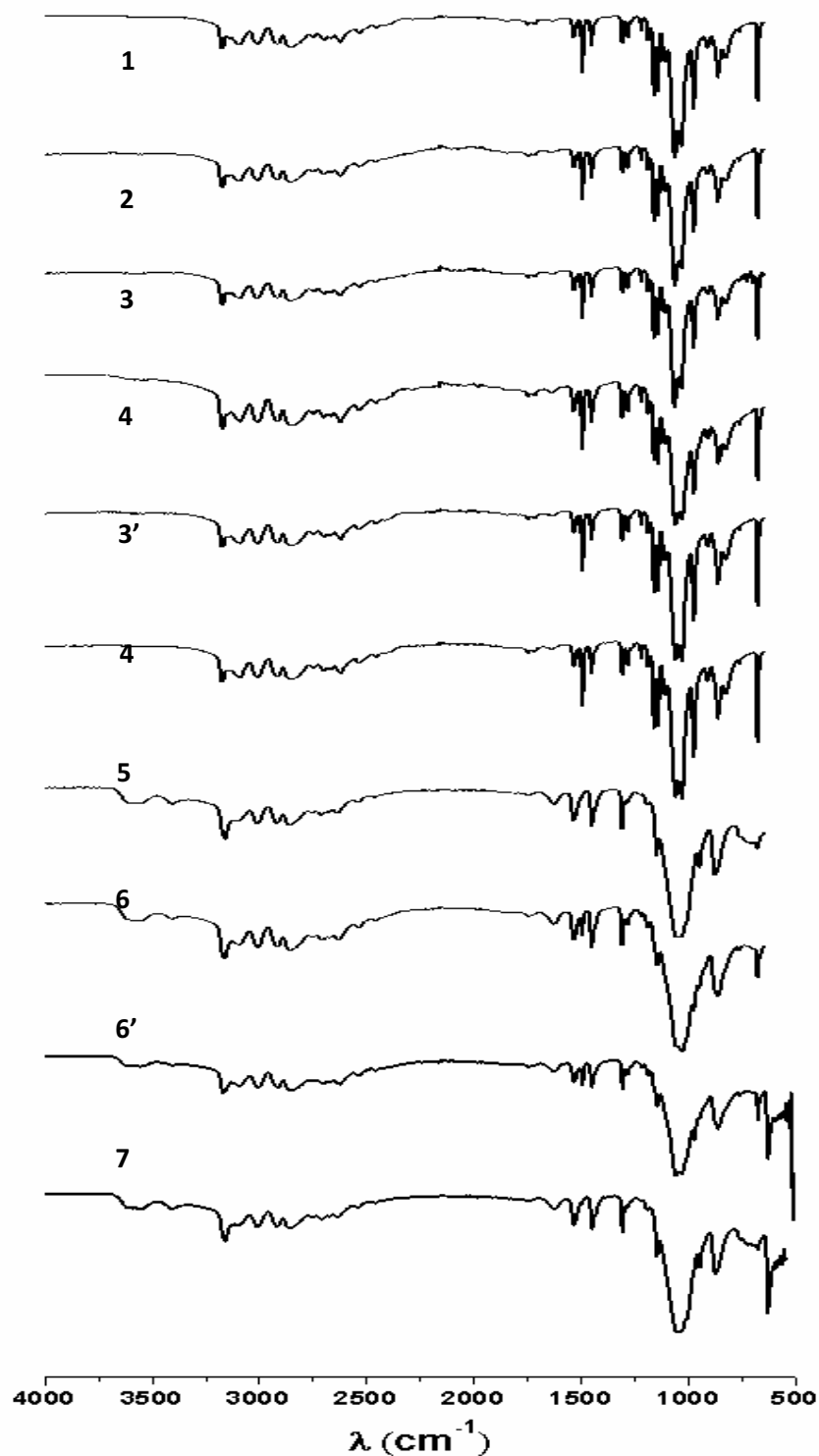


Figure 3.3: Infrared spectra of Samples **1-7, 3'** and **6'** at 293 K.
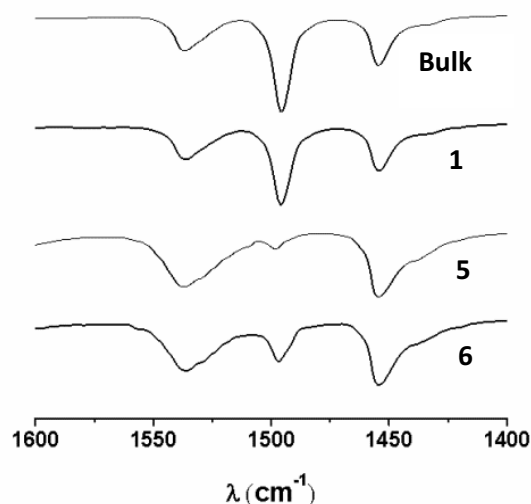
Figure 3.4: Selected IR spectra of the bulk and samples **1**, **5** and **6**.

In contrast IR spectrum of sample **5** obtained in presence of higher acid concentration presents different features in this area with the quasi disappearance of the vibrational mode at 1497 cm$^{-1}$. Moreover, the presence of a broad peak around 3600 cm$^{-1}$ characteristic of the presence of water tends to attribute this latter sample to the [Fe(Htrz)$_3$](BF$_4$)$_2$·xH$_2$O derivative. Samples **6** and **6'** obtained in presence of the highest concentration of acid (5 wt%) but with increasing the evaporation speed of the solution are composed of a mixture of samples [Fe(Htrz)$_2$(trz)](BF$_4$) and [Fe(Htrz)$_3$](BF$_4$)$_2$·3H$_2$O since the vibration mode at 1497 cm$^{-1}$ is clearly present but at a lower intensity compare to samples **1-4**. **This result implies that both the acid concentration and the evaporation speed influence on the composition but also on the size (see hereafter the TEM analysis) of the particles.**

### 3.2.2.2.2 Raman Spectroscopy

Selected Raman spectra were acquired in both the LS and HS states in figure 3.5. These Raman spectra compare well with those already reported in the literature.[229,230] In particular, the Raman modes between *ca.* 1000 and 1600 cm$^{-1}$ can be chiefly related to the internal stretching and deformation modes of the triazole ring; these frequencies are not expected to suffer major changes upon complexation nor upon the spin state change of iron ions. Internal modes of BF$_4$ ions are expected to appear around 780, 1070 cm$^{-1}$, but their intensity is rather weak. In the considered region of the spectra, only the spectral feature around 1300 cm$^{-1}$ can be used to distinguish the two compounds; the double-band character originating from the presence of two different, trz and Htrz, ligands. The mode at *ca.* 1311 cm$^{-1}$ is due to the Htrz ligand, while that at *ca.* 1285 cm$^{-1}$ is due to the trz ligand. The rough ratio of the trz:Htrz band

areas shows nearly 1:2, in agreement with the stoichiometry of trz and Htrz in **3**. In sample **5**, only remaining trace of $[Fe(Htrz)_2(trz)](BF_4)$ is observed (vibrational mode at 1285 cm$^{-1}$) while a clear mixture is revealed for sample **6** (broadening of the vibrational mode at 1310 cm$^{-1}$).
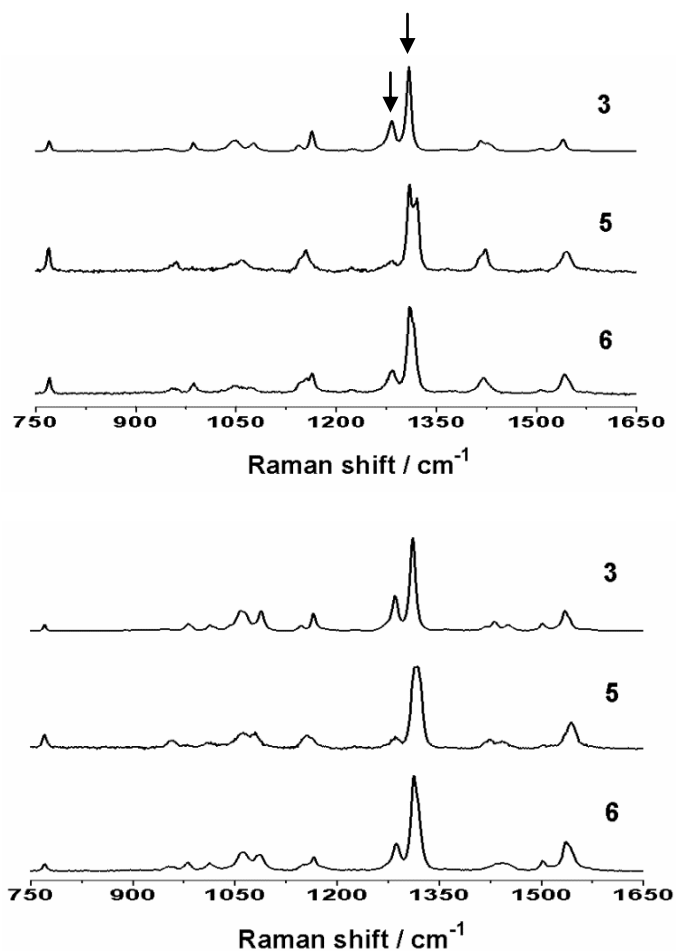


Figure 3.5: Selected Raman spectra in the HS (up) and LS state (bottom) for sample **3, 5** and **6.**


### 3.2.2.2.3 Nuclear Magnetic Resonance Spectroscopy

In order to obtain more quantitative information of samples **1-7**, various nucleus ($^1$H, $^{13}$C and $^{19}$F) solid state NMR data were recorded on selected samples (see figure 3.6). NMR measurements on spin crossover compounds are scarce because most of time the metal is paramagnetic and the corresponding spectrum is thus difficult to explain. In the present study the complex is diamagnetic at room temperature. $^1$H NMR spectrum of sample **3** exhibits three peaks corresponding to the triazole ligand at 7.91 ppm attributed to CH and 15.67 and 13.21 ppm attributed to NH. In this $[Fe(Htrz)_2(trz)](BF_4)$ compound, the different chemical

shift associated with each NH group of the two protonated ligand can be explained by their different position in the packing organization associated with specific strength of their participation in hydrogen contacts, the more shielded proton being involved in stronger hydrogen bonds. Inversely, the NMR spectrum of samples **5** and **7** (**[Fe(Htrz)$_3$](BF$_4$)$_2$·xH$_2$O**) present solely one peak at 15.48 for the 3 NH groups in agreement with a more symmetric structure. Additional peak at 4.51 ppm is attributed to water molecules. Concerning $^{13}$C NMR data, sample **3** is composed of two CH chemical shifts at 160.1 and 151.9 ppm associated with the deprotonated and protonated ligand (1:2 ratio), respectively, while as expected a single broad peak at *ca.* 156 ppm is observed in samples **5** and **7**. $^{19}$F NMR spectroscopy was also performed in order to better quantify the two species in the different compounds and in particular to probe the presence of [Fe(Htrz)$_2$(trz)](BF$_4$) traces in samples **5** and **7**. For sample **3**, the unique peak at -147.4 ppm is attributed to the fluorine atoms of the sole BF$_4$ group. In contrast, two peaks at -148.5 and -149.9 ppm are measured for samples **5** and **7** in accordance with the presence of two BF$_4$ counter-anions. Moreover, additional peak at -147 ppm is attributed to the [Fe(Htrz)$_2$(trz)](BF$_4$) derivative, but represents less than 1% both for samples **5** and **7**. Regarding sample **6** (and also sample **6'**), the two species are clearly present with *ca.* 40% of the [Fe(Htrz)$_2$(trz)](BF$_4$) derivative.
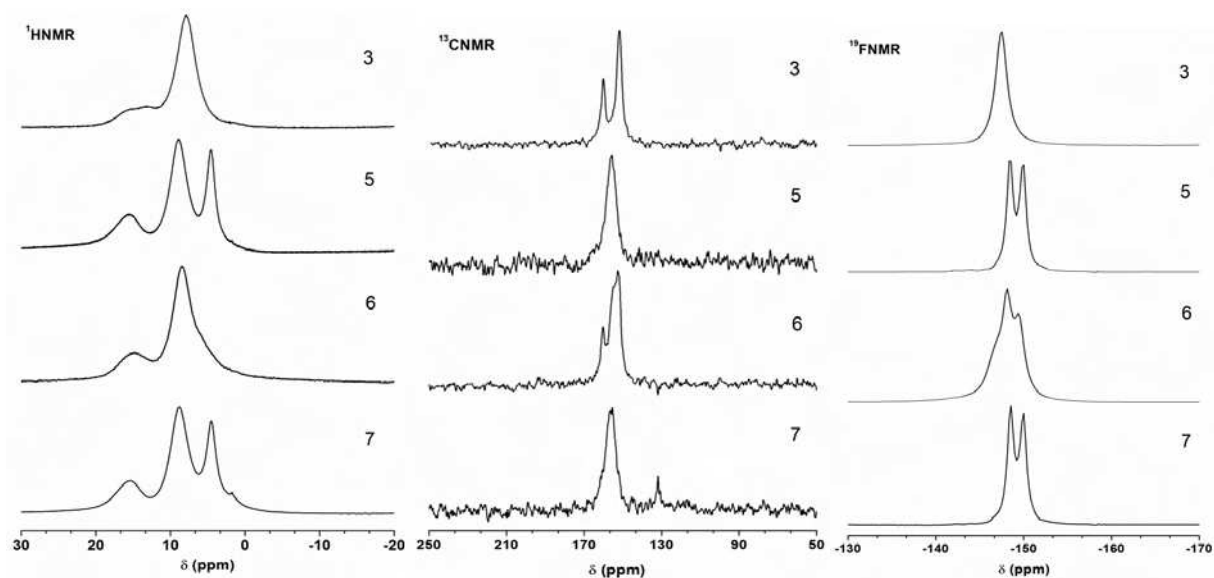


Figure 3.6: Solid state $^1$H, $^{13}$C and $^{19}$F NMR spectra of sample **3**, **5**, **6** and **7**.

| NMR δ, ppm | Sample **3** | Sample **5** | Sample **6** | Sample **7** |
|---|---|---|---|---|
| formula | $[Fe(Htrz)_2(trz)](BF_4)$ | $[Fe(Htrz)_3](BF_4)_2$ | $[[Fe(Htrz)_3](BF_4)_2]_{0.6}$ $[[Fe(Htrz)_2(trz)](BF_4)]_{0.4}$ | $[Fe(Htrz)_3](BF_4)_2$ |
| $^1H$ | 15.7 (1H, NH), 13.2 (1H, NH), 7.9 (6H, CH) | 15.5 (3H, NH), 8.8 (6H, CH), 4.5 (H2O) | 15.5 (3H, NH), 8.3 (6H, CH), 4.2 (H2O) | 15.6 (3H, NH), 8.9 (6H, CH),  4.5 (H2O) |
| $^{13}C$ | 151.9 (4C, CH), 160.1 (2C, CH) | 156.2 (6C, CH) | 152.4 (4C, CH), 155.7 (6C, CH), 160.2 (2C, CH) | 155.9 (6C, CH) |
| $^{19}F$ | -147.3 (4F, BF4) | -148.6 (4F, BF4), -149.9 (4F, BF4) | -146.5 (4F, BF4), -148.1 (4F, BF4), -149.6 (4F, BF4) | -148.5 (4F, BF4), -149.9 (4F, BF4) |

Table 3.4: Various nucleus ($^1H$, $^{13}C$ and $^{19}F$) solid state NMR data on selected samples

## 3.2.2.3 Powder X-ray Diffraction

Figure 3.7 shows the powder X-ray diffraction (PXRD) patterns of all samples.
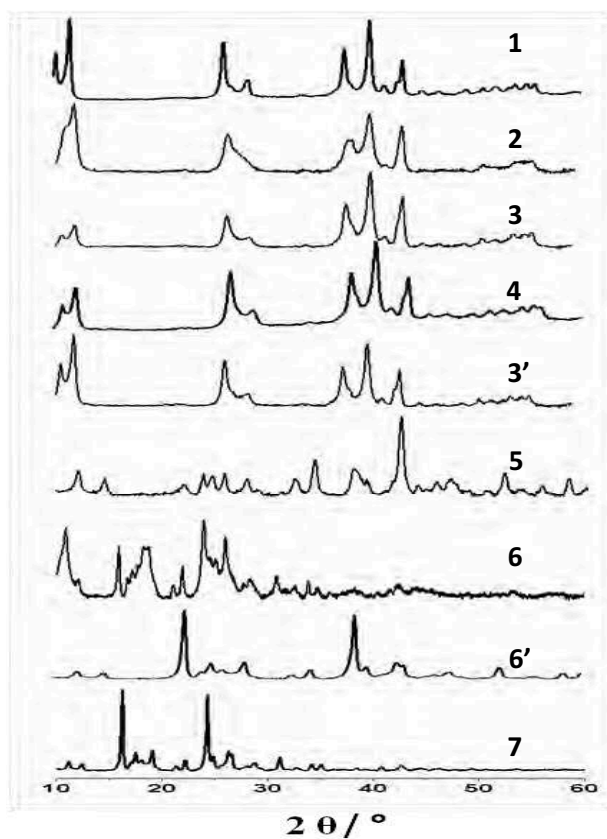


Figure 3.7: X-ray powder diffraction patterns of all samples

In agreement with the IR and Raman spectroscopy results, samples **1-4** and **3'** correspond to the $[Fe(Htrz)_2(trz)](BF_4)$ complex while samples **5** and **7** exhibit a different PXRD patterns corresponding to the $[Fe(Htrz)_3(BF_4)_2] \cdot xH_2O$ derivative. X-ray diffraction allows also for the estimation of the crystallite size using the Scherrer equation (see chapter 2 page75). Whatever the sample, the average crystallite size is measured between 30 and 50 nm with no evident correlation with the composition and the size of the particles. These crystallite sizes are in agreement with those reported for 30-600 nm $[Fe(NH_2\text{-}trz)_3]Br_2$ particles.[155] As already demonstrated by Raman and IR measurements, sample **6** and **6'** correspond to mixture samples; the relative proportion being difficult to obtain using such technique.

## 3.2.2.4 Morphological Characterization: TEM and HRTEM

Transmission electronic microscopy (TEM) and high resolution transmission electronic microscopy coupled with quantified energy dispersive X-ray spectroscopy analyses (HRTEM EDX) were used to determine the shape, the size and also the fine composition of the particles. Figure 3.8-3.16 presents a representative TEM image for each sample (**1-7**, **3'** and **6'**); see also Annex 2 for complementary TEM images. Each sample displays similar particle morphology forming rods with different length.
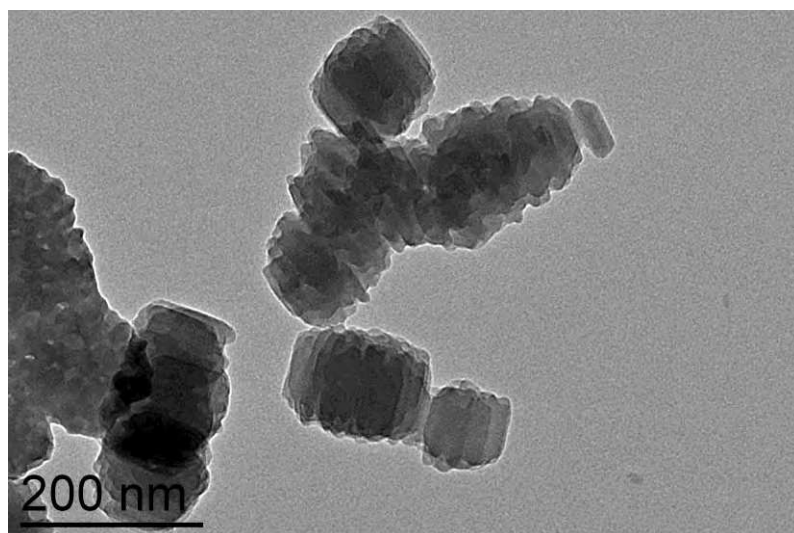


Figure 3.8: Selected TEM image of sample **1**
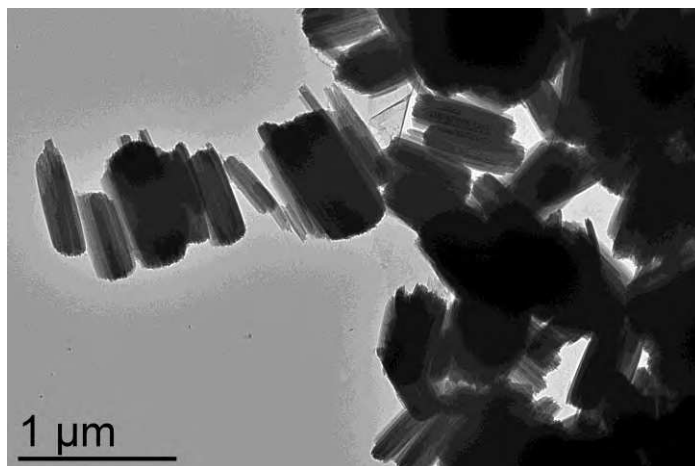
Figure 3.9: Selected TEM image of sample **2**
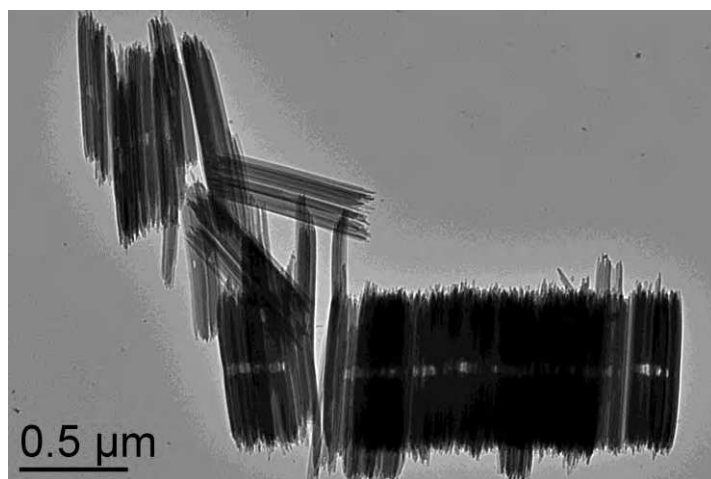


Figure 3.10: Selected TEM image of sample **3**
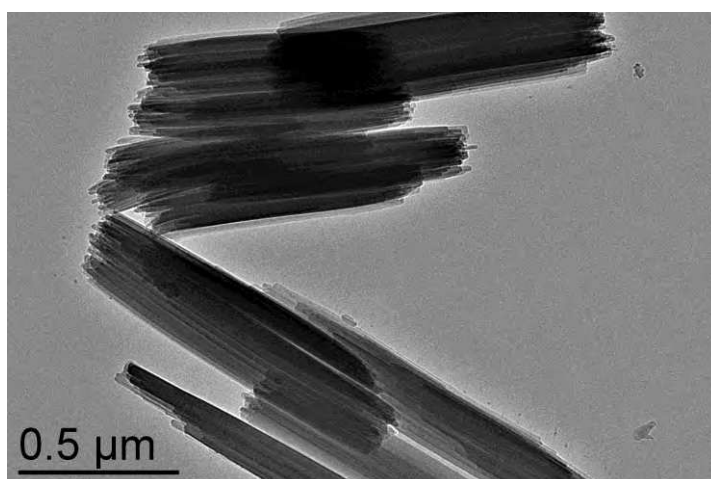


Figure 3.11: Selected TEM image of sample **4**
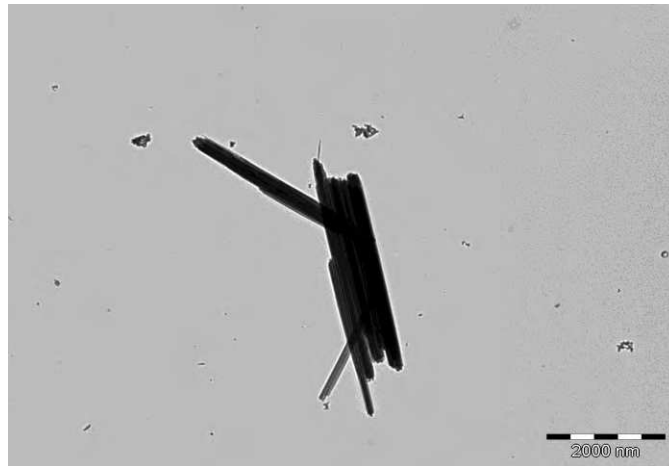
Figure 3.12: Selected TEM image of sample **3'**
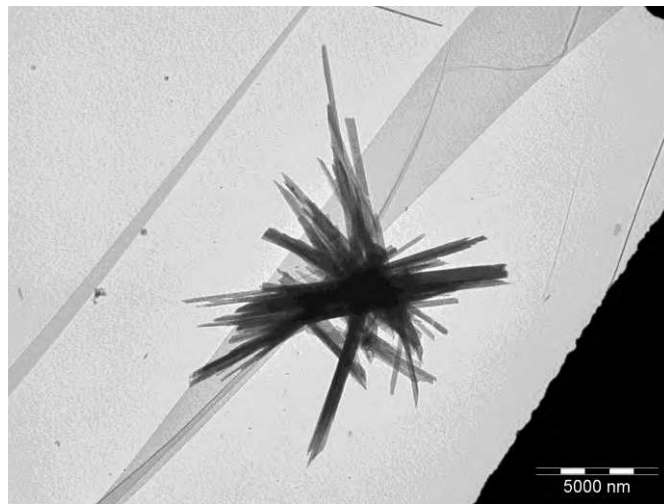


Figure 3.13: Selected TEM image of sample **5**
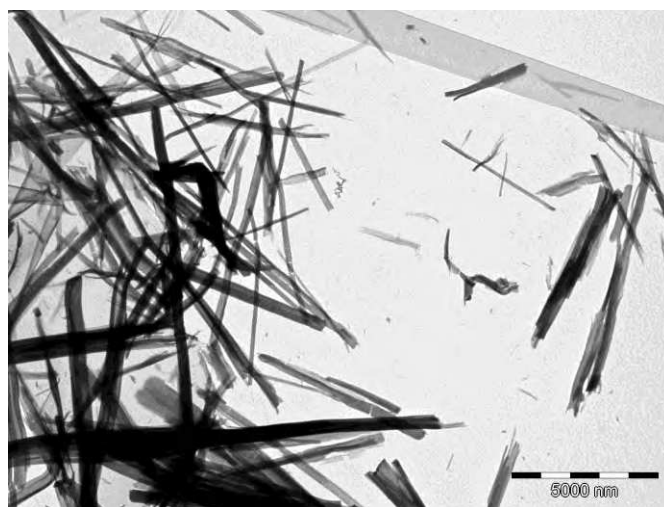


Figure 3.14: Selected TEM image of sample **6**

Figure 3.15: Selected TEM image of sample **6'**
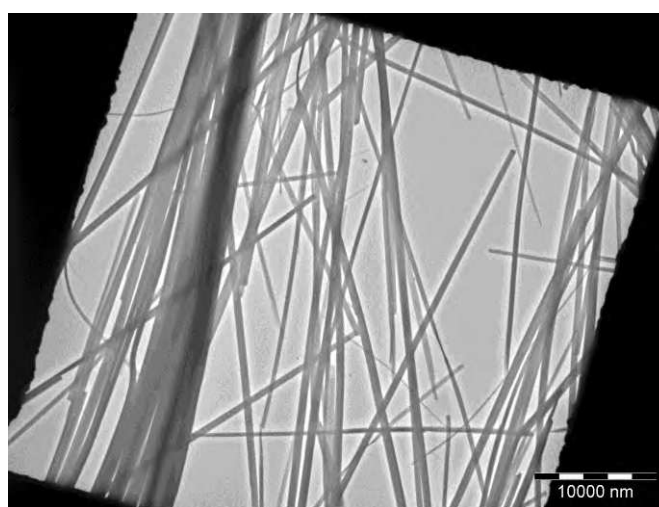


Figure 3.16: Selected TEM image of sample **7**

For sample **1**, the TEM image shows two orientations of the nano-crystals parallel and perpendicular to the grid surface and gave a mean length of 100 nm and a mean section of about 10 nm. Increasing the acid concentration from 0.1 to 3 wt%, rod sizes of the $[Fe(Htrz)_2(trz)](BF_4)$ compound (form A) from 100 nm to ca. 1.5 µm length were obtained, the width being difficult to determined. The average rod size of this derivative was extended to *ca.* 5 µm, with 2 wt% $HBF_4$, diminishing the evaporation speed of the solution (sample **3'**). **Then, increasing the concentration of acid (4 wt%,), the period of crystallization process is lengthened and longer (*ca.* 10 µm) and pure $[Fe(Htrz)_3](BF_4)_2 \cdot 3H_2O$ (form B) rods are obtained instead of the smaller $[Fe(Htrz)_2(trz)](BF_4)$ rods.** Similar experiments using a 5 wt% $HBF_4$ concentration solution associated with faster evaporation speeds of the solvent led to the formation of mixtures of short $[Fe(Htrz)_2(trz)](BF_4)$ and long $[Fe(Htrz)_3](BF_4)_2 \cdot 3H_2O$ rods. To go further and with the objective to obtain even longer and pure rods, a liquid-liquid

diffusion synthetic method was used in order to reduce the speed of the reaction while the slow evaporation of the solution was maintained. Indeed, using a 2 wt% $HBF_4$ concentration solution, pure $[Fe(Htrz)_3](BF_4)_2 \cdot 3H_2O$ rods with a mean size superior to 40 µm were obtained (sample **7**). It is interesting to notice that the crystallinity of these long rods was not sufficient enough for single crystal X-ray measurements. **So, we can observe that the control of the experimental conditions and in particular the $HBF_4$ concentration permits us to obtain a series of nano- and microrods with size range from 100 nm to longer than 40 µm** (see table 3.5 for the size distribution for the different samples).

| Sample | 1 | 2 | 3 | 4 | 3' | 5 | 6 | 6' | 7 |
|--------|---|---|---|---|-----|---|---|-----|---|
| wt% Acid | 0.1 | 0.5 | 2 | 3 | 2 | 4 | 5 | 5 | 2 |
| Nps Size | 100±14 nm | 640±100 nm | 1.1±0.1 µm | 1.4±0.3 µm | 4.5±0.9 µm | 10±2 µm | 11±8 µm | 25±10 µm | ≥ 40 µm |

Table 3.5: Particle size distribution for the different samples

HRTEM and Energy dispersive X-ray spectrometry (EDX) was also employed to characterize the fine composition of a single rod (see figure 3.17). The EDX pattern showing the analysis of the whole area in the right image reveals the presence of iron atoms on the micro-rods compared with the nacked copper grid as a reference which contains also carbon oxygen and silicon atoms.
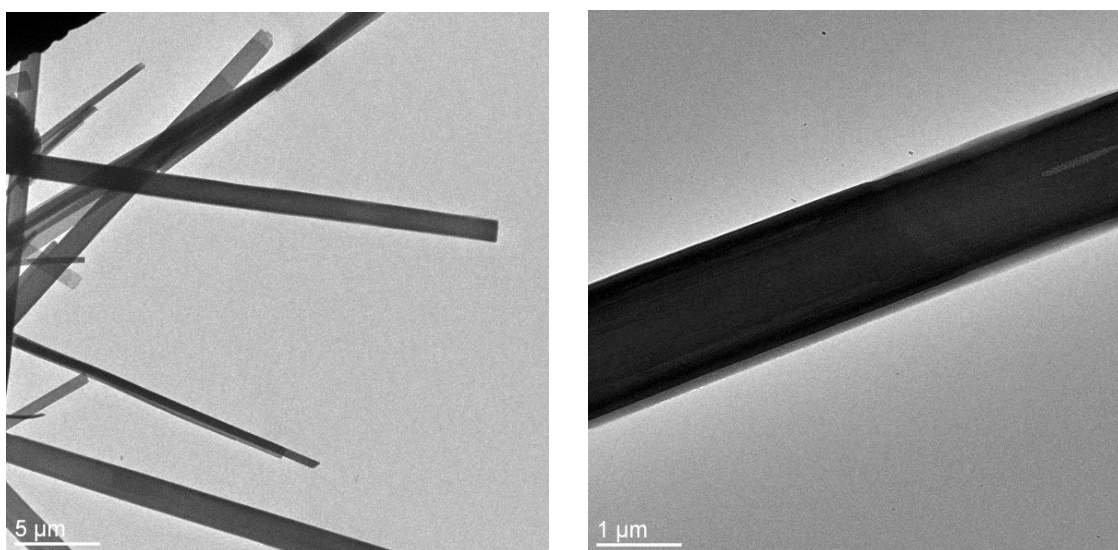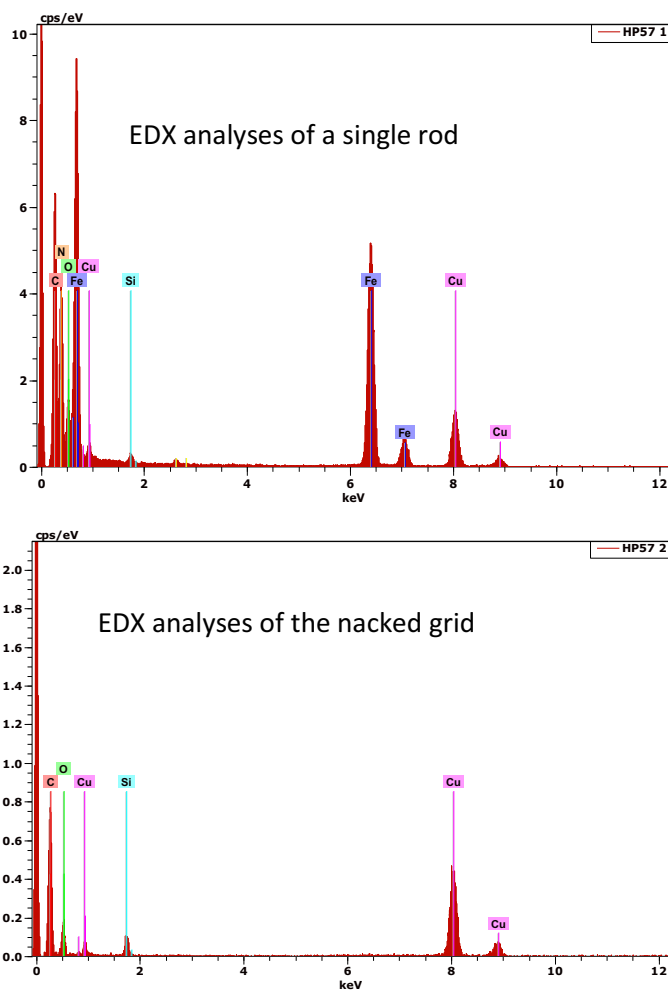
Figure 3.17: HRTEM and EDX analyses of sample **6'**

## 3.2.3 SCO Properties of the Different-Size Particles

### 3.2.3.1 Magnetic Properties

Figure 3.18-3.20 show the spin transition behavior measured thanks to the thermal variation of the magnetic susceptibility. The different samples were cycled between 220 and 400 K after a preliminary thermal treatment for the dehydration. For each sample, the value of $\chi T$ at high temperature of *ca.* 3.2 cm$^3$·K·mol$^{-1}$ corresponds well to Fe(II) complex in the high spin state. It is interesting to notice that the dehydration of the [Fe(Htrz)$_3$](BF$_4$)$_2$·3H$_2$O sample (**5** and **7**) lead to the decrease of the transition temperature, the [Fe(Htrz)$_2$(trz)](BF$_4$) being unsolvated. As expected, samples **1-4** and **3'** with the same composition as the corresponding bulk sample present close properties with the abruptness of the transitions, in both the warming and cooling modes. The transition temperatures are found at T$_{1/2\,(\downarrow)} \approx$ 352 K and T$_{1/2}$ $_{(\uparrow)} \approx$ 397 K for sample **1** while a narrow hysteresis is observed for longer **2-4** and **3'** rods (T$_{1/2}$

$_{(\downarrow)} \approx 350$ K and $T_{1/2 \,(\uparrow)} \approx 380$ K). This effects which was already observed for similar rod-shaped particles wrapped with $SiO_2$[41] can be explain by the morphology of the particles and the associated structural organization of the chains. For samples **5** and **6** the hysteresis loop is centered below ($T_{1/2 \,(\downarrow)} \approx 265$ K and $T_{1/2 \,(\uparrow)} \approx 278$ K) and at room temperature ($T_{1/2 \,(\downarrow)} \approx 278$ K and $T_{1/2 \,(\uparrow)} \approx 300$ K), respectively. The physical properties of sample **6** (and also sample **6'**) exhibit intermediate temperature transitions when compared to those measured for sample **1** (form A) and **5** (form B) and not the superposition of different singularities which might suggest that whatever the size of the rods in the mixture samples, both forms A and B of the compound are randomly present. **This result underlines that although a certain threshold of acid concentration is necessary, the slow evaporation speed remains the driving force to obtain the pure B form of the complex.**
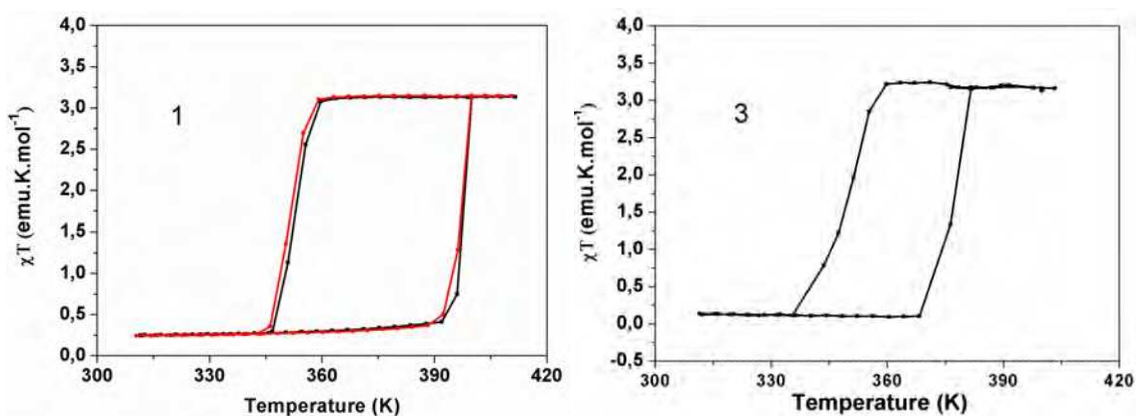


Figure 3.18: Magnetic measurements for samples **1** and **3** (form A). Hydrated sample in red and dehydrated sample in black.
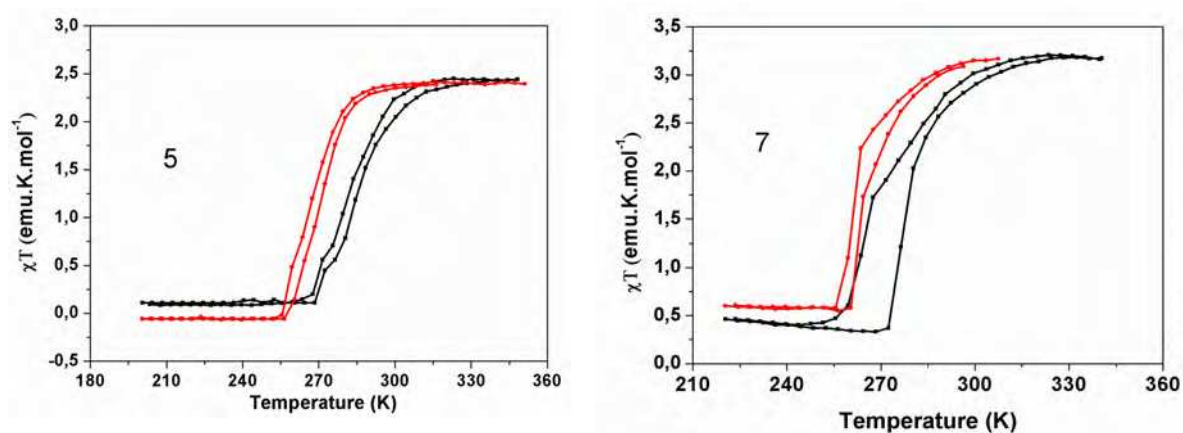


Figure 3.19: Magnetic measurements for samples **5** and **7** (form B). Hydrated sample in black and dehydrated sample in red.

119
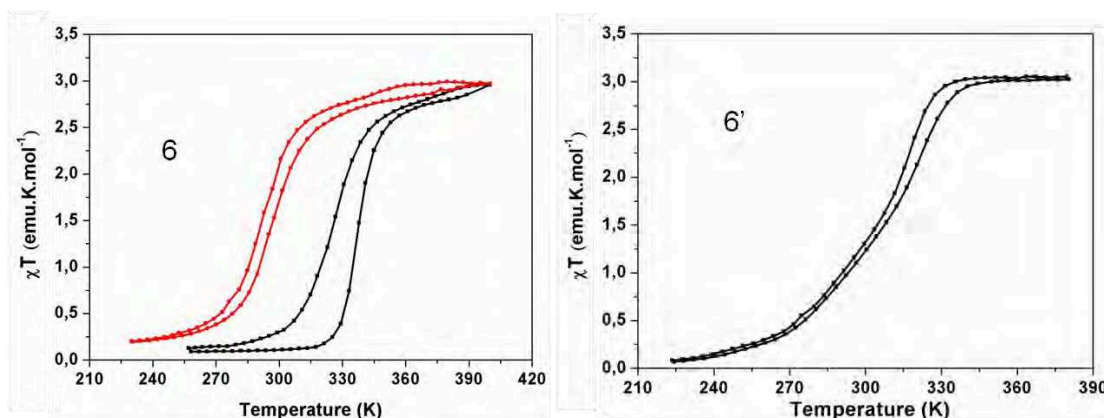
Figure 3.20: Magnetic measurements for samples **6** and **6'** (mixture of form A and B). Hydrated sample in red and dehydrated sample in black.

### 3.2.3.2 Optical Reflectivity

Due to the drastic change of color accompanying the spin transition from purple to colorless, it is of obvious interest to study also the optical behavior of the compounds in the visible range. Measurements were realized on scratched powder samples forming thin film on glass substrates. Figure 3.21 shows the thermal variation of the optical reflectance at 540 nm for each sample (see table 3.6 for detailed transition temperature). All samples were cycled between 200 and 450 K after a preliminary thermal treatment for the dehydration. Similar as the magnetic measurements, samples **1-4** and **3'** present close properties. The transition temperatures are found as $T_{1/2\ (\downarrow)} \approx 348$ K and $T_{1/2\ (\uparrow)} \approx 397$ K for sample **1** while a narrow hysteresis is observed for longer **2-4** and **3'** rods. For samples **5** and **7** the hysteresis loop is centered below room temperature ($T_{1/2\ (\downarrow)} \approx 265$ K and $T_{1/2\ (\uparrow)} \approx 275$ K) and ($T_{1/2\ (\downarrow)} \approx 265$ K and $T_{1/2\ (\uparrow)} \approx 276$ K), respectively. The physical properties of sample **6** (and also sample **6'**) exhibit intermediate transition temperatures when compared to those measured for samples **1** and **5** in accordance with the magnetic measurements.
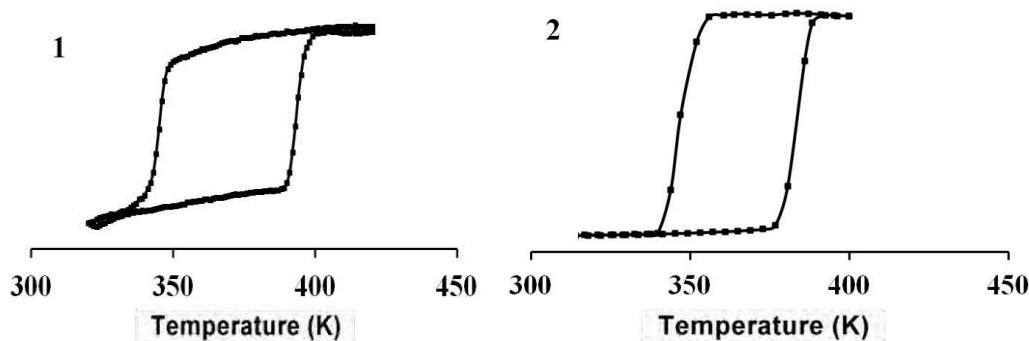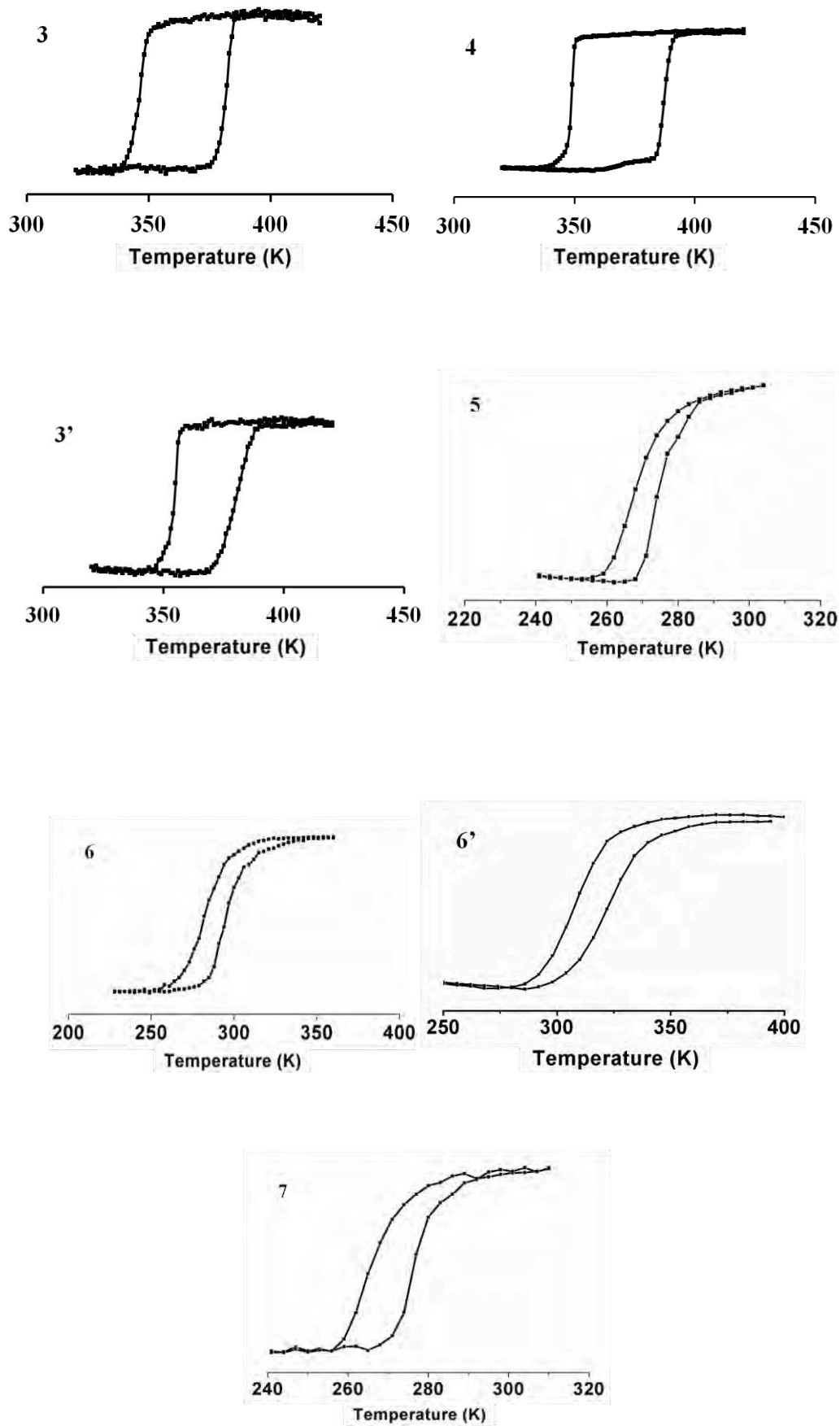
Figure 3.21: Optical reflectivity measurements of samples **1-7** (dehydrated sample).

| Sample | 1 | 2 | 3 | 4 | 3' | 5 | 6 | 6' | 7 |
|---|---|---|---|---|---|---|---|---|---|
| HBF$_4$ (wt%) | 0.1 | 0.5 | 2 | 3 | 2 | 4 | 5 | 5 | 2 |
| Transition temperature (K) | 348/397 | 348/380 | 348/379 | 350/382 | 352/378 | 265/275 | 278/292 | 310/326 | 265/276 |
| Form | A | A | A | A | A | B | mixture | mixture | B |

Table 3.6: Spin transition temperatures measured by optical reflectance for each sample (desolvated sample)

### 3.2.3.3 Differential Scanning Calorimetry

The calorimetric data (see figure 3.22) was recorded in the heating and cooling modes at 5 K/min in order to evaluate the enthalpy ($\Delta$H) and entropy ($\Delta$S) variations associated with the spin transitions of selected dehydrated samples (which were obtained by preliminary heating at 420 K).
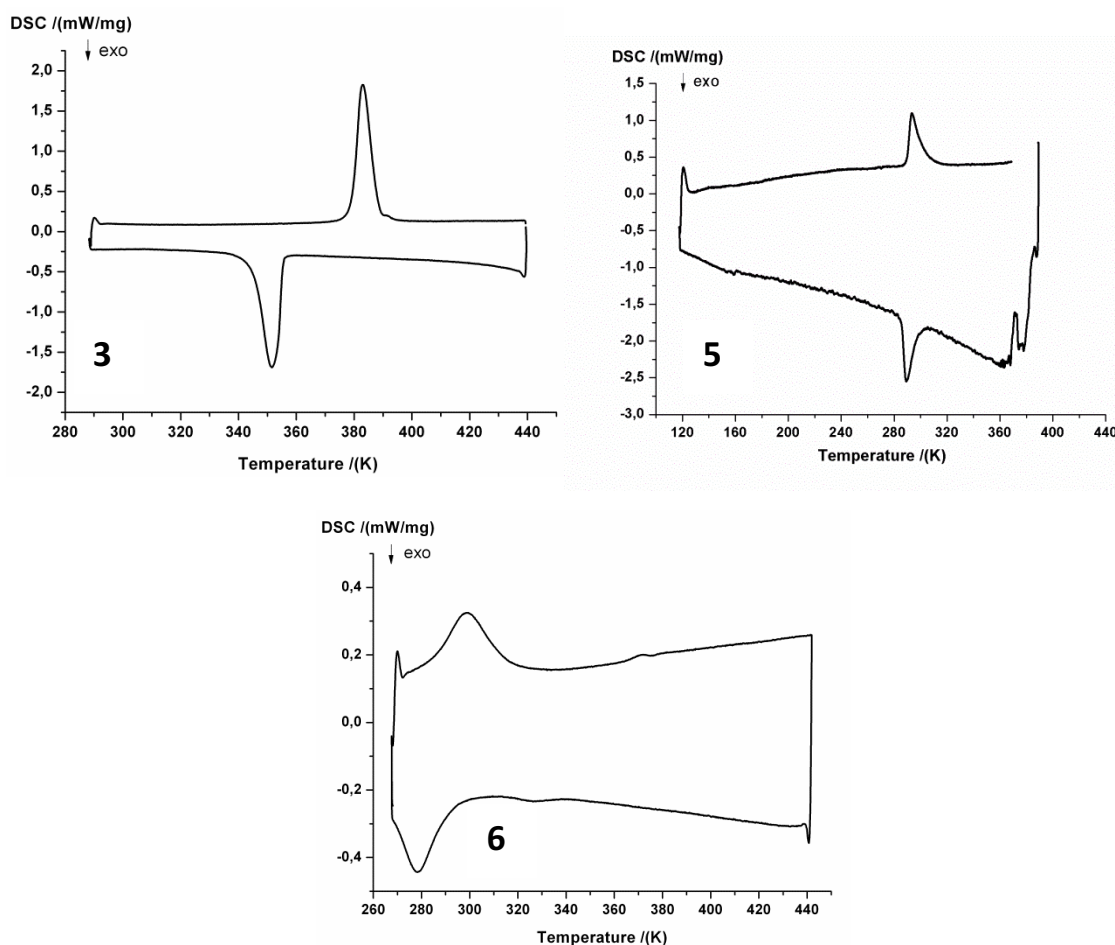


Figure 3.22: DSC measurements for sample **3**, **5** and **6** (dehydrated samples).

For the pure sample $[Fe(Htrz)_2(trz)](BF_4)$ (**3**), the DSC curve shows singularities at $T_{1/2 (\downarrow)}$ = 351 and $T_{1/2 (\uparrow)}$ = 383 K for the cooling and heating modes, respectively, while for the pure sample $[Fe(Htrz)_3](BF_4)_2 \cdot 3H_2O$ (**5**), these singularities appear at $T_{1/2 (\downarrow)}$ = 289 and $T_{1/2 (\uparrow)}$ = 293. In comparison with the magnetic measurements, the slight deviation of the transition temperature could be associated to the difference of the heating and cooling rates. The estimated ΔH and ΔS variations measured in the dehydrated forms are 20 and 16 kJ/mol and 56 and 61 J/K•mol for samples **3** and **5**, respectively. These values are common for iron(II) spin crossover compounds.

## 3.2.3.4 $^{57}$Fe Mössbauer Measurements

We have also recorded the $^{57}$Fe Mössbauer spectrum for samples **3**, **5** and **6** at 293 K (figure 3.23-3.25). As expected for sample **3**, the spectrum consists of one doublet with an isomeric shift of 0.418(6) mms$^{-1}$ and a quadrupole splitting of 0.286(9) mms$^{-1}$ attributed to the LS state, no residual HS state is observed. Inversely, two doublets with an isomeric shift of 0.41(1) (1.036(8)) mms$^{-1}$ and a quadrupole splitting of 0.20(2) (2.70(2)) mms$^{-1}$ attributed to the LS (HS) state are observed for sample **5**, in agreement with the magnetic data of its hydrated form. Indeed, the χT value of *ca.* 1.5 cm$^3$·K·mol$^{-1}$ measured at room temperature corresponds to the mixture of high spin and low spin state. Moreover, although sample **6** corresponds to a mixture of complexes only one LS doublet was observed (see table 3.7).
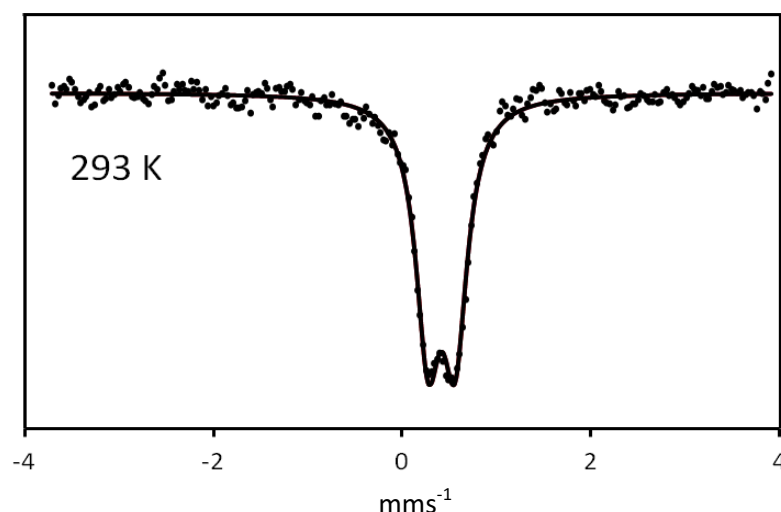


Figure 3.23: Mössbauer spectrum (dots) and fit (line) of sample **3**
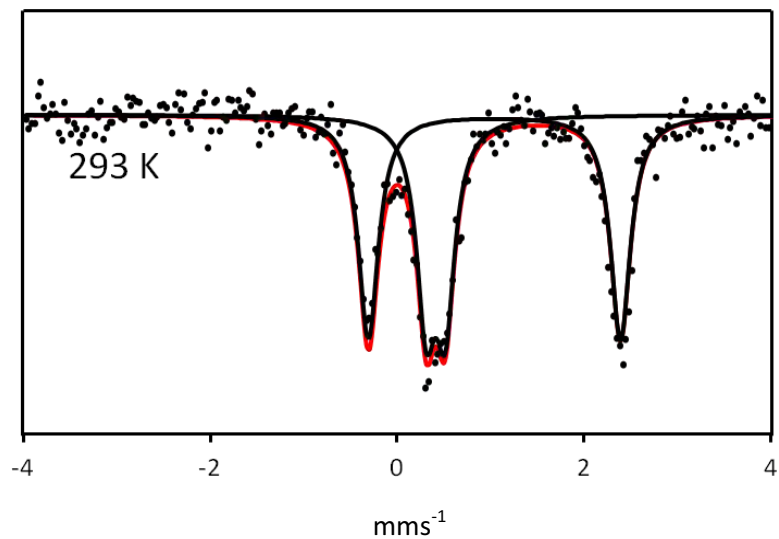
Figure 3.24: Mössbauer spectrum (dots) and fit (line) of sample **5**
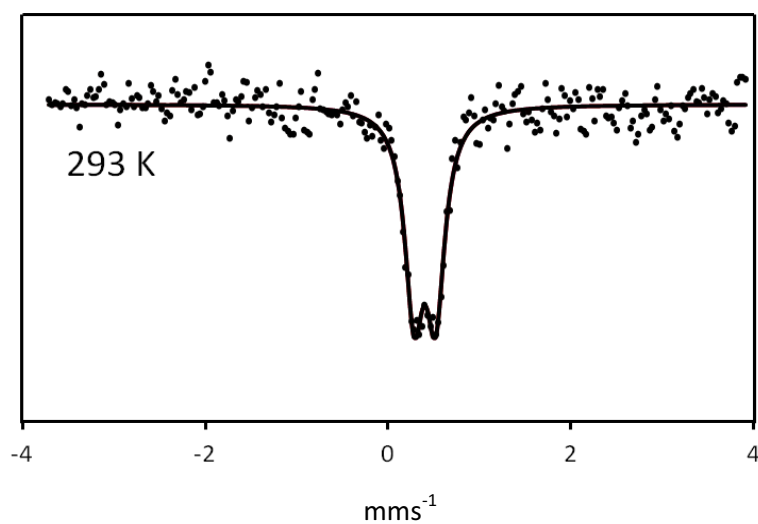


Figure 3.25: Mössbauer spectrum (dots) and fit (line) of sample **6**

| 293K | LS state | | | HS state | | | LS fraction |
|---|---|---|---|---|---|---|---|
| | $\delta$ | $\Delta E_Q$ | $\Gamma/2$ | $\delta$ | $\Delta E_Q$ | $\Gamma/2$ | |
| Sample **3** | 0.418(6) | 0.286(9) | 0.158(9) | | | | 100% |
| Sample **5** | 0.41(1) | 0.20(2) | 0.12(1) | 1.036(8) | 2.70(2) | 0.13(1) | 42% |
| Sample **6** | 0.402(1) | 0.24(2) | 0.13(2) | | | | 100% |

Table 3.7: Mössbauer hyperfine parameters

### 3.2.4 Discussion

Using simple homogeneous acid media it was possible to synthesize various size rod-shaped surfactant/polymer-free Fe-Triazole complex particles with different chemical compositions. All the physical characterizations revealed a correlation between the size of the particles and their composition, the smaller rods correspond to the $[Fe(Htrz)_2(trz)](BF_4)$ complex with a spin transition localized at high temperature ($T_{1/2\ (\downarrow)} \approx 352$ K and $T_{1/2\ (\uparrow)} \approx 397$ K), while the longer ones correspond to the fully protonated $[Fe(Htrz)_3](BF_4)_2 \cdot 3H_2O$ derivative with a spin transition just below room temperature ($T_{1/2\ (\downarrow)} \approx 265$ K and $T_{1/2\ (\uparrow)} \approx 278$ K). In fact, high concentrations of acid which preclude the deprotonation of the Htrz ligand associated with a slow evaporation speed of the complex solution lead to the slow stabilization of the $[Fe(Htrz)_3](BF_4)_2 \cdot 3H_2O$ long rod-shaped particles while $[Fe(Htrz)_2(trz)](BF_4)$ short rod-shaped particles are obtained for low acid concentrations. **Thus, we have demonstrated that not only the size but also the morphology of the objects can be tuned for a considered material.** These findings could be really useful for specific organization of these bistable objects using soft lithographic techniques, capillary assembly technique or dielectrophoresis in the competition for the understanding of the spatio-temporal behaviors and also for the transport measurements and switching of individual objects which constitute one of the foremost paradigms in molecular electronics.

### 3.2.5 Diluted $[Fe_{1-x}Zn_x(Htrz)_2(trz)](BF_4)$ Complexes

### 3.2.5.1 Synthesis of Metal Diluted Particles

The synthesis of the metal diluted particles was carried out under the same condition as sample **3**, so with 2 wt% $HBF_4$ (see chapter 3.2.1), but using a mixture of $Fe(BF_4)_2 \cdot 6H_2O$ and $Zn(BF_4)_2 \cdot 6H_2O$ salts. The molar ratio of $Fe(BF_4)_2 \cdot 6H_2O$ / $Zn(BF_4)_2 \cdot 6H_2O$ for sample **8** and **9** was 0.9 / 0.1 and 0.8 / 0.2, respectively.

### 3.2.5.2 Characterization of Diluted Metal Particles

#### 3.2.5.2.1 TEM and EDX Measurements

Representative TEM images of samples **8** and **9** are shown in figure 3.26. Each sample displays similar particle morphology forming micro-rods with an average length of ca. 1.5 µm

and a diameter of 200-300 nm similar to sample **3**. (see Annex 2 for complementary TEM images)
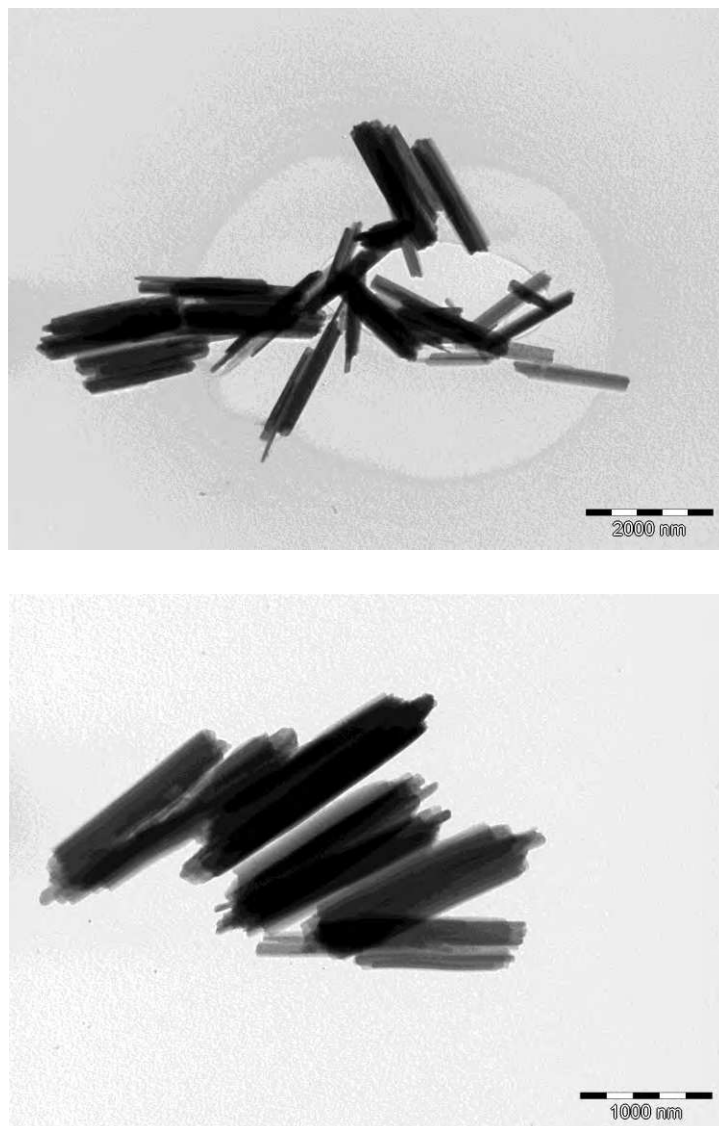


Figure 3.26: TEM images of samples **8** (up) and **9** (bottom)

In conjunction with the TEM observations, EDX measurements were also carried out in order to evaluate the Fe/Zn ratio in the samples and also to investigate the spatial distribution of the metal ions. The analysis results revealed 26 at.% of Zn in sample **8** and 43 at.% of Zn in sample **9**, which are identified therefore as $[Fe_{0.74}Zn_{0.26}(Htrz)_2(trz)](BF_4)$ and $[Fe_{0.57}Zn_{0.43}(Htrz)_2(trz)](BF_4)$, respectively. This means that the relative proportion of Zn versus Fe ions in the micro-rods is significantly higher than that introduced initially into the reaction mixture. On the other hand, the TEM-EDX analysis revealed also a homogenous distribution of the Zn and Fe ions within the volume of the micro-rods and no sign of ion segregation was observed (see figure 3.27).
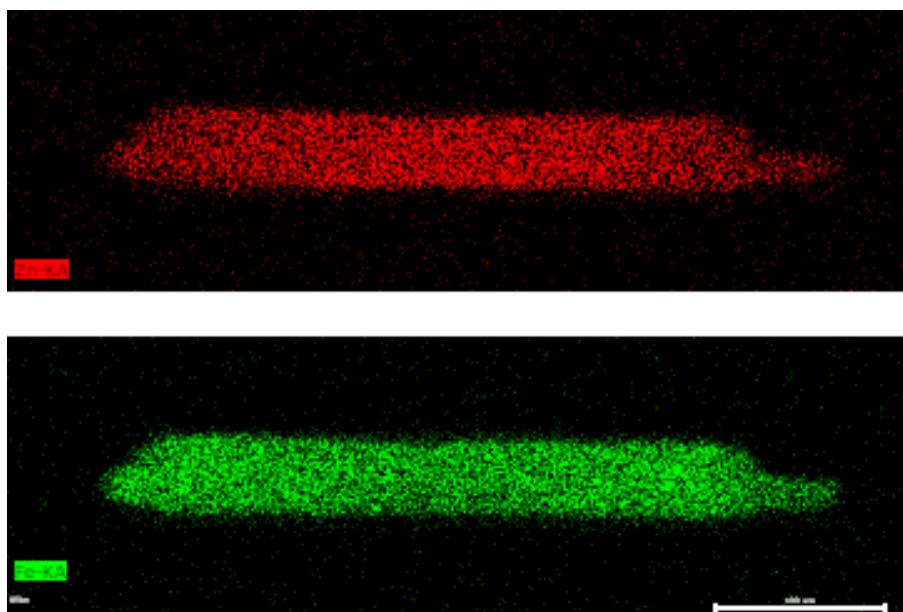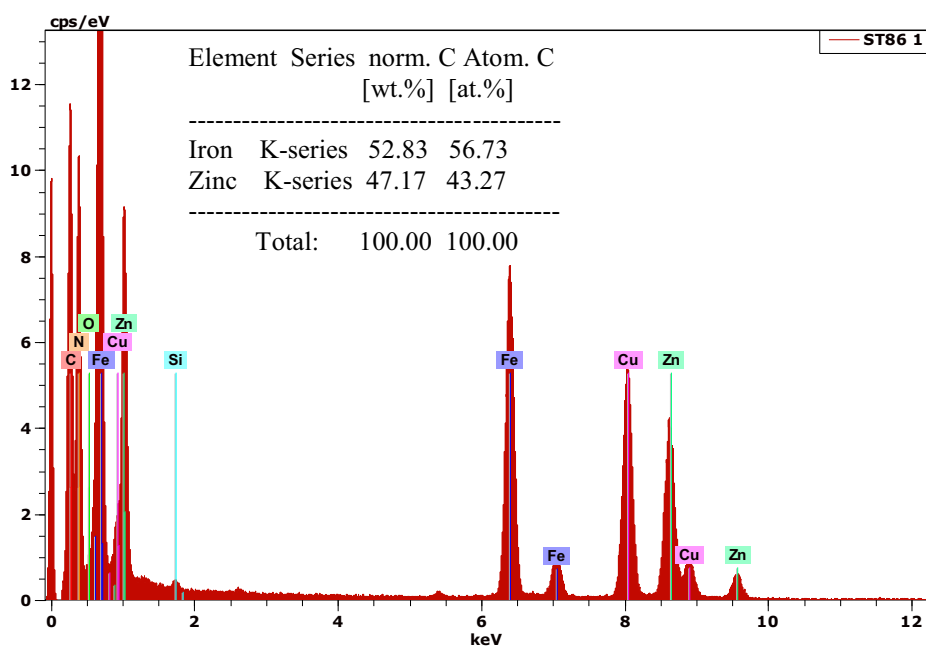
Figure 3.27: EDX spectra and Fe/Zn ratio for sample **9** (up); the distribution of metal ions in a representative rod (red/green dots stand for Zn/Fe atoms) (bottom).

### 3.2.5.2.2 XRD Measurements

The powder x-ray diffraction spectra (see figure 3.28) show a globally similar pattern for each compound, with some differences for sample **9**. For samples **3** and **8** the main diffraction peaks are grouped for values of $2\theta$ at 10 and 11 degrees, 18 and 19 degrees and 24, 25 and 26 degrees. The additional diffraction peaks visible in the spectra of sample **9** are consistent with a small HS fraction at room temperature in this compound (*vide infra*). Indeed, the LS to HS

transition involves a shift of the diffraction peaks to lower $2\theta$ angles due to the lattice expansion.[170] In particular the downshifts of the Bragg peaks around 24° - 26° upon the SCO is rather important, which are clearly observed in sample **9** as shoulders at lower angles. Overall these PXRD results can be interpreted in agreement with the EDX analysis indicating that the Zn ions do not form important segregation in our compounds and instead they replace some of the Fe centres and the compounds are closely isostructural. At this point it may be worth noting also that a recent refinement of the powder X-ray diffractograms of $[Fe(Htrz)_2(trz)](BF_4)$ in the two spin states[223] led to the same orthorhombic space group *Pnma*, i.e. the spin transition is isostructural in this compound.
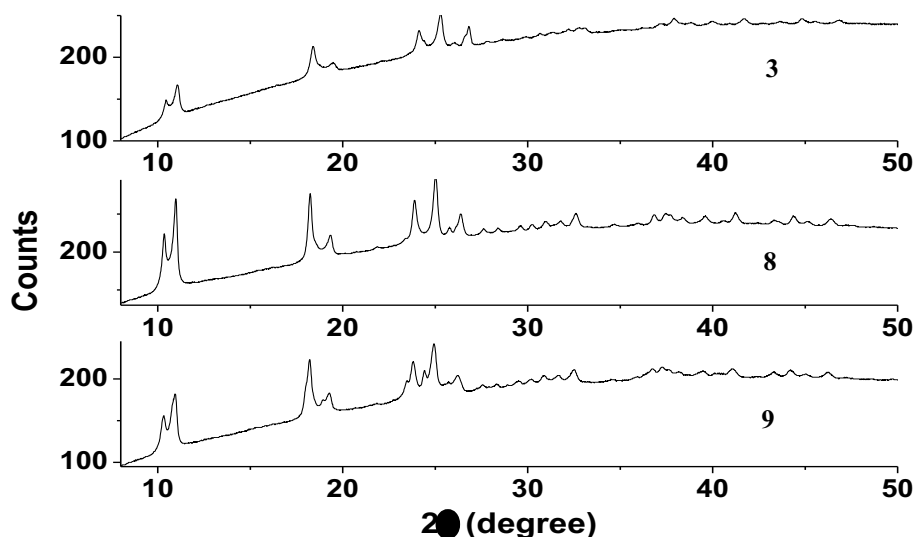


Figure 3.28: XRD diffractogram for sample **3**, **8** and **9**.

### 3.2.5.2.3 Vibrational Spectroscopy

Vibrational spectroscopy is also a useful technique to analyze the impact of metal dilution on the structure of our compounds. In addition, variable-temperature vibrational spectra provide a straightforward way to observe the spin transition. FTIR and Raman spectra of the three compounds are presented in the figure 3.29-3.30.

From the IR spectra of samples **3**, **8** and **9**, the particular vibrational modes at 1515 and 1499 cm$^{-1}$ can be attributed to the stretching deformation of the protonated and unprotonated ligands, respectively. The same peaks appear in all compounds confirming that their structure is very similar.
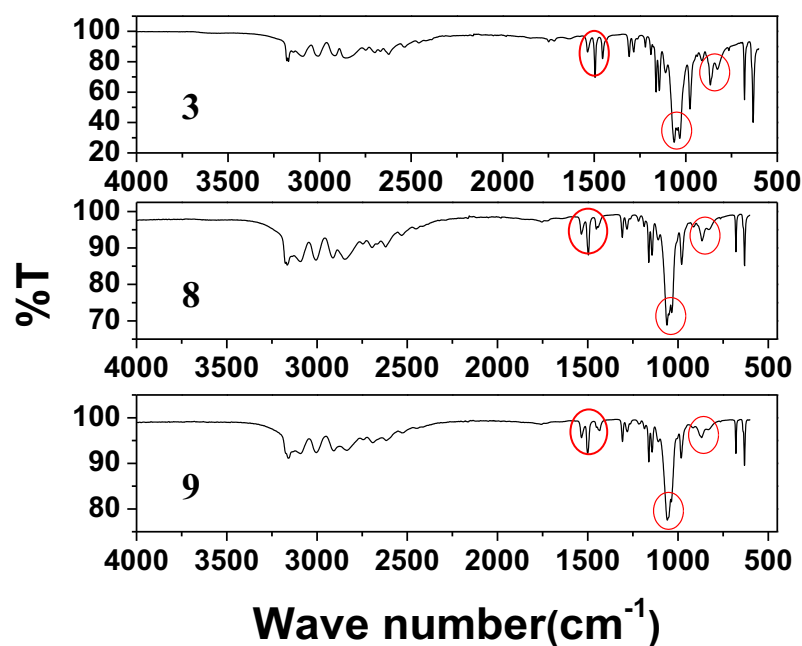
Figure 3.29: Room temperature FTIR spectra of samples **3**, **8** and **9**

However, in the LS state Raman spectra of the diluted compounds, we observe also additional peaks around 160 - 166 cm$^{-1}$ and a broadening of the peaks at 135 and 245 cm$^{-1}$ is also visible in both samples (sample **8** and sample **9**). These new frequencies should arise due to vibrational modes involving the displacements of Zn ions. As discussed previously[229] the Raman spectra of the compound [Fe(Htrz)$_2$(trz)](BF$_4$) exhibit very characteristic changes between 100 - 300 cm$^{-1}$ due to the spin transition. At 293 K (LS state) sample **3** displays intense Raman modes around 135, 197, 211, 285 and 299 cm$^{-1}$. When going to the HS state (413 K) one observes Raman peaks around 105, 136, 150 (shoulder), 180 and 190 cm$^{-1}$. These spectra are essentially the same.[229]
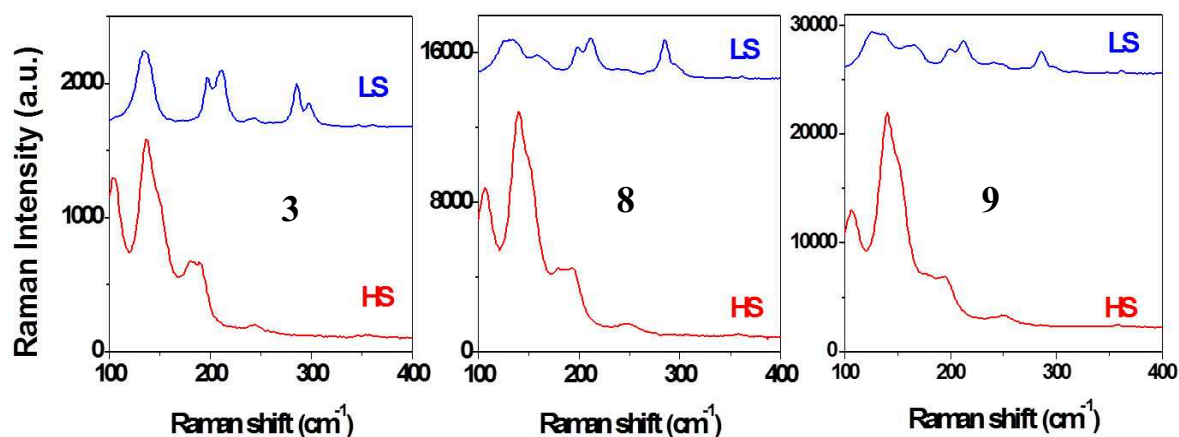


Figure 3.30: Low-frequency Raman spectra of samples **3**, **8** and **9**

129

### 3.2.5.3 Spin Crossover Properties of Diluted Metal Particles

**3.2.5.3.1 Optical Reflectivity**

The spin transition in these samples is visible through their optical properties since their color turns from violet to white upon heating. This bleaching of the $^1A \rightarrow {}^1T$ ligand-field absorption band (centered at ca. 545 nm) is completely reversible and provides thus a convenient way to follow the SCO phenomena in our samples. The thermal variation of the optical reflectance in the green spectral region is shown in figure 3.31 for each sample. As expected, the transition temperatures are shifted towards lower temperatures and the hysteresis width decreases for increasing Zn substitution.
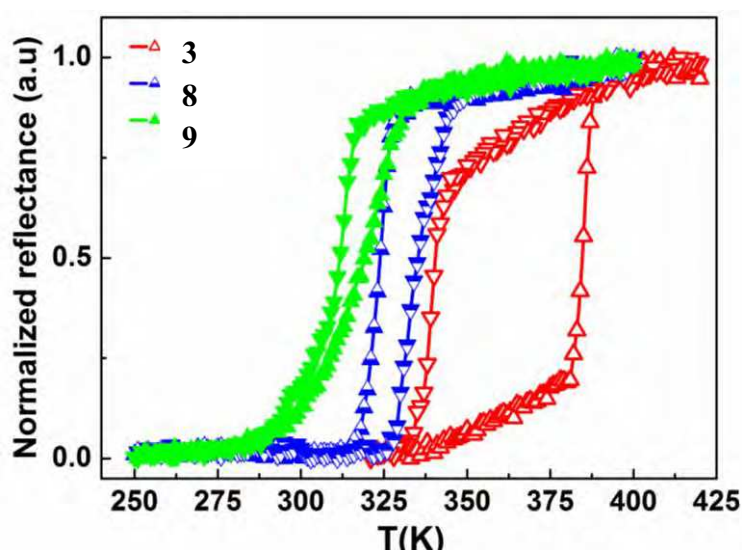
Figure 3.31: Optical reflectance spectra for samples **3**, **8** and **9**

This type of metal dilution effects is well-known and widely used by the spin crossover community to tune and investigate the spin transition properties. We have found a short report on the Zn dilution of small size nanoparticles of the same compound, wherein a similar – though somewhat less pronounced - shift of the spin transition was reported for 20% Zn doping.[154] The downshift of the spin transition upon Zn doping can be explained by the fact that the ionic radius of the $Zn^{2+}$ ion (96 pm) is much closer to the ionic radius of $Fe^{2+}$ ions in the HS state (92 pm) than in the LS state (75 pm), i.e. the LS lattice is destabilized due to the misfit of the Zn ions. On the other hand, the hysteresis in SCO compounds is known to occur due to the elastic interactions between the SCO centers. Since the Zn dilution leads to a decrease of the concentration of the SCO active iron ions, the cooperativity of the system

decreases, which is reflected by the shrinking of the hysteresis as well as by an increasingly gradual SCO.

### 3.2.5.3.1 Mössbauer Spectroscopy

Mössbauer spectroscopy was used to estimate the residual HS fraction in the samples. We have acquired $^{57}$Fe Mössbauer spectra at low temperatures (i.e. in the LS state). This spectrum is shown in figure 3.32 for sample **8** and **9** and the hyperfine parameters are collected in table 3.8 together with sample **3**. In each case the spectrum can be properly fitted by only one doublet, characteristic of the LS form of Fe(II). From these Mössbauer and Raman data we can thus conclude that the spin transition of the ferrous ions is complete in both the heating and cooling modes for each sample.
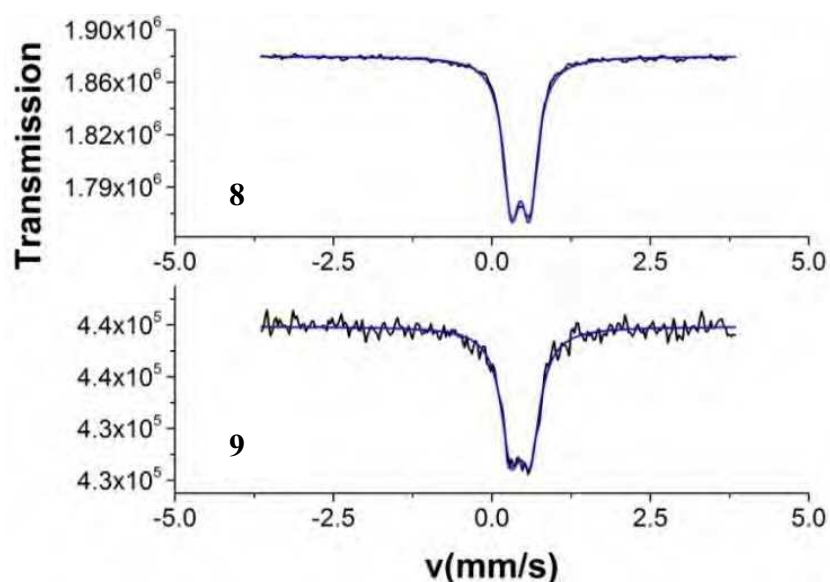


Figure 3.32: Mössbauer spectra (dots) and fit (line) at low temperatures of samples **8** and **9**

| sample | δ [mm/s] | $\Delta E_Q$ [mm/s] | Γ/2 [mm/s] |
|--------|----------|---------------------|------------|
| 3 | 0.412(1) | 0.270(1) | 0.161(1) |
| 8 | 0.451(2) | 0.289(3) | 0.155(3) |
| 9 | 0.45(1) | 0.31(2) | 0.19(2) |

Table 3.8: Spectrum analysis was performed by assuming a single low-spin ferrous species and Lorentzian line shapes. (δ -isomer shift vs. α-Fe; $\Delta E_Q$-quadrupole splitting; Γ/2-half width at half maximum.)

131

## 3.2.6 Electrical Properties of the $[Fe_{1-x}Zn_x(Htrz)](BF_4)$ Micro-Rods

The recent progress in the nanoscale synthesis and organization of SCO compounds has opened up novel perspectives for the study of charge transport properties of these materials at the nanoscale and even single molecule levels.[10-12,231] Indeed, a number of recent theoretical[162,232] and experimental[127,131,163-165,168,170,228,233-238] achievements with respect to the possible interplay between SCO and conductivity properties gives hope that in the near future SCO complexes might be integrated in functional nanoelectronic devices.

The charge transport properties of the SCO compound $[Fe(Htrz)_2(trz)](BF_4)$ were investigated and a strong dependence of the DC[170] and AC[233] conductivities on the spin state of iron(II) ions was revealed. The LS ($^1A_{1g}$) state was found systematically more conductive than the HS ($^5T_{2g}$) state in samples with different morphologies (nanoparticles and microrods) and sizes ranging from 15 nm to several μm. In addition the charge carrier relaxation frequencies displayed also a significant decrease when going from the LS to the HS state.[170] We tentatively ascribed these observations to a conduction process *via* polaron hopping. In the frame of this model the conductivity would rise upon the HS to LS switching due (chiefly) to an increase of the hopping frequency. This latter can be linked to the spin-state of the system through the variation of the phonon frequencies and/or that of the activation barriers for the hopping.[233] While their interpretation remains rather challenging at this stage, the accumulated experimental observations have already allowed several groups to elaborate simple nano-electronic devices based on this compound - providing appealing perspectives for nanoscale switching and memory applications.[163,168,228] It is worth noting also that interesting size effects can be anticipated when going from the activated hopping to the tunneling regime because the spin transition was reported to have an opposite effect on the charge transport in these two limiting cases.

The present work was motivated by the weak understanding of the physical phenomena which underlie the electrical conduction and its spin-state dependence in the title compound. The aim of zinc dilution here is to break the supposed chain of conduction along the chain structure by exploiting the fact that the 3d orbitals of Zn are fully occupied. On the other hand, the ionic radius of Zn(II) is close to the ionic radius of HS Fe(II) allowing for an isostructural substitution of the ferrous ions. We have studied the charge transport properties of three different powders (*ca.* 2 μm rods) with formulae $[Fe_{1-x}Zn_x(Htrz)_2(trz)](BF_4)$, where x = 0, 0.26 or 0.43. Besides the electrical properties, each powder was carefully characterized for its morphology, crystal structure and SCO properties as well.

Broadband dielectric spectroscopy provides access to a wide range of electrical properties. In particular, the complex conductivity $\sigma*(\omega, T)$ as their frequency and temperature dependences gives important information about the charge transport mechanism. The frequency dependence of the real part, $\sigma'(\omega)$, of $\sigma*(\omega)$ in both cooling and heating branches is reported in figure 3.33 for each compound (**3**, **8** and **9**) at different temperatures.
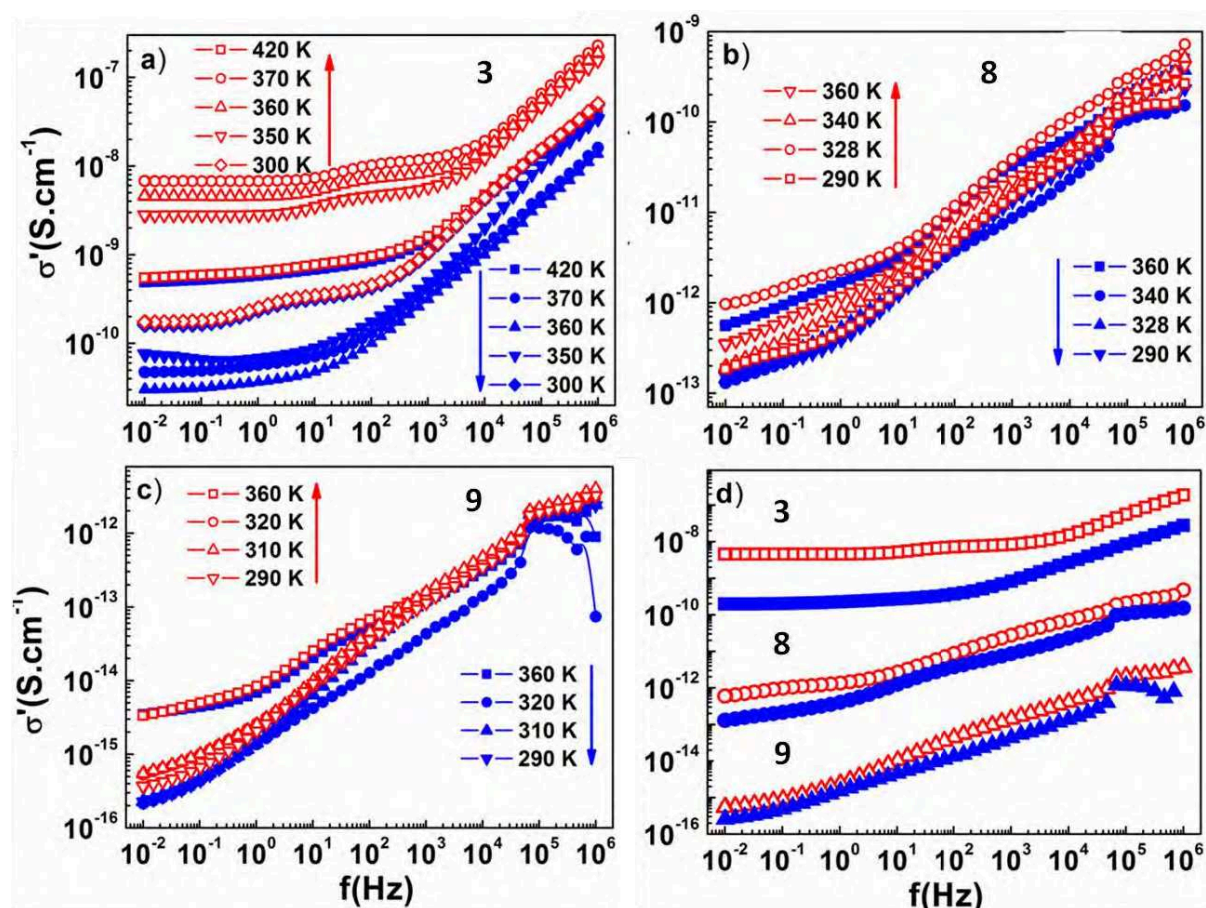


Figure 3.33: The frequency dependence of the real part, $\sigma'(\omega)$, of $\sigma*(\omega)$ in both cooling and heating branches for each compound at different temperatures

The shape of the dispersion curves and sample conductivity are strongly dependent on spin state and Zn dilution as shown in figure 3.33d. The Zn substitution reduces, in LS state, the conductivity by 4 and 7 orders of magnitude for **8** and **9** respectively, indicating the insulating nature of **8** and **9** samples. **For pure and diluted SCO the electrical conductivity of the LS state is higher than the HS state, but the conductivity differential is strongly reduced by Zn substitution.** For **3** the frequency behavior of the conductivity is strongly dependent on the spin-state and temperature (figure 3.33a). From the figure, $\sigma'(\omega)$ shows, at all temperatures, a typical low frequency plateau, characteristic to non-localized or long-range charge carrier mobility at lower frequencies and above the crossover frequency, $\omega_c$, it

increases with increasing frequency obeying a power law. Then, the ac conductivity spectra follow the Jonscher's power law[239]:

$$\sigma'(\omega) = \sigma_{DC} + A\,\omega^n = \sigma_{DC}\left[1 + \left(\frac{\omega}{\omega_C}\right)^n\right]$$

(3.1)

where $\sigma_{DC}$ is the DC conductivity, $\omega_c$ is the crossover frequency from DC to dispersive region representing the hopping frequency of charge carriers, $A$ is the temperature and frequency dependent parameter and $n$ is an exponent dependent on both frequency and temperature in the range $0 < n \leq 1$. **This behavior is characteristic of the charge transport in disordered materials and interpreted by Jonscher as universal dynamic response (UDR).**
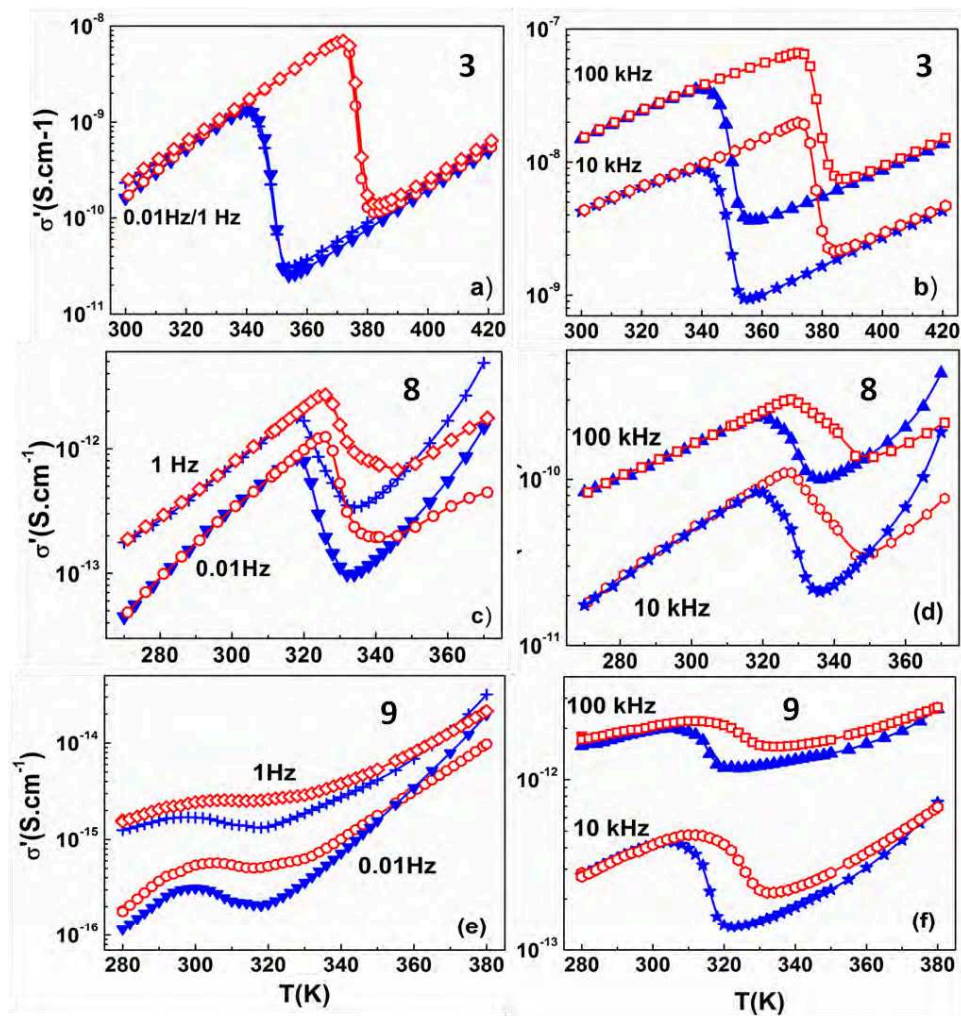


Figure 3.34: The thermal dependence of the real part of conductivity at fixed frequencies

The conductivity $\sigma'$ of the samples at $10^{-2}$ Hz (DC regime) and at 293 K (LS state) is *ca.* $10^{-10}$ S.cm$^{-1}$ for **3**, $10^{-13}$ S.cm$^{-1}$ for **8** and $10^{-16}$ S.cm$^{-1}$ for **9**. This huge decrease in conductivity upon Zn substitution is observed in the whole investigated frequency and temperature range, i.e., in both spin states and conductivity regimes (AC and DC). For **8** and **9** the low frequency plateau frequency is strongly reduced and the dispersion of the ac conductivity shifts to the lower frequency side i.e., $\omega_c$ decreases (figure 3.33b, 3.33c), indicating a more insulating character of the diluted samples. The Zn substitution reduces the discrepancy in the frequency behavior of conductivity between LS and HS states as seen in figure 3.33d. The experimental conductivity $\sigma'(\omega)$ for all the samples were fitted using Eq (3.1) and $\sigma_{DC}$, $\omega_c$ and $n$ were extracted from non-linear fitting procedure for each sample.

The thermal dependence of the real part of conductivity at fixed frequencies (figure 3.34) shows a hysteresis loop where the width is strongly dependent of the Zn dilution level. Upon increasing Zn fraction, the conductivity hysteresis loops become narrower and the spin transition temperatures are in good agreement with the optical reflectivity measurements. It can be noted that the hysteresis width is frequency independent for the undiluted sample **3**. With Zn dilution, the shape and width of the hysteresis loop are dependent of the applied frequency arising from the insulating nature of samples **8-9**. At the LS-HS transition the conductivity drops by two orders of magnitude for **3** (one order and less for **8** and **9** respectively), confirming that in SCO triazole complexes the LS state is more conductive than HS state. For sample **3**, the pure complex is either in the LS state (heating branch) or in the HS state (cooling branch) at 365 K (330 and 320 K for **8** and **9**). In each spin state, the conductivity increases with increasing temperature showing the semiconductor behavior of the SCO complex.

The dispersion behavior of the electrical conductivity in the frequency domain can also be interpreted in terms of conductivity relaxation time using the electric modulus, $M^* = 1/\varepsilon^*$, representation. In the $M^*$ representation, a relaxation peak is observed for the conductivity process in the frequency spectra of the imaginary part $M''$ of the complex electric modulus $M^*$. The frequency spectrum of the electrical modulus can be related to the mobility of the charge carriers. In particular, the broad relaxation peak, which is often seen in the $M''$ vs $\omega$ curves, represents the separation between long-range (or nonlocalized) and short-range (localized) conduction. Figure 3.35 shows the frequency response of the electric modulus at selected temperatures. It is important to notice that the spectra for each sample clearly present two overlapping peaks which we have fitted using the Havriliak−Negami (HN) empirical equation:

$$M* = M' + i\,M'' = M_\infty - \frac{(M_\infty - M_0)}{[1 + (i\omega\tau_M^*)^\alpha]^\beta}$$

(3.2)

where $M_\infty = 1/\varepsilon_\infty$ and $M_0 = 1/\varepsilon_0$ are the limiting low and high frequency modulus, $\tau_M$ is a mean characteristic relaxation time related to the peak frequency $\omega_M$ and $\alpha$ and $\beta$ are fractional shape parameters $(0 < \alpha, \beta < 1)$. The inverse of the maximum peak frequency of the $M''$ spectra represents the time scale of the transition from the long range to short mobility and is defined as the characteristic conduction relaxation time $(\tau_M = 1/\omega_M)$. The temperature dependence of the relaxation peak frequencies is shown in Figure 10. For each sample, we can observe the hysteresis associated with the spin transition due to a decrease of $\omega_M$ when going from the LS to the HS state, even if this variation is attenuated for increasing Zn doping level. One can note also that the relaxation frequencies for the same temperature and same spin state decrease drastically when Zn impurities are inserted. In the LS state the values of $\omega_M 1$ and $\omega_M 1$ are $5 \times 10^2$ s$^{-1}$ and $4 \times 10^4$ s$^{-1}$ for sample **3**, $4.5 \times 10^{-1}$ s$^{-1}$ and $2.7 \times 10^1$ s$^{-1}$ for sample **8**, and $8 \times 10^{-2}$ s$^{-1}$ and $2.3 \times 10^1$ s$^{-1}$ for sample **9**.
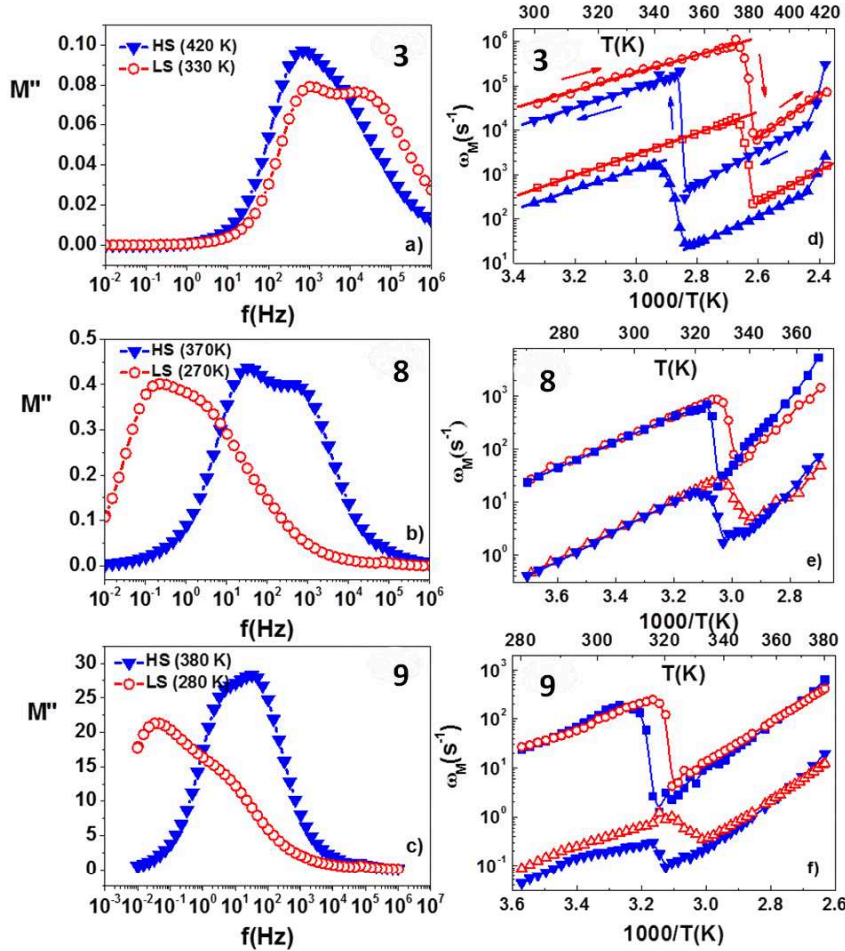


Figure 3.35: the frequency response of the electric modulus at selected temperatures.

So, we have demonstrated that spin crossover phenomena can be detected through the temperature dependence of ac conductivity and dielectric loss, and we show that virtually all material-dependent electrical parameters, such as electrical conductivity, electric modulus, cut off frequency, display a spin state dependence. In particular, we have shown that the spin transition from the LS to the HS state led to a systematic decrease of the electrical conductivities. All these results seem to confirm the conduction process *via* polaron hopping but taking into account the close structural and morphological similarity of the pure and Zn-diluted samples, these results indicate that the ferrous ions with open $3d^6$ electronic shell directly participate in the charge transport process, in contrast to the Zn(II) ions, which have a closed $3d^{10}$ shell.

# 3.3 CF$_3$SO$_3$ Derivatives of the Fe-Triazole Family of Compounds

Using similar homogeneous acid condition developed for the BF$_4$ derivatives, triflate analogues were also synthesized using triflic acid. It is worth to notice that concerning triflate derivatives only the bulk of the [Fe(Htrz)(trz)](CF$_3$SO$_3$) compound was already reported in the literature among the large family of Fe-triazole compounds.[240] We tried to synthesize the bulk of the [Fe(Htrz)$_3$](CF$_3$SO$_3$)$_2$ compounds modifying the nature of solvent like it was made for the [Fe(Htrz)$_3$](BF$_4$)$_2$ complex but without success.

### 3.3.1 Synthesis of Different-Size Particles

Samples **11** and **12** were prepared by rapidly mixing two aqueous solutions of CF$_3$SO$_3$H (1 and 3 wt%, respectively) containing Fe(CF$_3$SO$_3$)$_2$ salt and the 1,2,4-triazole ligand (see table 3.9). The resulting limpid solutions were let for slow evaporation at room temperature. Following a specific period, the flocculates were centrifugated, and washed by distilled water and absolute ethanol and finally dried under vacuum. For an acid concentration higher than 3%, no precipitation was obtained using comparable slow evaporation speed as that used for the elaboration of sample **11** and **12**. A named bulk sample (sample **10**) obtained in an aqueous solution and using the same concentrations of reactants but in absence of acid was also synthesized as a reference sample.

| Sample | **10** | **11** | **12** |
|---|---|---|---|
| $CF_3SO_3H$ (wt%) | 0 | 1 | 3 |
| Time | 6 hours | 12 days | 2 months |
| Yield (%) | 20 | 15 | 80 |

Table 3.9 Synthetic conditions of samples **10-12** (see also Annex 1)

## 3.3.2 Morphology of the Particles

Particle sizes were determined by transmission electron microscopy (TEM) using a JEOL JEM-1011 (100 kV) and by scanning electron microscopy (SEM) using a JEOL FEG JSM 6700F. High-resolution imaging was performed on a JEOL JSM 2100F (200 kV) equipped also with a SDD Bruker EDX detector (resolution: 127 eV) for elemental analysis. TEM samples were prepared by placing on a carbon coated copper grid a drop (10 µl) of the particles suspended in ethanol. TEM, SEM and high resolution electronic microscopy coupled quantified energy dispersive X-ray spectroscopy analyses (HRTEM EDX) were used to determine the shape, the size and to confirm the composition of the particles. Figure 3.36 presents representative images for samples **10**-**13**. See also Annex 2 for complementary TEM images. All samples display morphology forming acicular rods. This particular shape was not observed for $BF_4$ derivatives and maybe related to the fine structural organization of the present complex. Moreover, such morphology although with a large size dispersity is also observed for the bulk sample and could be explained by the slow precipitation phase (6 h) which permits the objects to self-assemble in comparison with other bulk Fe-triazole compounds. Table 3.10 shows the mean size for the different samples. In comparison with $BF_4$ compounds, it was not possible to obtain clearly different-size particles for the two triflate derivatives modifying the acid concentration notably because of the restricted usable concentration range of the triflic acid.

| Sample | **10** | **11** | **12** |
|---|---|---|---|
| $CF_3SO_3H$ (wt%) | 0 | 1 | 3 |
| Nps size | 1.5±0.8 µm | 1.2±0.3 µm | 20±9 µm |

Table 3.10 Mean size of the rods in samples **10-12**
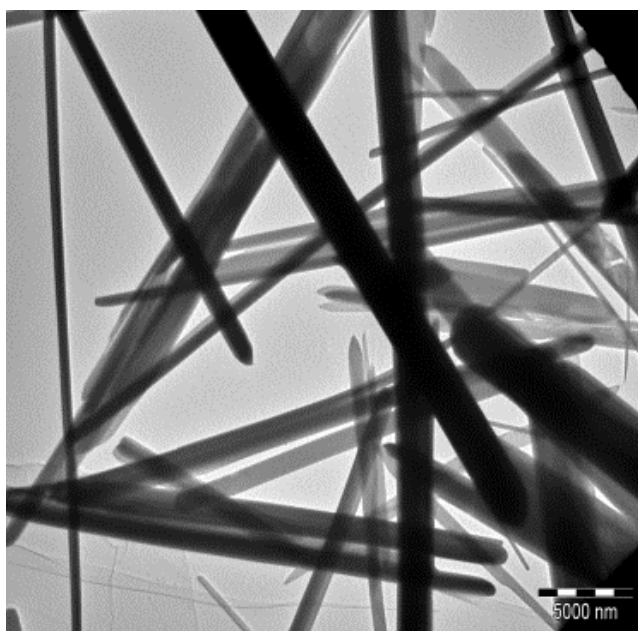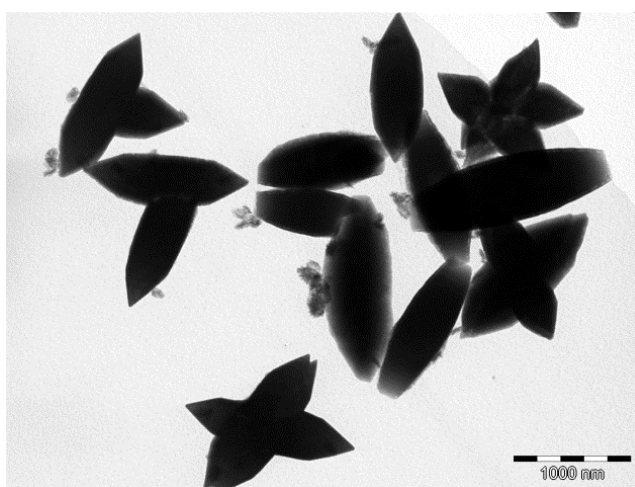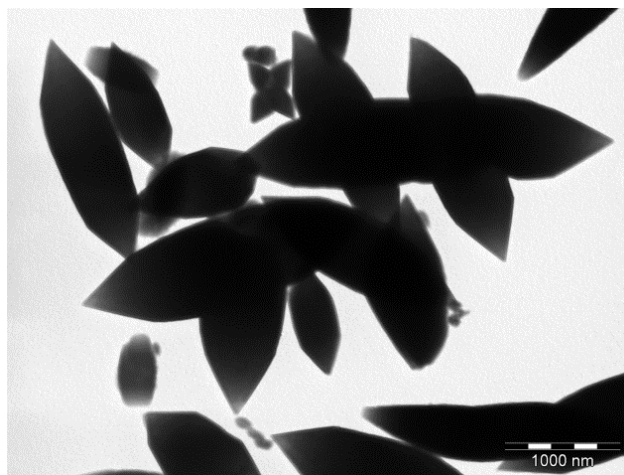
Figure 3.36: TEM images of samples **10** (up), **11** (middle) and **12** (bottom)

We also carried out Scanning Electronic Microscopy to confirm the structure of the samples. SEM sample was prepared by deposition of a thin platinum film on powder sample. A SEM JEOL JSM-6700F (30 kV) equipment with a field emission source (FESEM) was used. As shown in figure 3.37, micro particles forming sample **12** present well defined rod-shape with acicular morphology.
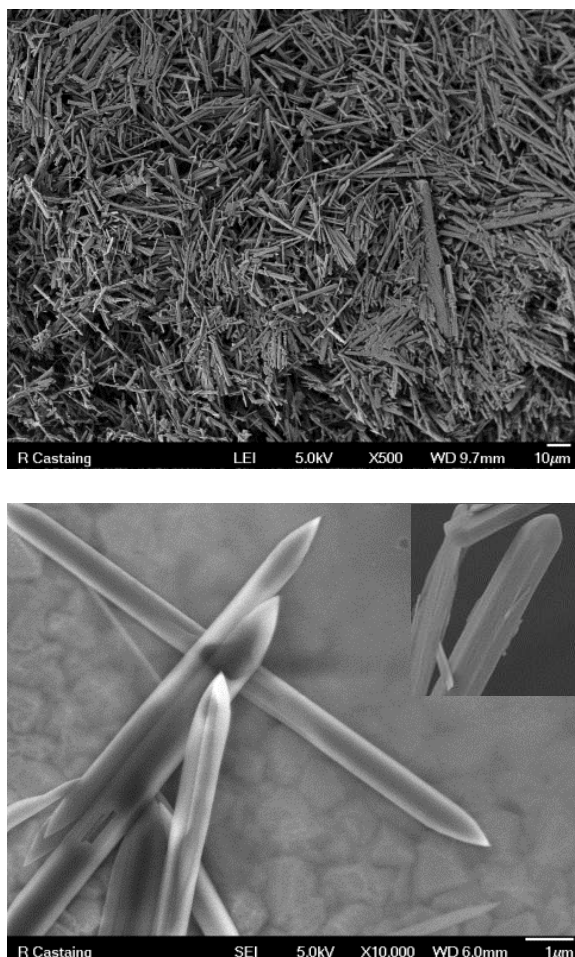


Figure 3.36: SEM images of sample **12**

HRTEM and Energy dispersive X-ray spectrometry (EDX) were also employed to characterize the composition of a single rod. Figure 3.38 shows HRTEM images of sample **12** and the corresponding EDX analysis carried out on the selected spherical area. From the EDX analysis, the presence of Fe, S and F atoms confirms well the composition of our aimed complex. Besides, because the F and Fe atoms appear at the same position at low energy, it is difficult to calculate the atom percentages. In addition, figure 3.39 shows also the compositional maps for Fe, F and S atoms corresponding to the full HRSTEM image and

indicate a homogeneous distribution of the Fe, F and S atoms in the particles confirming again the good composition of the sample.
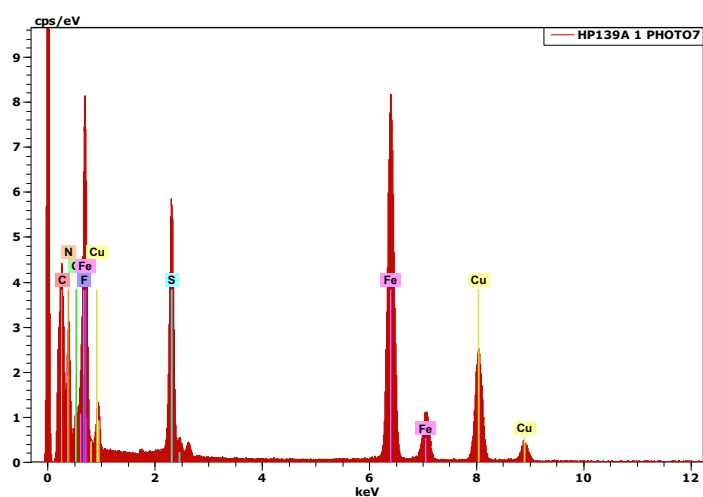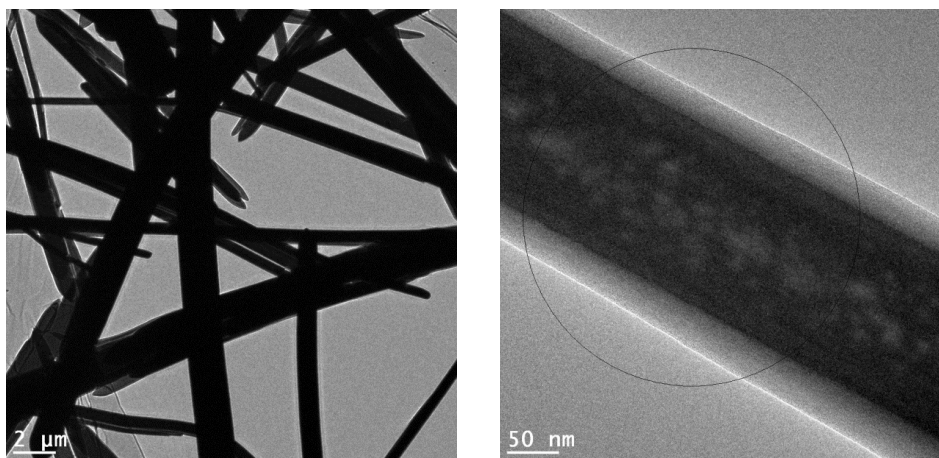


Figure 3.38: HRTEM and EDX analyses of sample **12**
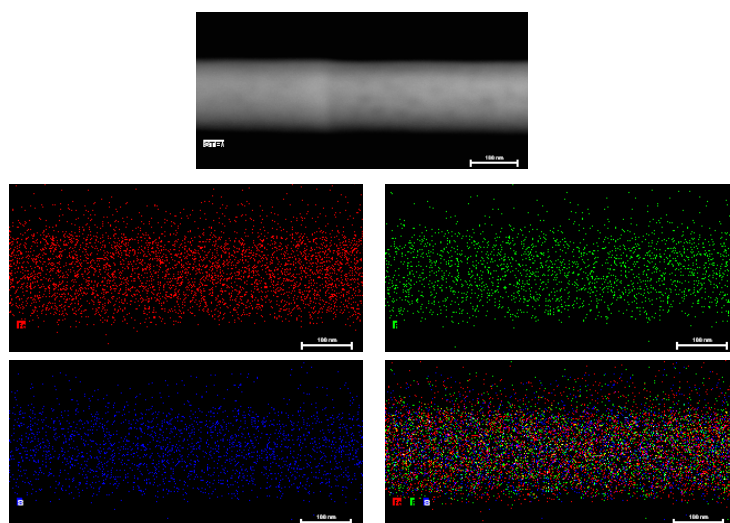


Figure 3.39: HRSTEM image and atom compositional maps (Fe: red, F: green, S: blue and mixture) of sample **12**

### 3.3.3 Composition of the Particles

FTIR spectra were recorded at room temperature with a Perkin Elmer Spectrum 100 spectrometer in ATR mode (resolution *ca.* 1 cm$^{-1}$) between 650 cm$^{-1}$ and 4000 cm$^{-1}$. Infrared spectra of samples **10-12** are shown in figure 3.40. Whatever the samples, the full spectra appear similar except the clear presence of water for sample **12 (**broad peak around 3600 cm$^{-1}$) and confirm the proposed formula. Nevertheless, from the zoomed spectrum of samples **10-12** (figure 3.41), it is clear in agreement with previous infrared spectra of the BF$_4$ derivatives that for samples **10** (bulk) and **11** (synthesized at low acid concentration), particular vibrational modes at 1515 and 1499 cm$^{-1}$ attributed to the stretching deformation of the protonated and unprotonated ligands, respectively, correspond to the [Fe(Htrz)$_2$(trz)](CF$_3$SO$_3$) composition. In contrast, IR spectrum of sample **12** obtained in presence of large acid concentration presents different features in this area with the disappearance of the vibrational mode at 1515 cm$^{-1}$. **In fact, like for the BF$_4$ derivatives the higher concentration of acid precludes the deprotonation of the Htrz ligand and the slow evaporation speed of the complex solution lead to the slow stabilization of the fully protonated ligand [Fe(Htrz)$_3$](CF$_3$SO$_3$)$_2$ derivative.** As reported by Sugiyarto and coworkers,[240] the [Fe(Htrz)$_2$(trz)](CF$_3$SO$_3$) complex presents spin crossover properties at low temperature (140 K), so we will focalize only on the spin crossover properties of the new [Fe(Htrz)$_3$](CF$_3$SO$_3$)$_2$ micro-rods (sample **12**).
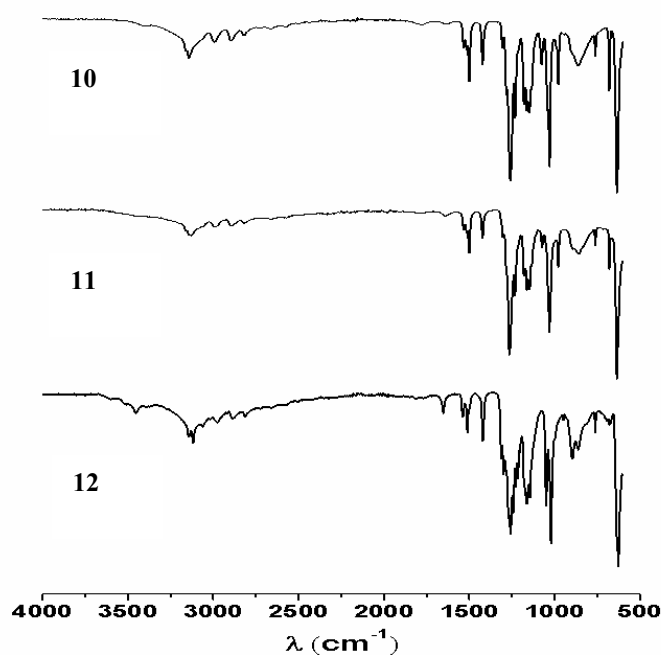


Figure 3.40**:** Infrared absorption spectra of samples **10**, **11** and **12** recorded at room temperature.
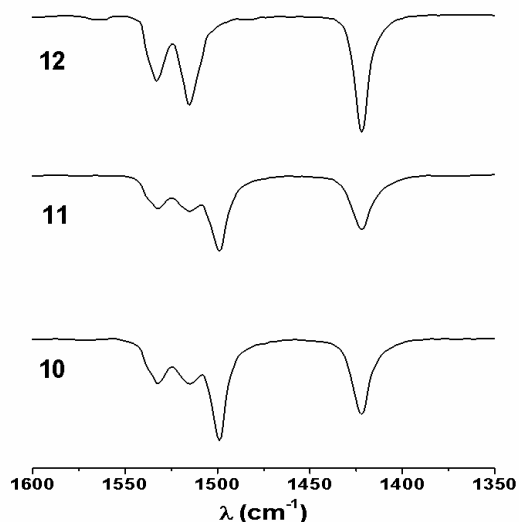
Figure 3.41: Selected infrared absorption zoom spectra of samples **10** (bottom) and **12** (up) recorded at room temperature.

## 3.3.4 Characterization of the [Fe(Htrz)₃](CF₃SO₃)₂ Micro-Rods

### 3.3.4.1 Thermogravimetric Analysis

The fine composition of the samples was obtained thanks to combined thermogravimetric analysis (TGA) and C, H, N elemental analysis (see table 3.11). TGA (figure 3.42) revealed the absence of water molecules for pure $[Fe(Htrz)_2(trz)](CF_3SO_3)$ sample **10**, while *ca.* 2 molecules of water per iron atom were identified for sample **12**. The weight loss for sample **12** is 4.1% (1.2·$H_2O$) for the first step (120°C) and 13 (280°C), 28 (400°C) and 37% (450°C) for the following steps (decomposition of the compound). For sample **10** the decomposition of the material starts at *ca.* 300°C. Thanks to the elemental analysis and the TGA measurement, the following formulae were obtained.
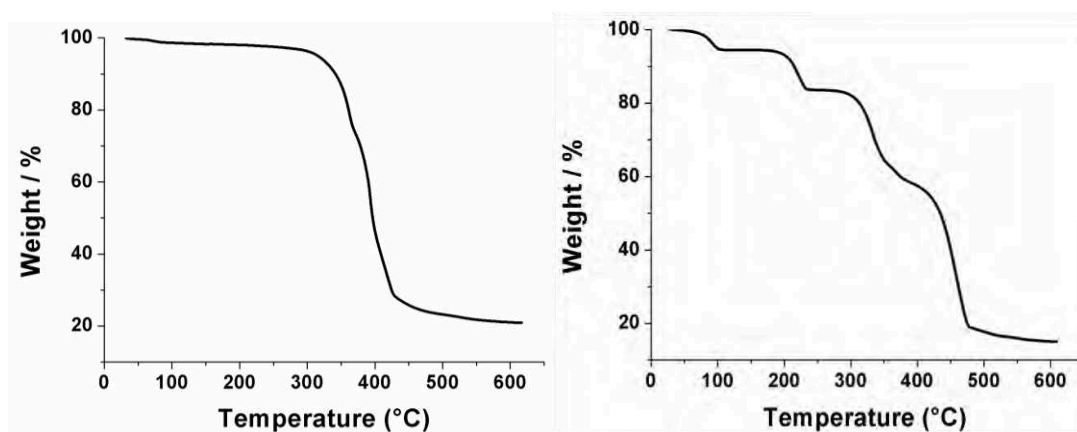


Figure 3.42: TGA analysis of sample **10** (left) and **12** (right)

| Compound | | C / % | H / % | N / % | Calculated Formula |
|---|---|---|---|---|---|
| **10** | exptl | 19.03 | 1.41 | 28.07 | [Fe(Htrz)$_2$(trz)](CF$_3$SO$_3$) |
| | calcd | 20.43 | 1.95 | 30.65 | |
| **12** | exptl | 16.47 | 1.95 | 21.61 | [Fe(Htrz)$_3$](CF$_3$SO$_3$)$_2$·1.2H$_2$O |
| | calcd | 16.41 | 1.60 | 22.30 | |

Table 3.11: Elemental analysis of samples **10** and **12** and the corresponding formula

## 3.3.4.2 Powder X-ray Diffraction

Figure 3.43 shows the powder X-ray diffraction (PXRD) patterns of samples **10** and **12** at room temperature. The patterns observed for the two samples have similarities with those measured for the BF$_4$ derivatives. In agreement with the IR spectroscopy results, sample **10** corresponds to the [Fe(Htrz)$_2$(trz)](CF$_3$SO$_3$) complex while samples **12** exhibits a different PXRD pattern corresponding to the [Fe(Htrz)$_3$(CF$_3$SO$_3$)$_2$]·xH$_2$O derivative. X-ray diffraction allows also for the estimation of the crystallite size using the Scherrer equation (see chapter 2 page 75). The average crystallite size for both samples measured was about 80 nm. These crystallite sizes are in agreement with those reported for 30-600 nm [Fe(NH$_2$-trz)$_3$]Br$_2$ particles[155].
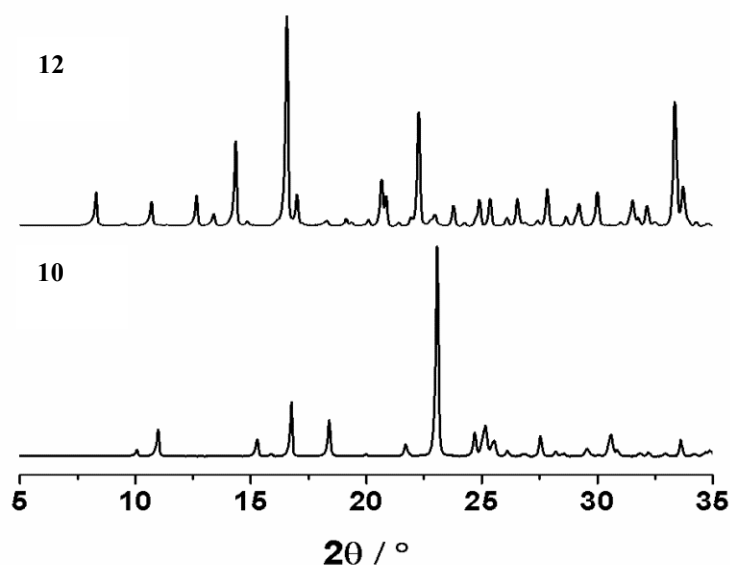


Figure 3.43: X-ray powder diffraction patterns of sample **10** and **12** at room temperature (HS state)

### 3.3.5 SCO Properties of the [Fe(Htrz)$_3$](CF$_3$SO$_3$)$_2$ Micro-Rods

### 3.3.5.1 Raman Spectra

Raman spectra were acquired for sample **12** at selected temperatures (figure 3.44). These Raman spectra compare well with those reported for similar complexes.[229,230] In sample **12**, internal modes of CF$_3$SO$_3$ ions are expected to appear around 760, 400 cm$^{-1}$, but their intensity is rather weak. The mode at *ca.* 1311 cm$^{-1}$ is observed which is due to the Htrz ligand. Besides, the spectral features around 100-300 cm$^{-1}$ and 1000-1600 cm$^{-1}$ assigned to metal-ligand stretching and internal ligand modes, respectively, can be identified as spin state markers. In particular, the LS marker bands are found at *ca.* 142, 208, 286, 1042, 1067 and 1083 cm$^{-1}$, and lower frequency HS marker bands at *ca.* 115, 142, 202, 1037 and 1067 cm$^{-1}$. **Furthermore, we also measured the Raman spectra at 300 K during both the cooling and heating process which revealed the room temperature bistability**.
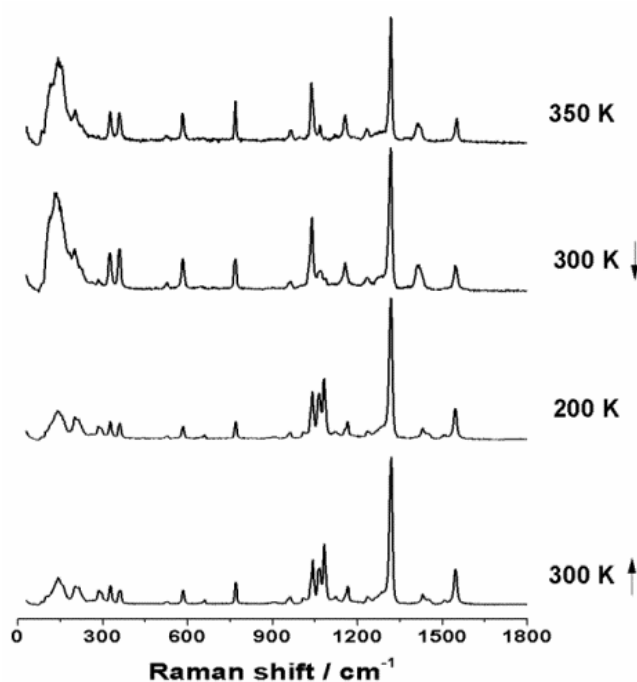


Figure 3.44: Raman spectra of sample **12** at selected temperatures.

### 3.3.5.2 Magnetic Susceptibility Measurements

In order to better probe the SCO behavior, the thermal variation of the magnetic susceptibility was investigated for both samples **10** and **12** (figure 3.45).
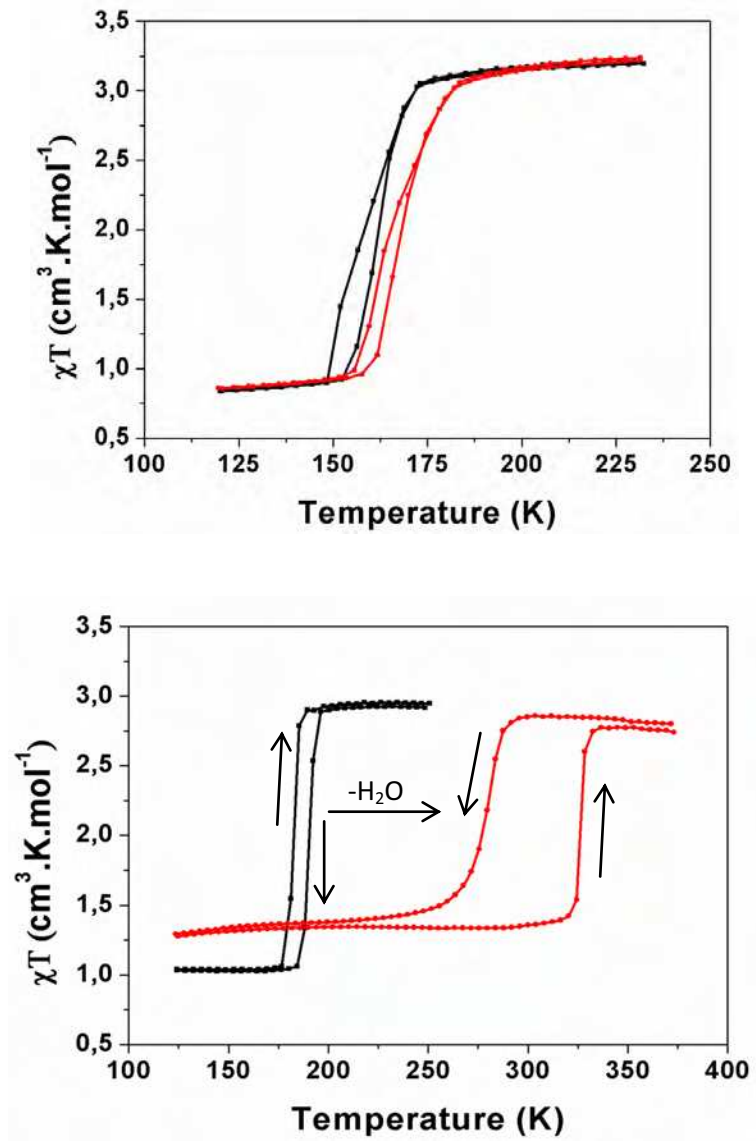
Figure 3.45: Magnetic measurements for sample **10** (up) and **12** (bottom) (hydrated sample in black and dehydrated sample in red).

| Sample | 10 | | 12 | |
|---|---|---|---|---|
| | First cycle | Second cycle | First cycle | Second cycle |
| Transition temperature (K) | 160/166 | 154/160 | 182/190 | 278/327 |

Table 3.12: Spin transition temperatures for samples **10** and **12** for two consecutive thermal cycles

Concerning sample **10**, these measurements revealed a rather low temperature SCO behavior compared to other compounds of this family with $T_{1/2(\downarrow)} \approx 154$ K and $T_{1/2(\uparrow)} \approx 160$ K (sample **10**) for the first cycle and $T_{1/2(\downarrow)} \approx 162$ K and $T_{1/2(\uparrow)} \approx 166$ K (sample **10**) for the second cycle. It is interesting to notice that lower transition temperatures ($T_{1/2(\downarrow)} \approx 130$ K and $T_{1/2(\uparrow)} \approx 150$ K) were reported for the same compound by Sugiyarto and co-workers.[240] No solvent is present within the structure, so the modification of the transition temperature for the second cycle could be related to the preliminary structural organization of the material. For sample **12**, the first thermal cycle was performed between 100 and 330 K and corresponds to the hydrated form of the sample which presents abrupt spin transition in both the warming and cooling modes. The transition temperatures are found at $T_{1/2(\downarrow)} \approx 182$ K and $T_{1/2(\uparrow)} \approx 190$ K. Following a preliminary thermal treatment at 400 K during 1 hour for dehydration, the second thermal cycle was performed between 100 and 380 K. For the second thermal cycle, the value of $\chi T$ at low temperature of *ca.* 1.25 cm$^3$·K·mol$^{-1}$ is slightly higher than that measured for the first cycle of *ca.* 1.0 cm$^3$·K·mol$^{-1}$. Structural modification certainly localized at the surface of the nanoparticles (see discussion hereafter) concomitant with the release of water could explain this effect. **The transition temperatures are found at $T_{1/2(\downarrow)} \approx 278$ K and $T_{1/2(\uparrow)} \approx 327$ K, revealing a large hysteresis loop of 50 K perfectly centered at room temperature. Such properties are very scarce and even unique for shaped materials** (see the discussion in chapter 3.3.6). In order to detect the stability of the dehydrated sample, after the magnetic measurement, we kept it in ambient air for two weeks and repeated the magnetic property measurements on the same sample.
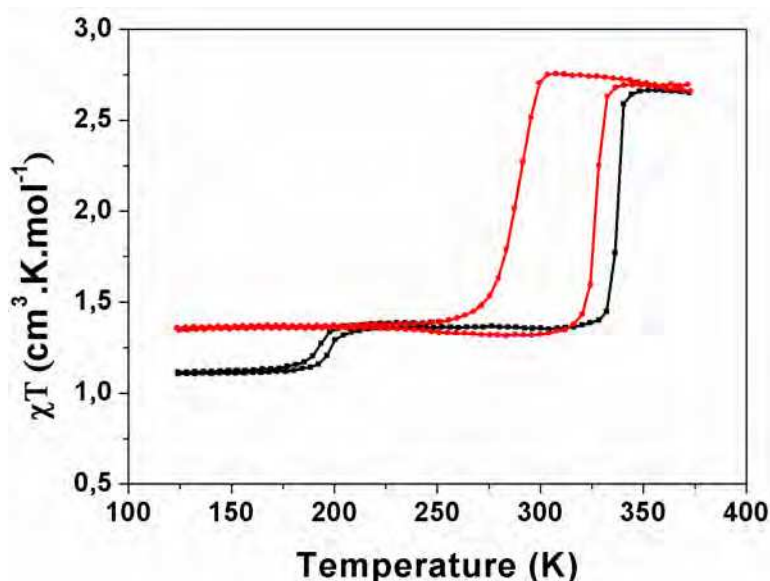


Figure 3.46: Magnetic measurements for sample **12** partially rehydrated sample in black and dehydrated sample in red).

The sample was again cycled two times between 100 K and 350 K starting at 250 K (cooling branch). In the next heating branch a two-step spin transition was observed at 200 and 337 K. The low temperature transition is due to the partial rehydratation of the rods. After dehydration treatment, we can again only observe the spin transition at room temperature ($T_{1/2(\downarrow)} \approx 288$ K and $T_{1/2(\uparrow)} \approx 327$ K), which means that the sample presents good reusability (see figure 3.46). Moreover, as already observed in the first measurement (figure 3.45), the value of $\chi T$ at low temperature increases for the dehydrated sample and thus the phenomenon attributed to the structural modification certainly localized at the surface of the nanoparticles is reversible.

### 3.3.5.3 Optical Measurements

As we can see in figure 3.47, a drastic color change of the sample from purple (low spin state) to colorless (high spin state) can be observed. Indeed, changes in the (M-L) bond distances affect the symmetry and electronic states of metal complexes. UV-vis spectroscopy is a very useful tool for the determination of the changes of electronic states due to the SCO phenomenon. UV spectroscopy was recorded using UV/Vis spectrophotometer equipped with a Labsphere RSA-PE-20 integrating sphere. Both measurements in the LS and HS states were performed at room temperature (within the hysteresis loop). The sample was heated or cooled out of the UV-Visible setup using an oven or liquid nitrogen, respectively.
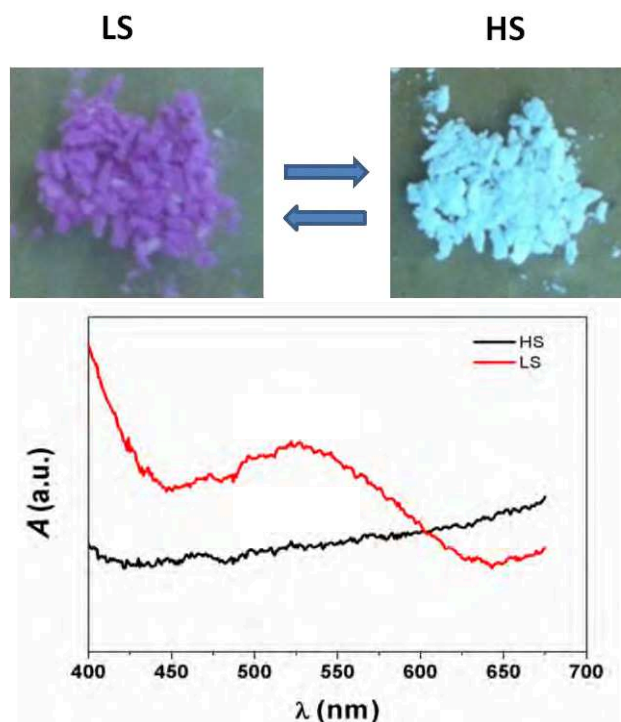


Figure 3.47: Color change (up) and UV spectroscopy (bottom) of the sample **12**.

In the LS state of the complex one can observe the $^1A \rightarrow {}^1T$ absorption centered at 530 nm. Switching from the LS to the HS state leads to the (reversible) bleaching of the absorption band at 530 nm and a weak, broad absorption appears in the near infrared range, which can be assigned to the $^5T \rightarrow {}^5E$ transition.

This clear color change permits to study also the optical behavior of the compound in the visible range (see figure 3.48-3.49). The thermal variation of the reflectance shows $T_{1/2(\downarrow)} \approx$ 172 K and $T_{1/2(\uparrow)} \approx$ 182 K for the hydrated and $T_{1/2(\downarrow)} \approx$ 283 K and $T_{1/2(\uparrow)} \approx$ 316 K for the dehydrated sample **12.** In the case of sample **10,** $T_{1/2(\downarrow)} \approx$ 145 K and $T_{1/2(\uparrow)} \approx$ 152 K for the dehydrated sample. All these results compare well with the magnetic measurements and confirm the large hysteresis loop perfectly centered at room temperature; the slight deviation of the transition temperature being due to the difference of the heating and cooling rates (2 K·min$^{-1}$ for magnetic measurements and 4 K·min$^{-1}$ for reflectivity measurements).
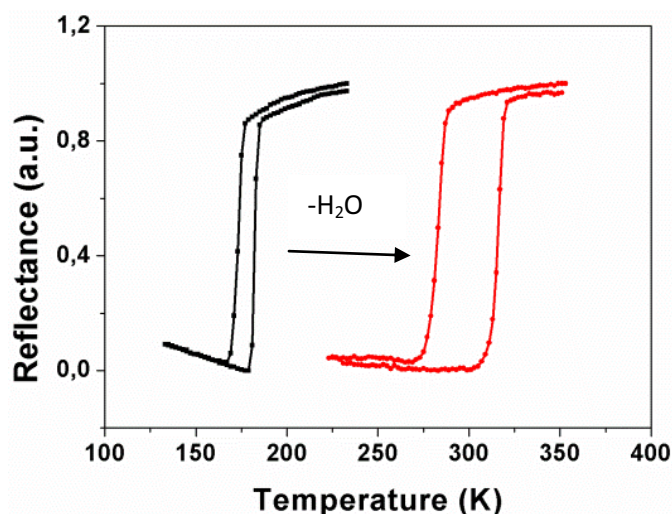


Figure 3.48: Optical reflectivity measurements of sample **12** (hydrated sample in black and dehydrated sample in red).
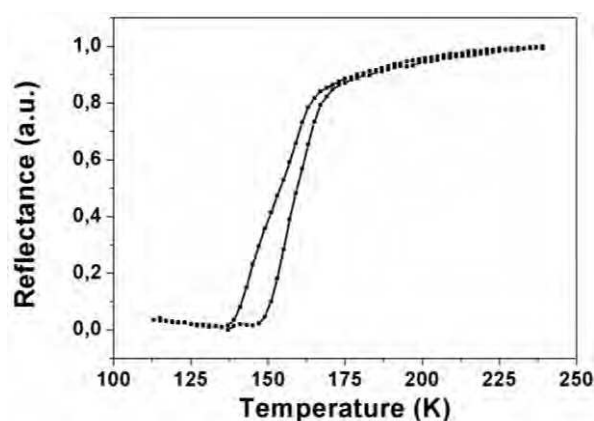


Figure 3.49: Optical reflectivity measurements of sample **10** (dehydrated sample).

Using this optical method, it was also possible to control that the SCO properties remain unaltered upon several thermal cycles after a preliminary dehydration process (see figure 3.50). The curves show no significant modification of the spin crossover properties after the tenth thermal cycle.
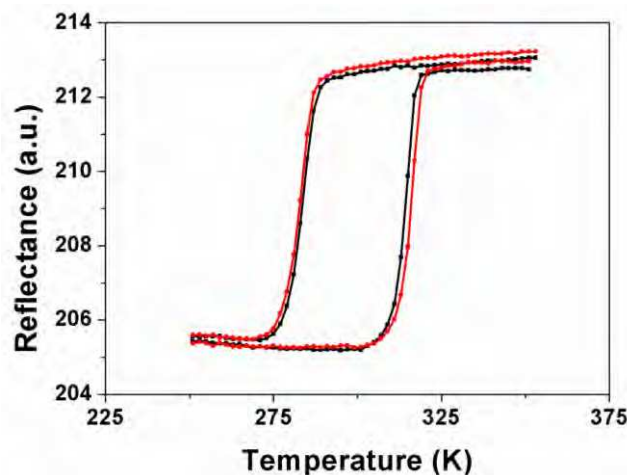


Figure 3.50: Optical reflectivity measurements for testing the hysteresis reproducibility of sample **12** (in black the first cycle and in red the tenth cycle)

## 3.3.5.4 Differential Scanning Calorimetry

The DSC curves were also recorded in the heating and cooling modes at 5 K/min in order to evaluate the enthalpy ($\Delta H$) and entropy ($\Delta S$) variations associated with the spin transition of sample **12** (see figure 3.51).
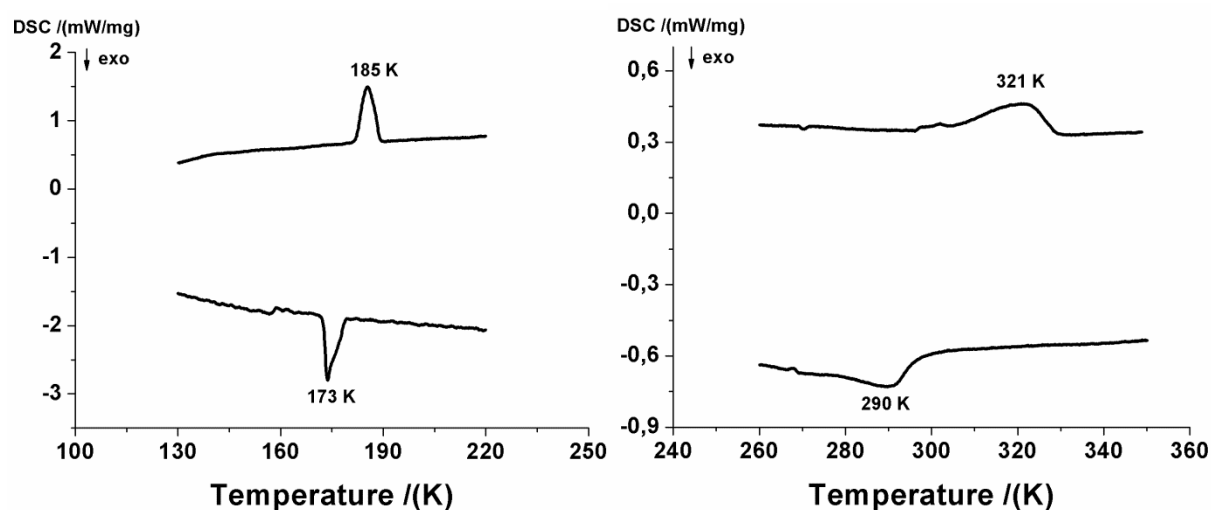


Figure 3.51: DSC measurements of the hydrated (left) and dehydrated (right) sample **12** on the heating/cooling modes

Respectively, the DSC curves show singularities at $T_{1/2(\downarrow)} \approx 173$ K and $T_{1/2(\uparrow)} \approx 185$ K for hydrated sample and at $T_{1/2(\downarrow)} \approx 290$ K and $T_{1/2(\uparrow)} \approx 321$ K for dehydrated sample. In comparison with the magnetic measurements, the slight deviation of the transition temperature could be associated to the difference of the heating and cooling rates (10 K·min$^{-1}$ for DSC measurements). The estimated $\Delta H$ and $\Delta S$ associated with the SCO are 12 KJ/mol and 43 J/mol·K, respectively, when corrected by the residual HS fraction at low temperature determined by Mössbauer Spectrometry (hereafter). These values are common for iron(II) spin crossover compounds.

## 3.3.5.5 $^{57}$Fe Mössbauer Spectroscopy

With the aim to determine more precisely the fraction of iron centres involved in the spin transition and to explain the slightly high magnetic susceptibility value measured at low temperature, $^{57}$Fe Mössbauer spectra were recorded for sample **12** at different temperatures (see figure 3.52). As expected, at 300 K the spectrum consists of one doublet with an isomeric shift of 1.043 mms$^{-1}$ and a quadrupole splitting of 2.618 mms$^{-1}$ attributed to the HS state. Inversely, two doublets with isomeric shift of 0.461 (1.090) mms$^{-1}$ and a quadrupole splitting of 0.226 (2.831) mms$^{-1}$ attributed to the LS (HS) state are observed at 240 and 80 K, in agreement with the magnetic data of its dehydrated form. The remaining 30% HS fraction at low temperature might be explained by the strong anisotropic morphology of the particles and the concomitant increase of the iron center portion localized at the surface which are possibly spin crossover inactive.

| Sample **12** | HS state | | | LS state | | | HS fraction |
|---|---|---|---|---|---|---|---|
| | $\delta$ | $\Delta E_Q$ | $\Gamma/2$ | $\delta$ | $\Delta E_Q$ | $\Gamma/2$ | |
| 300 K | 1.05(80) | 2.68(16) | 0.11(12) | | | | 100% |
| 240 K | 1.09(13) | 2.83(25) | 0.20(21) | 0.46(35) | 0.23(63) | 0.14(58) | 29% |
| 80 K | 1.17(16) | 3.23(32) | 0.20(27) | 0.50(59) | 0.22(13) | 0.17(11) | 30% |

Table 3.13**:** Table of the Mössbauer hyperfine parameters ($\delta$ = isomeric shift, $\Delta E_Q$ = quadrupole splitting, $\Gamma/2$ = half width at half maximum) of the dehydrated sample **12**
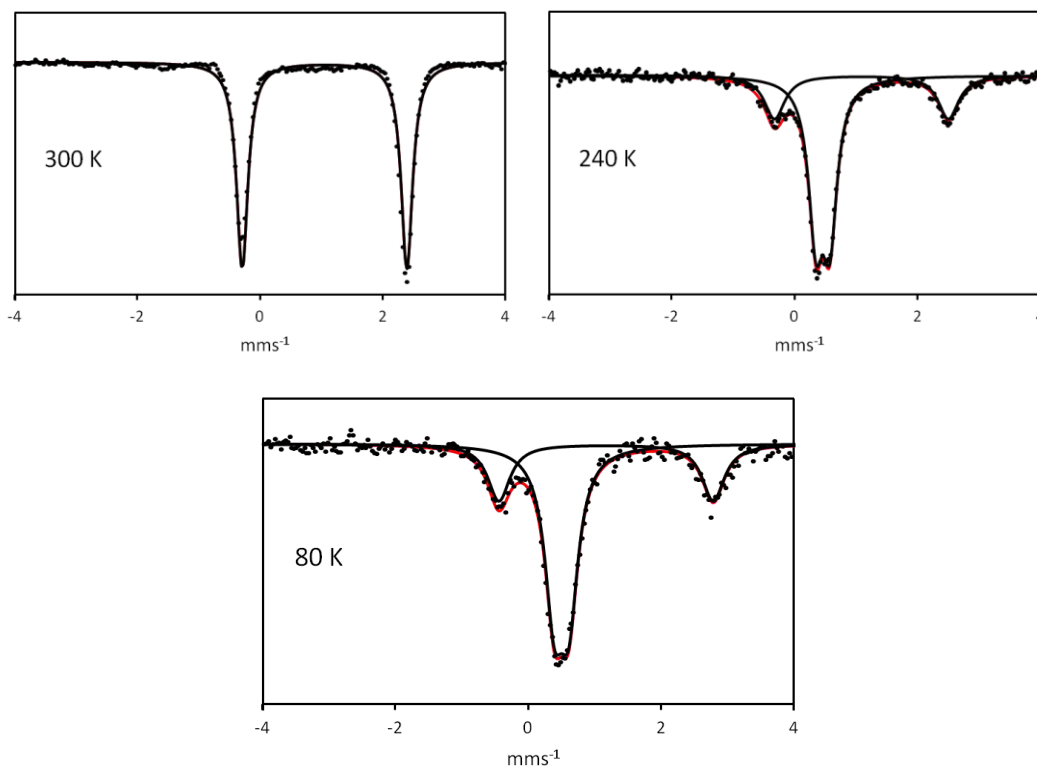
Figure 3.52: Variable temperature Mössbauer measurements of the dehydrated sample **12**

## 3.3.6 Discussion

One of the relevant great challenges concerning the spin crossover materials for memory device applications notably is to produce controlled size systems that exhibit properties at room temperature and with large hysteresis loop. The first example of bulk sample showing bistability at room temperature was reported only in 1993.[6] In this work, the authors controlled the spin transition temperature by mixing of 4-NH$_2$trz and Htrz ligands, and obtained the complex {[Fe(Htrz)$_{2.85}$(4-NH$_2$trz)$_{0.15}$]}(ClO$_4$)$_2$ exhibiting a hysteresis loop of 16 K centred at 296 K. Up to now only four other bulk compounds presenting such behavior have been reported. Similar [Fe(NH$_2$trz)$_3$](NO$_3$)$_{1.7}$(BF$_4$)$_{0.3}$ complex was also synthesized by mixing two counteranions revealing a 60 K hysteresis loop centred at 310 K.[95] In 2001, the dehydrated form of the Hofmann like clathrate coordination network [Fe(pz){Pt(CN)$_4$}] (pz = pyrazine) presenting a 25 K wide hysteresis loop centered at 290 K was reported.[49] The corresponding bpac (bis(4-pyridyl)acetylene) derivative exhibits hysteresis loop of 49 K (T$_{1/2(\downarrow)}$ = 251 K and T$_{1/2(\uparrow)}$ = 300 K).[49] More recently, the first molecular iron(II) complex [Fe(Ph(Imoxo)$_2$)(HIm)$_2$] (Ph(Imoxo)$_2$ = diethyl(E,E)-2,2'-[1,2-phenylenebis-(iminomethylidyne)]-bis[3-butanoate], HIm = imidazole) was shown to exhibit an abrupt spin

transition centred at approximately 297 K ($T_{1/2(\downarrow)}$ = 244 K and $T_{1/2(\uparrow)}$ = 314 K).[31] Although hysteretic spin crossover at room temperature is a prerequisite to go toward several applications such as inkless paper, display[6] and memory, the possibility to obtain regular and organized nano- and micro objects is also crucial. It has been shown that the elaboration of thin film[126,135] or nano- and microparticles[152,153,220] of the SCO clathrate (bpac and pz derivatives) leads to the decrease of the abrupt character of the transitions and also to the modification of the bistability temperatures out of the more suitable temperatures. In the present study, a large hysteresis loop of 50 K perfectly centered at room temperature ($T_{1/2(\downarrow)} \approx$ 278 K and $T_{1/2(\uparrow)} \approx$ 327 K) are found for micro-rods based on the [Fe(Htrz)$_3$(CF$_3$SO$_3$)$_2$] complex.

# Conclusions and Perspectives

The main objective of this thesis was to synthesize spin crossover nanomaterials with various sizes and various shapes, on one hand in order to probe what is the effect of the size reduction on the spin crossover properties and in the other hand to obtain room temperature spin transition objects for potential future application. The work focused on the synthesis of various sizes 3D Hofmann like Clathrate [Fe(pz){Ni(CN)$_4$}] nanoparticles and rod-shaped spin crossover particles based on compound from the well known Fe-triazole family.

To study the size reduction effect on the spin crossover properties, reverse nanoemulsion technique was developed for the synthesis of a series of [Fe(pz){Ni(CN)$_4$}] nanoparticles with sizes ranging from 2 to 107 nm and with the same environment. For the first time it was possible to obtain various ultra-small sized nanoparticles smaller than 10 nm embedded in NaAOT matrix. We probed the composition and size of the particles by TEM and HRTEM investigations associated with EDX analyses. The spin crossover behavior for the different samples was determined with accuracy by combined Raman and Mössbauer spectroscopy and magnetic measurements. The results obtained for the larger [Fe(pz){Ni(CN)$_4$}] nanoparticles (107, 71 and 12 nm) namely the loss of the cooperativity, the shift of the transition to lower transition temperatures and the increase of the residual HS fraction at low temperature for decreasing size, corroborate previous reports obtained for the analogous [Fe(pz){Pt(CN)$_4$}] nanoparticles. On the other hand, the properties of the ultra-small (2 and 3 nm) nanoparticles revealed the re-increase of the cooperativity and of the transition temperature with even the re-opening of a hysteresis loop for the smallest nanoparticles. This finding is in agreement with previous results concerning [Fe(pz){Ni(CN)$_4$}]/Chitosan composite which demonstrated the possibility of a memory effect (i.e. hysteresis) in ultra-small SCO particles. In order to find an origin to this unexpected behavior for such small SCO nanoparticles, we carried out a detailed Mössbauer study to determine the stiffness of the different nanoparticles by measuring their Debye temperature ($\theta_D$) and we disclosed a significant increase of $\theta_D$ for the smallest nanoparticles. Thus, the unusual SCO properties observed at low size can be explained thanks to the consideration of the size dependent elastic properties of the particles. Moreover, by means of NIS spectroscopy the size dependent vibrational DOS and its spin-state dependence have been probed. These spectra showed the high-frequency shift of the DOS when going from the HS to the LS state. The analysis of the vibrational entropy change accompanying the spin transition has put in evidence the main contribution coming from the

metal-ligand vibrational modes. The stiffness change of the material with the spin state change has been analyzed through the Debye sound velocity calculated from the acoustic part of the DOS. The study tends to conclude that the stiffness increases for the ultra small size (2 nm) nanoparticles and confirms the increase of the Debye temperature as a function of the size obtained by the more conventional Mössbauer investigation. As a perspective, we envisage to perform additional NIS measurements at different temperatures and on different-size [$^{57}$Fe(pz){Ni(CN)$_4$}] nanoparticles to complete the study on the evolution of their stiffness. Further works involving the size effect study on other spin crossover materials will be also necessary to confirm this novel and unexpected result.

Using simple homogeneous acid media we synthesized various size rod-shaped surfactant/polymer-free Fe-Triazole complex particles with different chemical compositions based on the tetrafluoborate and triflate derivatives. In the case of the BF$_4$ derivatives, all the physical characterizations revealed a correlation between the size of the particles and their composition, the smaller rods correspond to the [Fe(Htrz)$_2$(trz)](BF$_4$) complex with a spin transition localized at high temperature (T$_{1/2\,(\downarrow)}\approx$ 352 K and T$_{1/2\,(\uparrow)}\approx$ 397 K), while the longer ones correspond to the fully protonated ligand [Fe(Htrz)$_3$](BF$_4$)$_2\cdot$3H$_2$O derivative with a spin transition just below room temperature (T$_{1/2\,(\downarrow)}\approx$ 265 K and T$_{1/2\,(\uparrow)}\approx$ 278 K for the dehydrated compound). In fact, high concentrations of acid which preclude the deprotonation of the Htrz ligand associated with a slow evaporation speed of the complex solution lead to the slow stabilization of the [Fe(Htrz)$_3$](BF$_4$)$_2\cdot$3H$_2$O long rod-shaped particles while short rod-shaped [Fe(Htrz)$_2$(trz)](BF$_4$) particles are obtained for low acid concentrations. Thus, we have demonstrated that not only the size but also the morphology of the objects for a considered material can be tuned. Using the same approach, 2 μm rods of the Zn diluted [Fe$_{1-x}$Zn$_x$(Htrz)$_2$(trz)](BF$_4$) (x = 0.26 and 0.43) compounds were also synthesized. The metal substitution was found to be homogeneous, and the obtained compounds appeared closely isostructural. The iron ions kept their spin transition properties in the diluted samples, but as expected, a loss of cooperativity and a shift of the spin transition toward lower temperatures were observed with increasing the iron dilution by zinc. We reported also the first investigation of the influence of substitution of the "active" Fe centers by "inactive" Zn ions on the charge transport properties of a spin crossover compound. Indeed, electrical properties of the [Fe(Htrz)$_2$(trz)](BF$_4$) and Zn-diluted analogues spin crossover compound were studied by broadband dielectric spectroscopy in a large frequency and temperature range. We have demonstrated that spin crossover phenomena can be detected through the temperature dependence of AC conductivity and dielectric loss, and we showed that virtually all material-

dependent electrical parameters, such as electrical conductivity, electric modulus, cut off frequency, display spin-state dependence. In particular, we have shown that the spin transition from the LS to the HS state led to a systematic decrease of the electrical conductivities, which were related to the higher values of the activation energy in the HS state. All these results seem to confirm the conduction process *via* polaron hopping but taking into account the close structural and morphological similarity of the pure Fe and Zn-diluted samples, these results indicate that the ferrous ions with open $3d^6$ electronic shell directly participate in the charge transport process, in contrast to the Zn(II) ions, which have a closed $3d^{10}$ shell. Moreover, a similar homogeneous acid condition was used for the elaboration of highly anisotropic acicular rods of the $CF_3SO_3$ derivatives as well. Syntheses in absence or in presence of low concentration of acid allowed us to stabilize rod-shaped particles of the $[Fe(Htrz)_2(trz)](CF_3SO_3)$ derivative which presents a rather low temperature SCO behavior compared to other compounds of this family with $T_{1/2(\downarrow)} \approx 162$ K and $T_{1/2(\uparrow)} \approx 166$ K for the dehydrated form. In contrast, incorporation of larger concentration of acid as for the $BF_4$ derivative, led to the precipitation of micro-rods of the $[Fe(Htrz)_3](CF_3SO_3)_2$ form. This new compound presents a large hysteresis loop of 50 K perfectly centered at room temperature ($T_{1/2(\downarrow)} \approx 278$ K and $T_{1/2(\uparrow)} \approx 327$ K). Such properties are very scarce and even unique for shaped materials. Indeed, although hysteretic spin crossover at room temperature is a prerequisite to go toward several applications, the possibility to obtain regular and organized nano- and micro objects is also crucial. In our case, simple experiments led to the elaboration of already- shaped spin crossover objects with very appealing properties which will be certainly beneficial to undertake the relevant great challenges concerning both fundamental and applied perspectives. In particular, these very high aspect ratio bistable objects could be really useful using soft lithographic approaches or the dielectrophoresis to understand the spatio-temporal behaviors and the transport properties of organized individual objects which constitute one of the foremost paradigms in molecular electronics. Moreover, the largest measured "real" room temperature bistability reported for these objects is very promising for practical application in the fields of memory devices, display devices, inkless paper and MEMS (Micro Electro Mechanical Systems).

# Reference

[1] Cambi., L.; Gagnasso. Iron dithiocarbamates and nitrosodithiocarbamates. A. *Atti. Accad. Naz. Lincei* **1931**, *13*, 809.

[2] Baker, W. A.; Bobonich, H. M. Magnetic properties of some high-spin complexes of iron(II). *Inorganic Chemistry* **1964**, *3*, 1184-1188.

[3] Koenig, E.; Madeja, K. $^5T_2$-$^1A_1$ Equilibriums in some iron(II)-bis(1,10-phenanthroline) complexes. *Inorganic Chemistry* **1967**, *6*, 48-55.

[4] Decurtins, S.; Gütlich, P.; Köhler, C. P.; Spiering, H.; Hauser, A. Light-induced excited spin state trapping in a transition-metal complex: the hexa-1-propyltetrazole-iron (II) tetrafluoroborate spin-crossover system. *Chemical physics letters* **1984**, *105*, 1-4.

[5] Gütlich, P.; Hauser, A.; Spiering, H. Thermal and optical switching of iron (II) complexes. *Angewandte Chemie International Edition in English* **1994**, *33*, 2024-2054.

[6] Krober, J.; Codjovi, E.; Kahn, O.; Groliere, F.; Jay, C. A spin transition system with a thermal hysteresis at room temperature. *Journal of the American Chemical Society* **1993**, *115*, 9810-9811.

[7] Létard, J.-F.; Guionneau, P.; Goux-Capes, L. Towards spin crossover applications. In *Spin Crossover in Transition Metal Compounds Iii*; Topics in Current Chemistry; Springer Berlin Heidelberg, **2004**, *235*, 221-249.

[8] Létard, J.-F., Nguyen, O. Daro. N. **2005**, Patent FR 0512476.

[9] Bousseksou, A.; Molnár, G.; Salmon, L.; Nicolazzi, W. Molecular spin crossover phenomenon: recent achievements and prospects. *Chemical Society Reviews* **2011**, *40*, 3313-3335.

[10] Molnar, G.; Salmon, L.; Nicolazzi, W.; Terki, F.; Bousseksou, A. Emerging properties and applications of spin crossover nanomaterials. *Journal of Materials Chemistry C* **2014**, *2*, 1360-1366.

[11] Cavallini, M. Status and perspectives in thin films and patterning of spin crossover compounds. *Physical Chemistry Chemical Physics* **2012**, *14*, 11867-11876.

[12] Shepherd, H. J.; Molnár, G.; Nicolazzi, W.; Salmon, L.; Bousseksou, A. Spin crossover at the nanometre scale. *European Journal of Inorganic Chemistry* **2013**, *2013*, 653-661.

[13] Haasnoot, J. G. Mononuclear, oligonuclear and polynuclear metal coordination compounds with 1,2,4-triazole derivatives as ligands. *Coordination Chemistry Reviews* **2000**, *200–202*, 131-185.

[14] Lavrenova, L. G.; Shakirova, O. G. Spin crossover and thermochromism of iron(II) coordination compounds with 1,2,4-triazoles and tris(pyrazol-1-yl)methanes. *European Journal of Inorganic Chemistry* **2013**, *2013*, 670-682.

[15] Roubeau, O. Triazole-based one-dimensional spin-crossover coordination polymers. *Chemistry – A European Journal* **2012**, *18*, 15230-15244.

[16] Bertoni, R.; Cammarata, M.; Lorenc, M.; Matar, S. F.; Létard, J.-F.; Lemke, H. T.; Collet, E. Ultrafast light-induced spin-state trapping photophysics investigated in Fe(phen)$_2$(NCS)$_2$ spin-crossover crystal. *Accounts of Chemical Research* **2015**, *48*, 774-781.

[17] Bertoni, R.; Lorenc, M.; Tissot, A.; Boillot, M. L.; Collet, E. Femtosecond photoswitching dynamics and microsecond thermal conversion driven by laser heating in FeIII spin-crossover solids. *Coordination Chemistry Reviews* **2015**, *282–283*, 66-76.

[18] Levchenko, G. G.; Khristov, A. V.; Varyukhin, V. N. Spin crossover in iron(II)-containing complex compounds under a pressure. *Low Temperature Physics* **2014**, *40*, 571-585.

[19] Sato, O.; Tao, J.; Zhang, Y.-Z. Control of magnetic properties through external stimuli. *Angewandte Chemie International Edition* **2007**, *46*, 2152-2187.

[20] Halcrow, M. A. Structure: function relationships in molecular spin-crossover complexes. *Chemical Society Reviews* **2011**, *40*, 4119-4142.

[21] Shatruk, M.; Phan, H.; Chrisostomo, B. A.; Suleimenova, A. Symmetry-breaking structural phase transitions in spin crossover complexes. *Coordination Chemistry Reviews* **2015**, *289–290*, 62-73.

[22] Šalitroš, I.; Madhu, N. T.; Boča, R.; Pavlik, J.; Ruben, M. Room-temperature spin-transition iron compounds. *Monatsh Chem* **2009**, *140*, 695-733.

[23] Gentili, D.; Cavallini, M. Wet-lithographic processing of coordination compounds. *Coordination Chemistry Reviews* **2013**, *257*, 2456-2467.

[24] Gaspar, A. B.; Seredyuk, M. Spin crossover in soft matter. *Coordination Chemistry Reviews* **2014**, *268*, 41-58.

[25] Bethe, H. A. Splitting of terms in crystals. *Annals of Physics* **1929**. *3*, 133-206.

[26] Parr, R. G.; Ellison, F. O. The quantum theory of valence. *Annual Review of Physical Chemistry* **1955**, *6*, 171-192.

[27] Tanabe, Y.; Sugano, S. On the absorption spectra of complex ions. I. *Journal of the Physical Society of Japan* **1954**, *9*, 753-766.

[28] Tanabe, Y.; Sugano, S. On the absorption spectra of complex ions II. *Journal of the Physical Society of Japan* **1954**, *9*, 766-779.

[29] Gaspar, A. B.; Munoz, M. C.; Real, J. A. Dinuclear iron(ii) spin crossover compounds: singular molecular materials for electronics. *Journal of Materials Chemistry* **2006**, *16*, 2522-2533.

[30] Bousseksou, A.; Molnár, G.; Real, J. A.; Tanaka, K. Spin crossover and photomagnetism in dinuclear iron(II) compounds. *Coordination Chemistry Reviews* **2007**, *251*, 1822-1833.

[31] Weber, B.; Bauer, W.; Obel, J. An iron(II) spin-crossover complex with a 70 K wide thermal hysteresis loop. *Angewandte Chemie International Edition* **2008**, *47*, 10098-10101.

[32] Weber, S. XRDIFF: simulation of X-ray diffraction patterns. *Journal of Applied Crystallography* **1997**, *30*, 565-566.

[33] Gütlich, P.: Spin crossover in iron (II)-complexes. In *Metal Complexes*; Springer, **1981**, 83-195.

[34] Jager, E. G.; Haussler, E.; Rudolph, M.; Schneider, A. Structure Reactivity Correlations in Coordinatively Unsaturated Chelate Complexes. VI. Synthesis, Adduct Formation, Redox Potentials, and Photochromic Iodine Derivatives of Iron(II) Complexes with Schiff Base Ligands Possessing Electron-Withdrawing Substituents. *Zeitschrift Fur Anorganische Und Allgemeine Chemie* **1985**, *525*, 67-85.

[35] Lindoy, L. F.; Livingstone, S. E. Complexes of iron(II),cobalt(II) and nickel(II) with α-diimines and related bidentate ligands. *Coordination Chemistry Reviews* **1967**, *2*, 173-193.

[36] Sorai, M.; Seki, S. Magnetic heat capacity due to cooperative low-spin (remark: graphics omitted.) $^5T_2$ transition in Fe(phen)$_2$(NCS)$_2$ crystal. *Journal of the Physical Society of Japan* **1972**, *33*, 575-575.

[37] Dubois, J. M. Simultaneous changes in the equilibrium potential and potassium conductance in voltage clamped Ranvier node in the frog. *The Journal of physiology* **1981**, *318*, 279-295.

[38] Real, J. A.; Bolvin, H.; Bousseksou, A.; Dworkin, A.; Kahn, O.; Varret, F.; Zarembowitch, J. Two-step spin crossover in the new dinuclear compound [Fe(bt)(NCS)$_2$]$_2$bpym, with bt= 2, 2'-bi-2-thiazoline and bpym= 2, 2'-bipyrimidine: experimental investigation and theoretical approach. *Journal of the American Chemical Society* **1992**, *114*, 4650-4658.

[39] Gutlich, P.; Goodwin, H. A. Spin crossover - An overall perspective. *Spin Crossover in Transition Metal Compounds I* **2004**, *233*, 1-47.

[40] Abdul-Kader, K.; Lopes, M.; Bartual-Murgui, C.; Kraieva, O.; Hernández, E. M.; Salmon, L.; Nicolazzi, W.; Carcenac, F.; Thibault, C.; Molnár, G. Synergistic switching of plasmonic resonances and molecular spin states. *Nanoscale* **2013**, *5*, 5288-5293.

[41] Suleimanov, I.; Costa, J. S.; Molnár, G.; Salmon, L.; Bousseksou, A. The photo-thermal plasmonic effect in spin crossover@ silica–gold nanocomposites. *Chemical Communications* **2014**, *50*, 13015-13018.

[42] Akou, A.; Salmon, L.; Bartual-Murgui, C.; Thibault, C.; Vieu, C.; Molnár, G.; Bousseksou, A. Soft lithographic patterning of spin crossover complexes. Part 2: stimuli-responsive diffraction grating properties. *Journal of Materials Chemistry* **2012**, *22*, 3752-3757.

[43] Quintero, C. M.; Gural'skiy, I. y. A.; Salmon, L.; Molnar, G.; Bergaud, C.; Bousseksou, A. Soft lithographic patterning of spin crossover complexes. Part 1: fluorescent detection of the spin transition in single nano-objects. *Journal of Materials Chemistry* **2012**, *22*, 3745-3751.

[44] Suleimanov, I.; Kraieva, O.; Costa, J. S.; Fritsky, I. O.; Molnár, G.; Salmon, L.; Bousseksou, A. Electronic communication between fluorescent pyrene excimers and spin crossover complexes in nanocomposite particles. *Journal of Materials Chemistry C* **2015**, *3*, 5026-5032.

[45] Hernández, E. M.; Quintero, C. M.; Kraieva, O.; Thibault, C.; Bergaud, C.; Salmon, L.; Molnár, G.; Bousseksou, A. AFM imaging of molecular spin‐state changes through quantitative thermomechanical measurements. *Advanced Materials* **2014**, *26*, 2889-2893.

[46] Garcia, Y.; Niel, V.; Munoz, M. C.; Real, J. A.: Spin crossover in 1D, 2D and 3D polymeric Fe(II) networks. In *Spin Crossover in Transition Metal Compounds I*; Gutlich, P., Goodwin, H. A., Eds.; Topics in Current Chemistry, 2004; Vol. 233; pp 229-257.

[47] Kitazawa, T.; Gomi, Y.; Takahashi, M.; Takeda, M.; Enomoto, M.; Miyazaki, A.; Enoki, T. Spin-crossover behaviour of the coordination polymer FeII($C_5H_5N$)$_2$Ni-II(CN)$_4$. *Journal of Materials Chemistry* **1996**, *6*, 119-121.

[48] Niel, V.; Martinez-Agudo, J. M.; Munoz, M. C.; Gaspar, A. B.; Real, J. A. Cooperative spin crossover behavior in cyanide-bridged Fe(II)-M(II) bimetallic 3D Hofmann-like networks (M = Ni, Pd, and Pt). *Inorganic Chemistry* **2001**, *40*, 3838.

[49] Bartual-Murgui, C.; Ortega-Villar, N. A.; Shepherd, H. J.; Carmen Munoz, M.; Salmon, L.; Molnar, G.; Bousseksou, A.; Real, J. A. Enhanced porosity in a new 3D Hofmann-like network exhibiting humidity sensitive cooperative spin transitions at room temperature. *Journal of Materials Chemistry* **2011**, *21*, 7217-7222.

[50] Bartual-Murgui, C.; Salmon, L.; Akou, A.; Ortega-Villar, N. A.; Shepherd, H. J.; Muñoz, M. C.; Molnár, G.; Real, J. A.; Bousseksou, A. Synergetic effect of host–guest chemistry and spin crossover in 3D Hofmann-like metal–organic frameworks [Fe(bpac)M(CN)$_4$] (M=Pt, Pd, Ni). *Chemistry – A European Journal* **2012**, *18*, 507-516.

[51] Agustí, G.; Cobo, S.; Gaspar, A. B.; Molnár, G.; Moussa, N. O.; Szilágyi, P. Á.; Pálfi, V.; Vieu, C.; Carmen Muñoz, M.; Real, J. A.; Bousseksou, A. Thermal and light-induced spin crossover phenomena in new 3D Hofmann-like microporous metalorganic mrameworks produced as bulk materials and nanopatterned thin films. *Chemistry of Materials* **2008**, *20*, 6721-6732.

[52] Muñoz‑Lara, F. J.; Gaspar, A. B.; Muñoz, M. C.; Arai, M.; Kitagawa, S.; Ohba, M.; Real, J. A. Sequestering aromatic molecules with a spin‑crossover FeII microporous coordination polymer. *Chemistry-A European Journal* **2012**, *18*, 8013-8018.

[53] Ohtani, R.; Arai, M.; Hori, A.; Takata, M.; Kitao, S.; Seto, M.; Kitagawa, S.; Ohba, M. Modulation of spin-crossover behavior in an elongated and flexible Hofmann-type porous coordination polymer. *Journal of Inorganic and Organometallic Polymers and Materials* **2013**, *23*, 104-110.

[54] Sciortino, N. F.; ScherlGruenwald, K. R.; Chastanet, G.; Halder, G. J.; Chapman, K. W.; Létard, J. F.; Kepert, C. J. Hysteretic three-step spin crossover in a thermo-and photochromic 3D pillared Hofmann-type metal-organic framework. *Angewandte Chemie* **2012**, *124*, 10301-10305.

[55] Muño -Lara, F. J.; Gaspar, A. B.; Muño , M. C.; Ksenofontov, V.; Real, J. A. Novel iron (II) microporous spin-crossover coordination polymers with enhanced pore size. *Inorganic Chemistry* **2012**, *52*, 3-5.

[56] Delgado, T.; Tissot, A.; Besnard, C.; Guénée, L.; Pattison, P.; Hauser, A. Structural investigation of the high spin→ low spin relaxation dynamics of the porous coordination network [Fe(pz)Pt(CN)$_4$]· 2.6 H$_2$O. *Chemistry-A European Journal* **2015**.

[57] Otsubo, K.; Haraguchi, T.; Sakata, O.; Fujiwara, A.; Kitagawa, H. Step-by-step fabrication of a highly oriented crystalline three-dimensional pillared-layer-type metal–organic framework thin film confirmed by synchrotron X-ray diffraction. *Journal of the American Chemical Society* **2012**, *134*, 9605-9608.

[58] Agusti, G.; Ohtani, R.; Yoneda, K.; Gaspar, A. B.; Ohba, M.; Sanchez-Royo, J. F.; Munoz, M. C.; Kitagawa, S.; Real, J. A. Oxidative addition of halogens on open metal sites in a microporous spin-crossover coordination polymer. *Angewandte Chemie-International Edition* **2009**, *48*, 8944-8947.

[59] Bartual-Murgui, C.; Salmon, L.; Akou, A.; Ortega-Villar, N. A.; Shepherd, H. J.; Munoz, M. C.; Molnar, G.; Real, J. A.; Bousseksou, A. Synergetic sffect of host-guest chemistry and spin crossover in 3D Hofmann-like metal-organic frameworks Fe(bpac)M(CN)$_4$ (M=Pt, Pd, Ni). *Chemistry-A European Journal* **2012**, *18*, 507-516.

[60] Ohba, M.; Yoneda, K.; Agusti, G.; Munoz, M. C.; Gaspar, A. B.; Real, J. A.; Yamasaki, M.; Ando, H.; Nakao, Y.; Sakaki, S.; Kitagawa, S. Bidirectional chemo-switching of spin state in a microporous framework. *Angewandte Chemie-International Edition* **2009**, *48*, 4767-4771.

[61] Southon, P. D.; Liu, L.; Fellows, E. A.; Price, D. J.; Halder, G. J.; Chapman, K. W.; Moubaraki, B.; Murray, K. S.; Letard, J. F.; Kepert, C. J. Dynamic interplay between spin-crossover and host-guest function in a nanoporous metal-organic framework material. *Journal of the American Chemical Society* **2009**, *131*, 10998-11009.

[62] Clements, J. E.; Price, J. R.; Neville, S. M.; Kepert, C. J. Perturbation of spin crossover behavior by covalent post-synthetic modification of a porous metal-organic framework. *Angewandte Chemie* **2014**, *126*, 10328-10332.

[63] Sciortino, N. F.; Neville, S. M.; Lećard, J.-F. o.; Moubaraki, B.; Murray, K. S.; Kepert, C. J. Thermal-and light-induced spin-crossover bistability in a disrupted Hofmann-type 3D framework. *Inorganic Chemistry* **2014**, *53*, 7886-7893.

[64] Yoshida, K.; Akahoshi, D.; Kawasaki, T.; Saito, T.; Kitazawa, T. Guest-dependent spin crossover in a Hofmann-type coordination polymer Fe (4, 4'-bipyridyl)[Au(CN)$_2$]$_2$·nGuest. *Polyhedron* **2013**, *66*, 252-256.

[65] Cirera, J. Guest effect on spin-crossover frameworks. *Reviews in Inorganic Chemistry* **2014**, *34*, 199-216.

[66] Agusti, G.; Ohtani, R.; Yoneda, K.; Gaspar, A. B.; Ohba, M.; Sanchez-Royo, J. F.; Carmen Munoz, M.; Kitagawa, S.; Real, J. A. Oxidative addition of halogens on open metal sites in a microporous spin-crossover coordination polymer. *Angewandte Chemie-International Edition* **2009**, *48*, 8944-8947.

[67] Ohtani, R.; Yoneda, K.; Furukawa, S.; Horike, N.; Kitagawa, S.; Gaspar, A. B.; Munoz, M. C.; Real, J. A.; Ohba, M. Precise control and consecutive modulation of spin transition temperature using chemical migration in porous coordination polymers. *Journal of the American Chemical Society* **2011**, *133*, 8600-8605.

[68] Aravena, D.; Castillo, Z. A.; Muñoz, M. C.; Gaspar, A. B.; Yoneda, K.; Ohtani, R.; Mishima, A.; Kitagawa, S.; Ohba, M.; Real, J. A.; Ruiz, E. Guest modulation of spin-vrossover transition

temperature in a porous iron(II) metal–organic framework: xxperimental and periodic DFT studies. *Chemistry – A European Journal* **2014**, *20*, 12864-12873.

[69] Ohba, M.; Yoneda, K.; Agustí, G.; Muñoz, M. C.; Gaspar, A. B.; Real, J. A.; Yamasaki, M.; Ando, H.; Nakao, Y.; Sakaki, S.; Kitagawa, S. Bidirectional chemo-switching of spin state in a microporous framework. *Angewandte Chemie* **2009**, *121*, 4861-4865.

[70] Southon, P. D.; Liu, L.; Fellows, E. A.; Price, D. J.; Halder, G. J.; Chapman, K. W.; Moubaraki, B.; Murray, K. S.; Létard, J.-F.; Kepert, C. J. Dynamic interplay between spin-crossover and host−guest function in a nanoporous metal-organic framework material. *Journal of the American Chemical Society* **2009**, *131*, 10998-11009.

[71] Culp, J. T.; Chen, D. L.; Liu, J.; Chirdon, D.; Kauffman, K.; Goodman, A.; Johnson, J. K. Effect of spin-crossover induced pore contraction on $CO_2$-host interactions in the porous coordination polymers [Fe(pyrazine)M(CN)$_4$](M= Ni, Pt). *European Journal of Inorganic Chemistry* **2013**, *2013*, 511-519.

[72] Lara, F. J. M.; Gaspar, A. B.; Aravena, D.; Ruiz, E.; Muñoz, M. C.; Ohba, M.; Ohtani, R.; Kitagawa, S.; Real, J. A. Enhanced bistability by guest inclusion in Fe (II) spin crossover porous coordination polymers. *Chemical Communications* **2012**, *48*, 4686-4688.

[73] Bartual‑Murgui, C.; Akou, A.; Salmon, L.; Molnár, G.; Thibault, C.; Real, J. A.; Bousseksou, A. guest effect on nanopatterned spin-crossover thin films. *Small* **2011**, *7*, 3385-3391.

[74] Bartual‑Murgui, C.; Salmon, L.; Akou, A.; Ortega‑Villar, N. A.; Shepherd, H. J.; Muñoz, M. C.; Molnár, G.; Real, J. A.; Bousseksou, A. Synergetic fffect of host-guest chemistry and spin crossover in 3D Hofmann-like metal-organic frameworks [Fe(bpac)M(CN)$_4$](M= Pt, Pd, Ni). *Chemistry-A European Journal* **2012**, *18*, 507-516.

[75] Akou, A.; Bartual-Murgui, C.; Abdul-Kader, K.; Lopes, M.; Molnár, G.; Thibault, C.; Vieu, C.; Salmon, L.; Bousseksou, A. Photonic gratings of the metal-organic framework {Fe(bpac)[Pt(CN)$_4$]} with synergetic spin transition and host-guest properties. *Dalton Transactions* **2013**, *42*, 16021-16028.

[76] Bartual‑Murgui, C.; Akou, A.; Shepherd, H. J.; Molnár, G.; Real, J. A.; Salmon, L.; Bousseksou, A. Tunable spin-crossover behavior of the Hofmann-like network {Fe(bpac)[Pt(CN)$_4$]} through host-guest chemistry. *Chemistry-A European Journal* **2013**, *19*, 15036-15043.

163

[77] Bartual-Murgui, C.; Akou, A.; Thibault, C.; Molnár, G.; Vieu, C.; Salmon, L.; Bousseksou, A. Spin-crossover metal-organic frameworks: promising materials for designing gas sensors. *Journal of Materials Chemistry C* **2015**, *3*, 1277-1285

[78] Bao, X.; Shepherd, H. J.; Salmon, L.; Molnár, G.; Tong, M. L.; Bousseksou, A. The effect of an active guest on the spin crossover phenomenon. *Angewandte Chemie* **2013**, *125*, 1236-1240.

[79] Aromi, G.; Barrios, L. A.; Roubeau, O.; Gamez, P. Triazoles and tetrazoles: Prime ligands to generate remarkable coordination materials. *Coordination Chemistry Reviews* **2011**, *255*, 485-546.

[80] Grosjean, A.; Daro, N.; Kauffmann, B.; Kaiba, A.; Letard, J. F.; Guionneau, P. The 1-D polymeric structure of the $Fe(NH_2trz)_3(NO_3)_2$ center dot $nH_2O$ (with n = 2) spin crossover compound proven by single crystal investigations. *Chemical Communications* **2011**, *47*, 12382-12384.

[81] Roubeau, O.; Gomez, J. M. A.; Balskus, E.; Kolnaar, J. J. A.; Haasnoot, J. G.; Reedijk, J. Spin-transition behaviour in chains of Fe-II bridged by 4-substituted 1,2,4-triazoles carrying alkyl tails. *New Journal of Chemistry* **2001**, *25*, 144-150.

[82] Grosjean, A.; Daro, N.; Kauffmann, B.; Kaiba, A.; Letard, J.-F.; Guionneau, P. The 1-D polymeric structure of the $[Fe(NH_2trz)_3](NO_3)_2$[middle dot]nH2O (with n = 2) spin crossover compound proven by single crystal investigations. *Chemical Communications* **2011**, *47*, 12382-12384.

[83] Urakawa, A.; Van Beek, W.; Monrabal-Capilla, M.; Galan-Mascaros, J. R.; Palin, L.; Milanesio, M. Combined, modulation enhanced X-ray powder diffraction and Raman spectroscopic study of structural transitions in the spin crossover material $Fe(Htrz)_2(trz)(BF_4)$. *Journal of Physical Chemistry C* **2011**, *115*, 1323-1329.

[84] Krivokapic, I.; Enachescu, C.; Bronisz, R.; Hauser, A. The interaction between the spin transition and a crystallographic phase transition in the spin-crossover compound $Fe(bbtr)_3(ClO_4)_2$: Nucleation, formation of domains and fluctuations. *Inorganica Chimica Acta* **2008**, *361*, 3616-3622.

[85] Haasnoot, J. G. Mononuclear, oligonuclear and polynuclear metal coordination compounds with 1, 2, 4-triazole derivatives as ligands. *Coordination Chemistry Reviews* **2000**, *200*, 131-185.

[86] Lavrenova, L. G.; Shakirova, O. G. Spin crossover and thermochromism of iron (II) coordination compounds with 1, 2, 4-triazoles and tris(pyrazol-1-yl) methanes. *European Journal of Inorganic Chemistry* **2013**, *2013*, 670-682.

[87] Roubeau, O. Triazole-based one-dimensional spin-crossover coordination polymers. *Chemistry-A European Journal* **2012**, *18*, 15230-15244.

[88] Martin, J.-P.; Zarembowitch, J.; Dworkin, A.; Haasnoot, J. G.; Codjovi, E. Solid-state effects in spin transitions: influence of iron(II) dilution on the magnetic and calorimetric properties of the series [FexNi$_{1-x}$ (4, 4'-bis (1, 2, 4-triazole))$_2$(NCS)$_2$]. cntdot. H$_2$O. *Inorganic Chemistry* **1994**, *33*, 2617-2623.

[89] Constant-Machado, H.; Linares, J.; Varret, F.; Haasnoot, J.; Martin, J.; Zarembowitch, J.; Dworkin, A.; Bousseksou, A. Dilution effects in a spin crossover system, modelled in terms of direct and indirect intermolecular interactions. *Journal de Physique I* **1996**, *6*, 1203-1216.

[90] Tayagaki, T.; Galet, A.; Molnár, G.; Munoz, M. C.; Zwick, A.; Tanaka, K.; Real, J.-A.; Bousseksou, A. Metal dilution effects on the spin-crossover properties of the three-dimensional coordination polymer Fe (pyrazine)[Pt (CN)$_4$]. *The Journal of Physical Chemistry B* **2005**, *109*, 14859-14867.

[91] Lavrenova, L. G.; Ikorskii, V. N.; Larionov, S. V.; Bogatikov, A. N.; Gaponik, P. N. A new ferromagnet-dichlorobis (1-allyltetrazole) copper complex compound. *Russian journal of inorganic chemistry* **1993**, *38*, 1416-1417.

[92] Shvedenkov, Y. G.; Ikorskii, V. N.; Lavrenova, L. G.; Drebushchak, V. A.; Yudina, N. G. 1A1 5T2 Spin transition in the solid phases of FexNi$_{1-x}$(ATr)$_3$(NO$_3$)$_2$ (ATr = 4-amino-1, 2, 4-triazole). *Journal of structural chemistry* **1997**, *38*, 578-584.

[93] Martin, J.-P.; Zarembowitch, J.; Bousseksou, A.; Dworkin, A.; Haasnoot, J. G.; Varret, F. Solid state effects on spin transitions: magnetic, calorimetric, and moessbauer-effect properties of [FexCo$_{1-x}$(4, 4'-bis-1, 2, 4-triazole)$_2$(NCS)$_2$]. cntdot. H$_2$O mixed-crystal compounds. *Inorganic Chemistry* **1994**, *33*, 6325-6333.

[94] Krçber, J.; Codjovi, E.; Kahn, O. F. Groli re, C. Jay. A spin transition system with a thermal hysteresis at room temperature. *Journal of the American Chemical Society* **1993**, *115*, 9810-9811.

[95] Kahn, O.; Martinez, C. J. Spin-transition polymers: From molecular materials toward memory devices. *Science* **1998**, *279*, 44-48.

[96] J. van Koningsbruggen, P.; Garcia, Y.; Codjovi, E.; Lapouyade, R.; Kahn, O.; Fournes, L.; Rabardel, L. Non-classical Fe$^{II}$ spin-crossover behaviour in polymeric iron(II) compounds of formula [Fe(NH$_2$trz)$_3$]x2xH$_2$O (NH$_2$trz = 4-amino-1,2,4-triazole; X = derivatives of naphthalene sulfonate). *Journal of Materials Chemistry* **1997**, *7*, 2069-2075.

[97] Dickson, D. P. E.; Berry, F. J.: *Mössbauer spectroscopy*; Cambridge University Press, **2005**.

[98] Bousseksou, A.; McGarvey, J. J.; Varret, F.; Real, J. A.; Tuchagues, J.-P.; Dennis, A. C.; Boillot, M. L. Raman spectroscopy of the high-and low-spin states of the spin crossover complex Fe

(phen)$_2$(NCS)$_2$: an initial approach to estimation of vibrational contributions to the associated entropy change. *Chemical Physics Letters* **2000**, *318*, 409-416.

[99] Konig, E. Nature and dynamics of the spin-state interconversion in metal complexes. *Structure and Bonding* **1991**, *76*, 51-152.

[100] Akou, A.; Bartual-Murgui, C.; Abdul-Kader, K.; Lopes, M.; Molnar, G.; Thibault, C.; Vieu, C.; Salmon, L.; Bousseksou, A. Photonic gratings of the metal-organic framework {Fe(bpac)[Pt(CN)$_4$]} with synergetic spin transition and host-guest properties. *Dalton Transactions* **2013**, *42*, 16021-16028.

[101] Quintero, C. M.; Costa, J. S.; Demont, P.; Molnár, G.; Salmon, L.; Shepherd, H. J.; Bousseksou, A. Spin crossover composite materials for electrothermomechanical actuators. *Journal of Materials Chemistry C* **2014**, *2*, 2949-2955.

[102] Cavallini, M.; Bergenti, I.; Milita, S.; Ruani, G.; Salitros, I.; Qu, Z. R.; Chandrasekar, R.; Ruben, M. Micro-and nanopatterning of spin-transition compounds into logical structures. *Angewandte Chemie International Edition* **2008**, *47*, 8596-8600.

[103] Varret, F.; Boukheddaden, K.; Codjovi, E.; Goujon, A. Molecular switchable solids: towards photo-controlled magnetism. *Hyperfine interactions* **2005**, *165*, 37-47.

[104] Bousseksou, A.; Molnár, G.; Demont, P.; Menegotto, J. Observation of a thermal hysteresis loop in the dielectric constant of spin crossover complexes: towards molecular memory devices. *Journal of Materials Chemistry* **2003**, *13*, 2069-2071.

[105] Bonhommeau, S.; Guillon, T.; Lawson Daku, L. M.; Demont, P.; Sanchez Costa, J.; Létard, J. F.; Molnár, G.; Bousseksou, A. Photoswitching of the dielectric constant of the spin-crossover complex [Fe (L)(CN)$_2$]· H$_2$O. *Angewandte Chemie* **2006**, *118*, 1655-1659.

[106] Linares, J.; Codjovi, E.; Garcia, Y. Pressure and temperature spin crossover sensors with optical detection. *Sensors* **2012**, *12*, 4479-4492.

[107] Kahn, O.; Kröber, J.; Jay, C. Spin transition molecular materials for displays and data recording. *Advanced Materials* **1992**, *4*, 718-728.

[108] Luo, J.; Wu, H.; He, C.; Li, A.; Yang, W.; Cao, Y. Enhanced open-circuit voltage in polymer solar cells. *Applied Physics Letters* **2009**, *95*, 043301-043301-043303.

[109] Matsuda, M.; Isozaki, H.; Tajima, H. Electroluminescence quenching caused by a spin-crossover transition. *Chemistry Letters* **2008**, *37*, 374-375.

[110] Venezia, J. "Katharine Burr Blodgett: An innovative, accomplished schenectady native". *The Free George* **Retrieved 15 October 2014**.

[111] Soyer, H.; Mingotaud, C.; Boillot, M. L.; Delhaes, P. Spin crossover of a langmuir−blodgett film based on an Aamphiphilic Iron(II) complex. *Langmuir* **1998**, *14*, 5890-5895.

[112] Soyer, H.; Dupart, E.; Gómez-García, C. J.; Mingotaud, C.; Delhaès, P. First magnetic observation of a spin crossover in a langmuir-blodgett film. *Advanced Materials* **1999**, *11*, 382-384.

[113] Kitchen, J. A.; White, N. G.; Gandolfi, C.; Albrecht, M.; Jameson, G. N. L.; Tallon, J. L.; Brooker, S. Room-temperature spin crossover and Langmuir-Blodgett film formation of an iron(ii) triazole complex featuring a long alkyl chain substituent: the tail that wags the dog. *Chemical Communications* **2010**, *46*, 6464-6466.

[114] Cavallini, M.; Bergenti, I.; Milita, S.; Kengne, J. C.; Gentili, D.; Ruani, G.; Salitros, I.; Meded, V.; Ruben, M. Thin deposits and patterning of room-temperature-switchable one-dimensional spin-crossover compounds. *Langmuir* **2011**, *27*, 4076-4081.

[115] Kuroiwa, K.; Shibata, T.; Sasaki, S.; Ohba, M.; Takahara, A.; Kunitake, T.; Kimizuka, N. Supramolecular control of spin-crossover phenomena in lipophilic Fe (II)-1, 2, 4-triazole complexes. *Journal of Polymer Science Part A: Polymer Chemistry* **2006**, *44*, 5192-5202.

[116] Kuroiwa, K.; Shibata, T.; Sasaki, S.; Ohba, M.; Takahara, A.; Kunitake, T.; Kimizuka, N. Supramolecular control of spin-crossover phenomena in lipophilic Fe(II)-1,2,4-triazole complexes. *Journal of Polymer Science Part A: Polymer Chemistry* **2006**, *44*, 5192-5202.

[117] A. Bousseksou, C. V., J.-F. Létard, P. Demont, J.-P. Tuchagues, L. Malaquin, J. Menegotto, L. Salmon. Mémoire moléculaire et son procédé de fabrication (Molecular memory and method for making same). Brevet FR2829293, (**2003**), EP1430552 (**2004**).

[118] Matsuda, M.; Tajima, H. Thin film of a spin crossover complex $[Fe(dpp)_2](BF_4)_2$. *Chemistry Letters* **2007**, *36*, 700-701.

[119] Félix, G.; Abdul-Kader, K.; Mahfoud, T.; Gural'skiy, I. y. A.; Nicolazzi, W.; Salmon, L.; Molnár, G.; Bousseksou, A. Surface plasmons reveal spin crossover in nanometric layers. *Journal of the American Chemical Society* **2011**, *133*, 15342-15345.

[120] Tanaka, D.; Aketa, N.; Tanaka, H.; Tamaki, T.; Inose, T.; Akai, T.; Toyama, H.; Sakata, O.; Tajiri, H.; Ogawa, T. Thin films of spin-crossover coordination polymers with large thermal hysteresis loops prepared by nanoparticle spin coating. *Chemical Communications* **2014**, *50*, 10074-10077.

[121] Nakamoto, A.; Kojima, N.; XiaoJun, L.; Moritomo, Y.; Nakamura, A. Demonstration of the thermally induced high spin-low spin transition for a transparent spin crossover complex film, [Fe(II)(Htrz)$_3$]-Nafion (trz = triazole). *Polyhedron* **2005**, *24*, 2909-2912.

[122] Nakamoto, A.; Ono, Y.; Kojima, N.; Matsumura, D.; Yokoyama, T. Spin crossover complex film, [Fe$^{II}$(H-trz)$_3$]-Nafion, with a spin transition around room temperature. *Chemistry Letters* **2003**, *32*, 336-337.

[123] Ansell, M. A.; Zeppenfeld, A. C.; Yoshimoto, K.; Cogan, E. B.; Page, C. J. Self-assembled cobalt−diisocyanobenzene multilayer thin films. *Chemistry of Materials* **1996**, *8*, 591-594.

[124] Bell, C. M.; Keller, S. W.; Lynch, V. M.; Mallouk, T. E. New solids and surfaces, via coordination chemistry. *Materials Chemistry and Physics* **1993**, *35*, 225-232.

[125] Lin, C.; Kagan, C. R. Layer-by-layer growth of metal−metal bonded supramolecular thin films and its use in the fabrication of lateral nanoscale devices. *Journal of the American Chemical Society* **2002**, *125*, 336-337.

[126] Cobo, S.; Molnár, G.; Real, J. A.; Bousseksou, A. Multilayer sequential assembly of thin films that display room-temperature spin crossover with hysteresis. *Angewandte Chemie International Edition* **2006**, *45*, 5786-5789.

[127] Salmon, L.; Molnár, G.; Cobo, S.; Oulié, P.; Etienne, M.; Mahfoud, T.; Demont, P.; Eguchi, A.; Watanabe, H.; Tanaka, K. Re-investigation of the spin crossover phenomenon in the ferrous complex [Fe (HB(pz)$_3$)$_2$]. *New Journal of Chemistry* **2009**, *33*, 1283-1289.

[128] Shi, S.; Schmerber, G.; Arabski, J.; Beaufrand, J.-B.; Kim, D. J.; Boukari, S.; Bowen, M.; Kemp, N. T.; Viart, N.; Rogez, G.; Beaurepaire, E.; Aubriet, H.; Petersen, J.; Becker, C.; Ruch, D. Study of molecular spin-crossover complex Fe(phen)$_2$(NCS)$_2$ thin films. *Applied Physics Letters* **2009**, *95*, -.

[129] Naggert, H.; Bannwarth, A.; Chemnitz, S.; von Hofe, T.; Quandt, E.; Tuczek, F. First observation of light-induced spin change in vacuum deposited thin films of iron spin crossover complexes. *Dalton Transactions* **2011**, *40*, 6364-6366.

[130] Pronschinske, A.; Bruce, R. C.; Lewis, G.; Chen, Y.; Calzolari, A.; Buongiorno-Nardelli, M.; Shultz, D. A.; You, W.; Dougherty, D. B. Iron (II) spin crossover films on Au (111): scanning probe microscopy and photoelectron spectroscopy. *Chemical Communications* **2013**, *49*, 10446-10452.

[131] Pronschinske, A.; Chen, Y.; Lewis, G. F.; Shultz, D. A.; Calzolari, A.; Buongiorno Nardelli, M.; Dougherty, D. B. Modification of molecular spin crossover in ultrathin films. *Nano letters* **2013**, *13*, 1429-1434.

[132] Gopakumar, T. G.; Bernien, M.; Naggert, H.; Matino, F.; Hermanns, C. F.; Bannwarth, A.; Mühlenberend, S.; Krüger, A.; Krüger, D.; Nickel, F.; Walter, W.; Berndt, R.; Kuch, W.; Tuczek, F. Spin-crossover complex on Au(111): structural and electronic differences between mono-and multilayers. *Chemistry- A European Journal* **2013**, *19*, 15702-15709.

[133] Hammond, P. T. Form and function in multilayer assembly: New applications at the nanoscale. *Advanced Materials* **2004**, *16*, 1271-1293.

[134] Molnar, G.; Cobo, S.; Real, J. A.; Carcenac, F.; Daran, E.; Vien, C.; Bousseksou, A. A combined top-down/bottom-up approach for the nanoscale patterning of spin-crossover coordination polymers. *Advanced Materials* **2007**, *19*, 2163.

[135] Bartual-Murgui, C.; Akou, A.; Salmon, L.; Molnár, G.; Thibault, C.; Real, J. A.; Bousseksou, A. Guest effect on nanopatterned spin-crossover thin films. *Small* **2011**, *7*, 3385-3391.

[136] Bartual-Murgui, C.; Akou, A.; Shepherd, H. J.; Molnár, G.; Real, J. A.; Salmon, L.; Bousseksou, A. Tunable spin-crossover behavior of the Hofmann-like network {Fe(bpac)[Pt(CN)$_4$]} through host-guest chemistry. *Chemistry- A European Journal* **2013**, *19*, 15036-15043.

[137] Bartual-Murgui, C.; Akou, A.; Thibault, C.; Molnar, G.; Vieu, C.; Salmon, L.; Bousseksou, A. Spin-crossover metal-organic frameworks: promising materials for designing gas sensors. *Journal of Materials Chemistry C* **2015**, *3*, 1277-1285.

[138] Bartual-Murgui, C.; Ortega-Villar, N. A.; Shepherd, H. J.; Munoz, M. C.; Salmon, L.; Molnar, G.; Bousseksou, A.; Real, J. A. Enhanced porosity in a new 3D Hofmann-like network exhibiting humidity sensitive cooperative spin transitions at room temperature. *Journal of Materials Chemistry* **2011**, *21*, 7217-7222.

[139] Bartual-Murgui, C.; Salmon, L.; Akou, A.; Thibault, C.; Molnar, G.; Mahfoud, T.; Sekkat, Z.; Real, J. A.; Bousseksou, A. High quality nano-patterned thin films of the coordination compound {Fe(pyrazine)[Pt(CN)$_4$]} deposited layer-by-layer. *New Journal of Chemistry* **2011**, *35*, 2089-2094.

[140] Bartual-Murgui, C.; Akou, A.; Thibault, C.; Molnar, G.; Vieu, C.; Salmon, L.; Bousseksou, A. Spin-crossover metal-organic frameworks: promising materials for designing gas sensors. *Journal of Materials Chemistry C* **2015**, *3*, 1277-1285.

[141] Xia, Y.; Whitesides, G. M. Soft lithography. *Angewandte Chemie International Edition* **1998**, *37*, 550-575.

[142] Thibault, C.; Molnár, G.; Salmon, L.; Bousseksou, A.; Vieu, C. Soft lithographic patterning of spin crossover nanoparticles. *Langmuir* **2009**, *26*, 1557-1560.

[143] Botcha, A. K.; Basak, S.; Chandrasekar, R. Lithographically organized 1D nano-tape arrays composed of solution processable above room temperature spin crossover Fe (ii) coordination polymer. *RSC Advances* **2014**, *4*, 34760-34763.

[144] Pileni, M. Reverse micelles as microreactors. *The Journal of physical chemistry* **1993**, *97*, 6961-6973.

[145] Forestier, T.; Mornet, S.; Daro, N.; Nishihara, T.; Mouri, S.-i.; Tanaka, K.; Fouché, O.; Freysz, E.; Létard, J.-F. Nanoparticles of iron (II) spin-crossover. *Chemical Communications* **2008**, 4327-4329.

[146] Tokarev, A.; Salmon, L.; Guari, Y.; Nicolazzi, W.; Molnár, G.; Bousseksou, A. Cooperative spin crossover phenomena in [Fe (NH$_2$trz)$_3$](tosylate)$_2$ nanoparticles. *Chemical Communications* **2010**, *46*, 8011-8013.

[147] Gural'skiy, I. y. A.; Quintero, C. M.; Molnár, G.; Fritsky, I. O.; Salmon, L.; Bousseksou, A. Synthesis of spin-crossover nano-and micro-objects in homogeneous media. *Chemistry-A European Journal* **2012**, *18*, 9946-9954.

[148] Larionova, J.; Salmon, L.; Guari, Y.; Tokarev, A.; Molvinger, K.; Molnár, G.; Bousseksou, A. Towards the ultimate size limit of the memory effect in spin-crossover solids. *Angewandte Chemie International Edition* **2008**, *47*, 8236-8240.

[149] Tokarev, A.; Long, J.; Guari, Y.; Larionova, J.; Quignard, F.; Agulhon, P.; Robitzer, M.; Molnár, G.; Salmon, L.; Bousseksou, A. Spin crossover polysaccharide nanocomposites. *New Journal of Chemistry* **2013**, *37*, 3420-3432.

[150] Faulmann, C.; Chahine, J.; Malfant, I.; de Caro, D.; Cormary, B.; Valade, L. A facile route for the preparation of nanoparticles of the spin-crossover complex [Fe(Htrz)$_2$(trz)](BF$_4$) in xerogel transparent composite films. *Dalton Transactions* **2011**, *40*, 2480-2485.

[151] Durand, P.; Pillet, S.; Bendeif, E.-E.; Carteret, C.; Bouazaoui, M.; El Hamzaoui, H.; Capoen, B.; Salmon, L.; Hébert, S.; Ghanbaja, J. Room temperature bistability with wide thermal hysteresis in a spin crossover silica nanocomposite. *Journal of Materials Chemistry C* **2013**, *1*, 1933-1942.

[152] Boldog, I.; Gaspar, A. B.; Martínez, V.; Pardo-Ibañez, P.; Ksenofontov, V.; Bhattacharjee, A.; Gütlich, P.; Real, J. A. Spin-crossover nanocrystals with magnetic, optical, and structural bistability near room temperature. *Angewandte Chemie International Edition* **2008**, *47*, 6433-6437.

[153] Volatron, F.; Catala, L.; Rivière, E.; Gloter, A.; Stéphan, O.; Mallah, T. Spin-crossover coordination nanoparticles. *Inorganic Chemistry* **2008**, *47*, 6584-6586.

[154] Coronado, E.; Galán-Mascarós, J. R.; Monrabal-Capilla, M.; García-Martínez, J.; Pardo-Ibáñez, P. Bistable spin-crossover nanoparticles showing magnetic thermal hysteresis near room temperature. *Advanced Materials* **2007**, *19*, 1359-1361.

[155] Forestier, T.; Kaiba, A.; Pechev, S.; Denux, D.; Guionneau, P.; Etrillard, C.; Daro, N.; Freysz, E.; Létard, J.-F. Nanoparticles of [Fe(NH$_2$-trz)$_3$]Br$_2 \cdot$ 3H$_2$O (NH$_2$-trz = 2-Amino-1,2,4-triazole) prepared by the reverse micelle technique: influence of particle and coherent domain sizes on spin-crossover properties. *Chemistry-A European Journal* **2009**, *15*, 6122-6130.

[156] Nguyen, L. L.; Guillot, R.; Laisney, J.; Rechignat, L.; Bedoui, S.; Molnar, G.; Riviere, E.; Boillot, M.-L. Fe(Me$_2$-bpy)$_2$(NCSe)$_2$ spin-crossover micro- and nanoparticles showing spin-state switching above 250 K. *New Journal of Chemistry* **2015**, 39, 1603-1610.

[157] Tissot, A.; Rechignat, L.; Bousseksou, A.; Boillot, M.-L. Micro-and nanocrystals of the iron (iii) spin-transition material [Fe$^{III}$(3-MeO-SalEen)$_2$]PF$_6$. *Journal of Materials Chemistry* **2012**, *22*, 3411-3419.

[158] Raza, Y.; Volatron, F.; Moldovan, S.; Ersen, O.; Huc, V.; Martini, C.; Brisset, F.; Gloter, A.; Stephan, O.; Bousseksou, A.; Catala, L.; Mallah, T. Matrix-dependent cooperativity in spin crossover Fe(pyrazine)Pt(CN)$_4$ nanoparticles. *Chemical Communications* **2011**, *47*, 11501-11503.

[159] Tanasa, R.; Laisney, J.; Stancu, A.; Boillot, M.-L.; Enachescu, C. Hysteretic behavior of Fe(phen)$_2$ (NCS)$_2$ spin-transition microparticles vs. the environment: A huge reversible component resolved by first order reversal curves. *Applied Physics Letters* **2014**, *104*, 031909.

[160] Salmon, L.; Molnár, G.; Zitouni, D.; Quintero, C.; Bergaud, C.; Micheau, J.-C.; Bousseksou, A. A novel approach for fluorescent thermometry and thermal imaging purposes using spin crossover nanoparticles. *Journal of Materials Chemistry* **2010**, *20*, 5499-5503.

[161] Alam, M. S.; Stocker, M.; Gieb, K.; Müller, P.; Haryono, M.; Student, K.; Grohmann, A. Spin-state patterns in surface-grafted beads of Iron (II) complexes. *Angewandte Chemie International Edition* **2010**, *49*, 1159-1163.

[162] Aravena, D.; Ruiz, E. Coherent transport through spin-crossover single molecules. *Journal of the American Chemical Society* **2011**, *134*, 777-779.

[163] Etrillard, C.; Faramarzi, V.; Dayen, J.-F.; Letard, J.-F.; Doudin, B. Photoconduction in [Fe(Htrz)$_2$ (trz)](BF$_4$)$\cdot$H$_2$O nanocrystals. *Chemical Communications* **2011**, *47*, 9663-9665.

[164] Faulmann, C.; Jacob, K.; Dorbes, S.; Lampert, S.; Malfant, I.; Doublet, M.-L.; Valade, L.; Real, J. A. Electrical conductivity and spin crossover: a new achievement with a metal bis dithiolene complex. *Inorganic Chemistry* **2007**, *46*, 8548-8559.

[165] Mahfoud, T.; Molnár, G.; Cobo, S.; Salmon, L.; Thibault, C.; Vieu, C.; Demont, P.; Bousseksou, A. Electrical properties and non-volatile memory effect of the [Fe (HB(pz)$_3$)$_2$] spin crossover complex integrated in a microelectrode device. *Applied Physics Letters* **2011**, *99*, 053307.

[166] Meded, V.; Bagrets, A.; Fink, K.; Chandrasekar, R.; Ruben, M.; Evers, F.; Bernand-Mantel, A.; Seldenthuis, J.; Beukman, A.; Van der Zant, H. Electrical control over the Fe (II) spin crossover in a single molecule: Theory and experiment. *Physical Review B* **2011**, *83*, 245415.

[167] Nihei, M.; Takahashi, N.; Nishikawa, H.; Oshio, H. Spin-crossover behavior and electrical conduction property in iron (II) complexes with tetrathiafulvalene moieties. *Dalton Transactions* **2011**, *40*, 2154-2156.

[168] Prins, F.; Monrabal‑Capilla, M.; Osorio, E. A.; Coronado, E.; van der Zant, H. S. Room-temperature electrical addressing of a bistable spin-crossover molecular system. *Advanced Materials* **2011**, *23*, 1545-1549.

[169] Takahashi, K.; Cui, H.-B.; Okano, Y.; Kobayashi, H.; Einaga, Y.; Sato, O. Electrical conductivity modulation coupled to a high-spin-low-spin conversion in the molecular system [Fe$^{III}$(qsal)$_2$][Ni(dmit)$_2$]$_3$·CH$_3$CN·H$_2$O. *Inorganic Chemistry* **2006**, *45*, 5739-5741.

[170] Rotaru, A.; Molnár, G.; Salmon, L.; Demont, P.; Bousseksou, A. Spin state dependence of electrical conductivity of spin crossover materials. *Chemical Communications* **2013**, *48*, 4163-4165.

[171] Koo, Y. S.; Galán‑Mascarós, J. R. Spin crossover probes confer multistability to organic conducting polymers. *Advanced Materials* **2014**, *26*, 6785-6789.

[172] Dugay, J.; Giménez-Marqués, M.; Kozlova, T.; Zandbergen, H. W.; Coronado, E.; van der Zant, H. S. Spin switching in electronic devices based on 2D assemblies of spin-crossover nanoparticles. *Advanced Materials* **2015**, 18, 1288–1293.

[173] Cobo, S.; Ostrovskii, D.; Bonhommeau, S.; Vendier, L.; Molnár, G.; Salmon, L.; Tanaka, K.; Bousseksou, A. Single-laser-shot-induced complete bidirectional spin transition at room temperature in single crystals of (Fe$^{II}$(pyrazine)(Pt(CN)$_4$)). *Journal of the American Chemical Society* **2008**, *130*, 9019-9024.

[174] Shepherd, H. J.; Il'ya, A.; Quintero, C. M.; Tricard, S.; Salmon, L.; Molnár, G.; Bousseksou, A. Molecular actuators driven by cooperative spin-state switching. *Nature communications* **2013**, *4*.

[175] Chen, Y.-C.; Meng, Y.; Ni, Z.-P.; Tong, M.-L. Synergistic electrical bistability in a conductive spin crossover heterostructure. *Journal of Materials Chemistry C* **2015**.

[176] Shepherd, H. J.; Molnár, G.; Nicolazzi, W.; Salmon, L.; Bousseksou, A. Spin crossover at the nanometre scale. *European Journal of Inorganic Chemistry* **2013**, *2013*, 653-661.

[177] Arnaud, C.; Forestier, T.; Daro, N.; Freysz, E.; Létard, J.-F.; Pauliat, G.; Roosen, G. Observation of an asymmetry in the thermal hysteresis loop at the scale of a single spin-crossover particle. *Chemical Physics Letters* **2009**, *470*, 131-135.

[178] Boldog, I.; Gaspar, A. B.; Martínez, V.; Pardo- Ibañez, P.; Ksenofontov, V.; Bhattacharjee, A.; Gütlich, P.; Real, J. A. Spin-crossover nanocrystals with magnetic, optical, and structural bistability near room temperature. *Angewandte Chemie* **2008**, *120*, 6533-6537.

[179] Chakraborty, P.; Boillot, M. L.; Tissot, A.; Hauser, A. Photoinduced relaxation dynamics in iron (II) spin-crossover nanoparticles: the significance of crystallinity. *Angewandte Chemie International Edition* **2013**, *52*, 7139-7142.

[180] Coronado, E.; Galán-Mascarós, J. R.; Monrabal-Capilla, M.; García-Martínez, J.; Pardo-Ibáñez, P. Bistable spin-crossover nanoparticles showing magnetic thermal hysteresis near room temperature. *Advanced Materials* **2007**, *19*, 1359-1361.

[181] Forestier, T.; Kaiba, A.; Pechev, S.; Denux, D.; Guionneau, P.; Etrillard, C.; Daro, N.; Freysz, E.; Létard, J. F. Nanoparticles of [Fe (NH$_2$-trz)$_3$] Br$_2$· 3H$_2$O (NH$_2$-trz = 2-Amino-1, 2, 4-triazole) prepared by the reverse micelle technique: influence of particle and coherent domain sizes on spin-crossover properties. *Chemistry-A European Journal* **2009**, *15*, 6122-6130.

[182] Galán-Mascarós, J. R.; Coronado, E.; Forment-Aliaga, A.; Monrabal-Capilla, M. a.; Pinilla-Cienfuegos, E.; Ceolin, M. Tuning size and thermal hysteresis in bistable spin crossover nanoparticles. *Inorganic Chemistry* **2010**, *49*, 5706-5714.

[183] Il'ya, A.; Molnár, G.; Fritsky, I. O.; Salmon, L.; Bousseksou, A. Synthesis of [Fe(hptrz)$_3$](OTs)$_2$ spin crossover nanoparticles in microemulsion. *Polyhedron* **2012**, *38*, 245-250.

[184] Larionova, J.; Salmon, L.; Guari, Y.; Tokarev, A.; Molvinger, K.; Molnár, G.; Bousseksou, A. Towards the ultimate size limit of the memory effect in spin-crossover solids. *Angewandte Chemie* **2008**, *120*, 8360-8364.

[185] Létard, J.-F.; Guionneau, P.; Goux-Capes, L.: Towards spin crossover applications. In *Spin Crossover in Transition Metal Compounds Iii*; Springer, **2004**, 221-249.

[186] Martínez, V.; Boldog, I.; Gaspar, A. B.; Ksenofontov, V.; Bhattacharjee, A.; Gu̇lich, P.; Real, J. A. Spin crossover phenomenon in nanocrystals and nanoparticles of [Fe (3-Fpy)$_2$M(CN)$_4$] (MII= Ni, Pd, Pt) two-dimensional coordination polymers. *Chemistry of Materials* **2010**, *22*, 4271-4281.

[187] Neville, S. M.; Etrillard, C.; Asthana, S.; Létard, J. F. Light-induced stored information in nanoparticles. *European Journal of Inorganic Chemistry* **2010**, *2010*, 282-288.

[188] Raza, Y.; Volatron, F.; Moldovan, S.; Ersen, O.; Huc, V.; Martini, C.; Brisset, F.; Gloter, A.; Stephan, O.; Bousseksou, A. Matrix-dependent cooperativity in spin crossover Fe (pyrazine)Pt(CN)$_4$ nanoparticles. *Chemical Communication* **2011**, *47*, 11501-11503.

[189] Rotaru, A.; Varret, F.; Gindulescu, A.; Linares, J.; Stancu, A.; Létard, J.-F.; Forestier, T.; Etrillard, C. Size effect in spin-crossover systems investigated by FORC measurements, for surfaced [Fe(NH$_2$-trz)$_3$](Br)$_2$·3H$_2$O nanoparticles: reversible contributions and critical size. *The European Physical Journal B-Condensed Matter and Complex Systems* **2011**, *84*, 439-449.

[190] Tissot, A.; Bardeau, J.-F.; Rivière, E.; Brisset, F.; Boillot, M.-L. Thermo-and photoswitchable spin-crossover nanoparticles of an iron (II) complex trapped in transparent silica thin films. *Dalton Transactions* **2010**, *39*, 7806-7812.

[191] Tissot, A.; Enachescu, C.; Boillot, M.-L. Control of the thermal hysteresis of the prototypal spin-transition FeII(phen)$_2$(NCS)$_2$ compound via the microcrystallites environment: experiments and mechanoelastic model. *Journal of Materials Chemistry* **2012**, *22*, 20451-20457.

[192] Tokarev, A.; Salmon, L.; Guari, Y.; Molnár, G.; Bousseksou, A. Synthesis of spin crossover nano-objects with different morphologies and properties. *New Journal of Chemistry* **2011**, *35*, 2081-2088.

[193] van der Veen, R. M.; Kwon, O.-H.; Tissot, A.; Hauser, A.; Zewail, A. H. Single-nanoparticle phase transitions visualized by four-dimensional electron microscopy. *Nature chemistry* **2013**, *5*, 395-402.

[194] Volatron, F.; Catala, L.; Rivièe, E.; Gloter, A.; Stép an, O.; Mallah, T. Spin-crossover coordination nanoparticles. *Inorganic Chemistry* **2008**, *47*, 6584-6586.

[195] Zhang, L.; Wang, J.-J.; Xu, G.-C.; Li, J.; Jia, D.-Z.; Gao, S. Tuning size and magnetic thermal hysteresis in a new near room temperature spin crossover compound. *Dalton Transactions* **2013**, *42*, 8205-8208.

[196] Félix, G.; Nicolazzi, W.; Salmon, L.; Molnár, G.; Perrier, M.; Maurin, G.; Larionova, J.; Long, J.; Guari, Y.; Bousseksou, A. Enhanced cooperative interactions at the nanoscale in ppin-crossover materials with a first-order phase transition. *Physical review letters* **2013**, *110*, 235701.

[197] Stoleriu, L.; Chakraborty, P.; Hauser, A.; Stancu, A.; Enachescu, C. Thermal hysteresis in spin-crossover compounds studied within the mechanoelastic model and its potential application to nanoparticles. *Physical Review B* **2011**, *84*, 134102.

[198] Slimani, A.; Boukheddaden, K.; Varret, F.; Oubouchou, H.; Nishino, M.; Miyashita, S. Microscopic spin-distortion model for switchable molecular solids: Spatiotemporal study of the deformation field and local stress at the thermal spin transition. *Physical Review B* **2013**, *87*, 014111.

[199] Muraoka, A.; Boukheddaden, K.; Linarès, J.; Varret, F. Two-dimensional Ising-like model with specific edge effects for spin-crossover nanoparticles: A Monte Carlo study. *Physical Review B* **2011**, *84*, 054119.

[200] Kawamoto, T.; Abe, S. Thermal hysteresis loop of the spin-state in nanoparticles of transition metal complexes: Monte Carlo simulations on an Ising-like model. *Chemical Communication* **2005**, 3933-3935.

[201] Félix, G.; Nicolazzi, W.; Mikolasek, M.; Molnár, G.; Bousseksou, A. Non-extensivity of thermodynamics at the nanoscale in molecular spin crossover materials: a balance between surface and volume. *Physical Chemistry Chemical Physics* **2014**, *16*, 7358-7367.

[202] Molnár, G.; Niel, V.; Gaspar, A. B.; Real, J.-A.; Zwick, A.; Bousseksou, A.; McGarvey, J. J. Vibrational spectroscopy of cyanide-bridged, iron (II) spin-crossover coordination polymers: Estimation of vibrational contributions to the entropy change associated with the spin transition. *The Journal of Physical Chemistry B* **2002**, *106*, 9701-9707.

[203] Niel, V.; Martinez-Agudo, J. M.; Munoz, M. C.; Gaspar, A. B.; Real, J. A. Cooperative spin crossover behavior in cyanide-bridged Fe (II)-M (II) bimetallic 3D Hofmann-like networks (M= Ni, Pd, and Pt). *Inorganic Chemistry* **2001**, *40*, 3838-3839.

[204] Dubiel, S. M.; Cieślak, J.; Costa, B. F. O. Debye temperature of disordered bcc-Fe–Cr alloys. *Journal of Physics: Condensed Matter* **2010**, *22*, 055402.

[205] Schulz, C. E.; Wyllie, G. R. A.; Scheidt, W. R.: Mössbauer studies of Fe (II)-nitrosyl porphyrin model compounds. In *Hyperfine Interactions (C)*; Springer, **2002**, 321-324.

[206] Zadrozny, J. M.; Xiao, D. J.; Long, J. R.; Atanasov, M.; Neese, F.; Grandjean, F.; Long, G. J. Mössbauer spectroscopy as a probe of magnetization dynamics in the linear iron (I) and iron (II) complexes [Fe (C (SiMe$_3$)$_3$)$_2$]$^{1-/0}$. *Inorganic chemistry* **2013**, *52*, 13123-13131.

[207] Greenwood, N. N.; Gibb, T. C.: *Mössbauer spectroscopy*; CRC Press, **1971**.

[208] Boukheddaden, K.; Varret, F. A simple formula for the thickness correction of symmetrical mössbauer doublets. Application to spin cross-over systems. *Hyperfine interactions* **1992**, *72*, 349-356.

[209] Gütlich, P.; Köppen, H.; Steinhäuser, H. G. Deuterium isotope effect on the high-spin α low-spin transition in deuterated solvates of tris (2-picolylamine) iron (II) chloride. *Chemical Physics Letters* **1980**, *74*, 475-480.

[210] Konig, E.; Ritter, G.; Kulshreshtha, S. K. The nature of spin-state transitions in solid complexes of iron (II) and the interpretation of some associated phenomena. *Chemical Reviews* **1985**, *85*, 219-234.

[211] Yousif, A. A.; Winkler, H.; Toftlund, H.; Trautwein, A. X.; Herber, R. H. Lattice dynamics of some spin-crossover complexes: Mössbauer and VTFTIR measurements. *Journal of Physics: Condensed Matter* **1989**, *1*, 7103.

[212] Yu, Z.; Schmitt, G.; Hofmann, S.; Spiering, H.; Hsia, Y. F.; Gütlich, P. Lamb-Mössbauer factor in the spin crossover compound Fe (tpa)(NCS)$_2$. *Hyperfine Interactions* **1994**, *93*, 1459-1463.

[213] Paulsen, H.; Winkler, H.; Trautwein, A.; Grünsteudel, H.; Rusanov, V.; Toftlund, H. Measurement and simulation of nuclear inelastic-scattering spectra of molecular crystals. *Physical Review B* **1999**, *59*, 975.

[214] Ronayne, K. L.; Paulsen, H.; Höfer, A.; Dennis, A. C.; Wolny, J. A.; Chumakov, A. I.; Schünemann, V.; Winkler, H.; Spiering, H.; Bousseksou, A. Vibrational spectrum of the spin crossover complex [Fe (phen)$_2$(NCS)$_2$] studied by IR and Raman spectroscopy, nuclear inelastic scattering and DFT calculations. *Physical Chemistry Chemical Physics* **2006**, *8*, 4685-4693.

[215] Wolny, J. A.; Diller, R.; Schünemann, V. Vibrational spectroscopy of mono- and polynuclear spin-crossover systems. *European Journal of Inorganic Chemistry* **2012**, *2012*, 2635-2648.

[216] Wolny, J. A.; Rackwitz, S.; Achterhold, K.; Muffler, K.; Schünemann, V. Nuclear inelastic scattering of 1D polymeric Fe (II) complexes of 1, 2, 4-aminotriazole in their high-spin and low-spin state. *Hyperfine interactions* **2012**, *204*, 129-132.

[217] Chumakov, A.; Sturhahn, W. Experimental aspects of inelastic nuclear resonance scattering. *Hyperfine interactions* **1999**, *123*, 781-808.

[218] Paulsen, H.; Winkler, H.; Trautwein, A. X.; Grünsteudel, H.; Rusanov, V.; Toftlund, H. Measurement and simulation of nuclear inelastic-scattering spectra of molecular crystals. *Physical Review B* **1999**, *59*, 975.

[219] Sorai, M.; Seki, S. Phonon coupled cooperative low-spin $^1A_1$ high-spin $^5T_2$ transition in [Fe (phen) $_2$(NCS)$_2$] and [Fe(phen)$_2$(NCSe)$_2$] crystals. *Journal of Physics and Chemistry of Solids* **1974**, *35*, 555-570.

[220] Peng, H.; Tricard, S.; Félix, G.; Molnár, G.; Nicolazzi, W.; Salmon, L.; Bousseksou, A. Re‐appearance of cooperativity in ultra‐small spin‐crossover [Fe(pz){Ni(CN)$_4$}] nanoparticles. *Angewandte Chemie* **2014**, *126*, 11074-11078.

[221] Hu, M. Y.; Sturhahn, W.; Toellner, T. S.; Mannheim, P. D.; Brown, D. E.; Zhao, J.; Alp, E. E. Measuring velocity of sound with nuclear resonant inelastic x-ray scattering. *Physical Review B* **2003**, *67*, 094304.

[222] Forestier, T.; Mornet, S.; Daro, N.; Nishihara, T.; Mouri, S.; Tanaka, K.; Fouche, O.; Freysz, E.; Letard, J. F. Nanoparticles of iron(II) spin-crossover. *Chemical Communications* **2008**, 4327-4329.

[223] Grosjean, A.; Négrier, P.; Bordet, P.; Etrillard, C.; Mondieig, D.; Pechev, S.; Lebraud, E.; Létard, J. F.; Guionneau, P. Crystal structures and spin crossover in the polymeric material [Fe(Htrz)$_2$(trz)](BF$_4$) including coherent-domain size reduction effects. *European Journal of Inorganic Chemistry* **2013**, *2013*, 796-802.

[224] Haasnoot, J. G.; Vos, G.; Groeneveld, W. L. 1, 2, 4-Triazole complexes, III. Complexes of transition metal (II) nitrates and fluoroborates. *Z. Naturforsch. B* **1977**, *32*, 1421-1430.

[225] Kroeber, J.; Audiere, J.-P.; Claude, R.; Codjovi, E.; Kahn, O.; Haasnoot, J. G.; Groliere, F.; Jay, C.; Bousseksou, A. Spin transitions and thermal hysteresis in the molecular-based materials [Fe(Htrz)$_2$ (trz)](BF$_4$) and [Fe(Htrz)$_3$](BF4)$_2$.cntdot.H$_2$O (Htrz = 1, 2, 4-4H-triazole; trz = 1, 2, 4-triazolato). *Chemistry of Materials* **1994**, *6*, 1404-1412.

[226] Dirtu, M. M.; Neuhausen, C.; Naik, A. D.; Rotaru, A.; Spinu, L.; Garcia, Y. Insights into the origin of cooperative effects in the spin transition of [Fe(NH$_2$trz)$_3$](NO$_3$)$_2$: The role of supramolecular interactions evidenced in the crystal structure of [Cu(NH$_2$trz)$_3$](NO$_3$)$_2$·H$_2$O. *Inorganic Chemistry* **2010**, *49*, 5723-5736.

[227] Titos‐Padilla, S.; Herrera, J. M.; Chen, X. W.; Delgado, J. J.; Colacio, E. Bifunctional hybrid SiO$_2$ nanoparticles showing synergy between core spin crossover and shell luminescence properties. *Angewandte Chemie* **2011**, *123*, 3348-3351.

[228] Rotaru, A.; Dugay, J.; Tan, R. P.; Guralskiy, I. A.; Salmon, L.; Demont, P.; Carrey, J.; Molnár, G.; Respaud, M.; Bousseksou, A. Nano-electromanipulation of spin crossover nanorods: towards switchable nanoelectronic devices. *Advanced Materials* **2013**, *25*, 1745-1749.

[229] Moussa, N. O.; Ostrovskii, D.; Garcia, V. M.; Molnár, G.; Tanaka, K.; Gaspar, A. B.; Real, J. A.; Bousseksou, A. Bidirectional photo-switching of the spin state of iron (II) ions in a triazol based spin crossover complex within the thermal hysteresis loop. *Chemical Physics Letters* **2009**, *477*, 156-159.

[230] Urakawa, A.; Van Beek, W.; Monrabal-Capilla, M. a.; Galán-Mascarós, J. R.; Palin, L.; Milanesio, M. Combined, Modulation enhanced X-ray powder diffraction and Raman spectroscopic study of structural transitions in the spin crossover Material [Fe(Htrz)$_2$(trz)](BF$_4$). *The Journal of Physical Chemistry C* **2010**, *115*, 1323-1329.

[231] Ruiz, E. Charge transport properties of spin crossover systems. *Physical Chemistry Chemical Physics* **2014**, *16*, 14-22.

[232] Baadji, N.; Sanvito, S. Giant resistance change across the phase transition in spin-crossover molecules. *Physical review letters* **2012**, *108*, 217201.

[233] Lefter, C.; Gural'skiy, I. y. A.; Peng, H.; Molnár, G.; Salmon, L.; Rotaru, A.; Bousseksou, A.; Demont, P. Dielectric and charge transport properties of the spin crossover complex [Fe(Htrz)$_2$ (trz)](BF$_4$). *physica status solidi (RRL)-Rapid Research Letters* **2014**, *8*, 191-193.

[234] Meded, V.; Bagrets, A.; Fink, K.; Chandrasekar, R.; Ruben, M.; Evers, F.; Bernand-Mantel, A.; Seldenthuis, J. S.; Beukman, A.; Van der Zant, H. S. J. Electrical control over the Fe (II) spin crossover in a single molecule: Theory and experiment. *Physical Review B* **2011**, *83*, 245415.

[235] Osorio, E. A.; Moth-Poulsen, K.; van der Zant, H. S. J.; Paaske, J.; Hedegård, P.; Flensberg, K.; Bendix, J.; Bjørnholm, T. Electrical manipulation of spin states in a single electrostatically gated transition-metal complex. *Nano letters* **2009**, *10*, 105-110.

[236] Gopakumar, T. G.; Matino, F.; Naggert, H.; Bannwarth, A.; Tuczek, F.; Berndt, R. Electron-induced spin crossover of single molecules in a bilayer on gold. *Angewandte Chemie International Edition* **2012**, *51*, 6262-6266.

[237] Miyamachi, T.; Gruber, M.; Davesne, V.; Bowen, M.; Boukari, S.; Joly, L.; Scheurer, F.; Rogez, G.; Yamada, T. K.; Ohresser, P. Robust spin crossover and memristance across a single molecule. *Nature communications* **2012**, *3*, 938.

[238] Shi, S.; Schmerber, G.; Arabski, J.; Beaufrand, J. B.; Kim, D. J.; Boukari, S.; Bowen, M.; Kemp, N. T.; Viart, N.; Rogez, G. Study of molecular spin-crossover complex $Fe(phen)_2(NCS)_2$ thin films. *Applied Physics Letters* **2009**, *95*, 043303.

[239] Jonscher, A. K. Theuniversal'dielectric response. *Nature* **1977**, *267*, 673-679.

[240] Sugiyarto, K. H. Magnetic, Mössbauer, and electronic spectral properties of bis (1, 2, 4-triazole) triazolatoiron (II) trifluoromethanesulphonate monohydrate. *Jurnal Matematika & Sains* **2009**, *8*, 73-79.

# Annex 1: Experimental section

# I- Syntheses

All solvents and reagents were purchased from Sigma Aldrich and used without further purification.

## A- Synthesis of Different-Size Hofmann like Clathrate Nanoparticles

### A-1- Synthesis of Different-Size [$^{56}$Fe(pz){Ni(CN)$_4$}] Nanoparticles

Two reverse emulsions of $\omega$ = [H$_2$O]/[AOT] = 10 (NaAOT is sodium bis(2-ethylexyl sulfosuccinate)) were prepared separately, one containing Fe(BF$_4$)$_2$·6H$_2$O and pyrazine and the other containing K$_2$Ni(CN)$_4$. To 33 mL of 0.5 M NaAOT in hexane, 3 mL of K$_2$Ni(CN)$_4$ aqueous solution (0.10 M) was added and the biphasic system was stirred until a clear emulsion was obtained. The same procedure was applied to 3 mL of a 0.10 M aqueous solution of Fe(BF$_4$)$_2$·6H$_2$O with 10 equivalents of pyrazine. The two emulsions were cooled overnight in a fridge and then mixed with drop by drop addition rate at room temperature. The color of the mixture changes from yellow to orange. After 10 minutes of stirring, EtOH was added to the reaction mixture. The resulting flocculate was centrifuged, washed with 20 mL of ethanol and then dried under vacuum. This led to sample **1**.

Sample **2** was obtained by the same procedure as sample **1**, but with a fast addition rate of the two reverse nanoemulsions.

Sample **3** was obtained by the same procedure as sample **2**, but with a concentration in metal ions of 0.15 M.

Sample **4** was obtained by the same procedure as sample **3**, but mixing the two reverse emulsions at -30 °C.

Sample **5** was obtained with a concentration in metal ions of 0.20 M and mixing the two reverse emulsions at -15 °C.

### A-2- Synthesis of $^{57}$Fe(BF$_4$)$_2$·6H$_2$O

**$^{57}$Fe(BF$_4$)$_2$·6H$_2$O**. 57-Fe metal plate (130 mg, 2.3 mmol) was mixed with 0.3 mL of HBF$_4$ (50% wt, 4.8 mmol) and stirred at 70 °C under a N$_2$ atmosphere for 6 h, the solution

which was filtered led to a green solution of $^{57}Fe(BF_4)_2$. Then, the solution was evaporated under a $N_2$ atmosphere and a white powder was obtained.

## A-3- Synthesis of Different-Size [$^{57}$Fe(pz){Ni(CN)$_4$}] Nanoparticles

[$^{57}$Fe(pz){Ni(CN)$_4$}] nanoparticles were synthesized under the same condition as [$^{56}$Fe(pz){Ni(CN)$_4$}] nanoparticles. Sample **6** was synthesized as sample **2**, sample **7** as sample **5**.

| Sample | [Fe]/mol.L$^{-1}$ | $\omega$ | V$_{H2O}$(mL) | V$_{Hexane}$(mL) | Temperature/K |
|--------|-------------------|----------|---------------|------------------|---------------|
| 1 | 0.1 | 10 | 6 | 33 | 293 |
| 2* | 0.1 | 10 | 6 | 33 | 293 |
| 3 | 0.15 | 10 | 6 | 33 | 293 |
| 4 | 0.15 | 10 | 6 | 33 | 243 |
| 5 | 0.2 | 10 | 6 | 33 | 258 |
| 6* | 0.1 | 10 | 6 | 33 | 293 |
| 7 | 0.2 | 10 | 6 | 33 | 258 |

Table A.1: Preparation conditions of different samples, * fast mixture of the two nanoemulsions, and $\omega$ = [H$_2$O]/[AOT]

# B- Synthesis of Fe-triazole Nano- and Micro-Particles

## B1- Synthesis of BF$_4$ Derivative Nano- and Micro-Particles

Samples **1**-**5** were prepared by rapidly mixing two aqueous solutions (with 0.1, 0.5, 2, 3, 4, wt% of HBF$_4$, respectively) containing Fe(BF$_4$)$_2$·6H$_2$O (225 mg; 0.33 mol/l ) and the 1,2,4-triazole ligand (130 mg; 0.94 mol/l). The resulting 2 ml limpid solution was let for slow evaporation at room temperature; the flask being half covered. Following a specific period, the flocculates were centrifuged, and washed by 10 mL of distilled water and 30 mL of ethanol absolute and finally dried under vacuum. Sample **3'** was prepared as sample **3** (2 wt% HBF$_4$) but the evaporation speed was decrease opening more the cover of the flask (see scheme hereafter). Sample **6** and **6'** were prepared with 5 wt% of HBF$_4$ but the evaporation speed was increase (using such acid concentration and slow evaporation as that used for the

elaboration of sample **1-5**, any precipitation was obtained after several month). Sample **7** was prepared using the same reactant concentrations as sample **3** but a liquid-liquid (water-water) diffusion synthetic method was carried out instead of the direct mixture of the two reagents. A named bulk sample obtained using the same concentrations in an aqueous solution and in absence of acid was synthesized as a reference sample. Elemental analysis: calculated for [Fe(Htrz)$_2$(trz)](BF$_4$): C 20.66 %, H 2.31 %, N 36.14 %; measured: C 19.59 %, H 2.01 %, N 34.35 % (**1**), C 19.15 %, H 1.88 %, N 35.21% (**2**), C 19.74 %, H 1.74 %, N 34.79 % (**3**), C 19.82 %, H 1.93%, N 34.24 % (**3'**), C 19.80 %, H 2.21 %, N 35.71 % (**4**). Elemental analysis: calculated for [Fe(Htrz)$_3$](BF$_4$)$_2$.3H$_2$O: C 15.85, H 2.44 %, N 27.73%; measured: C 15.62 %, H 2.33 %, N 26.72 % (**5**), C 15.38 %, H 2.65 %, N 26.29 (**7**). Elemental analysis: calculated for [[Fe(Htrz)$_3$](BF$_4$)$_2$.3H$_2$O]$_{0.6}$ [[Fe(Htrz)$_2$(trz)](BF$_4$)]$_{0.4}$: C 16.79 %, H 2.79 %, N 29.39 %; measured: C 16.83 %, H 2.47 %, N 28.97 % (**6**), C 16.33 %, H 2.72 %, N 28.91% (**6'**). Solid state multinuclear NMR spectroscopy (400 MHz, δ, ppm): **$^1$H NMR**, 15.7 (1H, NH), 13.2 (1H, NH), 7.9 (6H, CH) (**3**), 15.5 (3H, NH), 8.8 (6H, CH), 4.5 (H$_2$O) (**5**), 15.5 (3H, NH), 8.3 (6H, CH), 4.2 (H$_2$O) (**6**), 15.6 (3H, NH), 8.9 (6H, CH), 4.5 (H$_2$O) (**7**), **$^{13}$C NMR**, 151.9 (4C, CH), 160.1 (2C, CH) (**3**), 156.2 (6C, CH) (**5**), 152.4 (4C, CH), 155.7 (6C, CH), 160.2 (2C, CH) (**6**), 155.9 (6C, CH) (**7**), **$^{19}$F NMR**, -147.3 (4F, BF$_4$) (**3**), -148.6 (4F, BF$_4$), -149.9 (4F, BF$_4$) (**5**), -146.5 (4F, BF$_4$), -148.1 (4F, BF$_4$), -149.6 (4F, BF$_4$) (**6**), -148.5 (4F, BF$_4$), -149.9 (4F, BF$_4$) (**7**).



Plastic container    Upper view of the container
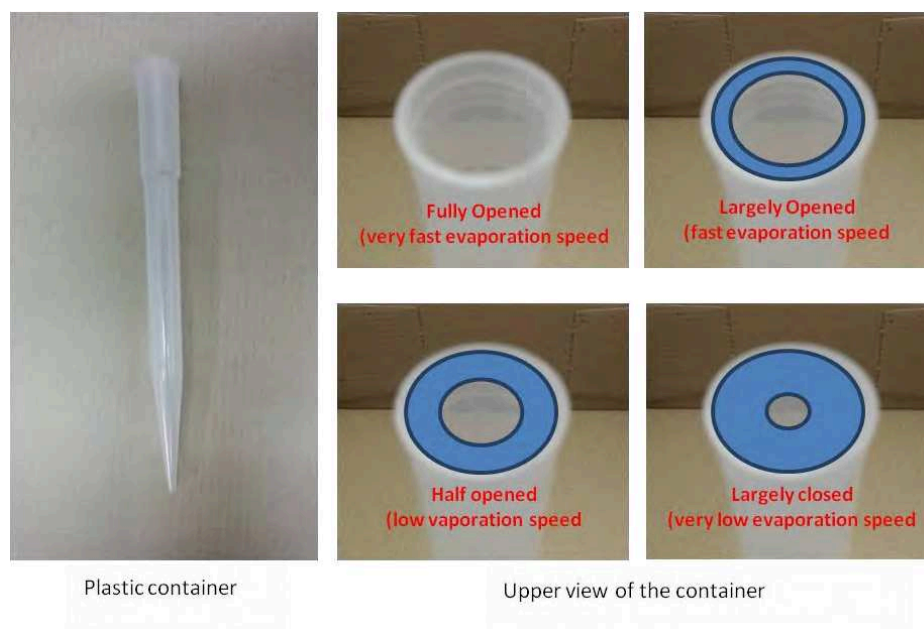
Plastic tube and configurations used for the evaporation control during the syntheses

**B2- Synthesis of Zn Diluted [Fe$_{1-x}$Zn$_x$(Htrz)$_2$(trz)](BF$_4$) Particles**

The Zn substituted samples were synthesized in a similar way as the [[Fe(Htrz)$_2$(trz)](BF$_4$)] complex, using 202 mg of Fe(BF$_4$)$_2$·6H$_2$O (0.9 eq) + 23 mg of Zn(BF$_4$)$_2$·6H$_2$O (0.1 eq) for sample **8**, and 180 mg of Fe(BF$_4$)$_2$·6H$_2$O (0.8 eq) + 45 mg of Zn(BF$_4$)$_2$·6H$_2$O (0.2 eq) for sample **9**. Elemental analysis from EDX gave Zn:Fe ratios of ca. 1:3 and 1:1.3 for **8** and **9**, respectively.

**B3- Synthesis of Triflate Derivative Micro-Particles**

Bulk [Fe(Htrz)$_2$(trz)](CF$_3$SO$_3$) complex (sample **10**) was prepared by rapidly mixing two aqueous solutions containing Fe(CF$_3$SO$_3$)$_2$ (236 mg; 0.33 mol/l ) and the 1,2,4-triazole ligand (130 mg; 0.94 mol/l), respectively. The resulting 2 ml limpid solution was let at room temperature. After *ca.* 6 hours, the flocculates were centrifuged, and washed by 10 ml of distilled water and 30 ml of absolute ethanol and finally dried under vacuum. Yield: 54 mg (*ca.* 20%).

Sample **11** was prepared by rapidly mixing two acidic aqueous solutions (1 wt% CF$_3$SO$_3$H) containing Fe(CF$_3$SO$_3$)$_2$ (236 mg; 0.33 mol/l ) and the 1,2,4-triazole ligand (130 mg; 0.94 mol/l), respectively. The resulting 2 ml limpid solution was let for slow evaporation at room temperature. Following *ca.* 7 days, the flocculates were centrifuged, and washed by 10 ml of distilled water and 30 ml of absolute ethanol and finally dried under vacuum. Yield: 34 mg (*ca.* 15%).

Sample **12** was prepared by rapidly mixing two acidic aqueous solutions (3 wt% CF$_3$SO$_3$H) containing Fe(CF$_3$SO$_3$)$_2$ (236 mg; 0.33 mol/l ) and the 1,2,4-triazole ligand (130 mg; 0.94 mol/l), respectively. The resulting 2 ml limpid solution was let for slow evaporation at room temperature. Following *ca.* 2 months, the flocculates were centrifuged, and washed by 10 ml of distilled water and 30 ml of absolute ethanol and finally dried under vacuum. Yield: 300 mg (*ca.* 80%).

Elemental analysis: calculated for sample **10** [Fe(Htrz)$_2$(trz)](CF$_3$SO$_3$): C 20.43 %, H 1.95 %, N 30.65 %; measured: C 19.03 %, H 1.41 %, N 28.07 %. Elemental analysis: calculated for sample **12** [Fe(Htrz)$_3$](CF$_3$SO$_3$)$_2$·1.2H$_2$O: C 16.47 %, H 1.95 %, N 21.61 %; measured: C 16.41 %, H 1.60 %, N 22.30 %.

# II- Characterization and Physical Measurements

**Elemental analysis**: Analysis for C, H, and N were performed after combustion at 850°C using IR detection and gravimetry by means of a Perkin–Elmer 2400 series II device.

**Thermal analysis**: Differential thermal analysis and thermogravimetric (DTA-TG) data were acquired simultaneously using a Perkin–Elmer Diamond thermal analyzer. DSC analysis was carried out on a Netsch DSC 204 instrument under helium purging gas (20 $cm^3 \cdot min^{-1}$) at a heating/cooling rate of 10 $K \cdot min^{-1}$. Temperature and enthalpy were calibrated using the melting transition of standard materials (Hg, In, Sn). The uncertainty in the transition enthalpy and entropy is estimated to be approximately 10% due to the subtraction of the unknown baseline.

**FTIR spectra**: FTIR spectra were recorded at room temperature with a Perkin Elmer Spectrum 100 spectrometer in ATR mode (resolution *ca.* 1 $cm^{-1}$) between 650 $cm^{-1}$ and 4000 $cm^{-1}$.

**Raman spectroscopy**: Raman spectra were collected between 350 and 80 K using a LabRAM-HR (Jobin–Yvon) Raman micro-spectrometer and a Linkam THMS-600 cryostage. The 632.8 nm line of a He–Ne laser was used as the excitation source and a spectral resolution of approximately 3 $cm^{-1}$ was obtained.

**Solid state $^1$H, $^{13}$C and $^{19}$F NMR spectra**: Solid state $^1$H, $^{13}$C and $^{19}$F NMR spectra were recorded with a Bruker Avance 400WB.

**UV spectroscopy**: UV spectroscopy was recorded using UV/Vis spectrophotometer equipped with a Labsphere RSA-PE-20 integrating sphere.

**X-ray powder diffraction**: Powder X-ray diffraction patterns were recorded using a PANalytical X'Pert equipped with a Cu X-ray tube, a Ge(111) incident beam monochromator ($\lambda$ = 1.5406 Å) and an X'Celerator detector. The extraction of peak positions and the determination of the crystallite size by means of the Scherrer equation were performed with the PC software package Highscore+ supplied by Panalytical.

**TEM and HRTEM analysis**: TEM samples were prepared by deposition of the nanoparticle suspension in ethanol on a carbon-coated copper grid. A TEM JEOL JEM 1400 (120 kV) and

a high-resolution TEM JEOL JEM 2100F (200 kV) that was equipped with a PGT X-ray analyzer were used for size and composition analysis of the nano-objects.

**SEM analysis**: SEM samples were prepared by deposition of platinum film on powder sample. A SEM JEOL JSM-6700F (30 kV) equipment with a field emission source (FESEM) was used.

**Optical reflectance**: The system that was used to follow the spin transition by variation in the optical reflectivity (543 nm band-pass filter) consisted of an Olympus BX51 optical microscope that was equipped with a charge-coupled device (CCD) camera IKON-M DU934N BV (Andor technology). The sample temperature was controlled by using a Linkam THMS600 liquid-nitrogen cryostat. Samples were preliminarily dehydrated at 120°C for 1 hour under a nitrogen flow. During the experiment, the temperature was changed at a rate of 4 $K \cdot min^{-1}$.

**Magnetic properties**: Magnetic susceptibility data were collected with a Quantum Design MPMS-XL SQUID magnetometer at heating and cooling rates of 2 $K \cdot min^{-1}$ at a magnetic field of 1 kOe.

**Mössbauer spectroscopy**: $^{57}$Fe Mossbauer spectra have been recorded using a conventional constant-acceleration-type spectrometer equipped with a 50 Ci $^{57}$Co source and a liquid-nitrogen cryostat. Spectra of the powder samples (ca. 50 mg) were recorded between 80 and 310 K. Least-squares fittings of the Mössbauer spectra have been carried out with the assumption of Lorentzian line shapes using the Recoil software.

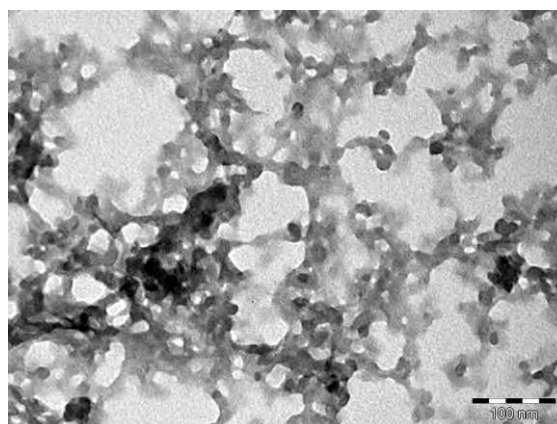# Annex 2: Complementary Electronic Microscopy Images

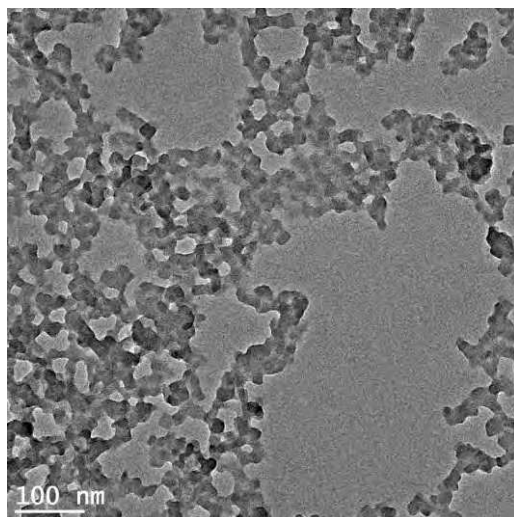## I- TEM and HRTEM Images of [Fe(pz){Ni(CN)$_4$}] Nanoparticles
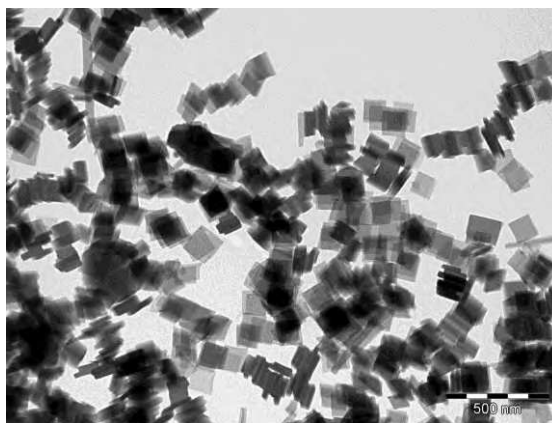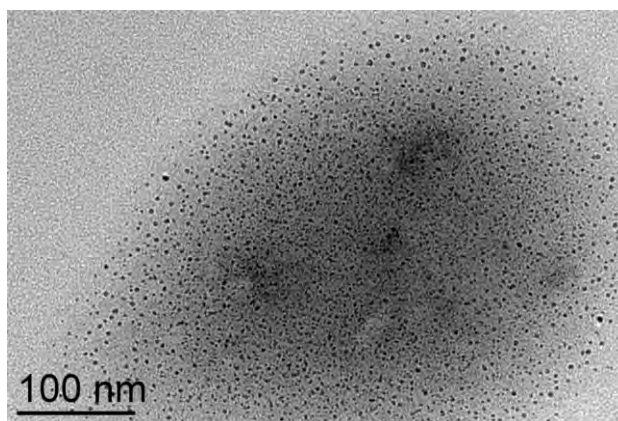


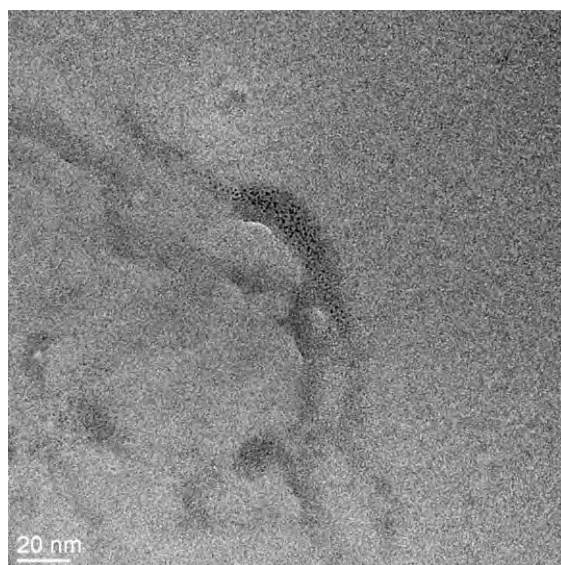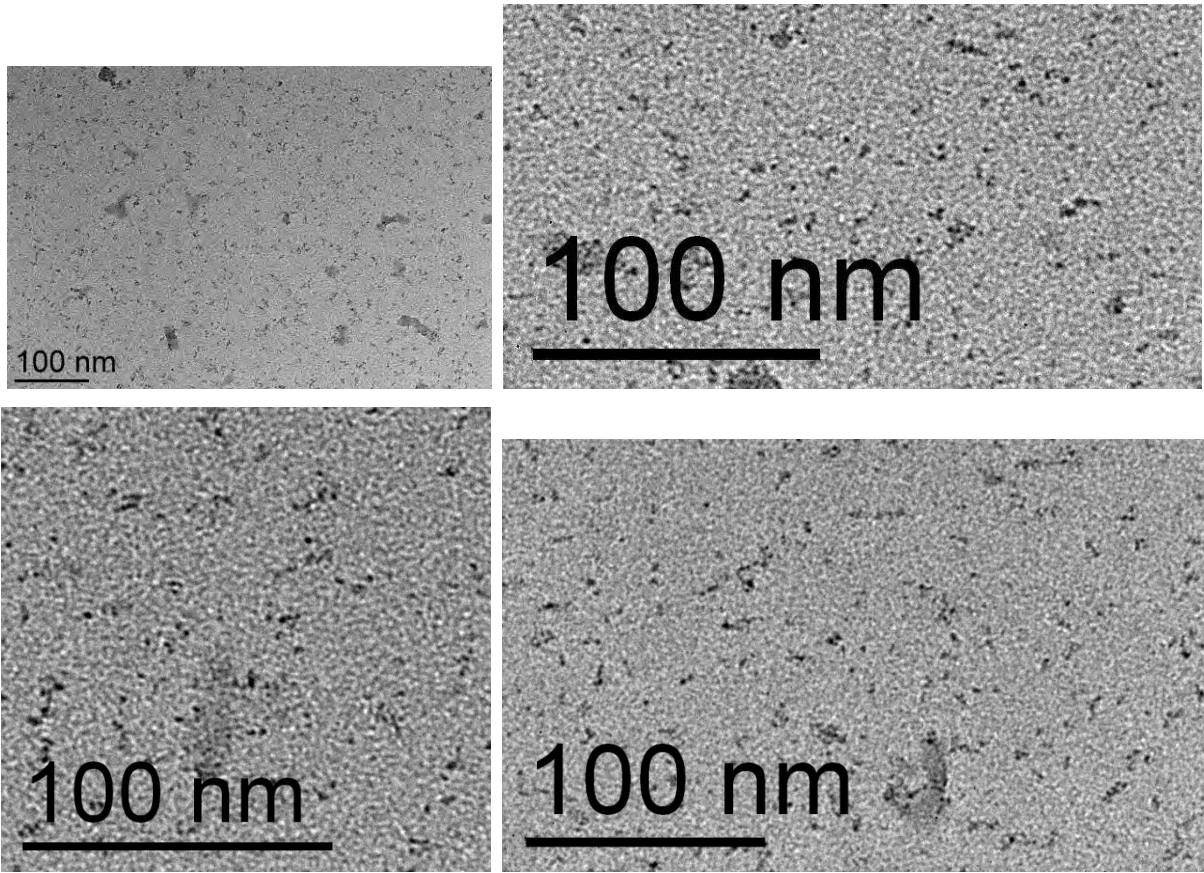TEM image of sample **1**
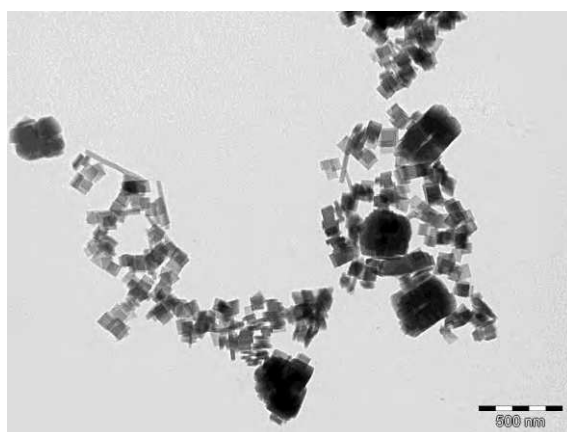


TEM image of sample **2**

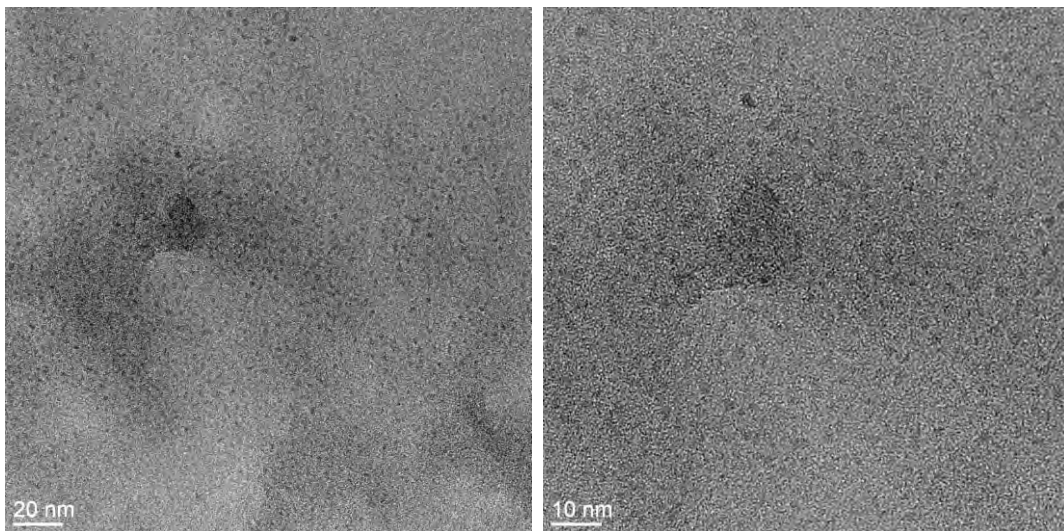TEM image of sample **3**
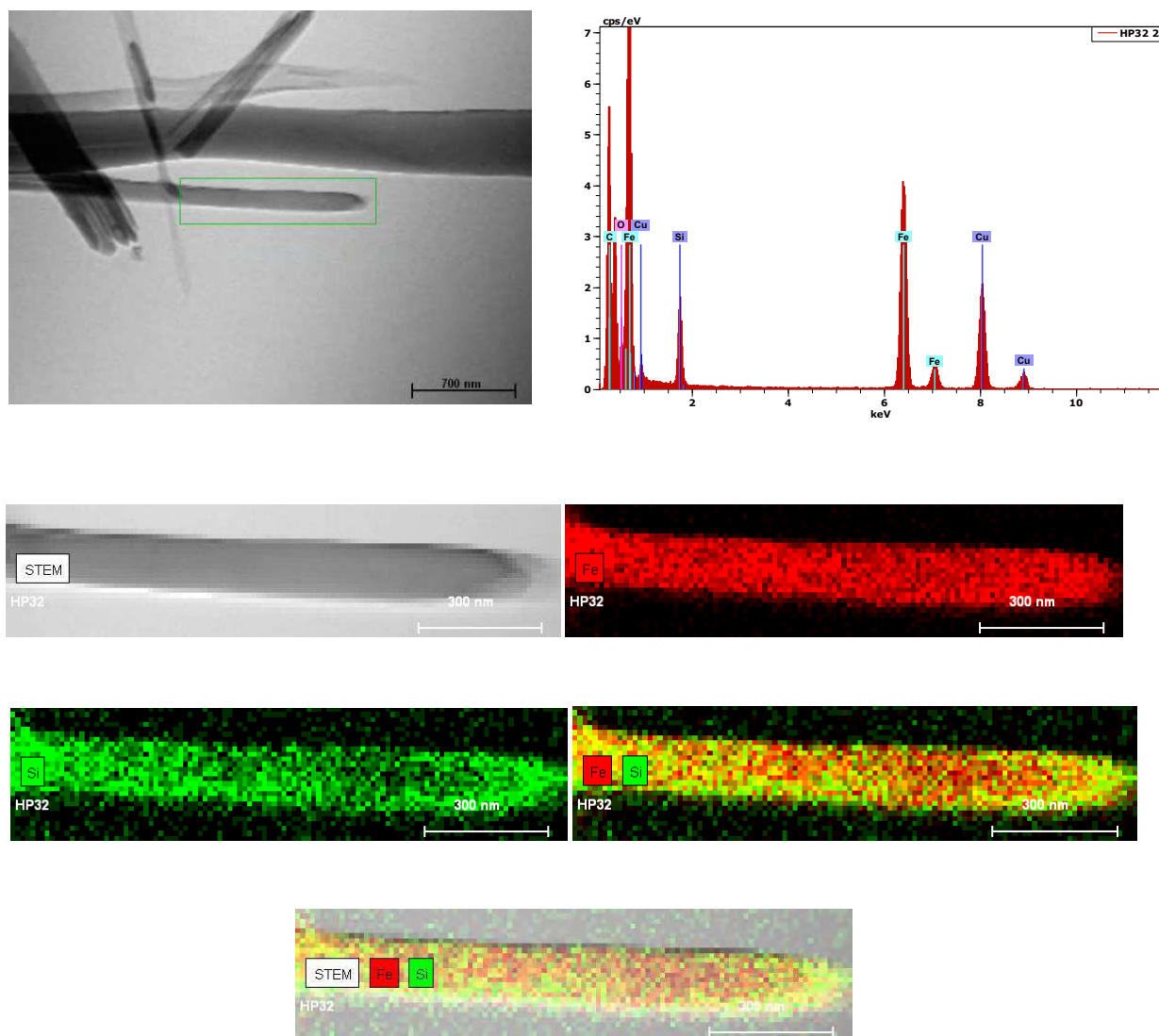


TEM image of sample **4**



HRTEM image of sample **4**
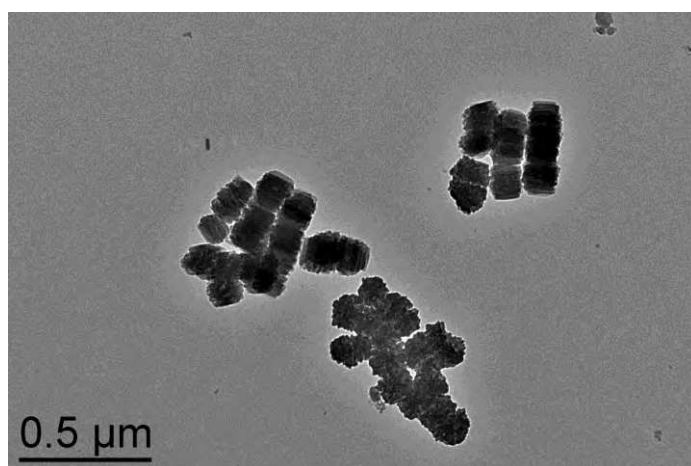
TEM images of sample **5**
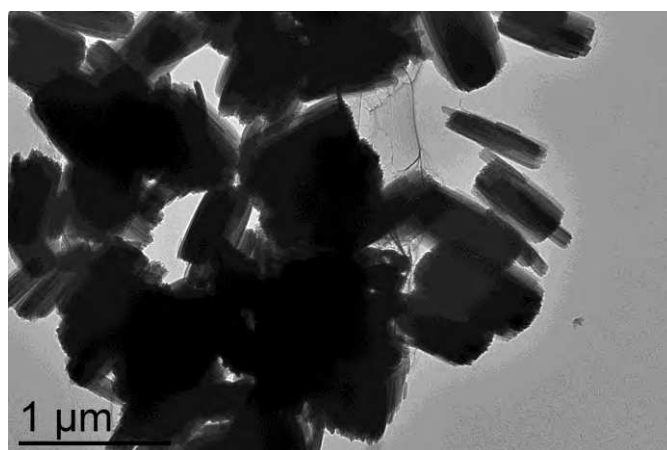


HRTEM image of Sample **5**

## II- TEM and HRTEM Images of Fe-triazole particles



High Resolution Transmission Electronic Microscopy (HRTEM), High Resolution Scanning Transmission Electronic Microscopy (HRSTEM) and Energy Dispersive X-ray spectroscopy (EDX) analyses of micro-rods **synthesized in glass containers (5wt% HBF4) revealing the presence of Si.** EDX measurements were collected from the area indicated in the STEM image. STEM EDX compositional maps for Fe and Si.
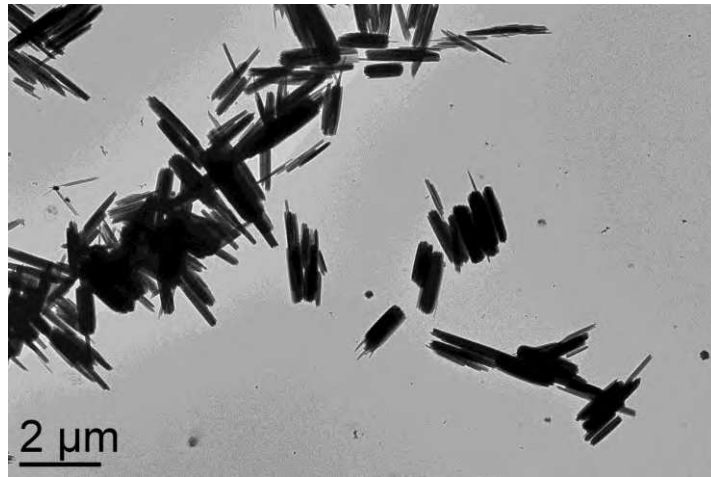
TEM image of sample **1**



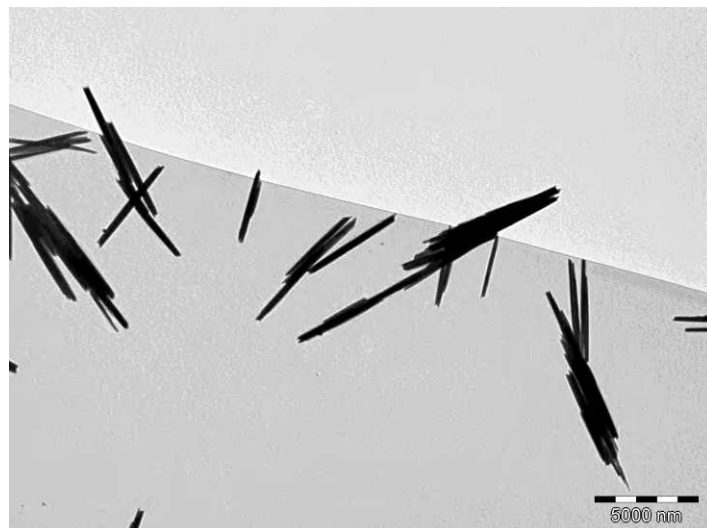TEM image of sample **2**
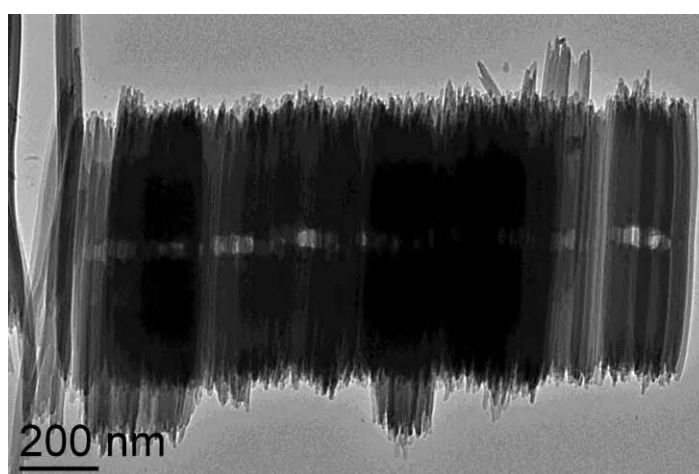


TEM image of sample **3**

TEM image of sample **3'**
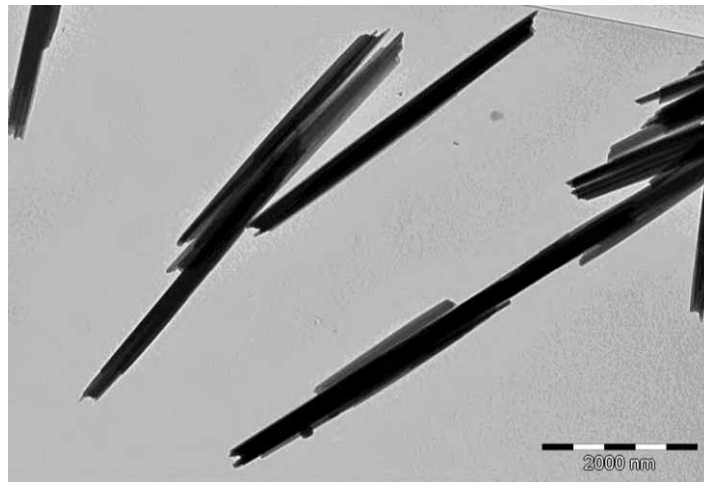




TEM images of sample **4**

TEM image of sample **5**
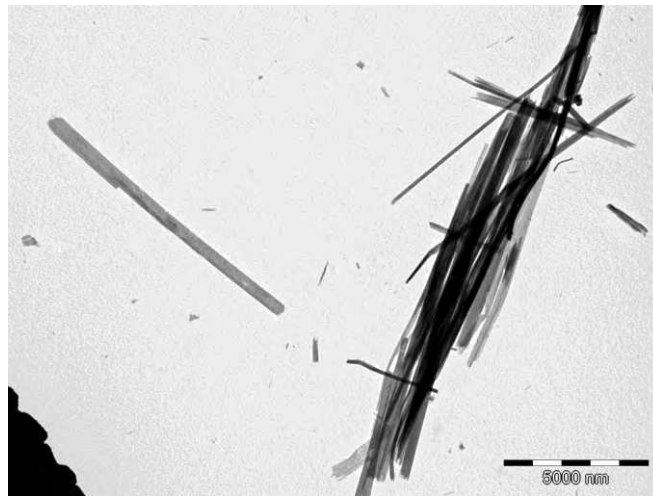


TEM image of sample **6'**



TEM image of sample **6**

TEM images of sample **7**
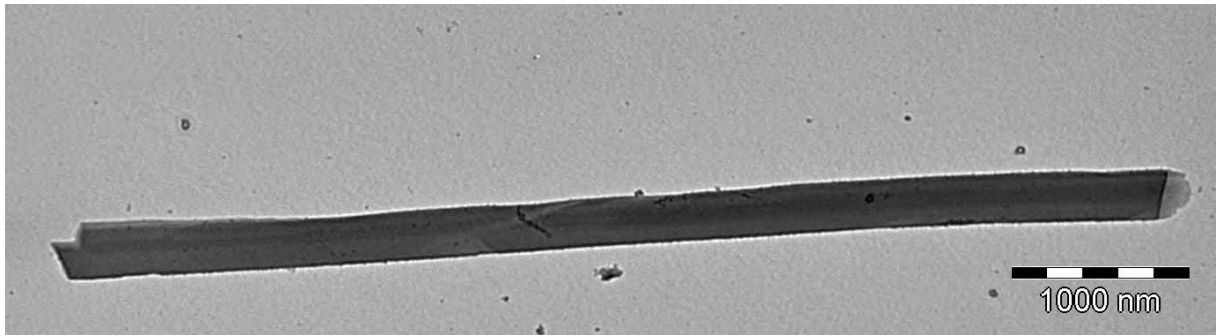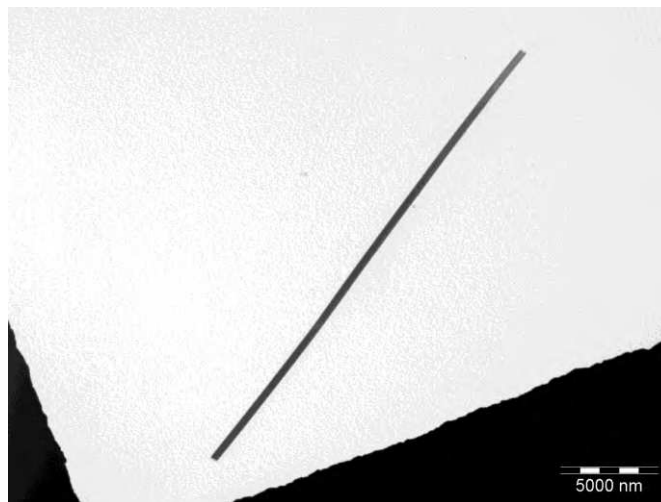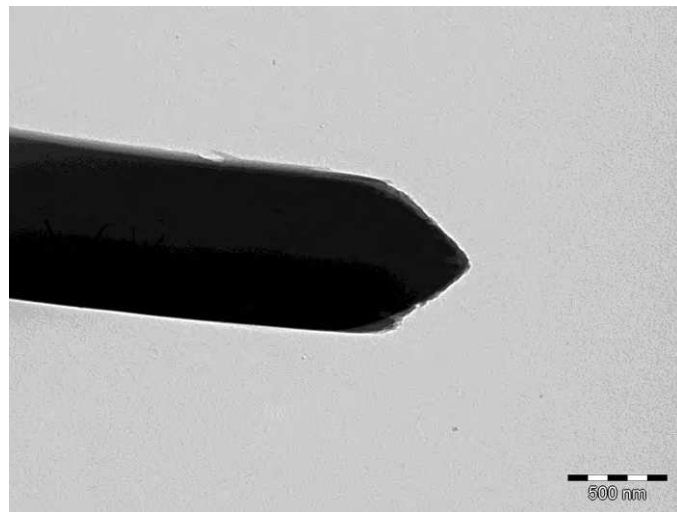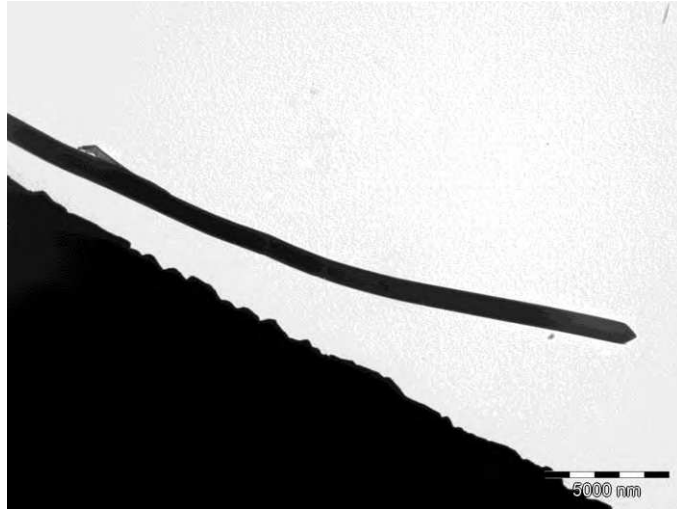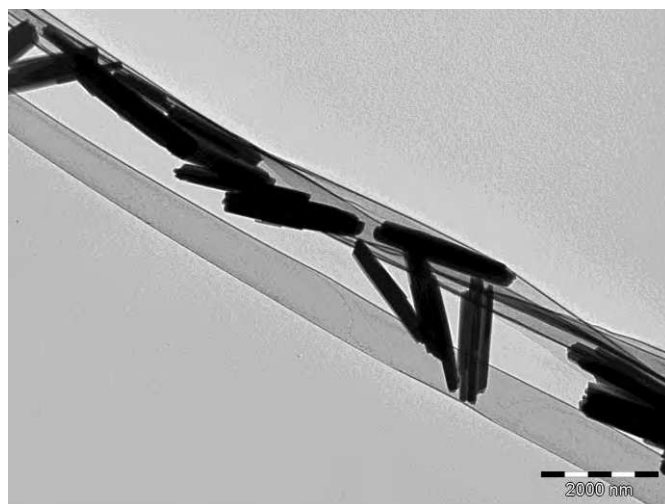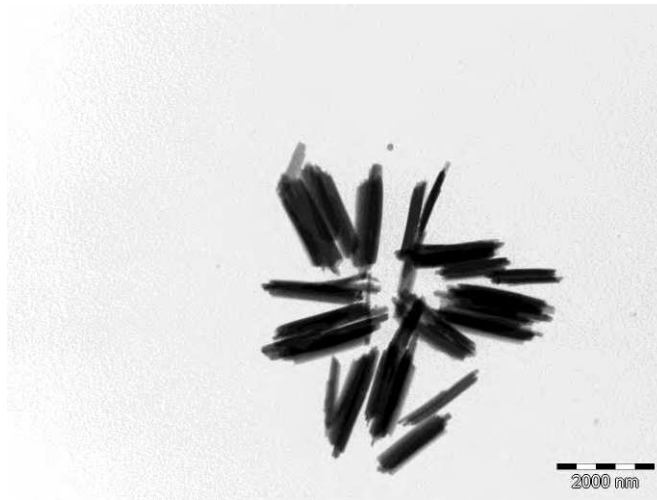


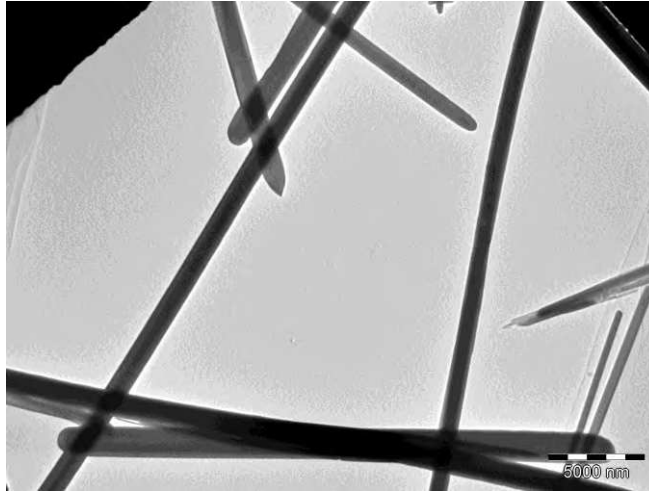TEM image of sample **8**
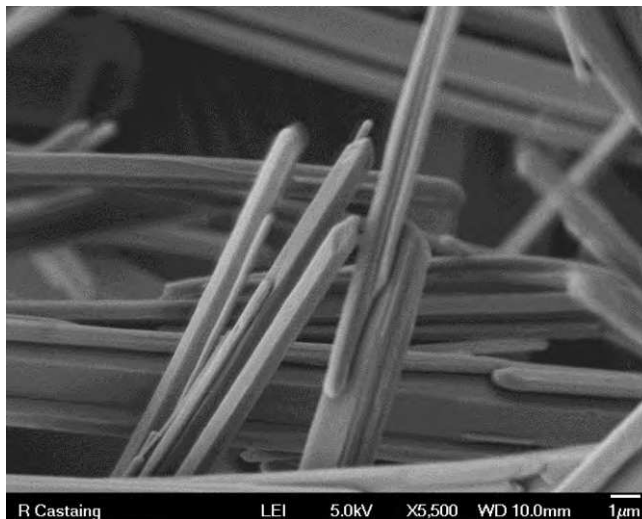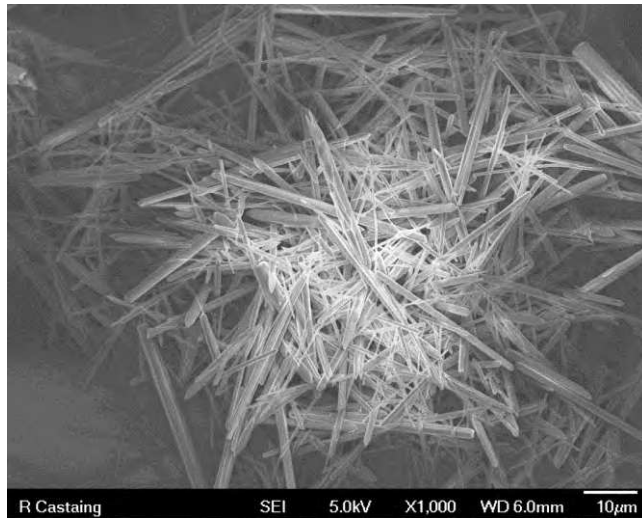
TEM image of sample **9**



TEM image of sample **10**



TEM image of sample **11**

TEM image of sample **12**



SEM images of sample **12**

# Annexes 3: Mössbauer Spectrometry: Method and Data

## I- Conventional Mössbauer and Nuclear Inelastic Scattering (NIS)

## A- Conventional Mössbauer

Mössbauer spectroscopy, also known as nuclear gamma resonance fluorescence spectroscopy, is a technique that probes transitions between the ground and low-lying excited states of the nucleus. The nucleus most favourite and amenable to Mössbauer spectroscopy is $^{57}$Fe and hence iron containing compounds are widely investigated. Because of sharp nuclear transitions, the Mössbauer effect provides an extremely high energy resolution in the range of neV (with the $\gamma$-ray energy in the keV range) and, hence, it can be used to probe the chemical environment of a nucleus via its hyperfine interactions with the surrounding electron distribution. The atoms surrounding a Mössbauer nucleus influence the local electronic field around this nucleus and therefore, one can characterize the type of bonding. The Mössbauer technique is widely used in many branches of science including solid-state physics, chemistry, biophysics, materials science, geology, biology and mineralogy. Recently, miniaturized Mössbauer spectrometers were sent to the planet Mars for the exploration of the surface of the planet to access past climate conditions and their suitability for life.

The Mössbauer effect is the recoil-free emission and absorption of a $\gamma$-quantum in a transition between the ground state and an excited state of certain nuclei bound in a solid. It can be well described in terms of quantum mechanical phenomena. A source nucleus in an excited state of energy $E_e$ undergoes a transition to the ground state $E_g$ by emitting a $\gamma$-quantum of energy $E_0 = E_e - E_g$. This $\gamma$-quantum may be resonantly absorbed by another nucleus of the same isotope, which then undergoes a transition from its ground state to its excited state. After the resonant absorption of the $\gamma$-quantum, the absorbing nucleus stays in the excited state for the mean lifetime $\tau$ (=141.8 ns for $^{57}$Fe). The subsequent deexcitation to its ground state either results in emission of either a conversion electron due to internal conversion (energy transfer from nucleus to the innermost electron shell) or a $\gamma$-quantum (nuclear resonance fluorescence). So in Mössbauer spectroscopy both a source ($\gamma$-emitter) and an absorber (the material under investigation) are needed. This phenomenon was discovered by Rudolf Ludwig Mößbauer in 1957, for which he received the Nobel prize in physics in 1961.

Electromagnetic waves interact with the nuclei in atoms by various processes that can follow resonant absorption of γ-quanta. In transmission Mössbauer spectroscopy, one counts the γ-quanta transmitted through the absorber versus the Doppler-shifted energy (in velocity units, mm s$^{-1}$). The recorded spectrum is characterized by line shapes, positions, intensities and widths. The most important Mössbauer spectral parameters are the isomer shift, electric quadrupole splitting and magnetic dipole splitting. They arise from the hyperfine interactions between the nucleus and its surrounding electric and/or magnetic field. As a consequence there will be a small perturbation in the nuclear energy levels. These hyperfine interactions are very small compared to the energy levels of the nucleus itself. The other important parameters are line width, Lamb-Mössbauer factor and relativistic effects (second-order Doppler shift).



**Mössbauer Equipment**
**LCC Toulouse**
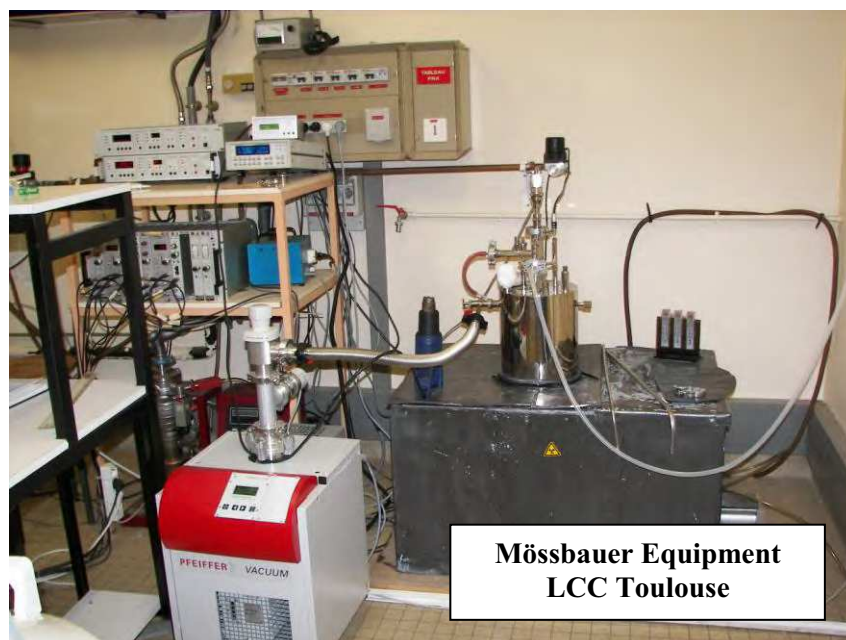
## B- Nuclear Inelastic Scattering

In Mössbauer spectroscopy, the process of recoil-free absorption or scattering of resonant photons by an ensemble of nuclei is essentially an elastic scattering process. The corresponding probability is given by the Lamb-Mössbauer factor $f_{LM}$. Incident photons $E \neq$ 14.4 keV are treated as nonresonant absorption, which may constitute the background and baseline of the spectrum. However, nuclear resonant scattering is also possible for the incident photons $E \neq$ 14.4 keV due to the influence of lattice dynamics on the absorption of γ-quanta by nuclei. In this case, the interaction involves the recoil of the scattering nucleus with energy transfer from or to the crystal lattice in order to fulfil the resonance condition. This process of

absorption with recoil (recoil fraction, 1−*f*) is called nuclear inelastic scattering (NIS), which appears as sidebands over an energy range of about ±100 meV.

Soon after the discovery of the Mössbauer effect, it was proposed by theorists that lattice vibrations should occur as sidebands of the absorption line, permitting the measurement of a phonon spectrum. However, in a conventional Mössbauer experiment it is very difficult to observe such vibrational sidebands that appear roughly ±100 meV in the vicinity of a resonance transition energy. The main reasons, which do not allow for the observations of sidebands are: 1. to scan an energy range of ±100.0 meV with Doppler shift, one needs a velocity of about 2080.1 m s$^{-1}$ and it is practically difficult to achieve such a high velocity with a good count rate and 2. a very intense radiation is required since the energy range of the phonon spectrum is typically $10^7$ times broader than the nuclear line width and the spreading of the recoil absorption probability over this energy range makes the cross section of inelastic scattering weak. Therefore, a very intense beam with typically $10^8$ phonons s$^{-1}$ is required and hence NIS is generally performed at synchrotron radiation sources. NIS does not deal with phonon dispersion relations but gives direct access to the vibrational density of phonon states (VDOS).



# II- Mössbauer Measurements of [Fe(pz){Ni(CN)$_4$}] Nanoparticles

Selected least-squares fitted Mössbauer data for sample **1-5** and log(A) versus T plot (A = Area of the full spectrum) with the fit of the Debye temperature. Hyperfine Mössbauer parameters of iron(II) ions at various temperatures are reported in the table for each sample. δ, $\Delta_{EQ}$ and Γ stand for the isomer shift vs metallic α-Fe at room temperature, the quadrupole splitting and the half-height line width, respectively. Values in parentheses are the error bars of statistical origin. Underline values without error bars were fixed during the fitting.
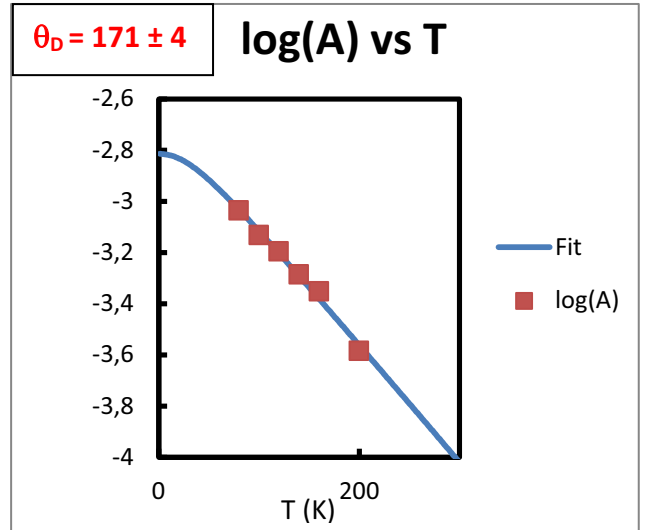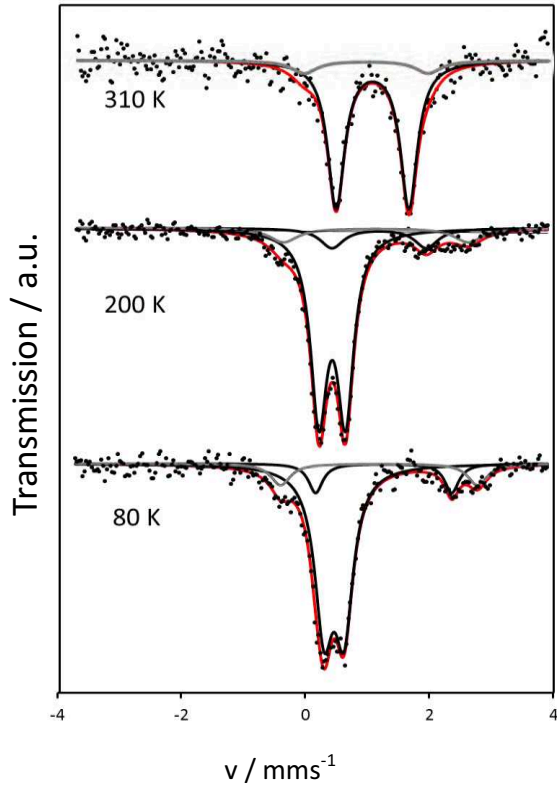
| T (K) | HS doublet | | | HS doublet | | | LS doublet | | | Area |
|-------|------------|------------|------------|------------|------------|------------|------------|------------|------------|----------|
| | $\delta$ | $\Delta E_Q$ | $\Gamma/2$ | $\delta$ | $\Delta E_Q$ | $\Gamma/2$ | $\delta$ | $\Delta E_Q$ | $\Gamma/2$ | |
| 310 | 1.07(1) | 1.18(2) | 0.17(1) | 0.96(1) | 2.00(4) | 0.25 | | | | 89/11/0 |
| 200 | 1.18(4) | 1.52(8) | 0.23(3) | 1.13 | 2.99 | 0.28(3) | 0.421(4) | 0.427(7) | 0.163(5) | 12/10/78 |
| 160 | 1.12(1) | 1.94(1) | 0.23(1) | 1.14(7) | 2.99(8) | 0.25 | 0.437(6) | 0.388(7) | 0.165(8) | 12/10/78 |
| 140 | 1.19(6) | 2.06(9) | 0.23 | 1.18(6) | 3.06(8) | 0.23 | 0.447(6) | 0.371(9) | 0.164(7) | 12/10/78 |
| 120 | 1.26(3) | 2.16(9) | 0.22 | 1.21(7) | 3.08(9) | 0.25 | 0.443(5) | 0.381(9) | 0.169(7) | 13/10/77 |
| 100 | 1.22(5) | 2.24(1) | 0.25 | 1.17(5) | 3.12(9) | 0.22 | 0.456(5) | 0.355(7) | 0.168(7) | 12/10/78 |
| 80 | 1.26(5) | 2.20(1) | 0.20 | 1.19(5) | 3.20(9) | 0.20 | 0.461(9) | 0.33(1) | 0.18(1) | 12/11/77 |

Sample **1** (107 nm)

199

$\theta_D = 169 \pm 5$

log(A) vs T
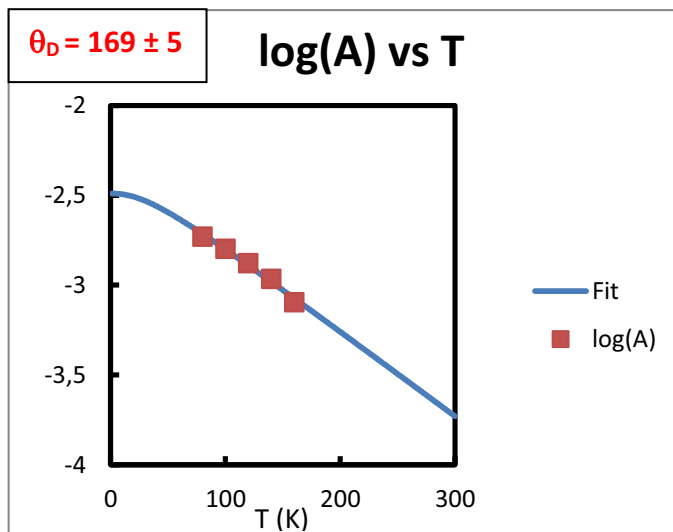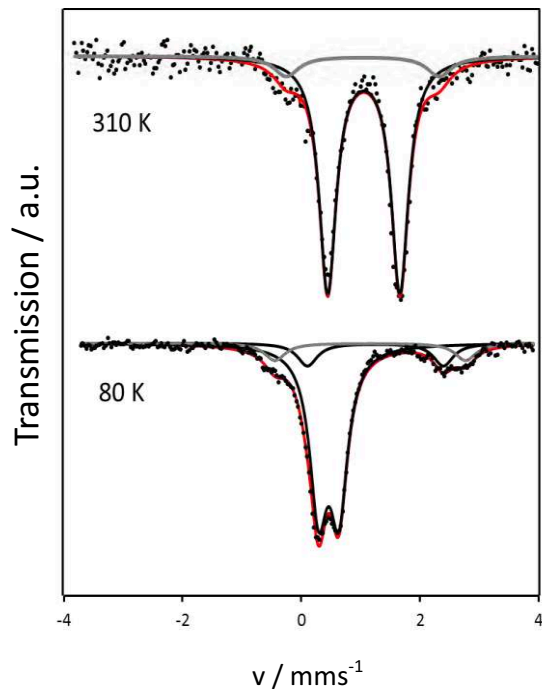
| T (K) | HS doublet | | | HS doublet | | | LS doublet | | | Area |
|-------|------------|----------|----------|------------|----------|----------|------------|----------|----------|----------|
|       | $\delta$ | $\Delta E_Q$ | $\Gamma/2$ | $\delta$ | $\Delta E_Q$ | $\Gamma/2$ | $\delta$ | $\Delta E_Q$ | $\Gamma/2$ |          |
| 310   | 1.047(5) | 1.19(1)  | 0.169(9) | 1.02(8)  | 2.21(2)  | 0.25(2)  |          |          |          | 89/11/0  |
| 160   | 1.19(5)  | 2.07(9)  | 0.17     | 1.16(7)  | 3.08(1)  | 0.22     | 0.437(8) | 0.367(1) | 0.169(8) | 12/10/78 |
| 140   | 1.17(3)  | 2.08(5)  | 0.18(5)  | 1.18(3)  | 3.10(7)  | 0.21(6)  | 0.449(4) | 0.346(6) | 0.167(6) | 12/11/77 |
| 120   | 1.21(4)  | 2.19(7)  | 0.23(7)  | 1.13(3)  | 3.16(8)  | 0.22(7)  | 0.454(4) | 0.359(6) | 0.172(5) | 12/11/77 |
| 100   | 1.23(3)  | 2.19(5)  | 0.21(5)  | 1.16(3)  | 3.14(8)  | 0.23     | 0.464(4) | 0.356(6) | 0.174(5) | 13/11/76 |
| 80    | 1.25(3)  | 2.29(5)  | 0.20(5)  | 1.16(3)  | 3.21(7)  | 0.21(6)  | 0.459(4) | 0.343(6) | 0.181(5) | 13/10/77 |

Sample **2** (71 nm)
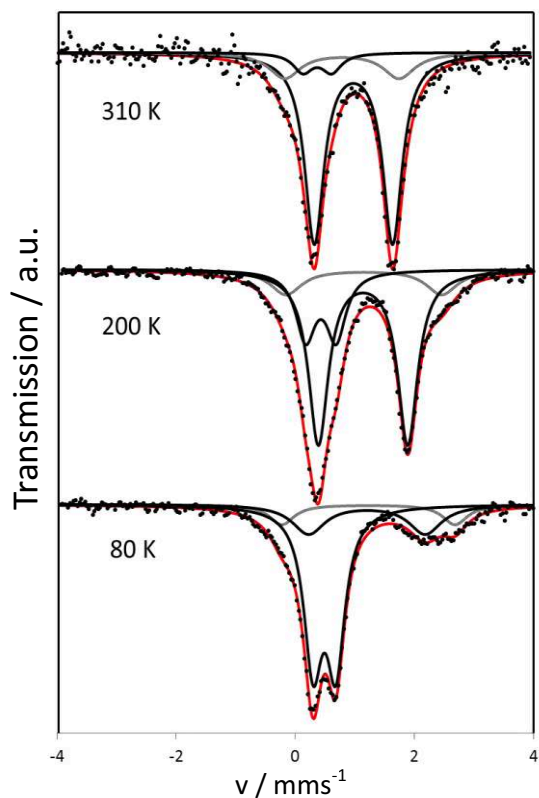
$\theta_D = 197 \pm 9$

log(A) vs T
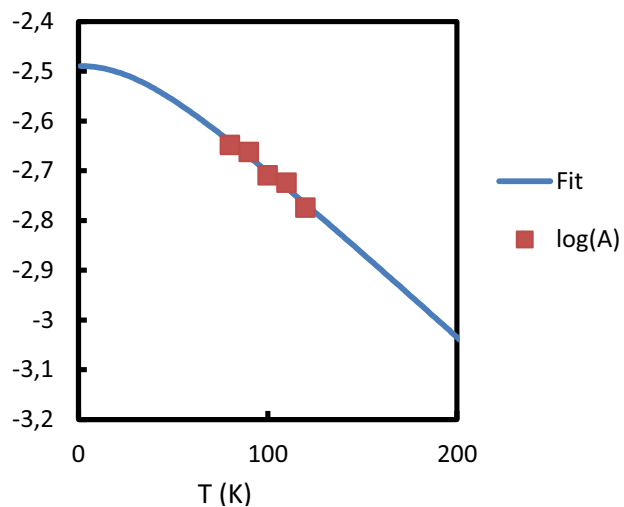
| T (K) | HS doublet | | | HS doublet | | | LS doublet | | | Area |
|---|---|---|---|---|---|---|---|---|---|---|
| | $\delta$ | $\Delta E_Q$ | $\Gamma/2$ | $\delta$ | $\Delta E_Q$ | $\Gamma/2$ | $\delta$ | $\Delta E_Q$ | $\Gamma/2$ | |
| 310 | 1.06 (1) | 1.28(1) | 0.2(1) | 0.89(1) | 2.1 | 0.3 | 0.44 | 0.36 | 0.2 | 80/11/8 |
| 200 | 1.12(1) | 1.502(8) | 0.202(6) | 1.13(3) | 2.62(1) | 0.32(2) | 0.413(9) | 0.51(2) | 0.2(1) | 62/14/24 |
| 120 | 1.11(1) | 1.90(1) | 0.19(1) | 1.19(1) | 2.9 | 0.28(2) | 0.494(6) | 0.359(9) | 0.176(8) | 20/16/64 |
| 110 | 1.11(1) | 1.96(1) | 0.25(1) | 1.19(1) | 2.9 | 0.33(2) | 0.491(3) | 0.369(5) | 0.181(4) | 17/17/66 |
| 100 | 1.13(1) | 1.93(1) | 0.28(1) | 1.26 | 2.9 | 0.30(1) | 0.489(5) | 0.376(8) | 0.178(4) | 17/16/67 |
| 90 | 1.15(1) | 1.99(1) | 0.33(1) | 1.26(2) | 2.9 | 0.34(1) | 0.489(4) | 0.380(6) | 0.183(5) | 18/15/67 |
| 80 | 1.15 | 1.96(1) | 0.33(1) | 1.22(1) | 2.91(1) | 0.25 | 0.487(5) | 0.383(8) | 0.187(7) | 22/12/66 |

Sample **3** (10 nm)

201
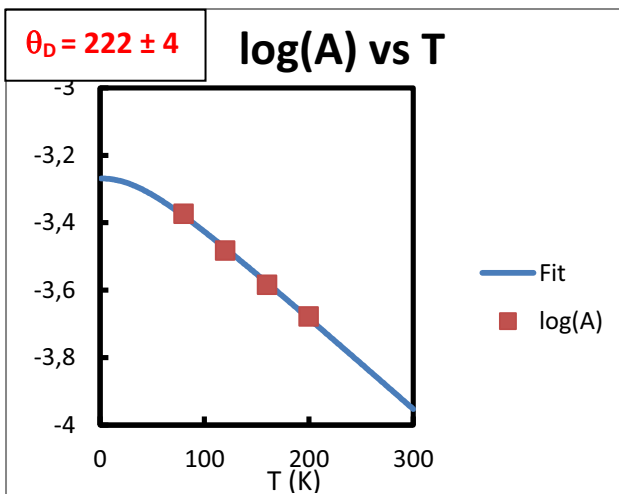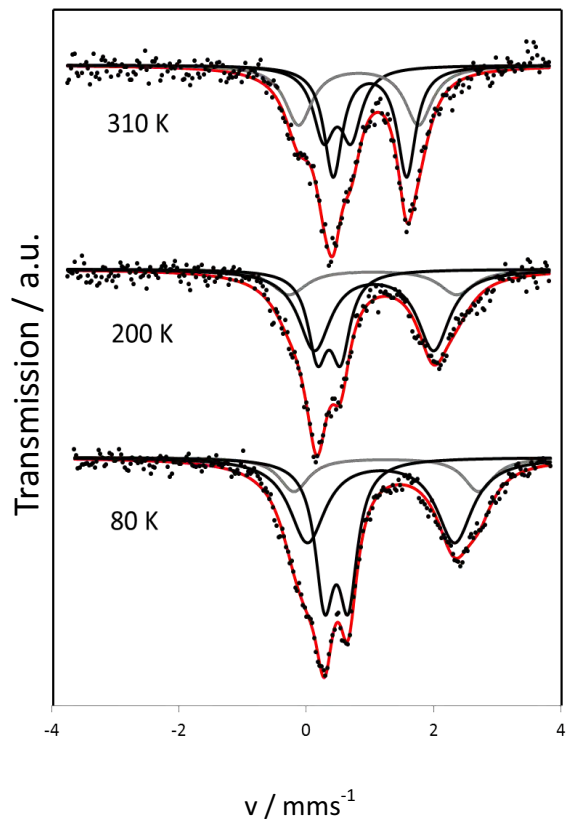
| T (K) | HS doublet | | | HS doublet | | | LS doublet | | | Area |
|---|---|---|---|---|---|---|---|---|---|---|
| | $\delta$ | $\Delta E_Q$ | $\Gamma/2$ | $\delta$ | $\Delta E_Q$ | $\Gamma/2$ | $\delta$ | $\Delta E_Q$ | $\Gamma/2$ | |
| 310 | 1.06(1) | 1.22(3) | 0.20(1) | 0.92(1) | 2.01(1) | 0.28(2) | 0.51(1) | 0.49(1) | 0.20(1) | 63/21/16 |
| 200 | 1.12(1) | 1.85(1) | 0.3(1) | 1.1 | 2.6 | 0.33(1) | 0.42(1) | 0.36(2) | 0.18(1) | 51/18/31 |
| 160 | 1.12(1) | 2.04(1) | 0.28(1) | 1.2 | 2.8 | 0.25(1) | 0.46(1) | 0.35(1) | 0.18(1) | 48/13/39 |
| 120 | 1.15(1) | 2.22(1) | 0.29(1) | 1.2 | 2.8 | 0.27(1) | 0.47(1) | 0.36(1) | 0.17(1) | 42/18/40 |
| 80 | 1.17(1) | 2.31(1) | 0.34(1) | 1.25(5) | 2.9 | 0.28(1) | 0.472(9) | 0.37(1) | 0.18(1) | 46/15/39 |

Sample **4** (3 nm)

$\theta_D = 261 \pm 6$

**log(A) vs T**
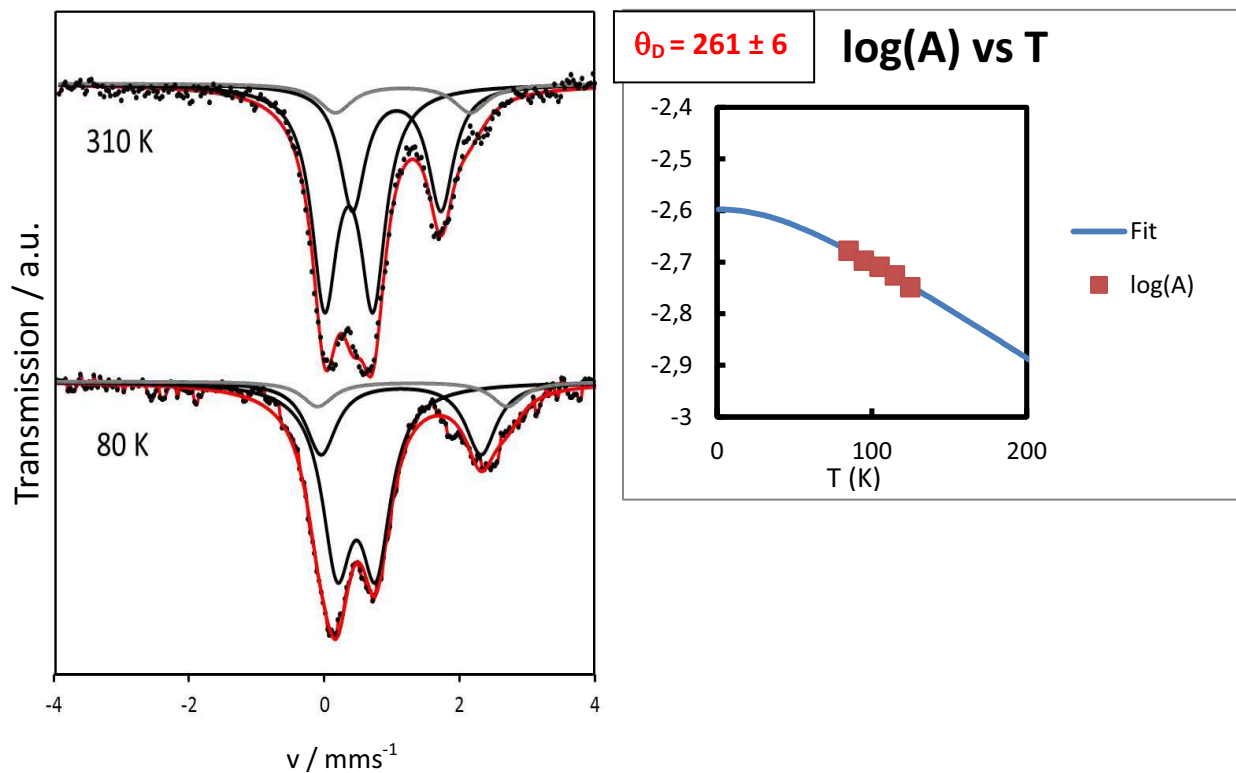
| T (K) | HS doublet | | | HS doublet | | | LS doublet | | | Area |
|---|---|---|---|---|---|---|---|---|---|---|
| | $\delta$ | $\Delta E_Q$ | $\Gamma/2$ | $\delta$ | $\Delta E_Q$ | $\Gamma/2$ | $\delta$ | $\Delta E_Q$ | $\Gamma/2$ | |
| 310 | 1.054(8) | 1.31(1) | 0.23(1) | 1.14(2) | 2.0 | 0.3 | 0.348(7) | 0.68 | 0.224(8) | 33/10/56 |
| 125 | 1.09(1) | 2.31(1) | 0.23(1) | 1.31(1) | 2.80(1) | 0.30(1) | 0.478(6) | 0.57(1) | 0.253(8) | 30/6/64 |
| 115 | 1.10(1) | 2.34(1) | 0.29(1) | 1.34(1) | 2.80(6) | 0.3 | 0.483(6) | 0.566(8) | 0.256(7) | 30/7/63 |
| 105 | 1.11(1) | 2.33(2) | 0.26(1) | 1.29(1) | 2.8 | 0.26(1) | 0.475(7) | 0.55(1) | 0.268(9) | 26/10/64 |
| 95 | 1.13(1) | 2.37(1) | 0.28(1) | 1.32(1) | 2.8 | 0.30(1) | 0.472(9) | 0.56(1) | 0.26(1) | 29/8/63 |
| 85 | 1.13(1) | 2.36(1) | 0.27(1) | 1.3 | 2.8 | 0.28(1) | 0.47(1) | 0.57(1) | 0.27(1) | 28/10/63 |

Sample **5** (2 nm)

# Annex 4: List of Publications

1) **Haonan Peng**, Simon Tricard, Gautier Félix, Gábor Molnár, William Nicolazzi, Lionel Salmon* and Azzedine Bousseksou*
   Re-Appearance of Cooperativity in Ultra-Small Spin-Crossover [Fe(pz){Ni(CN)$_4$}] Nanoparticles
   *Angew. Chem. Int. Ed.*, 2014, 53, 10894-10898 (**Frontispiece**)

2) **Haonan Peng**, Gábor Molnár, Lionel Salmon* and Azzedine Bousseksou*
   Matrix-Free Synthesis of Spin Crossover Micro-Rods Showing a Large Hysteresis Loop Centered at Room Temperature
   *Chem. Commun.,* 2015, 51, 9346-9349

3) **Haonan Peng**, Gábor Molnár, Lionel Salmon* and Azzedine Bousseksou*
   Spin Crossover Nanometric and Micrometric Rod-Shaped Particles Synthesized in Homogeneous Acid Media
   **Eur. J. Inorg. Chem.** 2015, 3336–3342

4) Constantin Lefter, Il'ya A. Gural'skiy, **Haonan Peng**, Gábor Molnár, Lionel Salmon, Aurelian Rotaru, Azzedine Bousseksou and Philippe Demont*
   Dielectric and Charge Transport Properties of the Spin Crossover Complex [Fe(Htrz)$_2$(trz)](BF$_4$)
   *Phys. Status Solidi RRL.* 2014, 8, 191–193

5) Gautier Félix, Mirko Mikolasek, **Haonan Peng**, William Nicolazzi, Gábor Molnár, Aleksandr I. Chumakov, Lionel Salmon, and Azzedine Bousseksou*
   Study of the Lattice Dynamics in Spin Crossover Nanoparticles through Nuclear Inelastic Scattering
   *Phys. Rev. B.*, 2015, 91, 024422

6) Constantin Lefter, Simon Tricard, **Haonan Peng**, Gábor Molnár, Lionel Salmon, Philippe Demont, Aurelian Rotaru*, Azzedine Bousseksou
   Metal Substitution Effects on the Charge Transport and Spin Transition Properties of [Fe$_{1-x}$Zn$_x$(Htrz)$_2$(trz)](BF$_4$)
   *J. Phys. Chem. C*. 2015, 119, 8522–8529

7) Jie Luan, Jian Zhou, Zhan Liu, Bowen Zhu, Huisi Wang, Xin Bao*, Wei Liu, Ming Liang Tong*, Guo Peng, **Haonan Peng**, Lionel Salmon and Azzedine Bousseksou
   Polymorphism Dependent Spin Crossover: Hysteretic Two-step Spin Transition with an Ordered [HS–HS–LS] Intermediate Phase
   *Inorg. Chem.* 2015, 54, 5145–5147

Mössbauer Spectroscopy

# Re-Appearance of Cooperativity in Ultra-Small Spin-Crossover [Fe(pz){Ni(CN)$_4$}] Nanoparticles**

Haonan Peng, Simon Tricard, Gautier Félix, Gábor Molnár, William Nicolazzi,
Lionel Salmon,* and Azzedine Bousseksou*

205
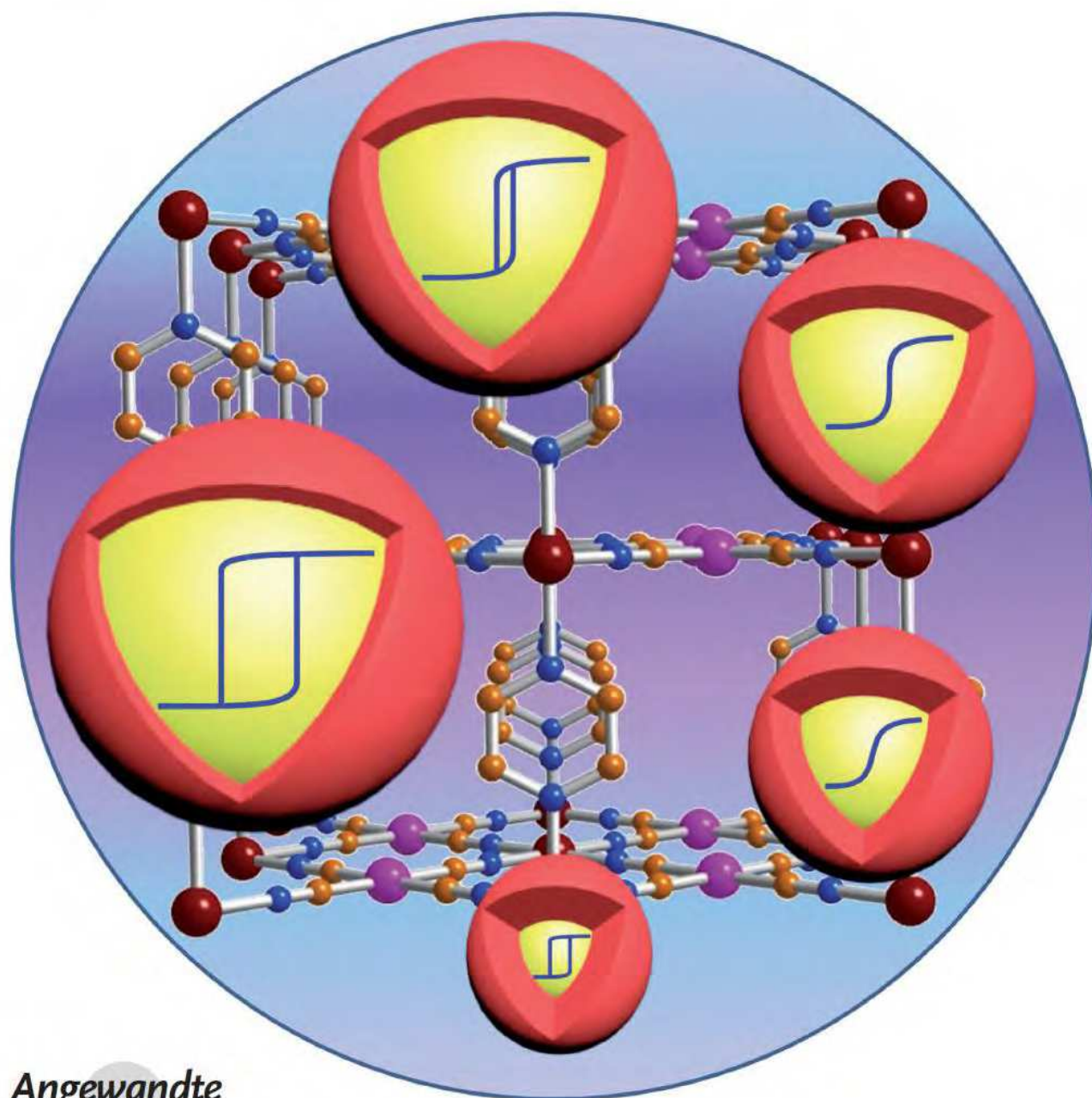
# Synthesis of Spin Cossover Mirco- and Nano-Particles and Study of the Effect of Their Sizes and Morphorlogies on Their Bistability Properties

Nowadays, the idea that molecule can be used as an active element in an electronic device stimulates scientific activity of chemistry and physics laboratories worldwide. The information storage capacity from technological demands is growing exponentially, which relies much on the development of nanosciences. The objective is to store data as quickly as possible in a device as small as possible. One of the most promising strategies is based on the concept of molecular bistability, the switching between two electronic states of a molecule in the same way that a binary switch. It is thus possible to pass in a reversible and detectable manner from one state (OFF = 0) to another state (ON = 1) under the influence of a controlled external stimulus. The spin transition (ST) phenomenon that switches the system between high spin (HS) and low spin (LS) states is a typical example of molecular bistability. The two states can be distinguished with different magnetic, optical and structural properties and can be induced by an external perturbation like the temperature, the light, the pressure, a magnetic field or the inclusion of a guest molecule. When the structural changes associated with the spin transition are transmitted in a cooperative manner across the network molecules, the transitions will occur with steepness and possibly accompanied by hysteresis loop (the first order transition). So, spin transition molecular materials should offer many opportunities in terms of applications in the field of electronics, information storage, digital display, photonics and photo-magnetism. Among the different families of compounds, coordination polymers arouse much interest due to their bistability near room temperature. The judicious choice of ligands and counter-anions make possible to modulate the final properties of these compounds and even in some cases to synergistically combine different physical properties. The work developed in this thesis attempt to address the different issues related to the challenge of coordination polymers based nanoscale materials with spin transition. The synthesis of inorganic bistable materials, their development in micro- and nanoparticles, thin layers, their organization and their physical properties are shown. The materials in the microscopic scale have mostly the same physical properties as those measured at the macroscopic scale. However, at the nanoscale, materials can exhibit physical properties that are far from those of bulk compounds. It is therefore imperative to understand more about the phenomena related to material size decrease to develop nanotechnology. The fundamental study of these nanomaterials is necessary and represents a major challenge today, which is of prime importance for the development of future applications. The development of nanoscale materials through the control of certain systematic models permits to improve our understanding of specific effects at the nanoscale. For example, in the case of spin crossover complex, the most important question is: how downsizing effect influences the transition temperature, the cooperativity and the width of hysteresis loop? In this context, this thesis is devoted to the design and the synthesis of various size spin crossover nano and micro-materials with different morphologies. To accomplish this, we developed the reverse-micelle technique and adopted innovative matrix-free synthetic approaches.

**Auteur :** Haonan PENG

**Titre :** Synthèse de micro- et nanoparticules à transition de spin : étude des effets de tailles et de morphologies sur leurs propriétés de bistabilité

**Directeurs de thèse :** Lionel SALMON et Azzedine BOUSSEKSOU

**Date de soutenance :** Le 20 juillet 2015

## Résumé de thèse

De nos jours, l'idée qu'une molécule puisse être utilisée comme élément actif dans un dispositif électronique stimule l'activité scientifique des laboratoires de chimie et de physique dans le monde entier. Le phénomène de transition de spin (TS) qui commute une molécule entre états haut spin (HS) et bas spin (BS) est un exemple typique de bistabilité moléculaire. Ainsi, les matériaux moléculaires à transition de spin devraient offrir de nombreuses possibilités en termes d'applications dans le domaine de l'électronique, le stockage de l'information, l'affichage numérique, la photonique et le photo-magnétisme. Les matériaux à l'échelle microscopique ont généralement les mêmes propriétés physiques que celles mesurées à l'échelle macroscopique. Cependant, à l'échelle nanométrique, les matériaux peuvent présenter des propriétés physiques qui sont différentes de celles des composés massifs. Il est donc impératif de mieux comprendre les phénomènes liés à la diminution de la taille pour développer les nanotechnologies. Dans le cas des complexes à transition de spin, une question importante émerge : comment influence la réduction de taille de ces matériaux sur la température de transition, la coopérativité et la largeur de la boucle d'hystérésis (effet mémoire) ? Dans ce contexte, cette thèse est consacrée à la conception et à la synthèse de nano- et microparticules à transition de spin de différentes tailles et de différentes morphologies. Pour ce faire, nous avons développé la technique des micelles inverses et adopté de nouvelles approches de synthèse innovantes en l'absence de matrice.

## Mots clé

Transition de Spin, Complexe de fer, Nanoparticules, Micelles Inverses, Proprieties Elastiques, Proprieties Magnetiques, Proprieties Electriques